UNIVERSITY OF TECHNOLOGY SYDNEY

DOCTORAL THESIS

Electron beam processing and spectroscopic characterisation of 2D materials and novel nanostructures

---

Author:
Christopher ELBADAWI

Supervisor:
Assoc. Prof. Charlene LOBO
Prof. Igor AHARONOVICH
Prof. Kostya OSTRIKOV

A thesis submitted in fulfillment of the requirements
for the degree of Doctor of Philosophy

in the

School of Mathematical and Physical Sciences

June 2, 2018

Declaration of Authorship

I, Christopher ELBADAWI, declare that this thesis titled, "Electron beam processing and spectroscopic characterisation of 2D materials and novel nanostructures" and the work presented in it are my own. I confirm that:

- This work was done while in candidature for a research degree at this University.
- Where any part of this thesis has previously been submitted for a degree or any other qualification at this University or any other institution, this has been clearly stated.
- Where I have consulted the published work of others, this is always clearly attributed.
- Where I have quoted from the work of others, the source is always given. With the exception of such quotations, this thesis is entirely my own work.
- I have acknowledged all main sources of help.
- Where the thesis is based on work done by myself jointly with others, I have made clear exactly what was done by others and what I have contributed myself.
- This research is supported by an Australian Government Research Training Program Scholarship.

Signed: Production Note:
Signature removed prior to publication.

Date: 6/6/2018

Abstract

Interest in the inorganic two-dimensional (2D) materials black phosphorus (BP) and hexagonal boron nitride (hBN) has exponentially risen due to the distinct advantages they possess over their bulk counterparts. Excellent and unique mechanical, electronic and optical properties have recently been discovered which can potentially span a large range of conceptually new applications such as high speed flexible electronics, sub-diffractional nanophotonic devices, strain engineered variable sensors and robust quantum information processing systems.

To take advantage of these unique properties a greater understanding of the underlying chemical mechanisms involved in the manipulation/modification of BP and hBN is required. In this project, the nanofabrication tool focused electron beam induced processing (FEBIP) is used to do this all within a scanning electron microscope (SEM). FEBIP is a nanofabrication technique in which electrons are used to decompose surface adsorbed precursor molecules, typically under a constant partial pressure of a precursor gas. A highly focused beam can be used to deposit or etch nanoscale structures on a solid substrate. This technique differentiates itself from classical growth methods through other unique aspects, which include; growth of fully realised three-dimensional (3D) nanostructures, selective surface termination, defect generation and real-time imaging of chemical reaction fronts.

The aim of this project was to elucidate experimentally the fundamental processes that govern the chemical reactions occurring during FEBIP. The first study outlined in this thesis involves the creation of an automated scanning program to reliably manipulate the electron beam for accurate data acquisition and pattern formation. To showcase these capabilities, 3D Pt nanostructures such as high aspect ratio pillars and helices fabricated with $Pt(PF_3)_4$-mediated electron beam induced deposition. Post-growth annealing in a water vapour environment was found to improve Pt deposit purity by volatilising phosphorus contaminants in the form of phosphoric acid. Annealing in H_2O under optimized conditions, yielded platinum that is pure within the detection limit of wavelength dispersive x-ray spectroscopy.

Following from the information obtained through purification of phosphorus contaminants, attention was focused on the simulation of degradation of the highly unstable few-layer BP via electron beam irradiation performed *in-situ*. The real time imaging capabilities allowed for rapid stabilisation techniques to be found via controlled gas mixing and temperature dependent studies. The degradation pathway was found to proceed through the creation of phosphoric acid in a H_2O environment and is shown to be dependent on temperature. A low temperature heat cycle was then formulated to remove intercalated water and oxygen species to cease the degradation of few-layer BP for up to four weeks per heat cycle.

Next, chemical dry etching of hexagonal Boron Nitride (hBN) was performed in a water vapour environment to create nanostructure geometries such as high resolution patterns, nanoribbons, and particles with high fidelity. Steps are also taken toward deterministic generation of defects and single photon emitters in hBN. The product of the electron induced dissociation of hBN at the surface of the material results in the production of nitrogen and boron radicals which then react with H_2O to produce boric and nitric acids. These then can be used as etch precursors for other materials such as silver nanowires. This two step etching process was then reimagined using an *in-situ* delocalised plasma and electron beam irradiation to widen the scope of etch-able materials such as silver, using a gas phase etch process.

These results broaden the scope of material selection available in FEBIP. The exploitation of the unique aspects demonstrated with this technique in this project increases the applicability and versatility of FEBIP as a prominent tool for nanofabrication of 2D materials and complex 3D nanostructures. Furthermore, the results presented here constitute' the first step towards integration of few-layer BP and hBN into high-performance optoelectronic devices, quantum information systems and various environmental sensor applications.

Acknowledgements

Firstly, I would like to thank my supervisors and advisors Assoc. Prof. Charlene Lobo, Prof. Igor Aharonovich, Prof. Milos Toth and Prof. Kostya Ostrikov who gave me the opportunity to undertake this project. Throughout my candidature I was always given the time, support and guidance as well as creative freedom to pursue developments that may have evolved during my research. All of their hard work and academic expertise has been invaluable to me and for that I am extremely grateful.

The work done in this project would not have been possible without the support of my fellow and former PhD colleagues; Tran Trong Toan, Dr. Olivier Lee, Mehran Kianinia, John Scott, James Bishop, Johannes Froch, Dr. Xu Zaiquan, Minh Nguyen, Kerem Bray, and Mika Tham who would selflessly take their own time to work and assist with my research, thus I would like to extend my gratitude.

I would like to give a big thanks to Geoff McCredie, Katie McBean, Mark Berkahn and Herbert Yuan for their unparalleled technical expertise and continued assistance in the MAU throughout the candidature. I would also like to thank everyone else in the MAU, for which we had to endure the highs and lows together, thanks for all the good times. A special mention must go out to soon to be/former PhD candidates, Joshua Pritchard, Fadi Bonnie and Aaron Colusso for great moral support and friendship over the years.

I must also express thanks to everyone at UTS, I felt very welcomed and was given a lot of opportunities throughout my time here. I was lucky enough to meet people across many disciplines and have befriended many wonderful people over this time. A very special thank-you must go to the beautiful Ali Hunt who was always there for me and supported me during my time here. I would not be in this position without you.

Next, I would like to show my appreciation to all collaborators that I have had the pleasure to work with, including; Prof. Kostya Ostrikov and the plasma team, Dr. Sumeet Walia, Prof. Vipul Bansal and the team at RMIT, Dr. Miroslav Kolibal from BRNO university of technology and Dr. Erin Gloag and the ithree institute who have assisted/allowed me to assist in various projects over the years. A special mention must go to Prof. Kostya Ostrikov and CSIRO for providing a scholarship top-up.

Finally, a special thanks to my family and friends for their continued support, even if I wasn’t deserving of it throughout the candidature. In particular my parents, who have fully supported me wholeheartedly throughout my life, I am forever indebted to you and hope I made you proud.

Publications

Peer-reviewed publications list:

- Pure Platinum Nanostructures Grown by Electron Beam Induced Deposition. **C. Elbadawi**, M. Toth, and C. Lobo. ACS applied materials and interfaces (2013), 5(19), 9372-9376.

- Electron beam directed etching of hexagonal boron nitride. **C. Elbadawi**, T. T. Trang, J. Scott, M. Kolibal, T. Šikola, Q. Cai, L. Li, T. Taniguchi, K Watanabe, M. Toth, I. Aharonovich and C. Lobo. Nanoscale (2016), 16182-16186.

- Ambient stabilization of few-layered black phosphorus by thermal cycling. **C. Elbadawi**, R. Tormo Queralt, X. Zaiquan, J. Bishop, T. Ahmed, S. Kuriakose, S. Walia, M. Toth, I. Aharonovich and C. Lobo. Submitted.

- Robust multicolor single photon emission from point defects in hexagonal boron nitride. T. T. Trang, **C. Elbadawi**, C. Lobo, D. Totonjian, G. Grosso, H. Moon, I. Aharonovich, and M. Toth. ACS Nano (2016), 7331-7338.

- Ambient protection of few-layer black phosphorus via sequestration of reactive oxygen species. S. Walia, S. Balendhran, T. Ahmed, M. Singh, **C. Elbadawi**, M.D. Brennan, P. Weerathunge, M. Karim, F. Rahman, A. Rassell, J. Duckworth, A. Ramanathan, G.E. Collis, C.J. Lobo, M. Toth, J.C Kotsakidis, B. Weber, F. Michael, J.M. Dominguez-Vera, M.J.S. Spencer, I. Aharonovich, S. Sriram, M. Bhaskaran and V. Bansal. Advanced materials (2017) May 12.

- Localization of narrowband single photon emitters in nanodiamonds. K. Bray, R. Sandstrom, **C. Elbadawi**, M. Fischer, M. Schreck, O. Shimoni, C. Lobo, M. Toth, and I. Aharonovich. ACS applied materials and interfaces (2016), 8(11), 7590-7594.

- Engineering and localization of quantum emitters in large hexagonal boron nitride layers. S. Choi, T. T. Trang, **C. Elbadawi**, C. Lobo, W. Xuewen, S. Juodkazis, G. Seniutinas, M. Toth, and I. Aharonovich. ACS applied materials and interfaces (2016), 29642-29648.

- Growth of Three Dimensional Nanostructures by Electron Beam Induced Deposition. J. Bishop, **C. Elbadawi**, M. Kianinia, J. Pritchard, C. Lobo, and M. Toth. Submitted.

- Micro-Patterned Surfaces that Exploit Stigmergy to Inhibit Biofilm Expansion. E. Gloag, **C. Elbadawi**, C. Zachreson, I. Aharonovich, M. Toth, I. Charles, L. Turnbull and C. Whitchurch. Frontiers in Microbiology (2017), 7 (2016): 2157.

- Single Photon Emission from Plasma Treated 2D Hexagonal Boron Nitride. Z. Xu, **C. Elbadawi**, T. T. Trang, M. Kianinia, X. Li, D. Liu, T. B. Hoffman, M. Nguyen, S. Kim, J. H. Edgar, X. Wu, L. Song, S. Ali, M. Ford, M. Toth and I. Aharonovich. Submitted.

- Deterministic Nanopatterning of Diamond Using Electron Beams. J. Bishop, M. Fronzi, **C. Elbadawi**, V. Nikam, J. Pritchard, M. Ford, I. Aharonovich, C. J. Lobo and M. Toth. ACS Nano (2017), 10.1021/acsnano.8b00354 24 Jan 2018.

- Ultra-bright emission from hexagonal boron nitride defects as a new platform for bio-imaging and bio-labelling. **C. Elbadawi**, T. T. Trang, O. Shimoni, D. Totonjian, C. J. Lobo, G. Grosso, H. Moon, D.R. Englund, M.J. Ford, I. Aharonovich and M. Toth. SPIE BioPhotonics Australasia. Vol. 10013. International Society for Optics and Photonics, 2016.

Conference Presentations

Conference presentation list:

- Nanotechnology Workshop for Early Career Researchers, Flinders University, July 2013. Oral presentation: Localized fabrication of pure platinum nanostructures – Awarded best presentation
- FEBIP 2016, TU Wien Austria, Vienna July 2016. Oral presentation: Electron beam restructuring of hexagonal Boron Nitride for applications in photonics and polaritonics
- SPIE BioPhotonics Australasia, Adelaide October 2016. Oral presentation: "Ultra-bright emission from hexagonal boron nitride defects as a new platform for bio-imaging and bio-labelling." SPIE BioPhotonics Australasia. Vol. 10013. International Society for Optics and Photonics, 2016.
- COMMAD 2016, UNSW, Sydney 2016 Oral Presentation: Electron beam driven defect creation in hexagonal Boron Nitride for photonic applications
- 253rd American Chemical Society National Meeting and Expo, San Francisco 2017 Oral presentation: Directed deposition and etching using electron beam and plasma irradiation

List of Figures

List of Abbreviations

2D	Two-Dimensional
AFM	Atomic Force Microscope
BP	Black Phosphorus
BSE	Backscattered Electron
CASINO	Monte Carlo Simulation of Electron Trajectory in Solids
CCD	Charge-Coupled Device
CNT	Carbon Nanotubes
CVD	Chemical Vapour Deposition
DFT	Density Functional Theory
EBID	Electron Beam Induced Deposition
EBIE	Electron Beam Induced Etching
EBL	Electron Beam Lithography
EDS	Energy-Dispersive X-ray Spectroscopy
ESEM	Environmental Scanning Electron Microscope
FEBIP	Focused Electron Beam Induced Processing
FLBP	Few Layer Black Phosphorus
FEG	Field Emission Gun
FIB	Focused Ion Beam
FWHM	Full Width at Half-maximum
GIS	Gas Injection System
hBN	Hexagonal Boron Nitride
HBT	Hanbury Brown and Twiss
$\mathbf{MoS_2}$	Molybdenum Disulfide
$\mathbf{MoO_3}$	Molybdenum trioxide

NIDAQ	National Instruments Data Acquisition Device
RF	Radio Frequency
RIE	Reactive Ion Etching
ROS	Reactive Oxygen Species
PSB	Phonon Side Band
PL	Photoluminescence
SAED	Selected Area Electron Diffraction
SEM	Scanning Electron Microscope
SDD	Silicon Drift Detector
SPE	Single Photon Emitter
TMD	Transition Metal Dichalcogenides
TEM	Transmission Electron Microscope
WDS	Wavelength-Dispersive X-ray Spectroscopy
ZPL	Zero Phonon Line

List of Symbols

FEBIP model

Adsorption

N_d	Concentration of precursor adsorbates (molecules/Å^2)
s_d	Precursor adsorbate sticking coefficient
J_d	Precursor molecular flux (Å$^2 s^{-1}$)
p	Gas pressure (Pa)
m	Molecular mass of the precursor (g)
A_d	Precursor molecule surface area (Å^2)
t	Time (s)

Desorption

E_d	Energy barrier for desorption (J/molecule)
v_0	Vibrational frequency of the adsorbed molecule (Hz)

Diffusion

r	Radial distance from electron beam axis (Å)
D	Diffusion coefficient (Å^2 s^{-1})
E_{diff}	Energy barrier for diffusion (J/molecule)
T	Temperature (K)
k_b	Boltzmann constant (J/K)
D_0	Diffusion prefactor (Å^2 s^{-1})

Dissociation	
N_D	Number of deposited molecules per unit area (molecules/Å^2)
f	Electron flux (e/Å^2/s)
σ_d	Adsorbate dissociation cross-section (Å^2)
V_D	Volume of the deposited material (Å^3)

Interaction volume	
A	Atomic weight (g/mol)
EL	Landing energy (keV)
p	Density (g/cm^3)
Z	Atomic number

Typical Experimental parameters used for studies completed in this thesis

ESEM conditions

Beam current	0.1 - 8 nA
Accelerating voltages	1 - 30 keV
gas pressures	8 - 20 Pa

Plasma Conditions

Frequency	131 MHz
Power	5 W

PL conditions

Laser frequencies	533 nm, 632 nm
Power	300 μW

Raman Conditions

Laser frequencies	633 nm

Contents

Chapter 1

Preamble

1.1 Introduction

A key driving force behind recent nanoscience research has been investigation of the material properties which differ significantly from their bulk counterparts [1–3]. Two-dimensional (2D) materials are a prime example of this [4–6], where enormous work has been put into understanding the distinct nature of 2D materials in recent times (see figure 1.1). Compared to traditional three-dimensional (3D) bulk semiconductors, the electronic and optical properties of 2D materials often results in fascinating phenomena. This can be attributed to the unique properties possessed by 2D materials, such as hyperbolicity [7] and strong in-plane anisotropy [8]. This allows for conceptually new uses such as strong spontaneous emission enhancement [9], strain engineered conductance [10], negative refraction [11], phonon polariton propagation [12] or strong exciton-phonon interactions [13, 14] as examples.

Figure 1.2 showcases the breadth of 2D materials' electronic properties. From graphene which exhibits a zero band gap [16] to black phosphorus (BP) and molybdenum disulfide (MoS_2) which showcase variable semi-conducting properties and contrasts well with the large band gap, and highly insulating hexagonal boron nitride (hBN). In this project the main focus will be to exploit the exceptional properties of hBN and BP, and push for potential integration with unique applications. Particular highlights include a large push for photonic and optoelectronic [1] devices due to

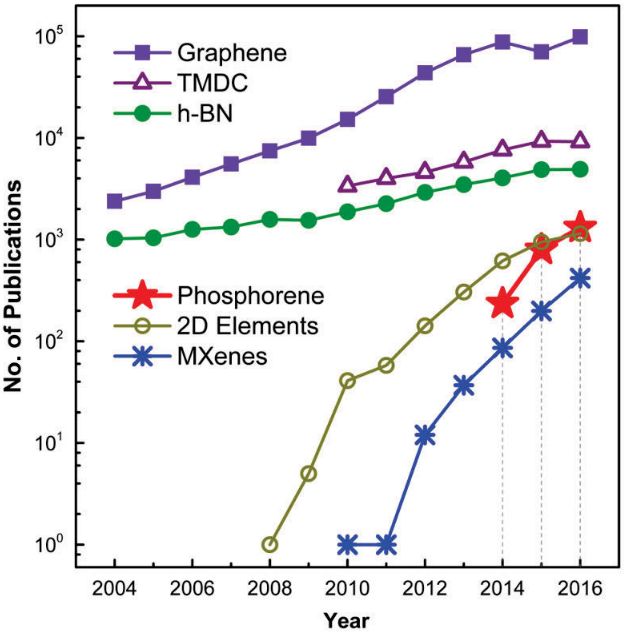

FIGURE 1.1: A comparison of the number of publications for 2D materials during the last decade is (the y axis is log scale) [15].

the discovery of room temperature ultra bright single photon emitters in hBN [17]. BP also possesses quite unique properties which include strong mechanical and electronic properties for integration with high speed flexible electronic devices [18]. In fact, few-layer BP has the added advantage of in plane anisotropy [19–21], which allows for layer dependent variable bandgap [15] and stress/strain response for functional sensors [10, 22].

Despite the advantageous and unique material properties of hBN and BP, fundamental issues still exist with the manipulation of these materials. A greater understanding in the underlying mechanisms and chemical manipulation of the 2D materials at the nanoscale is required and there is an increasing requirement for new nanofabrication tools and techniques to do this [23]. One such method is called focused electron beam induced processing (FEBIP) [24]; a nanofabrication technique which has drawn considerable appeal in terms of the novel capabilities offered.

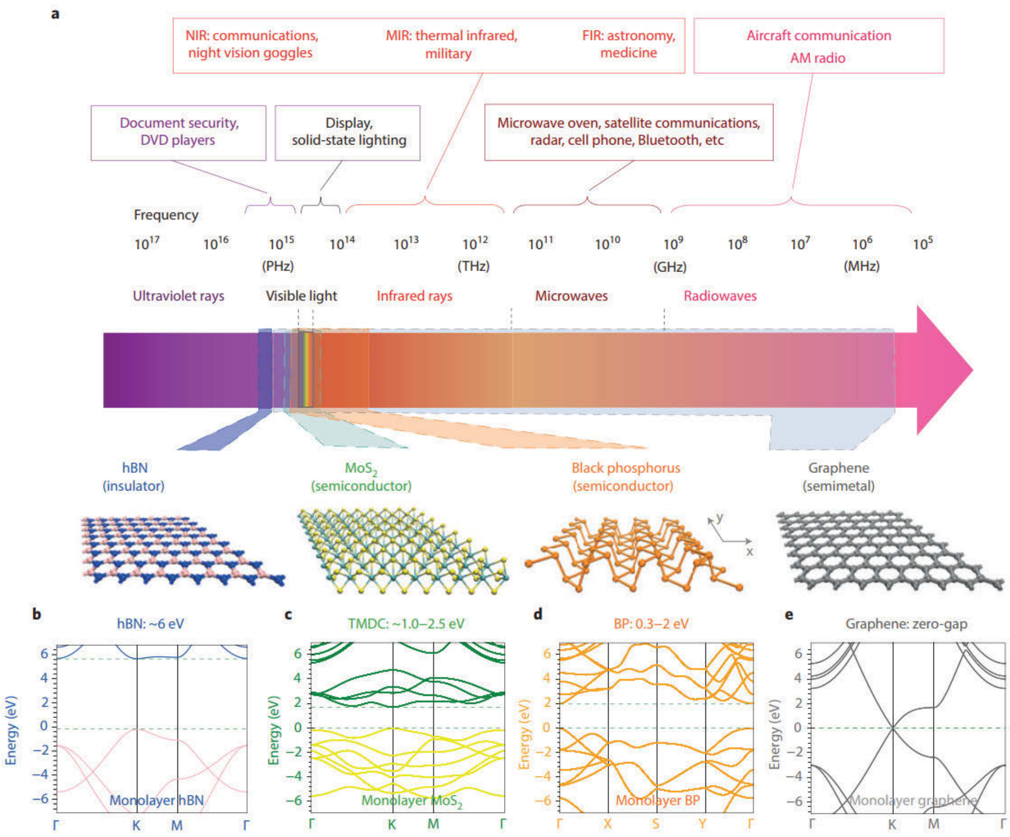

FIGURE 1.2: (a) The electromagnetic spectrum and the applications that utilise the different spectral ranges are presented in the top portion. The effective electromagnetic spectral range and atomic structures of hBN, MoS_2, BP and graphene are shown in the bottom of the panel, respectively. The band structures of single-layer hBN (b), MoS_2 (c), BP (d) and graphene (e) are illustrated. [1]

1.1.1 Nanofabrication

FEBIP is a vapour phase nanofabrication technique that can deposit or etch material deterministically with nanoscale precision. The FEBIP process is a dry chemical dissociation technique which targets a specific material. It works by scanning an electron beam over a substrate in the presence of a precursor gas. The electron beam interacts with the adsorbed precursor or substrate, locally decomposing it into either volatile or non-volatile components. This processing technique then allows for quick, precise control and maneuverability for the creation of high resolution patterns at predefined locations directly within a scanning electron microscope. The unique combination of chemical deposition/etching and spatial resolution has seen a surge in the creation of functional nanostructures using FEBIP [25–28]. Examples include; 3D helices displaying circular dichroism [29], ultra-sharp [30] or magnetic [31] atomic force microscope tips and field emission devices [32]. Having the capability of creating structures with such fine control and reproducibility will be advantageous for probing 2D materials and exploring very fascinating theorised properties [33, 34] where nanoscale precision is needed.

1.1.2 FEBIP and 2D materials

FEBIP has previously been deployed on the 2D material graphene and carbon in general, where extensive work has been done using electron beam induced etching (EBIE) in the presence of water. This work is well characterised and understood and this system has been used to etch a wide range of organic materials including; graphene [35, 36], single and multi-walled carbon nanotubes [37], single crystal [38, 39] and nanocrystalline diamond [40]. However, broad deployment and exploitation of other 2D materials, namely hBN and BP is limited. On one end, device processing and nanomanipulation of hBN is extremely restricted owing to the extreme chemical and thermal inertness of this material [41]. While the other, BP is an unstable material under standard atmospheric conditions [42]. This work will mainly focus on electron beam induced processing of these inorganic 2D materials. FEBIP in this instance will not solely rely on etching or deposition, but will also utilize a number of unique capabilities developed during the course of this project. Recent examples include; fully realised 3D dimensional nanostructures (as seen in Chapter 4), deterministic surface termination [43], crystal orientation selective etching [39] and real time imaging of chemical reaction fronts (Chapter 5). In terms of applicability with this project, FEBIP versatility will be used to realise a deep understanding of the reaction processes in material such as BP (Chapter 5), and manipulate 2D materials such as hBN by driving various chemical reactions at the nanoscale using the electron beam for defect generation and geometric control (Chapter 6, 7).

1.2 Aims and objectives

The overall aim of this project is to develop a nanofabrication tool capable of manipulating 2D materials of hBN and few-layer BP which have inherent difficulties in processing. A deeper understanding of the chemical processes occurring during the irradiation is also required to exploit these reactions for new and novel ways to perform FEBIP. The specific aims, processes and applications that will be studied in this work directly are:

- To create an automated pattern generator to control e-beam processing and allow for robust quantitative result extraction for FEBIP and simultaneously have the ability to directly etch or deposit complex nanostructured arrays. Direct examples of 3D nanostructure fabrication will be shown using EBID and a inorganic platinum precursor (Chapter 4).
- Use of FEBIP to chemically dry etch and control the nanostructure dimensions of hBN and few-layer BP (Chapter 5, 7).
- Applications of FEBIP for use in photonics by creation of defects and single photon emitters in the material hBN (Chapter 6).
- Investigation of a material system response in various environments using FEBIP. Examples include the simulation of degradation via electron beam irradiation of few-layer BP in various environments to drive chemical reactions and ultimately stabilise the material through temperature dependent studies (Chapter 5). Another being the creation of reactive products, such as nitric acid via a two step EBIE or universal gas phase etching system, which allows for a greater number of metals to be etched via EBIE (Chapter 8)

Chapter 2

Background

2.1 Focused electron beam induced processing

In this project FEBIP will be used to create complex high resolution 3D nanostructures (Chapter 4) and to dry chemical etch the 2D materials BP (Chapter 5) and hBN (Chapter 7). The unique abilities of this technique will also be employed for the observation of chemical reaction fronts in real time of BP and defect generation of hBN as shown in Chapter 5 and Chapter 6 respectively. A thorough understanding of the technique is needed to achieve these goals. This chapter will give an outline of the standard model used for FEBIP and an in depth look at the electron, precursor and substrate interactions and how each parameter affects the results obtained in the project.

2.1.1 How FEBIP works

FEBIP is a deterministic direct write technique where an electron beam is used to drive chemical reactions at the substrate-electron beam interface in the presence of a precursor gas. A schematic of the FEBIP process is shown in figure 2.1. The type of chemical reaction that takes place is determined by the precursor introduced and/or the type of substrate. FEBIP can be broken up into two main categories, deposition and etching as shown in figure 2.2.

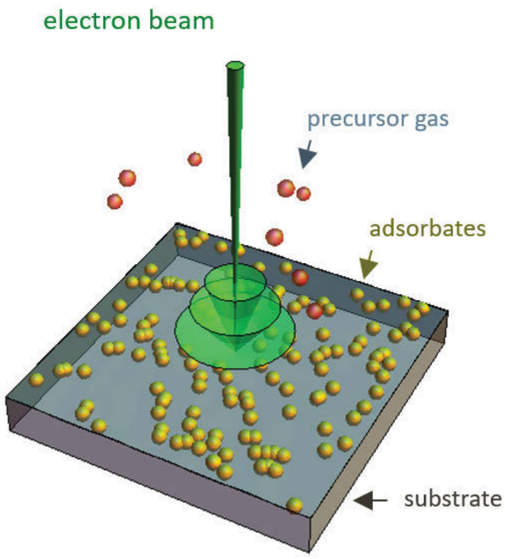

FIGURE 2.1: A simple schematic of FEBIP, with the role of the electron beam, precursor molecules, precursor adsorbates and substrate highlighted. Schematic adapted from [44].

2.1.2 Electron beam induced deposition

Vapour-phase fabrication of nanoscale metals most commonly employs organometallic precursors. Gas-mediated, focused electron beam induced deposition (EBID) [45] is one such fabrication technique that offers several advantages over commonly employed technologies like chemical vapor deposition and atomic layer epitaxy. Most significantly, EBID permits room temperature localised deposition with high $(< 10\,\mathrm{nm})$ resolution [46] without the use of lithographic masks and resists [47, 48]. Structures fabricated using EBID include nanodot (as shown in figure 4.5a, which will be described further in Chapter 5) and wire arrays [47–49], magnetic nanowires [50], tips for magnetic force microscopy [51], contacts to nanowires and carbon nanotubes [52], plasmonic nanostructures [53] and metallic seeds used to catalyse the growth of individual nanowires [54]. Complex freestanding three dimensional nanostructures can also be created [28, 29]. The main limitation of EBID without post-purification, is that the deposited materials are typically highly impure, consisting of metal or oxide grains with a diameter of $\sim 1 - 5\,\mathrm{nm}$ embedded in an amorphous matrix rich in precursor

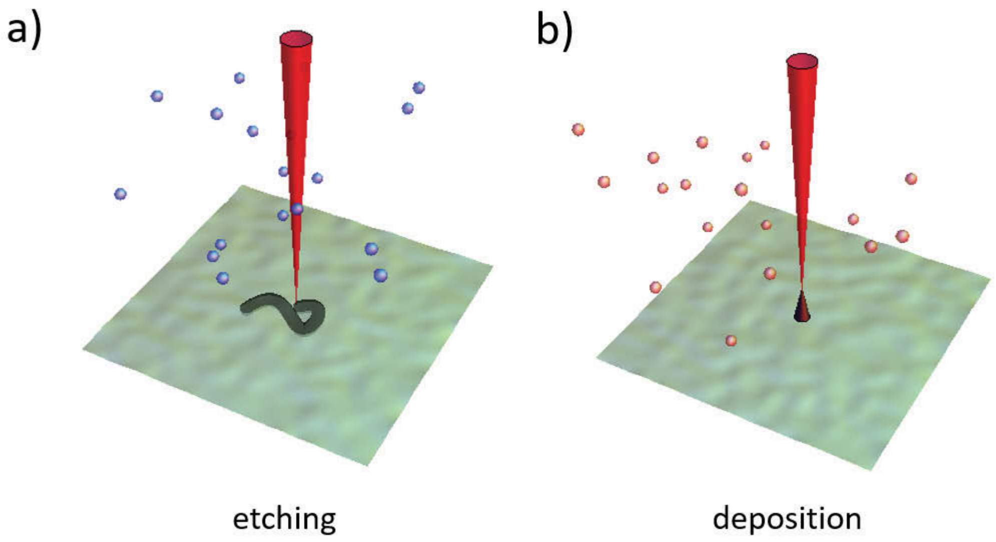

FIGURE 2.2: A schematic of the processes for EBIE (a) and EBID (b). Schematic adapted from [44].

ligands [45, 51, 55–63]. The precursors are often organometallics and the matrix generally contains $\gtrsim 50$ at.% carbon, yielding deposits that behave as granular materials with percolative transport properties [56–59, 64].

The EBID process works by scanning an electron beam over a substrate in the presence of a precursor gas. The incident electrons locally dissociate the adsorbed precursor on the substrate, decomposing it into volatile and non-volatile components. The non-volatile components become pinned to the substrate and form a deposit, as shown in figure 2.2b and the volatile component is released into the gas phase and eventually pumped out of the system.

During deposition however, non-volatile by-products can be produced. These are not easily removed, and result in generally high levels of contamination in EBID. This is one of the main drawbacks of this technique and relatively high purity EBID-grown materials have been realised in a limited number of cases, where (i) low-carbon-content precursors are available [65–71], (ii) substrate heating or precursor gas mixtures are used to improve purity [71–77], (iii) ultra-high-vacuum techniques are used to produce ultra-clean, reactive substrate surfaces [78, 79], or (iv) annealing, ozone, electron or plasma processing is used to modify as-grown deposits. [45, 53, 55, 80, 81] However, EBID purity is inadequate for the fabrication of most devices and functional materials without further post processing [82].

2.1.3 Electron beam induced etching

Electron beam induced etching is a direct write technique where the electron beam interacts with the substrate and adsorbed precursor molecule resulting in a deterministic dry chemical etch of the target substrate. The impinging electrons can locally split bonds in the precursor and/or substrate and generate reactive fragments of the precursor or react to active surface sites on the substrate surface, forming a volatile component which is evacuated from the chamber, leaving behind a deterministic etch pit. As the etching proceeds through a dry chemical reaction pathway the resultant material is left undamaged, unlike the comparable focused ion beam (FIB) milling or reactive ion etching (RIE) dry etching techniques [83–85], which typically result in ion implantation and amorphisation of the exposed substrate. EBIE also extends to etching with a greater material selectivity which offers a unique way to target individual layers, making this a very promising tool to use for fabricating two dimensional material heterostructured devices [86].

To date, the use of EBIE has been quite limited due to organic contamination found in most SEM systems [87, 88] and by extension a poor understanding of the process and mechanisms involved. With the ability of this technique to etch most forms of carbon using the precursor H_2O, understanding of the processes and mechanisms using this technique has been realised recently. A large portion of this work has been performed on organic systems, including; graphene, carbon nanotubes (CNT), amorphous carbon and diamond [35–39, 89] to understand and optimise the electron beam parameters. Nanoscale resolutions have also been showcased with < 10nm wide gaps etched in carbon using H_2O-mediated EBIE [90]. A number of methods have been highlighted to overcome the limiting factors of EBIE or FEBIP in general, which include organic contamination [82, 91] and lack of suitable precursors. One such method is by improving system and substrate cleanliness [35, 92] and use of suitable precursor-substrate systems [93]. In this work, novel systems are developed to build on this foundation via investigation of FEBIP processes applied to the 2D materials hBN (Chapter 7, 6) and phosphorene (Chapter 7), as well as for high purity metal deposition (Chapter 4). In parallel, this knowledge is extended to developing new chemical reaction pathways of etching material systems using a combination of plasma and EBIE, as shown in Chapter 8.

2.2 FEBIP processes and interactions

2.2.1 Substrate-precursor molecule interaction

As simple as FEBIP sounds, the underlying reactions for the deposit or etch pattern formed in FEBIP experiments are inherently complex and multifaceted. In particular, the substrate and precursor interactions are quite complicated as they involve adsorption, diffusion and desorption, as shown in figure 2.3. These are all dependent on environmental parameters such as temperature and pressure. There is a large interplay between the substrate-precursor and the electron beam parameters: for example a molecule can adsorb to a surface from the gas phase and undergo surface diffusion. The residence time determines whether a molecule is adsorbed for a sufficient time period to undergo electron beam induced dissociation. The dissociation cross section indicates how likely dissociation is to occur for the adsorbed molecule and the sticking probability governs whether or not the molecule adsorbs in the first place. These interactions are not universal and as can be seen with examples of EBIE, there can be substantial variances in the way a precursor and substrate interact under electron beam irradiation. This is shown in examples of EBIE where etching may be temperature dependent or independent [40, 94] based on the etch mechanism (role of the electron beam and precursor during EBIE). An additional example, EBID can be influenced by a selection of precursors sensitive to temperature which create varying bonding strength to the substrate via chemisorption which has compounding effects on growth rates and purity. [95].

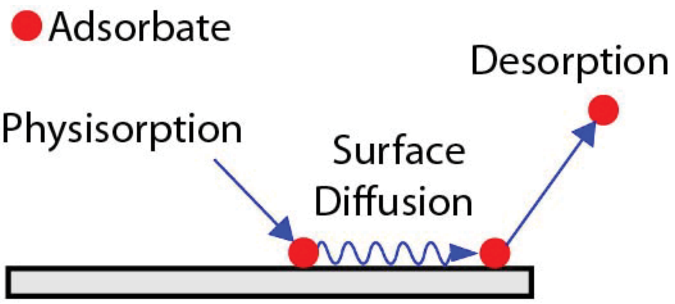

FIGURE 2.3: Illustration highlights surface-adsorbate interactions which also corresponds with the standard model in terms of adsorption, desorption and diffusion (surface migration).

2.2.2 Standard Model for FEBIP

The main interactions that occur within an FEBIP experiment include the interaction between substrate, precursor and electrons. The experimental parameter space includes characteristics of the precursor molecule, substrate, beam parameters and environmental parameters. A continuum model has been widely used to give reaction rate kinetics for adsorbates during FEBIP. The standard model will be defined next, followed by an in-depth view of the interactions occurring during FEBIP. The standard model incorporates the following equations [24].

Rate of change of precursor adsorbate concentration as a function of time, $\frac{\partial N_d(r,t)}{\partial t}$:

$$\frac{\partial N_d(r,t)}{\partial t} = s_d J_d(1 - N_d(r,t)A_d) - \frac{N_d(r,t)}{\tau_d} + D_d\left[\frac{\partial^2 N_d(r,t)}{\partial r^2} - \frac{\partial N_d(r,t)}{\partial r}\right] - \frac{\partial N_D(r,t)}{\partial t} \tag{2.1}$$

Rate of change of deposited molecule coverage as a function of time:

$$\frac{\partial N_D(r,t)}{\partial t} = -\sigma_d f(r) N_d \tag{2.2}$$

Starting with equation 2.2, we will look at the rate of change for EBID:
From the rate of the deposited molecules and rate of change of adsorbate concentration being solved numerically, important calculations can be made to correspond with experimentation. The equations will yield the spatial and temporal evolution of the deposit coverage N_D (molecules/Å^2). The number of decomposed molecules per unit area, N_D is dependent on the electron flux, f (e/Å^2/s), this is the number of electrons impinging a surface area per second (the electron flux f can be derived from measurements of beam current (I_b) and diameter (r)) and the adsorbate dissociation cross-section, σ_d (Å^2). The dissociation cross section takes into account the entire energy spectrum of electrons crossing the solid vacuum interface, and is then summed over all possible dissociation pathways.The deposit growth rate $\frac{\partial N_D}{\partial t} s^{-1}$and deposit height evolution can then be inferred. Deposit height is given by $h(r,t) = V_D N_D$, V_D is the volume of the deposited material.

For EBIE:
The etching equations are analogous to the deposition equations. The deposition precursor parameters are replaced by equivalents for the etch precursor, otherwise the equations are the same. The vertical etch rate, $\frac{\partial N_E}{\partial t}$ during EBIE is proportional to the rate of dissociated molecules outlined in 2.2 can be define as follows:

$$\frac{\partial N_E(r,t)}{\partial t} = V_E \sigma_e f(r) N_e \tag{2.3}$$

Where σ_e determines the dissociation cross-section for generation of radical etchants necessary to chemically volatilise the target material and V_E is the volume occupied by a single molecule removed from the substrate during EBIE.

Defining the remaining four terms in the standard model as shown in 2.1:

Adsorption, $s_d J_d(1 - N_d(r,t)A_d$: the first term characterises the adsorption of a precursor molecule onto the substrate surface with the following parameters. The concentration of precursor adorbates, N_d (Molecules/Å^2) and precursor molecular flux, J_d (Å$^2 s^{-1}$)) determine the amount of precursor available in the system and are governed by the gas pressure (Pa), molecular mass (kg) of the precursor and temperature (K). The precursor adsorbate sticking coefficient, s_d gives the probability for adsorption to occur and the surface coverage is also dependent on the precursor molecule surface area, A_d (Å^2) and the amount of time elapsed, t (s).

Desorption ($\frac{N_d(r,t)}{\tau_d}$): the second term characterises the desorption rate of the adsorbed molecules which is dependent of the desorption time, τ_d (s). The desoprtion time is strongly influenced by the temperature and is defined as:

$$\tau = \frac{1}{v_0} exp\left(\frac{E_d}{k_b T}\right) \tag{2.4}$$

Where E_d is the energy barrier for desorption, which can be seen is strongly dependent on temperature, T (K). k_b is the Boltzmann constant and v_0 is the vibrational frequency of the adsorbed molecule.

Diffusion, $D_d\left[\frac{\partial^2 N_d(r,t)}{\partial r^2} - \frac{\partial N_d(r,t)}{\partial r}\right]$: This surface diffusion or migration of adsorbed precursor molecules is also highly dependent on temperature, where the diffusion coefficient, D_d (Å^2/s) is defined as:

$$D_d = D_0 exp\left(\frac{-E_{diff}}{k_b T}\right) \tag{2.5}$$

Where D_0 is the diffusion prefactor and E_{diff} is the energy barrier for diffusion to take place. The radial distance from the electron beam axis, r (Å), also plays an important role in determining the rate of diffusion as precursor depletion takes place under the electron beam fluence which will be further detailed next.

Dissociation, $\frac{\partial N_{D/E}(r,t)}{\partial t}$: the fourth term describes the rate of molecule decomposition on a substrate through electron dissociation of the precursor molecules as described above for electron beam deposition (N_D) and etching (N_E) in equation 2.2 and 2.3 respectively.

2.2.3 Electron-precursor interaction

Dissociation is the breaking up or decomposition of a parent molecule in an adsorbed state into its constituent parts through electron interaction. There are thought to be three important dissociation channels for this work[96], they are; dissociative electron attachment, dissociative ionisation, dipolar dissociation, with possible beam heating [97] as another. The cross section of dissociation is crucial in determining dissociation rate, and therefore the removal or growth of the target material through the interaction, and dissociation of precursor gas through electron bombardment. The cross section is dependent on the electron energy and is expressed as the probability that an electron breaks a bond in a precursor molecule.

To obtain the cross section, a comparison of the incoming electrons and the outgoing ion-atom flux of the precursor must be made [98]. There is however inherent difficulties in measuring the dissociation cross section as it relies on many parameters. These include, the geometry and bonding nature of the precursor, the dissociation pathways and the environmental conditions for the e-beam and adsorption of the precursor.

However, more applicable to this work is the dissociation channels for EBIE which is not as widely studied. Not all EBIE processes are equal, and etch mechanisms can vary widely based on the role of the electron beam, substrate and precursor molecules [39, 40]. This has been further evidenced by work done on hBN seen in Chapter 7, where temperature independence is realised during EBIE of hBN.

2.2.4 Electron-substrate interaction

The electron beam consists of primary electrons (PEs). When these primary electrons collide with the substrate they are inelastically or elastically deflected. When an inelastic collision occurs, a fraction of the primary electron energy can be transferred to other electrons which will also go on to interact with further electrons and scatter. These are known as secondary electrons (SE) if their energy is < 50 eV or Backscattered electrons (BSE) if their energy is > 50 eV. The volume which encloses all PE, SE and BSE electrons and their scattering events is known as the interaction volume (this also includes auger electrons, X-ray generation, etc (see figure 2.4).

The interaction of the electron beam and sample can be approximated by the Kanaya-Okayama equation, R_{KO} the electron range (μm), given by [100]:

$$R_{KO} = \frac{27.6AE_L^{\frac{5}{3}}}{\rho Z^{\frac{8}{9}}} \tag{2.6}$$

A = atomic weight (g/mol)

E_L = landing energy (keV)

ρ = density (g/cm^3)

Z = atomic number

The interaction volume depth and shape is dependent on the initial electron beam or PE energy, where the mean free path describes the average length an electron travels between collisions and is dependent on their energy. It is also dependent on the

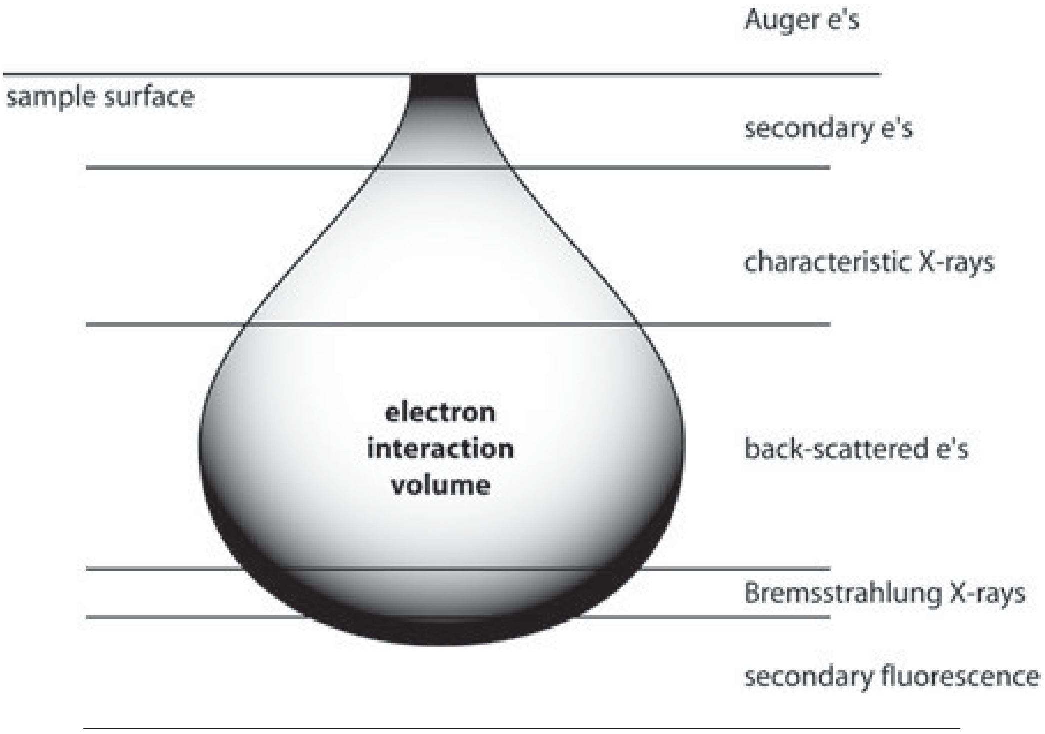

FIGURE 2.4: Example of an Interaction volume generated from a primary electron beam. The depth range of secondary, backscattered and X-ray generation is also illustrated. Figure from [99]

atomic number of the elements being bombarded, where a higher atomic number correlates to a larger number of elastic and inelastic collisions which leads to a reduced interaction volume depth.

The interaction volume is usually pear shaped, and is an important factor to consider during growth and analysis, especially when creating 3D nanostructures with overhanging deposition, the interaction volume determines where the material growth occurs and should not penetrate the overhanging deposit created (shown in Chapter 4, EBID of Pt). The interaction volume is also an important factor when determining SE yield which is shown to largely contribute to FEBIP deposition or etching rates [101].

During EBIE the interaction volume can also play a substantial role in the roughening that is seen to occur due to BSE radius and scattering in the gas phase particularly at high and low accelerating voltages respectively. A number of techniques can be used to minimise these effects including using lower accelerating voltages (reducing backscattered electron radius) and gas injection systems which supply a high partial pressure precursor molecules directly into the point of interest and allows the SEM system to remain in high vacuum reducing scattering. In this work, a unique approach was taken to suppress this roughening issue which can be exclusively applied using 2D materials or thinned materials at high accelerating voltages. This approach effectively removes the backscattered electron radius resulting in substantially reduced roughening and is discussed in more detail in Chapter 7, EBIE of hBN. For greater and precise approximations of electron beam interactions, Monte Carlo simulations [102] is used and highlighted in Chapter 5, 7, 6, 8.

2.3 2D materials

Since the discovery of graphene in 2004 [103], the number of studies on two dimensional materials have exponentially risen due to the unique advantages they possess over their bulk counterparts, which include optical, mechanical and electronic properties; these materials include Transition metal dichalcogenides (TMD) and monoelemental 2D materials [86, 104]. The monoelemental 2D materials that possess the most promising properties include; graphene, phosphorene, silicene, germanene, and have opened a new range of applications for thin film optic and electronic devices [5, 8]. In the next section, a background will be given for two promising 2D materials that have stood out in recent times due to their unique properties and the challenges that must be overcome to allow for the integration of these materials in functional devices. The first being the monoelemental material black phosphorus, which is a very unique 2D material due to the in-plane anisotropy showcased and use as a two dimensional variable semiconductor[105]. The other being hBN, which has been highlighted due to its wide band gap and favorable optical characteristics and hyperbolic properties.

2.3.1 BP

Black Phosphorus was first mechanically exfoliated in 2014, followed by a demonstration of *p*-type semiconductor transport properties [8]. Since this report, a surge in research has been performed on its unique physical properties and accompanying applications [19, 106, 107].

Phosphorene comprises of a single atomic layer of phosphorus atoms which is mechanically exfoliated from its bulk counterpart known as BP, whereas few-layer BP is known as more then one atomic layer of BP but usually less then 100nm thick. The crystal structure of phosphorene is arranged in a hexagonal lattice similar to graphene and the layers held through van der waals forces analogous to other two dimensional materials. Unlike most 2D materials, phosphorene also possesses sp3 hybridisation in plane within the phosphorene structure which results in a puckered honeycomb lattice, as shown in figure 2.5.

The unique puckered honeycomb structure leads to many interesting properties, namely the mechanical properties which see significant flexibility in plane against applied stress [10, 18, 109], implying the possibility of integrating this material into flexible devices. Uniaxial compressive strain is also reported to switch few-layer BP from a direct bandgap material to an indirect semiconductor, metal or semi metal [110]. Anisotropic electric-transport, thermal transport and optical properties [20, 21, 111, 112] are also seen as a consequence of the puckered honeycomb structure, where anisotropic in-plane conductivity has been theorised/observed in few-layer BP resulting in electronic and phonon dispersion [19, 20]. Tunability of the band structure has also been theoretically demonstrated by applying a slight tensile or compressive strain which leads to drastic change in transport properties and as a result an atypical enhancement of the Seebeck coefficient is realised [113].

In contrast to graphene, which is a 2D zerogap conductor, few-layer BP is a 2D

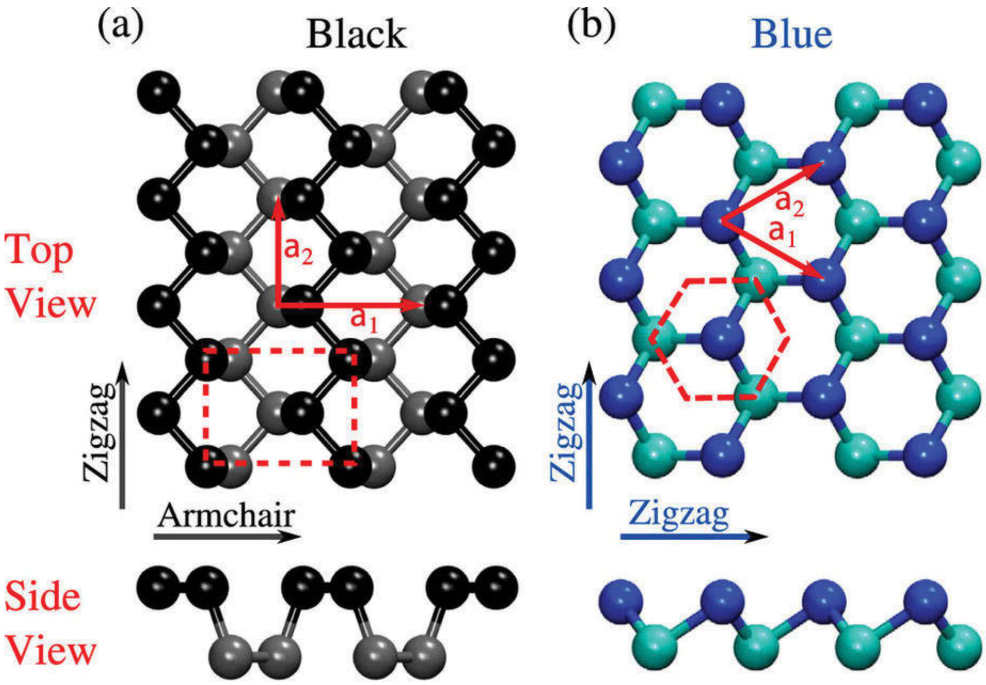

FIGURE 2.5: The crystal structure for (a) armchair phosphorene and (b) zigzag phosphorene. Atoms in different planes are denoted by different colours and the in-plane lattice vectors are shown in the top view. [108].

semiconductor with a finite band gap which is easily tunable through variable thickness or surface terminations as shown in figure 2.6. Its promising optoelectronic properties include a high carrier mobility (hole mobility has been experimentally measured at 1000 cm^2/V_s and theoretically predicted up to 26,000 cm^2/V_s [5, 20, 114]), and direct tuneable anisotropic layer dependant band gap from 0.5 to 2.0 eV [21]. Combined with material flexibility has made this a promising material to use as a p-type device for many applications including flexible thin film high frequency transistors (TFT), batteries, ultraprecise gas sensors and photonic devices [5, 18, 115–117].

Despite of all the unique and promising properties, most of its applications have not been realised due to the vulnerability and rapid degradation of this material in ambient conditions in a matter of days [106, 118–121], an example is shown in figure 2.7, where untreated and treated few-layer BP flakes degrades in less then three days.

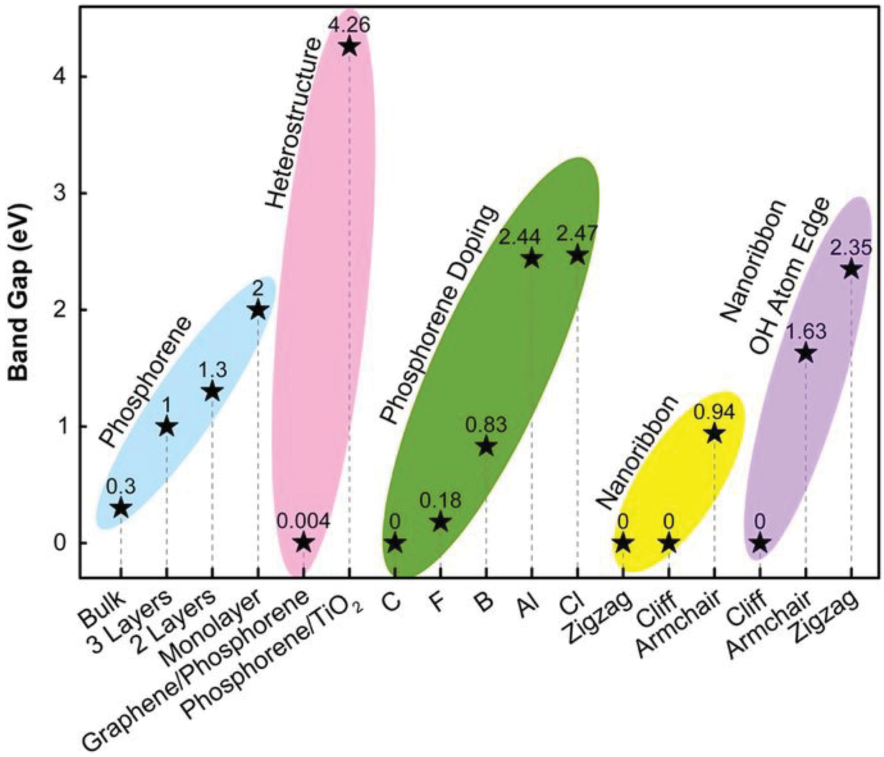

FIGURE 2.6: Variable bandgap is illustrated through various changes in few-layer BP, including variable thickness and surface termination. [15]

Even though BP is the most stable allotrope of phosphorus, it still shows low chemical stability which causes irreversible damage to the few-layer BP material [4]. This instability is widely believed to be due to the free lone pairs in phosphorous, and high reactivity with H_2O in the presence of an exciting source.

The degradation of few-layer BP has been studied previously [119, 123–126], but the reaction mechanism and the main reactants are still ambiguous and inconsistent. DFT calculations [118] supported by experimental data [106, 119] suggests that the initial reaction involves the dissociative chemisorption of O_2 onto few-layer BP flakes creating oxide bubbles, making them more hydrophilic than pristine few-layer BP. Consequently, when water diffused onto the oxide bubbles, creation of phosphoric acid ensued in a very exothermic reaction [118], the phosphoric acid then diffuses along the flake causing accelerated degradation, a drop of pH was also shown experimentally [106]. In contrast, recent studies [127] realise the passivation of few-layer

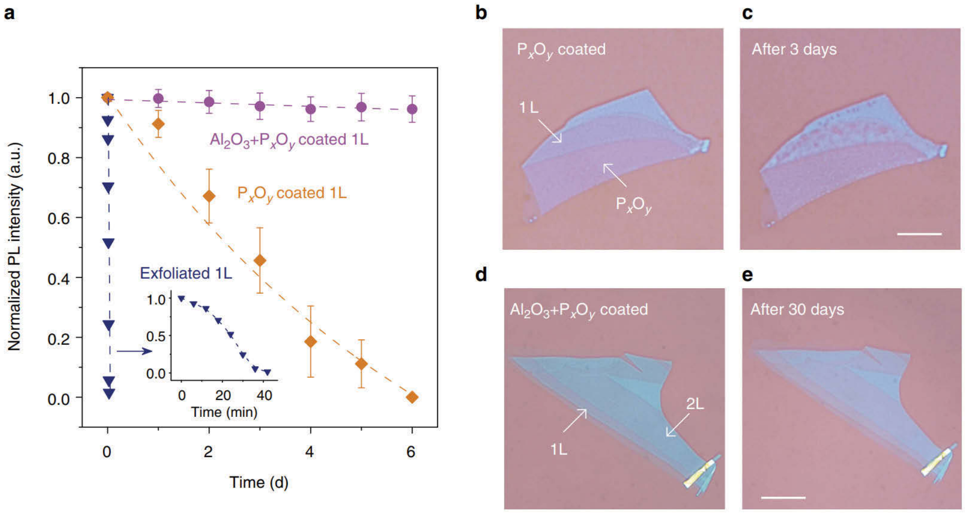

FIGURE 2.7: (a) PL intensity of a monolayer phosphorene samples with various treatments: exfoliated 1L phosphorene (blue), 1L phosphorene with P_xO_y capping layer (orange) and 1L phosphorene with dual passivation layers of P_xO_y and Al_2O_3 (pink). (b,c) Optical microscope images of a 1L phosphorene sample with P_xO_y capping layer only, before (b) and after 3 days (c). (d,e) shows optical microscope images of phosphorene with two capping layers of P_xO_y and Al_2O_3, before (d) and after 30 days (e). Scale bar, $10\mu m$. [122]

BP due to the same oxide layer, without any observable changes in the optoelectrical properties of few-layer BP. In general, most of the papers agree that H_2O, O_2 and photo-assisted energy are simultaneously required for the degradation reaction to proceed [118, 119, 124, 128, 129]. The potential products and intermediates species created in the reaction are reported to be mainly H_3PO_4 and P_xO_y [106, 119]. However, how the reaction mechanism proceeds is not conclusive. This lack of clarity has resulted with ineffective passivation techniques being used to stop degradation of few-layer BP, with most relying on coatings of aluminum oxide to passivate for several weeks [115, 127], however, a long-term passivation technique has yet to be discovered.

In Chapter 5, using in-situ ESEM a greater understanding of the degradation mechanisms is gained using controlled environments via exposure of few-layer BP flakes under electron beam irradiation. This was then extended to ultimately stabilise the few-layer BP flakes by using a low temeprature heat cycle to remove adsorbed and intercalated H_2O for the BP flakes.

2.3.2 hBN

Hexagonal Boron nitride (hBN) is a two-dimensional van der Waals material comprising of layers of Boron and Nitrogen. It is also structurally very similar to graphene possessing a honeycomb hexagonal lattice as shown in figure 2.8. hBN possesses a stacking configuration of AA bonding, where the Boron atoms sit directly atop of a Nitrogen atom [130], also highlighted in figure 2.8. Due to this layered stacking sequence structure held via van der waals forces, it is possible to exfoliate bulk hBN crystals through mechanical exfoliation techniques [131, 132], or liquid exfoliation [133]. It is extremely chemically and thermally stable up to $1200°$C, and possesses a high melting point of approximately $2600°$C [41] and exhibits excellent thermal conductivity (300 – 2000 $Wm^{-1}K^{-1}$) [134]. hBN is also a group III-V semiconductor and possesses a direct bandgap of 5.97 eV when in bulk and 6.07 eV as a monolayer [135]. As it is highly insulating, it is currently widely used as an overlaying or separating material for graphene or TMD devices and is also has quite a few promising applications including electronics [136], photonics [137, 138] and catalysis [139].

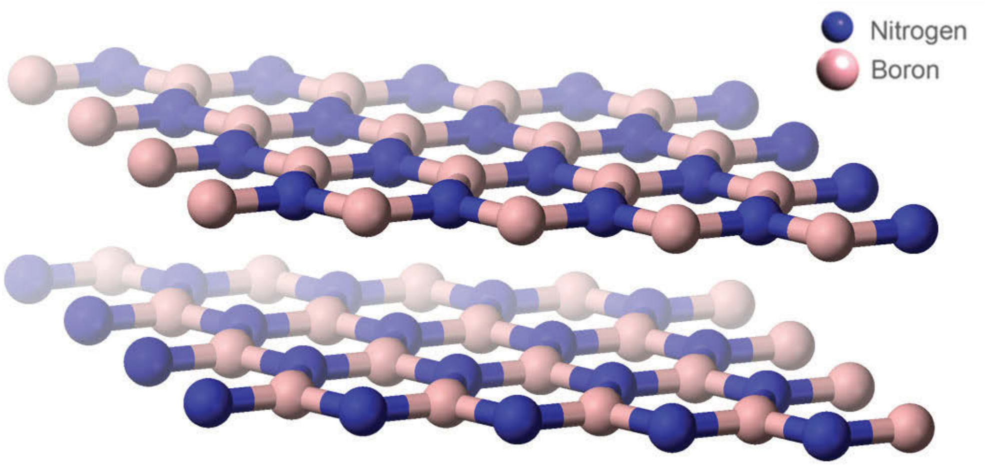

FIGURE 2.8: Layers of the hexagonal form of Boron nitride (analogous to graphene) is depicted, with alternating Boron and Nitrogen atoms.

Recently hBN has garnered much interest due to the unique properties exhibited in the two-dimensional form. An example of this includes hBN being naturally hyperbolic (dieelectric functions are opposite in and out of plane) allowing for sub wavelength focusing and guiding in polaritonics, and super resolution [138, 140]. For more information, see 2.3.4. The optical properties of hBN have also recently been of interest since the first demonstration of direct bandgap emission in the UV region [135]. As hBN is also a wideband gap material it has been shown to host many optical active sub band gap defect sites. The discovery of single photon emitters (single photon emissions occurs after optical or electrical excitation where only a single photon is emitted within its fluoresence lifetime) in hBN is the first instance of a stable quantum emitter at room temperature in a 2D material and has therefore attracted considerable interest for quantum technologies [141].

2.3.3 hBN single photon emitters

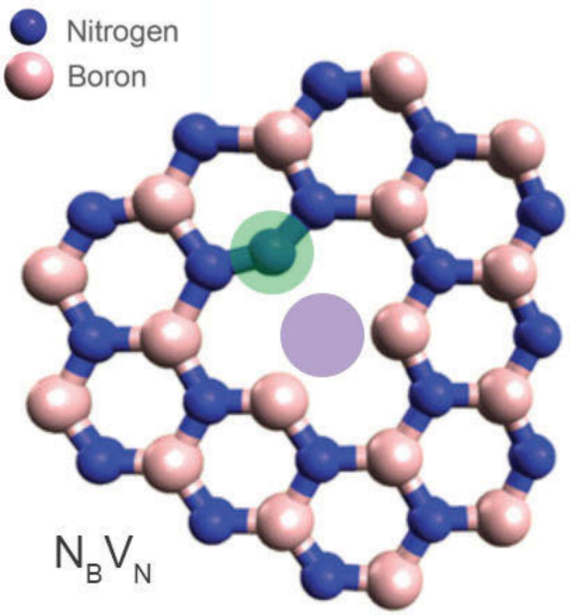

FIGURE 2.9: The antisite nitrogen vacancy (highlighted with a purple circle) within hBN where a substitutional nitrogen is in place of the boron site (highlighted with a green circle). This defect is hypothesised to be the source of the hBN single photon emission. [17]

hBN is the first known two dimensional material to host Single photon emitters at room temperature [141]. It is currently proposed that due to the large bandgap many active ground and excited defect states can exist. Density functional theory (DFT) calculations showing the most likely defect candidate is the antisite nitrogen vacancy defect, denoted by $N_B V_N$. The structure of this defect involves a N atom which sits on the B atom site with an adjacent vacancy on the N site, this is illustrated in figure 2.9. This defect found in hBN is thought to follow an extended three-level model energy system [17].

In a quantum two level system, a charged particle will jump between two quantum states depending on the energy input. Absorption of sufficient energy will result in the promotion of a charge into an excited state, relaxation will occur depending on the excited state lifetime and will result in an emission of a photon corresponding to the energy level. This is known as spontaneous emission [142, 143]. The optical transitions between the two states is illustrated as excitation and emission in figure 2.10. A three level system comprises of three quantum states, a ground, excited and metastable state. Relaxation can occur now either through the emission pathway or through the metastable state non-radiatively with a distinct lifetime as shown in figure 2.10.

Unsaturated defect states found in hBN that follow this three level energy system, result in the generation of single photons. Single photon emitters are an essential building block to realising quantum technologies, in the form of a qubit.

A qubit is analogous to a classical bit which is able to exist in a state of 0 and 1 only. However a qubit is also capable of existing in more then one state, more specifically it is able to have a coherent superposition of 0 and 1. This result is explained in the linear superposition wavefunction of a qubit which is governed by the superposition principle and is shown by [144]:

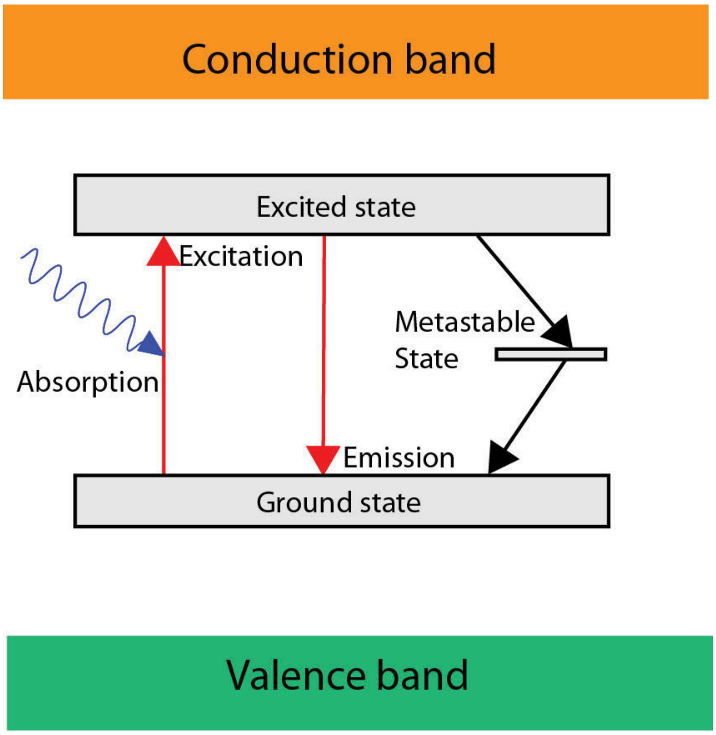

FIGURE 2.10: The three optical states in a quantum three level system are highlighted as ground, excited and metastable state. After absorption, excitation occurs and relaxation across either the radiative excitation pathway or through the non-radiative metastable state.

$$|\psi\rangle = \alpha|0\rangle + \beta|1\rangle \tag{2.7}$$

$|\psi\rangle$ indicates the qubit state and the above equation highlights the probability amplitudes, α and β of what the state will be. As this is probability based the squares of the amplitudes must equal to 1 in the form of, $|\alpha| + |\beta| = 1$. This principle allows individual qubits to store more information than a classical bit, paving the way for exponential increases in computational speeds [145].

Single photon emitters may be used to lay the foundation for quantum information processing, as the qubit information can be transmitted through single photons via photon polarisation. The two states, α and β can represent the vertical and horizontal polarization states of a single photon emitter. This can be represented on a bloch sphere as illustrated in figure 2.11. α and β in this case will have three degrees

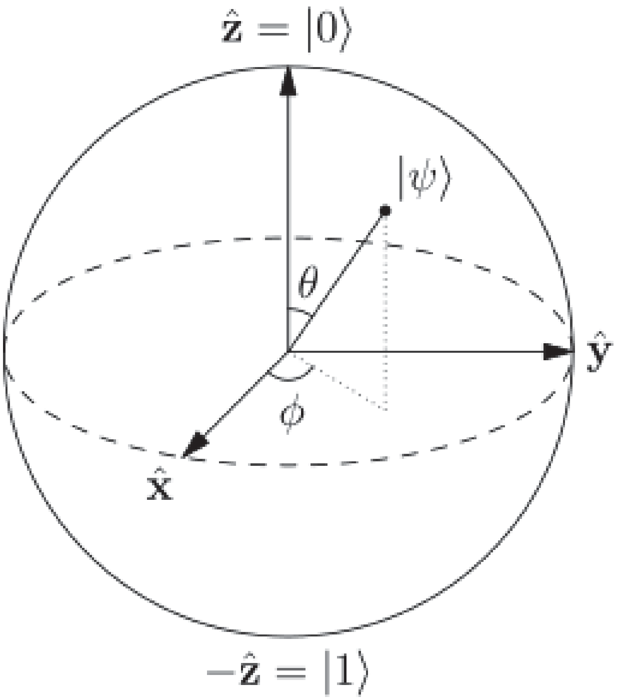

FIGURE 2.11: A bloch sphere with a co-ordinate system and angles θ, ϕ to represent the qubit state of ψ [144, 146]

of freedom and can represent any co-ordinate position on a bloch sphere with the limitation of $|\alpha| + |\beta| = 1$ and can be shown as:

$$\alpha = e^{i\psi} cos\frac{\theta}{2} \tag{2.8}$$

$$\beta = e^{i(\psi+\phi)} sin\frac{\theta}{2} \tag{2.9}$$

These equations can be visualised in figure 2.11.

An ideal single photon emitter will have photons which are indistinguishable from one another and emit exactly one photon at a time on demand. These emitters will play a crucial role in quantum computing and security [147]. The fascinating properties that set hBN apart from other single photon sources is the ability to host emitters in a 2D material at room temperature. Hosting in a two dimensional material offers several advantages over the 3D counterparts. The emitter will be located very close to the surface and exhibit very little scattering within the lattice, resulting in ultra bright emission with negligible signal loss. In fact hBN is the brightest recorded emission in the visible region at room temperature [141]. The emitter lifetime is very short, in the range of 3 ns allowing for high frequency clocking. The emission is also fully polarisable and exhibits indistinguishability to hold quantum information. A fully linear polarisation from the emitted light suggests that the defect centre possesses a single linearly polarized dipole transition. The defect centre also shows a very high photo-stability with no bleaching and blinking for an extended period of time. At this point these properties can not be fully utilised and integrated into devices as there is no controllable way to engineer deterministic single photon emitters (SPE) in hBN. SPE defect generation will be studied in Chapter 6 where deterministic defect generation is explored via electron beam irradiation in various environments. The photophysical properties of the emitters, showing their photoluminescence spectra, polarisation properties, and photon emission statistics (autocorrelation functions) will also be showcased.

2.3.4 Naturally hyperbolic material

Hyperbolic dispersion is another fascinating property unique to some 2D materials which includes hBN. It is due to the differences in bonding strengths in and out of plane in the material lattice, typical of a Van Der Waals crystals. The inter-plane atoms in Van Der Waals crystals are covalently bonded resulting in high inter-plane bonding strength, compared with the weaker physical bonding out of plane, where layers of the material are held via Van Der Waals forces. [148]. Due to this anisotropic nature of the material, hBN has recently shown naturally hyperbolic properties [12], which means that the dielectric constants in plane and out of plane have opposite signs [149]. It is one of the first known materials to possess this property, where excitation of hBN using a narrow energy band between the longitudinal and transverse optical modes and forces propagation of surface phonon-polariton modes which are constrained by the changes in dielectric functions of the hBN [7], an example of this propagation is shown in figure 2.12. This property has been utilised to demonstrate phonon-polariton tuning [140] which are sub-diffractional, highly directional volume-confined polariton modes, sub-diffractional imaging in the infrared region with nanoscale resolution [11, 150, 151] and lasing [135, 152].

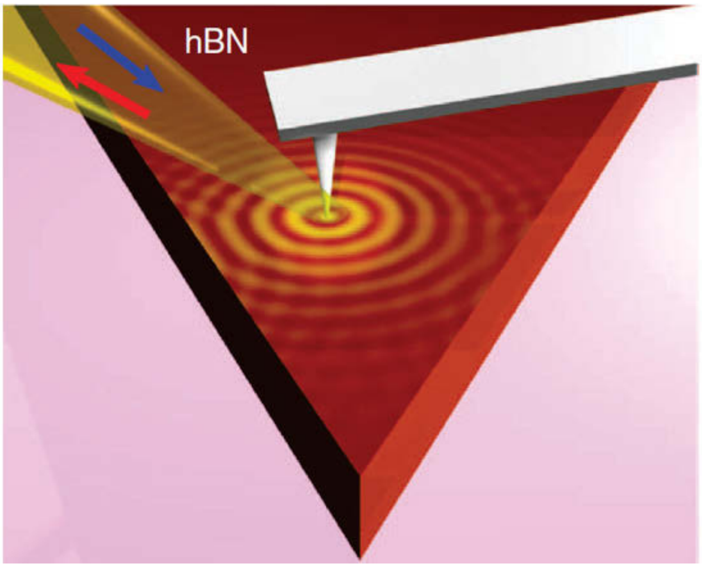

FIGURE 2.12: Real-space imaging of surface phonon polaritons on hBN. Arrows denote the incident and back-scattered IR light. The phonon polariton waves launched and reflected by the two edges of a tapered hBN crystal is shown via yellow rings. [140]

These properties then allow hBN to be fully integrated with other two dimensional materials such as graphene and transition metal dichalcogenides resulting in flexible and compact vertical photonic or electronic devices. However, the applicability and wide deployment of hBN in scalable devices is presently limited by a lack of suitable nanoscale processing techniques, particularly growth and etching. In Chapter 7 a new method is developed to etch hBN deterministically using electron beam induced etching.

2.4 Remaining chapter summary

The Thesis will focus on electron beam chemistry of the chemically inert 2D material hBN and the highly unstable 2D material, black phosphorus. The thesis results will be split into the following main Chapters:

Chapter 3, Experimental procedures - This Chapter will give a background and describe all experimental techniques used in this project.

Chapter 4, Programmable patterning and EBID - In this Chapter, the development process of designing, programming and depositing or etching 3D nanostructures using FEBIP will be illustrated. 3D nanostructures of Pt are then created using EBID. Next, the array of techniques that could be used to purify EBID deposits is improved by utilising compositional analysis and developing ways to chemically target the non-volatile products formed during EBID.

Chapter 5, mechanistic and stabilisation study of few-layer BP - The main objective in this Chapter is to achieve a deep understanding of the degradation mechanism and provide insight into the nature of the chemical reaction pathways itself via exposure of few-layer BP flakes under electron beam irradiation in various controlled gaseous environments. In addition, temperature-dependent experiments were performed in order to establish the nature of the reaction. The main goal of this work is to find a way to stabilise this material, and allow for the integration of few-layer BP into high-performance optoelectronic devices and sensors in ambient conditions.

Chapter 6 hBN emitter creation - In this Chapter single photon emitters are created via electron beam irradiation in various environments for deterministic defect generation. The photo-physical properties of the emitters are also studied, showing their photoluminescence spectra, polarisation properties, photon emission statistics and autocorrelation functions.

Chapter 7, EBIE of hBN - This Chapter builds on top of the foundation laid for EBIE to develop novel systems focused on etching two dimensional materials such as hBN. A new method is developed to etch hBN deterministically using electron beam induced etching using a single highly abundant and economically feasible precursor, H_2O. Precise nanoscale resolution patterning of hBN is showcased without the need for multi-step processes or masking layers. The aim of this work is to extend the outreach of this technique and take the first steps to selectively etch a range of two-dimensional materials using EBIE.

Chapter 8, Bottom-up etching of Ag - The understanding of the electron beam induced etching of hBN electron-substrate interaction mechanism is taken a step further in this Chapter, as the roles of the electron beam, precursor and substrate are not as straightforward as most EBIE systems which typically involve etching a mono-elemental material. This work involves a two element crystalline system (Boron and Nitrogen) and is based on the formation of reactive products during the EBIE of hBN which extends to etch other materials deterministically. This is the first reported instance of using electron induced products from a substrate as an etchant and as a result a multiple step EBIE process is realised, with the novelty of directional etching. This innovative chemistry found also paved the way for a new hybrid EBIE process know as plasma enhanced EBIE. The combination of in-situ radical generation of precursor molecules, and deterministic creation of highly active surface sites resulted in high resolution etching of Ag nanowires.

Chapter 9, Conclusions - This Chapter will summarise the results found in this thesis and give insight into future directions of these results.

Chapter 3

Experimental procedures

An introduction to scanning electron microscopy, and all other experimental techniques and processes performed will be given in this chapter. An environmental scanning electron microscope was used for all FEBIP experiments in this project.

3.1 SEM

In a typical scanning electron microscope (SEM) [153], a steady stream of electrons is generated from the electron gun which acts as a cathode. The source of the electrons is usually a heated tungsten filament. The anode then attracts electrons strongly causing them to accelerate towards it, with typical energies ranging from 1-30keV. The electron beam is then concentrated by the condenser lens in an electromagnetic field and focused to a very fine point through the objective lens, a simple schematic is shown in figure 3.1. The beam then passes through scanning coils which deflect the beam in the x and y axes so that it scans over rectangular region of the sample surface. The interaction of the primary beam with the sample leads to the generation of scattering events such as secondary electrons and backscattered electrons which gives a topographical image dependent on SE yield and composition of the material with nanometer resolution. The scattering events can also create X-rays, when emitted, give compositional concentration information.

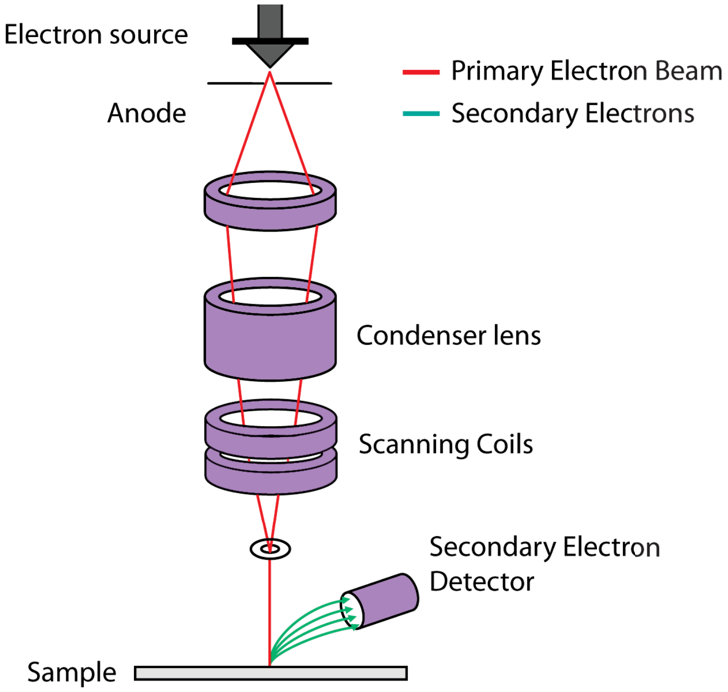

FIGURE 3.1: A simple schematic of an SEM operation, with the anode, cathode, lens and coils highlighted.

3.2 Environmental SEM

In the context of FEBIP an environmental SEM is used, where a pressure of precursor gas is introduced in the chamber. An environmental SEM is able to operate under low vacuum conditions at pressures of 10-1300 Pa. This is achieved through differential pumping of the column and chamber, with pressure limiting apertures being used to achieve a large pressure gradient between the specimen in the chamber and the column [154].

These conditions allow for imaging of specimens in wet conditions and in their natural state, as well as minimising charging through the use of a gaseous secondary electron detector (GSED). A positive bias is run through the GSED detector attracting secondary electrons towards it. As the electrons accelerate towards the positive bias of the GSED, they may ionise gas molecules in the path if the ionisation threshold of the gas is exceeded. As a result of this ionising collision, a positive ion is ejected as well as an additional electron. The positive ion is attracted to the negatively charged sample, effectively neutralising or subduing charging effects. The electrons go on to ionise further gas molecules, ejecting further electrons, and creating a gas cascade (Fig. 3.2).

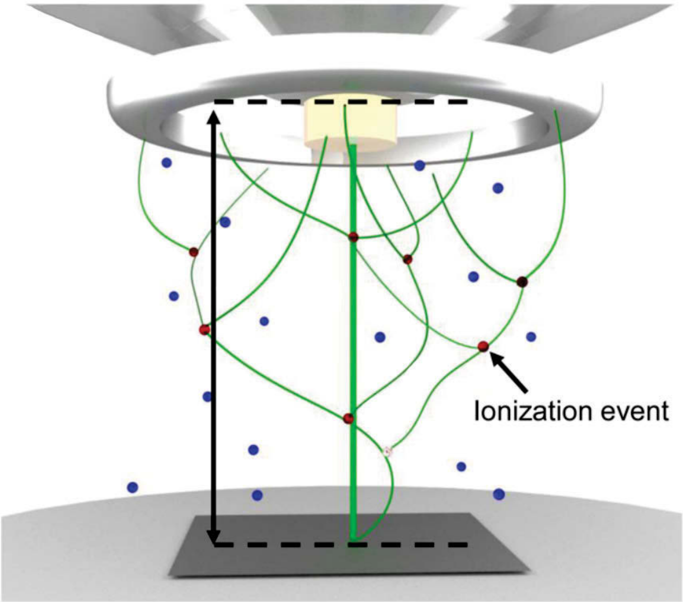

FIGURE 3.2: The gas cascade process is illustrated in this schematic, with amplification due to ionisation events occurring to produce additional secondary electrons [155].

SEM and Transmission electron microscopy (TEM) have typically been used to perform FEBIP, which is modified to allow a delivery system of precursor molecules to the chamber. A dedicated SEM known as the Nova nanoSEM Sirion column is used for FEBIP experiments in this project. The Sirion offers high spatial resolution due to the Field emission gun (FEG) and InLens detector for high vacuum or a magnetic immersion lens gaseous secondary electron detector [156] also known as a helix detector under ESEM conditions.

A FEG is a tungsten filament with an extremely sharp pointed Muller type emitter, which is held at a large negative potential relative to a nearby electrode. The sufficient potential gradient causes field electron emission. Due to the very narrow point the sufficient potential emits coherent energy emission, and is able to produce three orders of magnitude greater current density compared to a traditional tungsten filament emission resulting in a much higher resolution achievable compared to traditional thermionic tungsten filaments guns.

An InLens detector is a secondary electron detector which is located in the electron column of a microscope and rotates symmetrically around its axis. A large magnetic field is used to efficiently collect secondary electrons and is heightened at smaller working distances. The result is a much improved signal to noise ratio.

Multiple SEM's and ex situ chambers using various chemicals and precursors were used in the various projects performed. This was achieved through a gas network system. The advantage of this is that multiple gases can be loaded and accessed easily and multiple gases can be delivered at the same time to a number of machines.

The gases were loaded into gas boxes which remained cool and under high vacuum conditions, while being isolated from the lines by manual and pneumatic valves. The flow rate of the gases are precisely controlled by either mass flow controllers or needle valves with an accompanying bypass to evacuate the lines.

3.3 Gas delivery

The Sirion SEM uses a differentially pumped field emission gun (FEG) with ultra-high resolution (UHR) imaging capabilities. This versatile SEM offers exceptionally high spatial resolution with access to the gas lines, which makes real-time imaging and recording of reactions taking place in-situ a very real possibility.

In this project three separate modes of precursor delivery to the chamber have been used, and are outlined below:

Gas injection system

A gas injection system (GIS) is a quick and easy way to deliver the precursor molecules into the chamber. The GIS is attached to the SEM with the precursor held within, the needle is brought close to the substrate, and precursor molecules are injected directly to the substrate surface area of interest. This creates a partial pressure within the chamber, with a higher partial pressure at the tip of the needle compared to high vacuum conditions throughout the rest of the chamber. A typical GIS is shown in figure 3.3

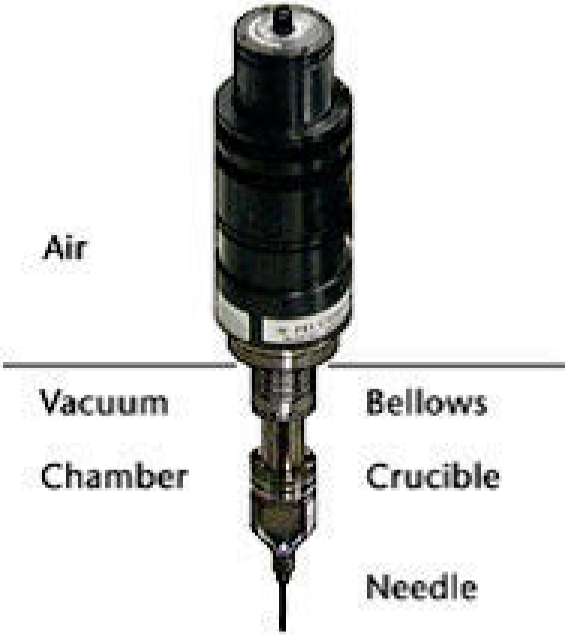

FIGURE 3.3: A typical Gas injection system, highlighting the vacuum and air side components is shown.

Reaction cell

The introduction of a sub-chamber reaction cell [157] could be considered a mix between the previous methods. The precursor gas is introduced directly into a reaction cell, which is sealed off from the rest of the chamber except through a pressure-limiting aperture through which the electron beam enters the cell. The pressure in the cell and

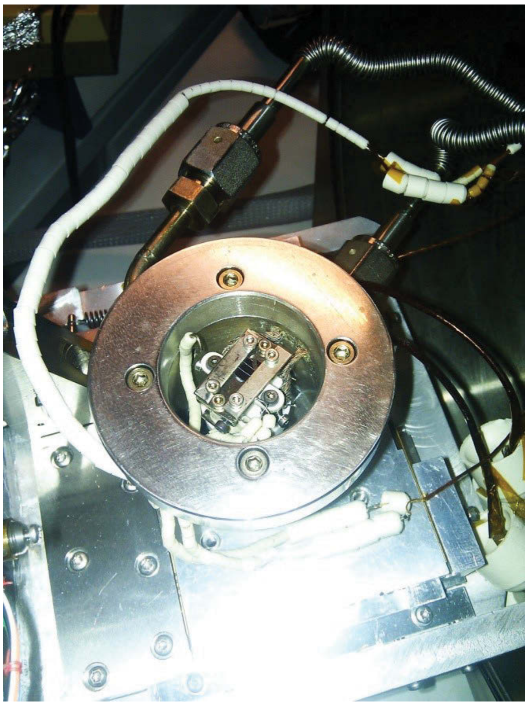

FIGURE 3.4: A custom built environmental reaction cell housing an in-situ heating substrate holder and gas inlets.

chamber can be measured separately and due to a higher pressure gradient inside the reaction cell most residual contaminants remain in the ESEM chamber. Hence there is a much larger ratio of precursor molecules to residual molecules, allowing for enhanced reproducibility of experimental work. A custom built reaction cell is shown in figure 3.4.

ESEM

Another method is to operate the chamber in ESEM mode, where a known pressure of precursor molecules is held throughout the whole chamber. This mode is enabled through differential pumping of the column. This allows for accurate readings of gas pressure within the chamber.

3.4 Gas/precursor network

The gas network system used in this project houses many gas and precursor molecules, allowing for easy access and mixing directly to the SEM chamber. The gases and precursor are controlled and directed by a series of manual and pneumatic valves. Flow restriction is provided by needle valves and mass flow control. A detailed schematic of the networked gas lines are shown below in figure 3.5, which allows for chemical etching, deposition of a wide range of materials and surface functionalization.

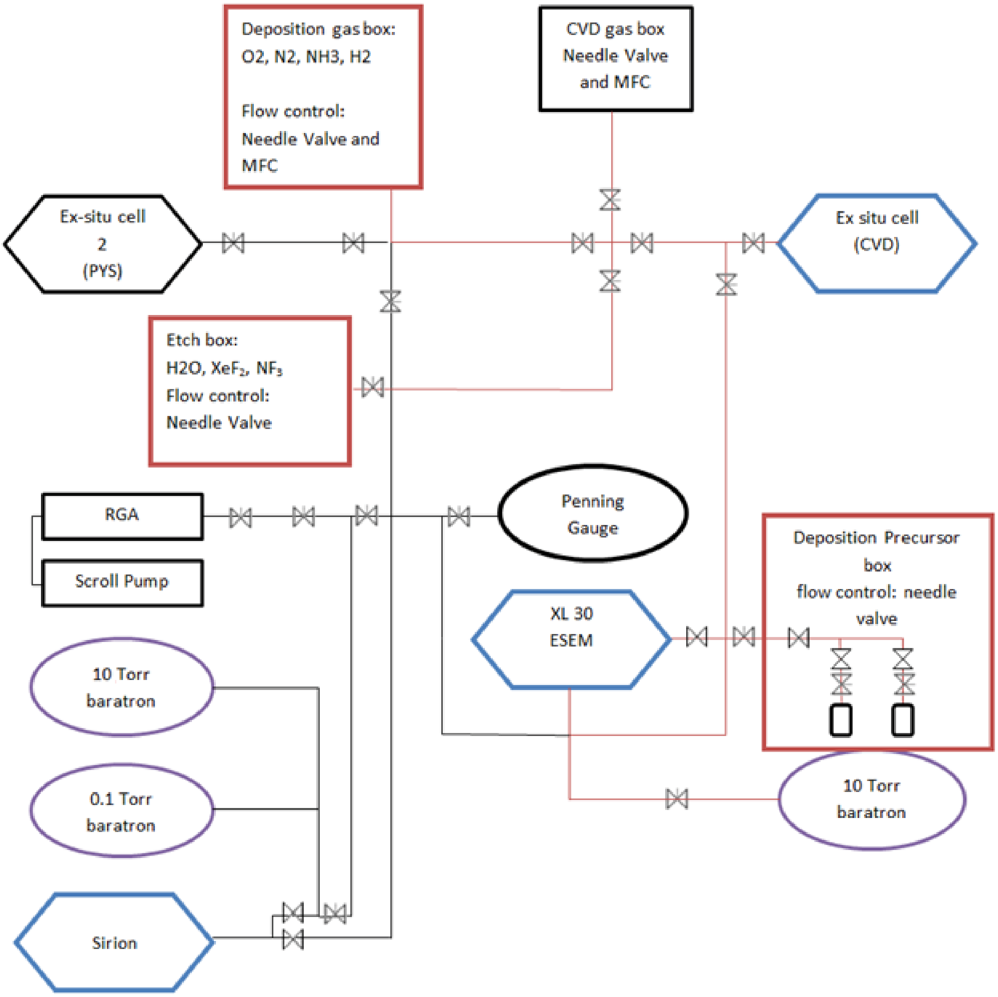

FIGURE 3.5: A schematic of the gas network system. The etch, depostion and high pressure gas locations are shown and the means of mass transport to each experimental set up.

3.5 Cleaning and cleanliness

3.5.1 High vacuum pumping and plasma cleaning

The Sirion SEM system is constantly pumped under high vacuum using an Edwards x10 series scroll pump and turbo molecular pump, bringing the base pressure in the column down to around 3×10^{-6} mbar. There is also a dedicated plasma cleaner attached to the SEM, which is used to ionise the residual hydrocarbons, H_2O and contaminants within the SEM. Plasma cleaning involves a very efficient process of the removal of contaminants or residual gases from surfaces through the use of energetic plasma created from a gaseous species. The plasma is created using high radio frequency (RF) signal to ionise gases (usually argon, oxygen or air) at low pressures. The ions and free radicals interact with any surface and effectively break most organic bonds, to create lower molecular weight compounds with higher vapour pressures which are then easily evacuated from the system.

The samples and chamber is subject to an oxygen plasma using a low power (5 W) RF remote plasma system (EVACTRON model C from XEI scientific). During FEBIP experiments performed on hBN the plasma cleaner was used to minimise contamination and thus increase reproducibility of experiments. The same remote plasma unit was active during plasma enhanced EBIE experiments outlined in Appendix E, a schematic including a plasma head attached to an SEM is shown in figure 3.6.

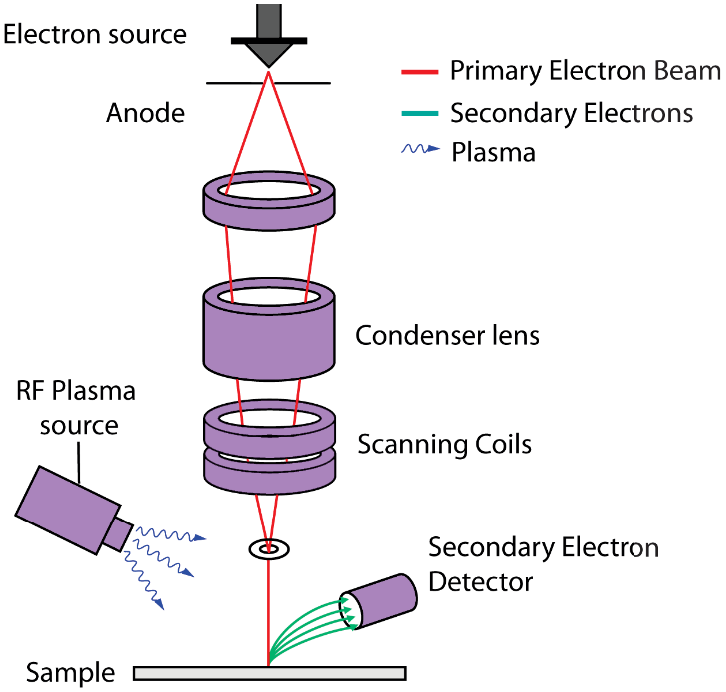

FIGURE 3.6: A simple schematic of an SEM operation with an in-situ plasma head attachment.

3.5.2 Substrate cleaning and general cleanliness

Samples and components installed into an SEM undergoes a rigorous cleaning regime. The standard cleaning procedure involves a first step of soaking parts or substrates in a series of strong solvents such as acetone, IPA and ethanol and ultra sonicated for 30-40 mins per solvent. The final ultra sonicating process includes rinsing in milliq water and sonicating for a further 5-10 minutes. The parts are then either dried with nitrogen or baked overnight to eliminate any residual water.

Piranha cleaning is also used to rid samples of most organic contaminants. Piranha solution is a strongly oxidising agent as it contains a mix of hydrogen peroxide (H_2O_2) and sulfuric acid (H_2SO_4). Piranha solution also makes sample surfaces hydrophilic through hydroxylation of the sample surface.

3.6 Monte Carlo simulations

The Monte Carlo software CASINO can simulate scattering events and signals produced (Secondary electron, backscattered electrons, cathodoluminesence and X-ray generation) by a standard SEM primary electron beam in the range of 0.1 to 30 keV [102, 158]. CASINO implements Monte Carlo methods in which elastic scattering events are modeled explicitly using random numbers generated with weighting factors to produce an appropriate statistical distribution of scattering events. This allows for the energy deposition profiles, penetration range, backscattered coefficients and radius to be accurately computed given correct electron beam and substrate parameters.

The software was used to determine electron penetration range, backscattered electron coefficients and radius for suspended and non suspended hBN in Chapter 7 and ion penetration ranges outlined in Chapter 6. Casino simulations were also performed for energy deposition profiles of EBID deposits, necessary to find correct dimensions for accurate compositional analysis (Chapter 4).

3.7 X-ray spectroscopy

X-ray analysis relies on the distinct energy bands (orbital shells) that exist for every element. In the case of X-ray spectroscopy in a SEM [153], the primary electron beam excites orbital shell electrons to higher energy bands. Upon their relaxation an X-ray is produced with a characteristic energy corresponding to the difference in energy between the orbital shells which are unique for all elements, this process is shown in figure 3.7. This allows for accurate compositional information to be obtained.

The compositional proportion of each element in a sample can be determined by comparing the intensity of X-rays for an unknown sample against a pure element or compound-element standards with known composition, while accounting for matrix effects such as the atomic number (Z) which relates to the stopping power, absorption and fluorescence corrections (ZAF) [159] and overlap conditions [160].

The two main X-ray microanalysis techniques used in this project include Energy dispersive X-ray spectrometry (EDS) and wavelength dispersive X-ray spectrometry (WDS). The fundamental differences between these analysing techniques lie in the detectors used and the way the X-rays are detected and measured.

3.7.1 EDS

Energy-dispersive X-ray spectroscopy (EDS) is the study of these characteristic X-rays emitted from a sample under high energy electron bombardment in an SEM. This technique gives qualitative and quantitative chemical composition of the samples being analysed.

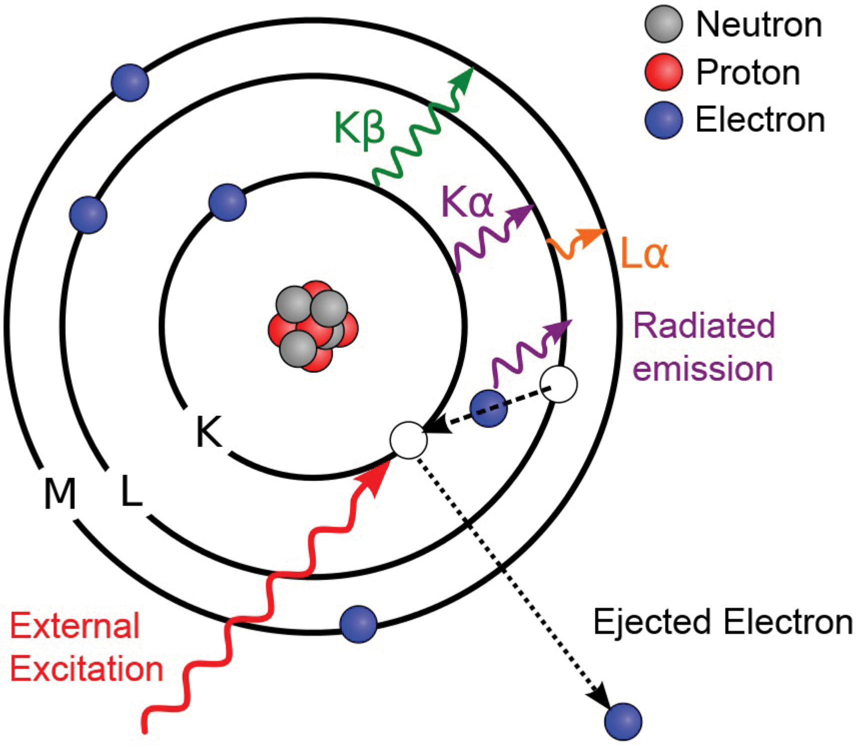

FIGURE 3.7: Schematic of the atom model is used to explain the characteristic X-ray emission produced from external excitation and relaxation in the atomic lattice. Adapted from [161] ©

EDS analysis performed in this project uses a silicon drift detector (SDD). Like most solid state detectors, the number and magnitude of X-rays ejected is measured by the amount of ionisation that is produced in the detector material as a result of the ejected characteristic X-ray. A SDD is made up of high purity silicon with a very low leakage current allowing for very high count rates.
The high count rates allow for X-ray mapping to be performed to gauge composition and effects of FEBIP on various materials, including Ag nanowires, Silver Nitrate, Aluminium nitride, hBN and BP in Chapters 5, 7, 8 and Appendix E.

3.7.2 WDS

Wavelength dispersive X-ray spectroscopy utilities an electromechanical system equipped with diffracting crystals and multiple gas ionisation detectors. Detecting X-rays this way yields very high spectral resolution (about 3-25 eV) and sensitivity necessary to distinguish between X-rays with very small energy differences. A comparison of EDS and WDS resolution is shown in Chapter 4, figure 4.5. The various diffracting crystals used also makes the detection of soft X-rays emitted by boron or beryllium possible.

Spectrometer mechanism

The operation of the crystal spectrometers is based upon the principle of diffraction according to Bragg's law, which equates to:

$$n\lambda = 2d\sin\theta \tag{3.1}$$

Where:

$n = 1, 2, 3\ldots$

λ = wavelength of the X-rays being diffracted

d = inter planar spacing of the diffracting crystal

θ = Bragg angle (angle between crystal surface and incident diffracted X-rays)

X-rays produced by initial electron bombardment and that satisfy Bragg's law will be diffracted towards the detectors. X-rays that do not satisfy Bragg's law will not be diffracted and undergo destructive interference and will be absorbed by the surroundings [162], see figure 3.8.

Crystals of known d spacing are used as analysing crystals in the spectrometer. The angular position of the detector changes in accordance with Bragg's Law so that a particular wavelength for a particular element will be diffracted to the detectors for quantitative analysis [163].

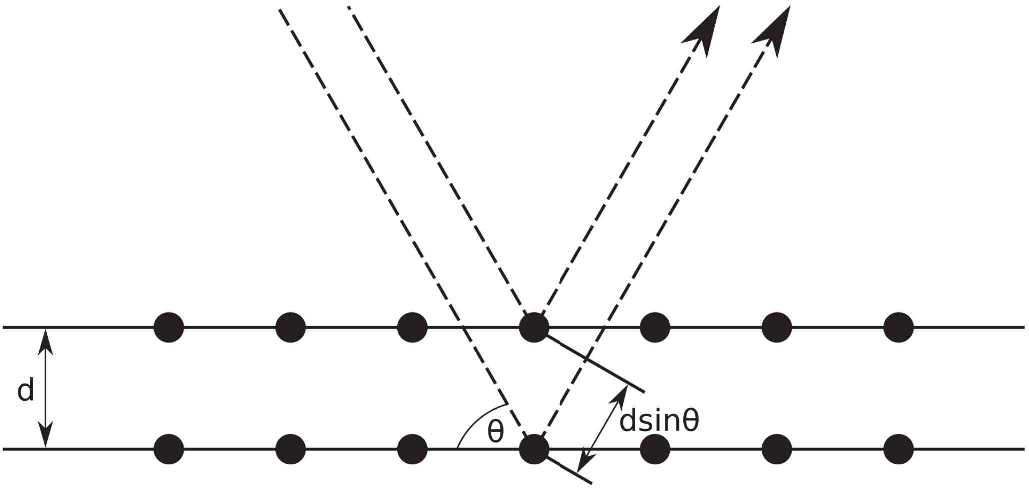

FIGURE 3.8: An example of Bragg diffraction is shown where two identical beams of light are scattered at two different locations. Constructive interference will occur when the lower beam travels an additional length of 2dsinθ which is a integer multiple of the wavelength of the incoming beam.

Along every point of the spectrometer scanning range, the distance between the X-ray source and crystal must always be equal to the distance between the crystal and the detector. The Microspec WDS spectrometer used in this project is equipped with a fully focusing Johansson geometry Rowland circle and is connected to the SEM at an inclined angle which allows the sample to remain horizontal. Therefore X-ray take off angle can be easily defined as the inclined angle. Using Bragg's law the angular scanning range of the spectrometer mechanism determines the analysis range for a given diffracting crystal.

WDS analysis was used to resolve Platinum and phosphorus spectral peaks in Chapter 4 and has shown to be accurate to approximately 1-2% using known elemental composition samples. Combined with the precision for measured intensity data for the standards measured, an accuracy of +/-2% is given, this will be the uncertainty for all WDS measurements taken.

3.8 Auger electron spectroscopy

Auger electron spectroscopy [164] is based on the Auger effect. This effect is an electronic process where higher energy electrons or photons are used to knock core shell electrons out of an atom. This leaves behind a hole which is an unstable state and is then filled by an outer shell electron.

The energy difference in the outer and core shell energies is then released during this transition. If the energy released is greater then an outer shell electron orbital binding energy, this energy can be transferred and cause ejection of this outer shell electron. The kinetic energy of the emitted electron will be:

$$E_{aug} = E_K - E_{L1} - E_{L2} \tag{3.2}$$

where E_K, E_{L1}, E_{L2} are the electron binding energies for the core level, first outer shell, and second outer shell respectively. This process is shown in figure 3.9.

In this work a nano-Auger Electron Spectrometer (AES, Omicron nanoSAM) was utilised and operated under ultrahigh vacuum conditions for highly surface sensitive composition analysis on hBN after electron beam irradiations performed in Chapter 7.

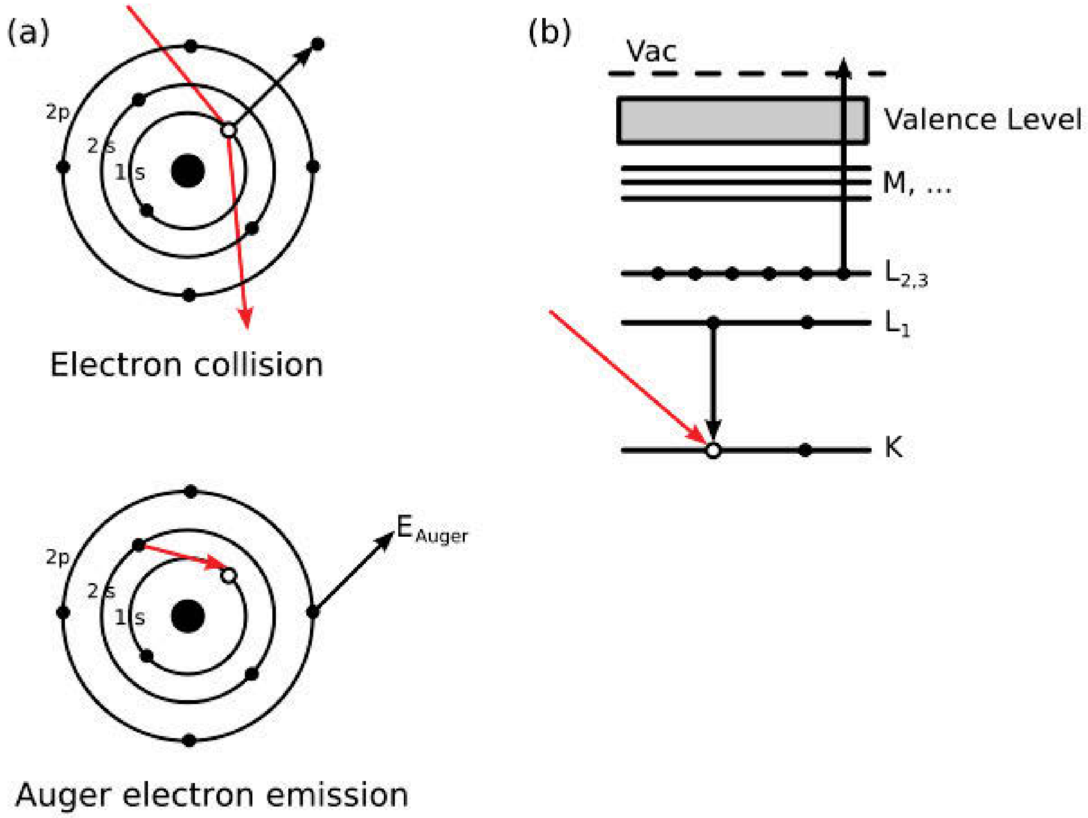

FIGURE 3.9: The Auger deexcitation process is illustrated in (a). A hole is created in the 1s level, which is filled by a 2s level electron when an electron impinges it, creating a transition energy of 2s to 1s. A 2p electron is then ejected from the transfer of this transition energy. Two hole are then left behind on the 2s and 2p orbital to form the final atomic state. (b) is illustrating the process using spectroscopic notation, $KL_1L_{2,3}$.

3.9 Transmission electron microscopy and selected area electron diffraction

Selected area electron diffraction is a technique performed within a transmission electron microscope (TEM) [165]. A TEM uses high accelerating voltages (100-400 keV) through thinned samples, which are usually 100s of nm thick. This is to enable the sample to act as a diffraction grating for the high energy electrons. The spacing of atoms are in the order of an angstrom and the high energy electrons have a wavelength on the order of a hundredth of an angstrom, the electrons typically pass through the samples with the atoms acting as a diffraction grating. Some fraction of these high energy electrons will be diffracted according to the crystalline structure of the sample, leaving a diffraction pattern behind. Each material has its own unique crystallographic signature which is made up of atomic spacing and a unit cell and allows for identification of a particular material or group of materials and their specific crystalline structure. TEM imaging was undertaken in the project to find the crystallographic structure of the fragments created during EBIE of hBN (Chapter 7), this was confirmed by selected area electron diffraction (SAED).

3.10 AFM

Atomic force microscopy (AFM) is routinely used to determine the surface topography of substrates with exceptional accuracy [166]. The operation of an AFM involves scanning over a sample surface with a probe consisting of a fine tip and a flexible cantilever. As the tip approaches the sample, the interactions between the surface and the tip will cause deflections in the cantilever. These deflections are usually detected using a laser, which is shone at end of the cantilever and reflected into a photodiode. The probe is mounted upon a three dimension piezoelectric scanner which is used to scan an area of interest and compensate for deflections detected in the photodiode to give the surface topography of the scanned region. A schematic of this process is illustrated in figure 3.10.

The Dimension 3100 from Veeco was used for all measurements in tapping mode to obtain surface topography information from FEBIP processes in Chapter 7 where etch rates can be obtained by measuring pit depths.

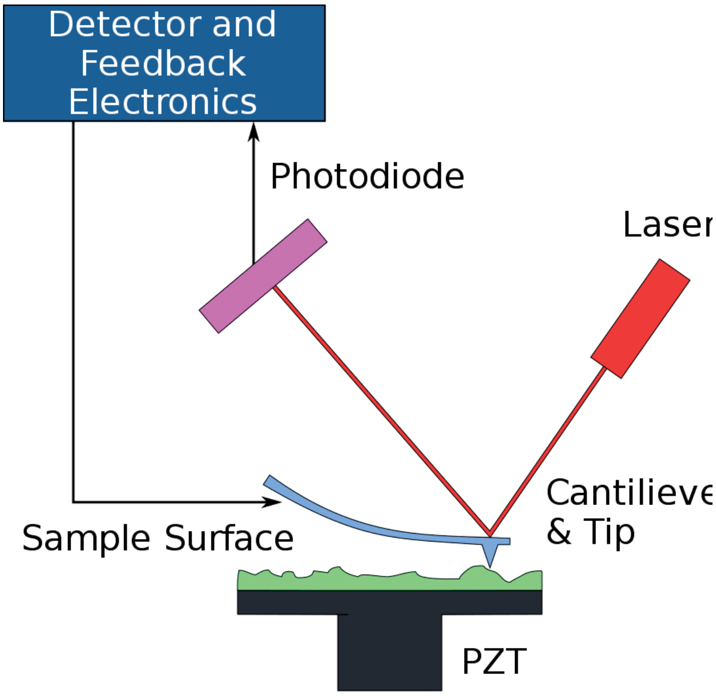

FIGURE 3.10: A schematic of an AFM using the deflections of a laser beam to map the topography of a sample surface.

3.11 Confocal microscopy

Confocal microscopy is an optical imaging technique. Enhanced resolutions can be obtained using a confocal microscope over a wide field microscope. The idea behind this is to use a point illumination source and eliminate out of focus signal through the use of a pinhole and an optically conjugate plane in front of the detector. However, the increase in resolution results in a decrease in signal as the pinhole acts to block a majority of the fluorescence.

Photoluminescence (PL) spectroscopy [167], polarisation, lifetime and single photon emission measurements were characterised using an in-house built confocal microscope and Hanbury Brown and Twiss (HBT) interferometer setup as shown in figure 3.11. A more detailed schematic can be found in figure 6.2, Chapter 6. The two excitation sources mainly used include a continuous 532nm laser and a 510 nm pulsed laser. These lasers are used for PL spectra, g(2)(τ) correlation, stability characterisation and for lifetime measurements, respectively. Autocorrelation measurements were performed using a Picoquant Picoharp 300 time-correlated single-photon counting system. X-Y scanning of a sample was performed using a Newport scanning mirror and a dichroic 532nm mirror is used to filter laser on emission and act as a beam splitter.

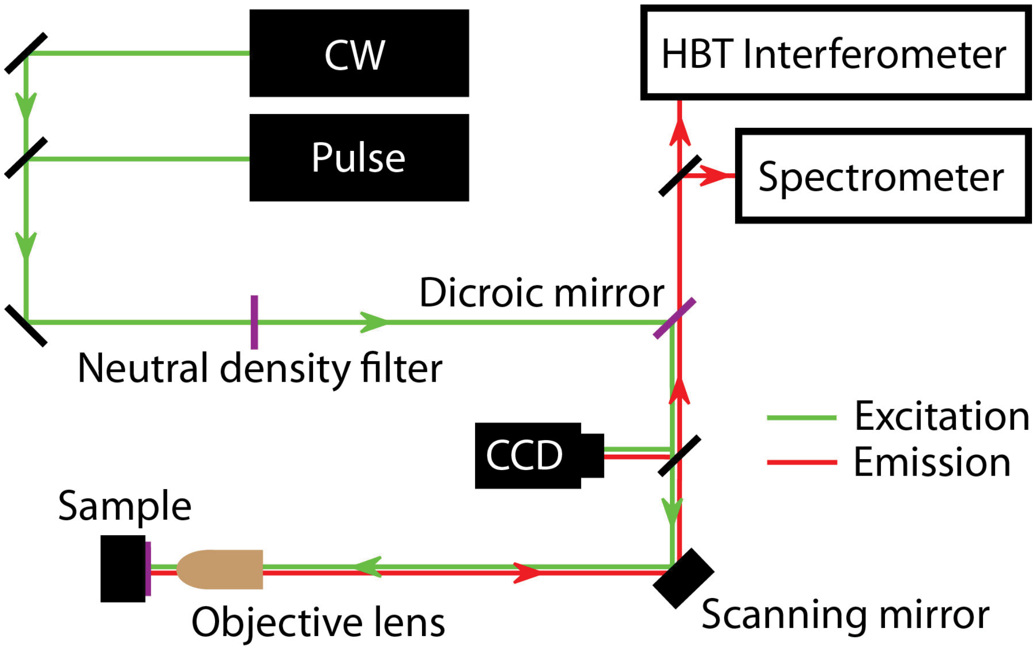

FIGURE 3.11: A simple schematic of the confocal setup used. With excitation and collection pathways highlighted as well as main components.

The electron irradiation process used in this work results in changes to the local material structure and generation of defects is seen under various environments in hBN. Confocal microscopy was thus used to obtain photo physical properties on defects created in hBN before and after electron beam irradiation as highlighted in Chapter 6.

3.12 Raman spectroscopy

Raman spectroscopy [168] works by observing vibrational modes of the material through inelastic scattering of monochromatic light which shows vibrational, rotational and low-frequency modes of the material being analysed. The excitation laser can undergo scattering in two ways: loss of energy due to excitation of rotational, vibrational or electric states or gain in energy due to relaxation of an excited state, this is known as Stokes and anti-Stokes Raman scattering. These transitions appear appear as distinct lines in a spectrum, and are separated from the laser frequency by a characteristic shift to lower or higher quantised energy levels.

The hBN Raman mode is used to identify crystal quality after EBIE in Chapter 7. The use of Raman spectroscopy with BP, allow for the identification of degradation in the material by monitoring the A_g^1 and B^1 and A_g^2 optical modes in Chapter 5. Raman measurements were performed using a Renishaw inVia Raman microscope with a 633 nm excitation laser.

3.13 Photolithography

Photolithography is a microfabrication technique used to create micron resolution patterns on a substrate. A light sensitive chemical known as a photoresist is typically spin coated onto a substrate and aligned with a hard mask containing the required pattern. The exposed photoresist is then illuminated with UV which acts to either cross-link or make soluble the exposed regions depending on which resist is used. Development either removes the exposed or unexposed region leaving behind a mask for further processing. Photo-lithography was used for substrate mapping and contacts for electrical characterisation for projects in outlined in Chapters 5,7,6,8 and Appendix E.

3.14 Metal sputtering

Physical sputtering of metals was performed to deposit thin films of various different materials over the course of this project. Physical sputtering works via momentum exchange of highly energised particles impacting atoms in the target material. An atom will be ejected if the energy of the particles is greater than the surface binding energy of the target material. An Edwards RF plasma sputterer was used to deposit Ag, Cu, Co, Ni, Au and Ti for a range of projects included in Chapters 5, Appendix E.

3.15 Thermal annealing

Thermal annealing in the ex-situ chemical vapour deposition (CVD) chamber (shown in 3.12) was used to find potential gases that will react with the phosphorous contamination and rid the contamination for the EBID work performed in Chapter 4.

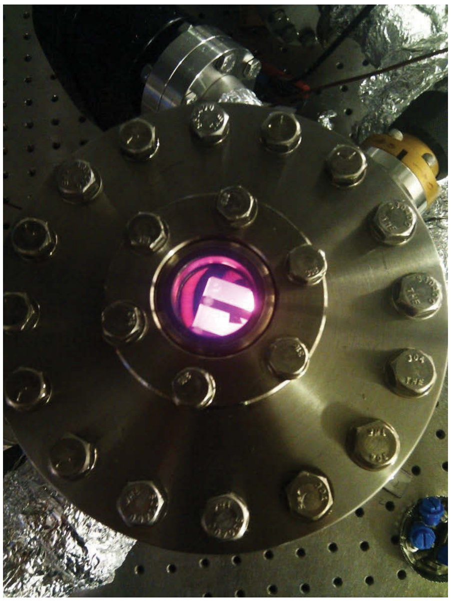

FIGURE 3.12: An image of the ex-situ CVD chamber in operation.

There is a wide variety of gases available to the CVD cell as well as a turbo molecular pump enabling pumping to high vacuum. The gases available for annealing experiments include H_2O, NH_3, O_2, XeF, NF_3 and H_2. A PG large heater is used for ex situ annealing, with temperatures of up to $1000°C$ using a single power source, in vacuum or with gases flowing. A thermocouple is clamped to the sample stage to give accurate temperature readings.

Chapter 4

Programmable patterning of three-dimensional Pt structures

4.1 Abstract

Direct examples of 3D nanostructure fabrication will be shown in this chapter. Localised, mask-free deposition of high purity platinum will be showcased through a combination of room temperature, direct-write electron beam induced deposition (EBID) using the precursor $Pt(PF_3)_4$ and a low temperature annealing process. First, the programming method for reproducible 3D nanostructures will be outlined, as well as the main parameters controlled. Also in this chapter the EBID decomposition pathway of $Pt(PF_3)_4$ is illustrated. This process likely involves the inefficient scission of PF_3 bonds leaving behind a P contaminated Pt deposit. A low temperature ($\leq 400°\mathrm{C}$) post-growth annealing method in H_2O was formulated, which leads to the complete purification of the Pt deposits. The annealing treatment removes phosphorous contaminants through a thermally activated pathway involving dissociation of H_2O and the subsequent formation of volatile phosphorus oxides and hydrides that desorb during annealing. The resulting Pt is indistinguishable from pure Pt films by wavelength dispersive X-ray spectroscopy (WDS).

4.2 FEBIP nanostructure patterning

4.2.1 Introduction

FEBIP requires precise and consistent electron beam placement and dwell times to allow for accurate and reproducible data acquisition. Extending this, being able to reliably manipulate the electron beam further enables the ability to utilise the strengths of EBID and EBIE of being a single step etching or deposition method. The growth of highly ordered arrays of structures including freestanding, overhanging three dimensional deposits can be realised and conversely etched ordered arrays or patterns of materials achieved.

Taking this viewpoint there needed to be an automated and methodological way to control the highly ordered and precise nature of nanofabrication using FEBIP in this project, as manually moving the electron beam spot will simply take too long and be imprecise in terms of dwell time, structure, size and spacing. The first project undertaken was to create a program to control the e-beam, which allows for the construction of complex structures and patterns. There are 3 main categories that need to be addressed; these are patterning, overhanging deposition and reproducibility of the structures (arrays).

4.2.2 FEBIP scanning pattern/function generator

The most basic principles in the program involved sending analog output voltages through a National Instruments data acquisition device (NIDAQ) to an external XY scan board on the SEM to control the e-beam. The external XY scan board voltage ranges from 5 to -5 V for both x and y directions and has an analog resolution with a point pitch on the order of 0.1 nm. The NIDAQ has an analog output resolution of well over 1000x1000 pixels over 5 to -5 V, and a MHz refresh rate (microsecond dwell times) which is very well suited for FEBIP. Four separate variants of the program were made in LabVIEW. The user interface (figure A.1) and coding (figure A.2) has been attached in Appendix A, with descriptions of the processes. A brief explanation of how each program variant works and its purpose will now be given.

Scanning pattern with varying dwell time

The basic premise of this program was to input a BMP picture file in 8-bit grey scale format. The BMP file would then be transformed into a 2D array dependent on the resolution of the image. The colour value determines the dwell time ofthe pixel, for example: white has the value of 255 and will result in 255 × dwell time of the e-beam at that pixel and conversely black with a value of 0 will result in no e-beam irradiation.

Using a Boolean structure every second row would be reversed of the 2D array and then transformed into a 1D array, so the electron beam scans in a serpentine fashion. The zero values then run through a shift register to remove and reshape the array so the e-beam does not irradiate at those values. Using a 'For' loop determines the number of rasters the pattern will perform. The array values are then sent out of the NIDAQ as an analog voltage with MHz refresh rate and sampling rate. This program is used for creating patterns and simple arrays of shapes and structures. Example patterns and arrays created from EBID of platinum are shown in figure 4.1.

Scanning pattern with constant dwell time

The most notable difference between this variant and the one previously described is in the way the program scans over time, and the dwell time per value. The 8-bit grey scale file is now utilised to a greater extent to allow bottom-up deposition of 3D nanostructures. This particular variant rasters in a serpentine fashion for all values, with a constant dwell time. After each pass, one is subtracted from every point and using a Boolean structure once the value reaches zero the e-beam does not scan over it. An example is shown below using this variant to create a pyramid structure in figure 4.2.

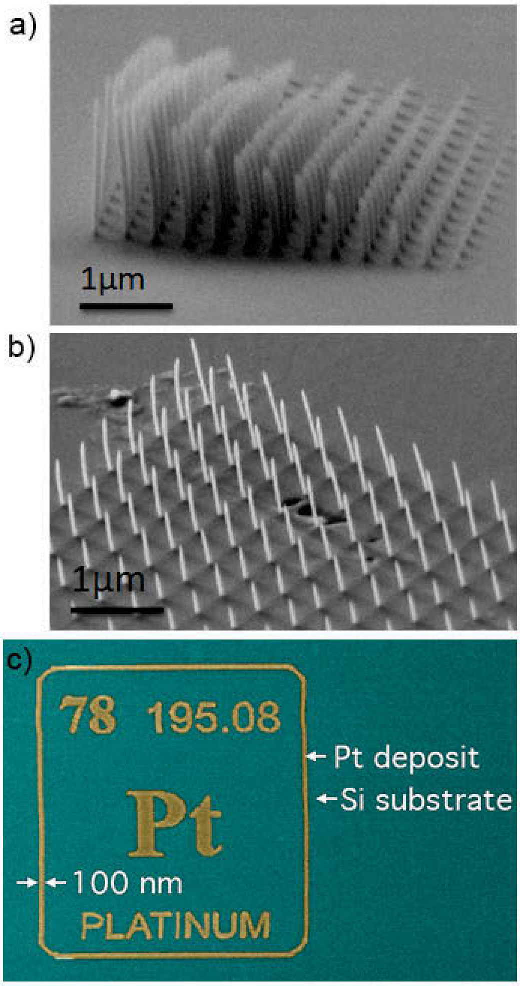

FIGURE 4.1: (a-b) A collection of Pt freestanding nanowire arrays deposited using the scanning pattern generator as a function of increasing dwell time. c) Pt periodic table symbol patterned using the scanning pattern generator.

Scanning pattern for arrays

In this variant, an individual structure would be deposited before moving to the next in an array. This program operates by offsetting the starting coordinates of the same structure over a loop. Dwell time can also be varied linearly per loop. This would be most useful for large arrays where scanning across multiple structures in a serpentine fashion would be less efficient and accurate then tackling one structure at a time. This method also reduces unwanted deposition and favours localised deposition. An example is given in figure 4.1, of a 2D array of Pt freestanding nanowires as a function

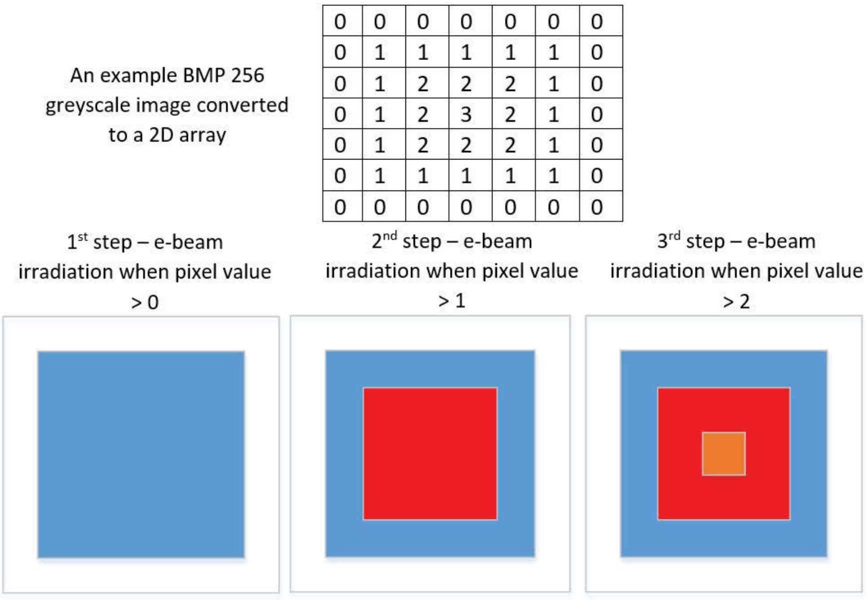

0	0	0	0	0	0	0
0	1	1	1	1	1	0
0	1	2	2	2	1	0
0	1	2	3	2	1	0
0	1	2	2	2	1	0
0	1	1	1	1	1	0
0	0	0	0	0	0	0

FIGURE 4.2: An example is shown of layered scanning pattern generation for bottom up nanofabrication.

of increasing dwell time.

Function scanner

This variant is specialised and purposefully created for complex 3D nanostructures. Custom coding is necessary for each shape desired where custom functions are inserted into the program. This variant is well suited for creation of overhanging nanostructures especially in terms of plasmonic antennas; such as Yagi-Uda, helix and conical spirals where surface plasmons propogate along the path of the helix, or is amplified by the Yagi-Uda antenna. An example of a conical spiral output is plotted in figure 4.3d. The dwell time is key, as well as accelerating voltage to achieve overhanging deposition as the interaction volume should be wholly within the deposited materials.

4.3 Patterning and three dimensional structures

FEBID nanofabrication has seen a surge in the creation of functional nanostructures, due to its unique combination of novel capabilities, such as:

- *In-situ* real time imaging allowing deposition to occur on any substrate surface or feature
- One step direct writing of a wide range of materials
- Deposition without requiring masks or resist layers
- High spatial resolution on par with or superior to electron beam lithography (EBL) and ion beam induced deposition, without ion bombardment damage

However, the biggest advantage of EBID as a nanofabrication technique compared to other techniques comes in the form of overhanging, multidirectional and high aspect ratio deposition. Due to this, the shape and size of deposits are not restricted in three dimensional planes, so it is possible to directly write complex 3D structures of virtually any shape with nanoscale precision. To fully exploit these capabilities a greater understanding of the interactions between the electron beam, substrate and precursor is needed, especially in terms of depositions in close proximity to one another and their interactions.

The most challenging part of three-dimensional EBID is the inherently complex and multifaceted interactions and reactions that take place during deposition. The main EBID interactions and mechanisms to be understood for three dimensional deposition are the large interplay between the precursor-deposit and the electron beam parameters and the substrate and precursor interactions.

The main parameters to control these interactions include:

- Accelerating voltage
- Current density
- Growth rates and regimes

- Interaction volume and charge effects

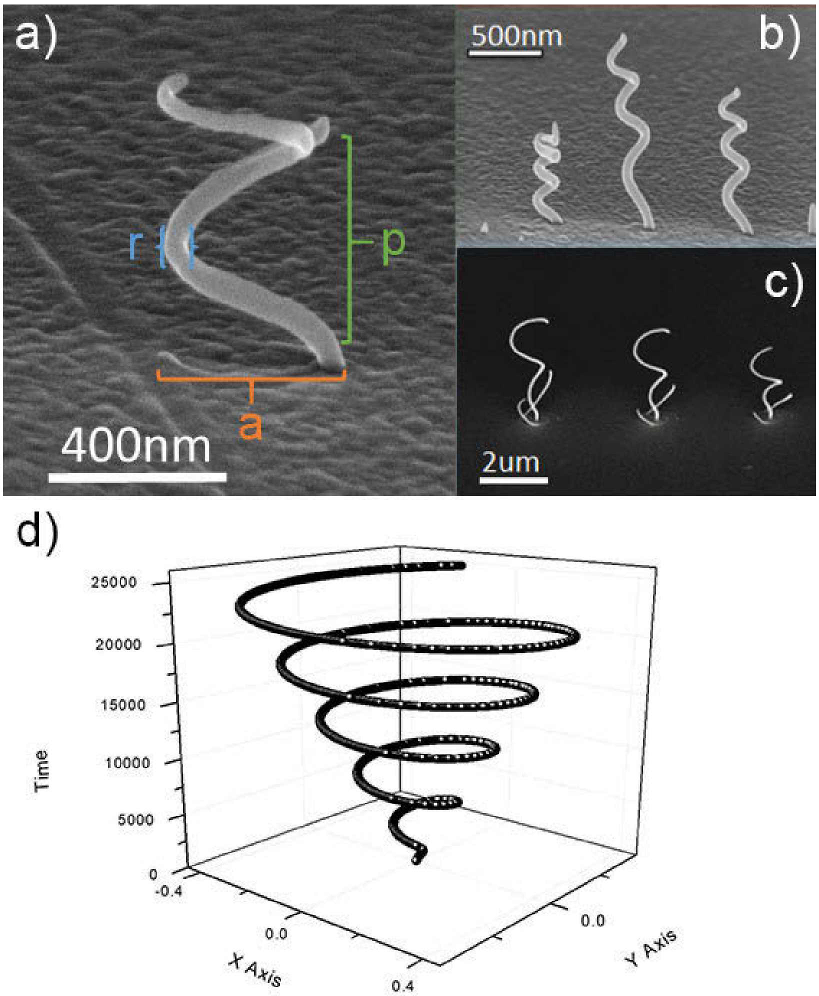

FIGURE 4.3: A series of 90 degree tilted SEM images of Pt spiral structures. (a) indicates the variables that control the dimension of the spirals. (b) shows a series of variable spirals and (c) a series of conical spirals fabricated. (d) illustrates the output voltages of a conical spiral plotted against time.

The 3D overhanging structures studied in this project include helices amongst others, examples of these are shown in 4.3a-c. These structures play a prominent role in the field of plasmonics and photonics as they can allow variation in direction and polarisation of light. The parameters that may be varied to control the 3D structure geometry and what they correspond too are listed below and also highlighted in figure 4.3a:

- Dwell time, p, regulates the pitch width of the spiral structure (also affects radius of deposit)
- Amplitude, a, controls the diameter of helix
- Resolution, r, controls radius of deposit to some extent and smoothness of the deposit transition (also affects pitch width)
- No. of revolution, controls the number of turns in the helix
- Others include amplitude of taper and frequency of increasing taper for conical helical structures

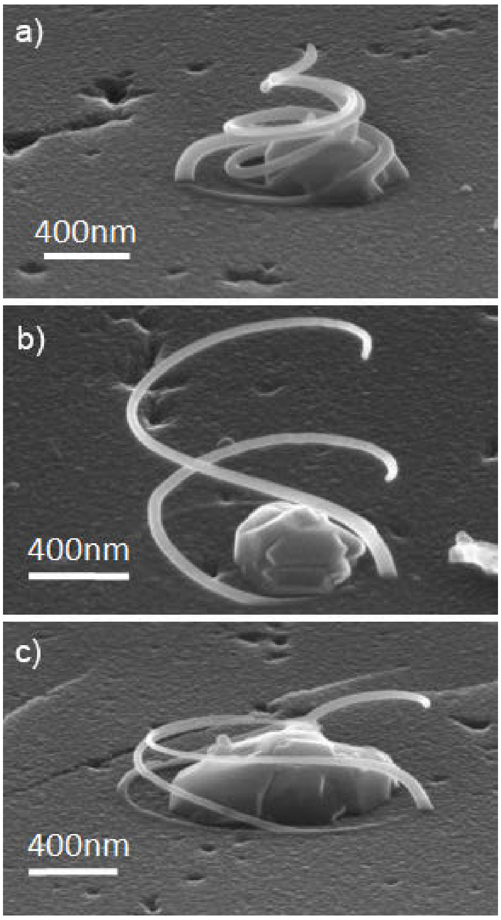

FIGURE 4.4: A series of SEM images of Pt spirals fabricated directly over individual Nanodiamonds.

4.4 EBID method

The EBID precursor Tetrakis(trifluorophosphine)platinum $Pt(PF_3)_4$ (Strem chemicals) is a high vapour pressure liquid at room temperature. It was loaded into a peltier-cooled stainless steel crucible under dry N_2, which was subsequently removed using multiple freeze-pump-thaw cycles.

The customised Sirion column SEM equipped with a FEG source was used for all depositions using the $Pt(PF_3)_4$ precursor. Gas delivery was initially done using a GIS 150 μm from the surface and 70 μm from the central beam axis. Pressure reading in the microscope was held at 4×10^{-5} keV (greater partial pressure at the end of the GIS needle).

Experiments were also performed using ESEM conditions. The chamber pressure was held at 0.025 keV, with a flow rate of 0.07 sccm, the EBID deposits were found to be more consistent under these environmental conditions, most likely due to an even pressure throughout the chamber. Deposition experiments then focused on varying accelerating voltages and dwell times. The results show that maximum control was achieved using the conditions typically at 10 kV accelerating voltage with a 0.5 nA highly focused Gaussian beam. These conditions allowed for very high resolution spiral structures deposited on any substrate with high precision. An example is shown in figure 4.3 and 4.4 where spiral Pt structures are grown on various substrates and directly a top of individual nanodiamonds. Unfortunately the deposits grown using the $Pt(PF_3)_4$ precursor suffered from high levels of Phosphorus contamination. In the following section, a purification technique was established to completely purify the Pt deposits grown using the $Pt(PF_3)_4$ precursor and EBID.

4.5 Pure platinum nanostructures grown by electron beam induced deposition

4.5.1 Introduction

Fabrication of Pt has attracted more attention than any other EBID-grown material. However, to date, there exists no technique for EBID of highly pure Pt. Best results have so far been achieved using the precursor $Pt(PF_3)_4$ [66–71, 80], which yields deposits in which phosphorus and fluorine are the major contaminants (oxygen is missing from most prior analyses). It is noted that high purity Pt deposits have been demonstrated using a combination of an EBID-grown seed layer and atomic layer deposition (ALD) [169], or by XeF_2-mediated, fluorine-induced decomposition of $Pt(PF_3)_4$ adsorbates [170]. However, both of these techniques exhibit lateral growth rates that are approximately equal to the corresponding vertical growth rates. They can therefore not be used for the growth of high resolution, high aspect ratio deposits, and limit the attainable geometries of self-supporting three-dimensional nanostructures.

Here, the fabrication of highly pure platinum achieved by EBID of $Pt(PF_3)_4$ in combination with post-growth removal of phosphorous contaminants by low temperature annealing in H_2O is demonstrated. The deposits contain > 94 at. % Pt, and are indistinguishable from reference Pt standards by wavelength dispersive X-ray spectroscopy (WDS). The required annealing temperature is sufficiently low ($\leq 400°\mathrm{C}$) to prevent both the decomposition of the Pt deposits and chemical etching of the substrate (which are observed at higher annealing temperatures). The purification method is both more effective and more widely applicable than prior methods involving substrate heating during EBID, and post-deposition annealing in vacuum, O_2 and NH_3 environments.

4.5.2 Methods and materials

EBID was performed using an ESEM installed with an in-situ environmental sub-chamber which enabled control over the substrate temperature during EBID, as described in Chapter 3, section 3.3 and Ref. [74, 171]. The sub-chamber was isolated from a differentially pumped electron column using a 200 μm pressure limiting aperture. After pump-down to $\sim 10^{-4}$ Pa, the pressure in the sub-chamber was maintained at 13 Pa using a pressure-feedback gas delivery system. A 10 keV, 10 nA, top-hat electron beam [62, 63] was defocused to a diameter of ~ 5 μm, yielding an electron beam flux of $\sim 3 \times 10^{17}$ $\mathrm{e}^-/\mathrm{cm}^2/\mathrm{s}$. Deposits such as the one shown in 4.5b were grown using a stationary, normal incidence beam on Si (111) substrates (with a native oxide), with a growth time of 30 minutes.

After deposition, samples were transferred in air to an ex-situ vacuum chamber (base pressure $\sim$ 10^{-4} Pa) equipped with a heating stage and a gas flow delivery system. Annealing was performed in vacuum, and in H_2O, O_2 and NH_3 environments (pressure $\sim$ 130 Pa). Compositional analysis was performed using a high vacuum SEM equipped with WDS. WDS was used instead of the more common EDS because WDS enables resolution of the $\mathrm{P}\ \mathrm{K}_\alpha$ and $\mathrm{Pt}\ \mathrm{M}_\alpha$ X-ray peaks which overlap in EDS spectra, as shown in figure 4.5c. WDS was performed using a beam energy of 10 keV to ensure that the electron interaction volume (simulated using standard Monte Carlo simulators of electron-solid interactions [172] was contained within the deposit (such as the one shown in figure 4.5b). Standards of known elemental composition were used to quantify WDS data, with a reproducibility of $\pm 2\%$. Each deposit was analysed once only, either after growth, or after a single post-growth anneal.

4.5.3 Results and discussion

As-grown deposits

Deposits grown at room temperature have a typical atomic composition of $47 \pm 5\%$ Pt, $30 \pm 5\%$ P and $15 \pm 10\%$ O. The composition variation is greater than the WDS analysis

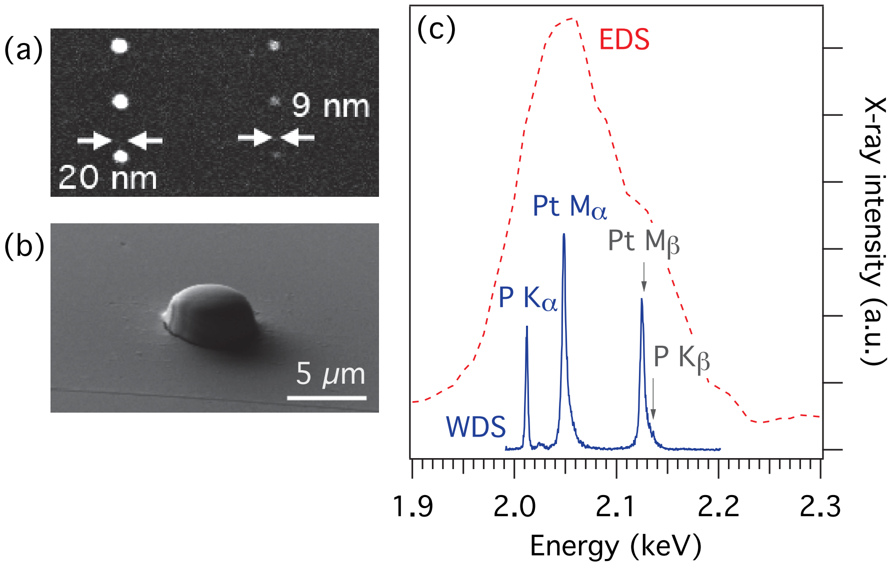

FIGURE 4.5: SEM images of a (a) nanodot array grown by $Pt(PF_3)_4$-mediated EBID using a Gaussian electron beam, and (b) deposit grown using a 5 μm, top-hat beam. (c) X-ray spectra showing the Pt M_α, Pt M_β, P K_α and K_β X-ray lines.

error of $\pm 2\%$ because of variations between individual deposits. The spread is caused by variations in electron beam current typical of thermionic tungsten hairpin electron sources (the deposit composition is known to vary with the beam current density used for $Pt(PF_3)_4$ EBID) [67], and due to uncontrolled partial decomposition of $Pt(PF_3)_4$ by residual gas molecules present in the vacuum chamber. The measured F content decreased with time when samples were stored in vacuum or in air, and was at or below the WDS detection limit in samples stored overnight prior to WDS analysis. The most likely F removal pathway involves the desorption of chemisorbed fluorine, which is expected to be accelerated by H_2O adsorbates [170] with an overall reaction of the form:

$$2\,F + 2\,H_2O \longrightarrow 2\,HF_{(g)} + H_{2(g)} + O_{2(g)}$$

The trace amounts of fluorine and the presence of oxygen in the as-grown deposits indicate efficient dissociation and desorption of PF_3 and fluorine during EBID, accompanied by oxidation of phosphorus by residual contaminants (mainly H_2O) present in the vacuum chamber. These results correspond well with those of prior ultra-high vacuum surface science studies which show that the deposition process involves these reaction pathways [70, 71]:

$Pt(PF_3)_4 \xrightarrow[e-e-]{-PF_3} Pt(PF_3)_3$

$Pt(PF_3)_3 \xrightarrow[e^-]{-F^-} Pt_xP_y$

$Pt_xP_y \xrightarrow[e-e-]{+H_2O} Pt_xP_yO_z$

The last two pathways, involving P-F bond cleavage, and phosphorus oxidation by residual water vapour, occur concurrently under prolonged e-beam irradiation (e^-) and/or substrate heating (Δ) during deposition. Substrate heating during deposition can significantly improve the composition of some EBID-grown materials [55, 72–74]. However, in the present case of $Pt(PF_3)_4$-EBID, the deposit composition was observed to improve only at temperatures $\gtrsim 100°C$, reaching a Pt content of ~ 72 at.% at $\sim 120°C$. This extent of purification is inadequate, and the approach is impractical because $Pt(PF_3)_4$ has a thermal decomposition temperature of $\sim 130°C$ [173]. Thermal decomposition of the adsorbates causes delocalised (chemical vapor) deposition, thereby compromising the localised, direct-write capability of EBID.

Post-growth annealing

Figure 4.6 shows the composition of deposits annealed in vacuum ($P \sim 10^{-4}$ Pa) for one hour at temperatures of 400, 600 and 750°C. Temperatures $\gtrsim 600°C$ caused significant structural decomposition of the deposits, illustrated by the image shown in figure 4.6. Annealing in vacuum at temperatures $\leq 600°C$ caused an insignificant decrease in the concentration of phosphorous impurities in the deposits. Similarly, annealing in O_2 and NH_3 environments had no significant effect on composition at temperatures lower than the deposit decomposition temperature.

Conversely, low temperature annealing in H_2O vapor can increase the Pt content to a degree that is indistinguishable from reference, high purity Pt films by WDS analysis. Figure 4.7 shows the deposit composition as a function of H_2O annealing time at 250 and 400°C. At 400°C, annealing times of 20, 40 and 300 minutes yield Pt concentrations of ~75, 92, and 94 at.%, and P concentrations of ~17, 2 and 2 at.%, respectively

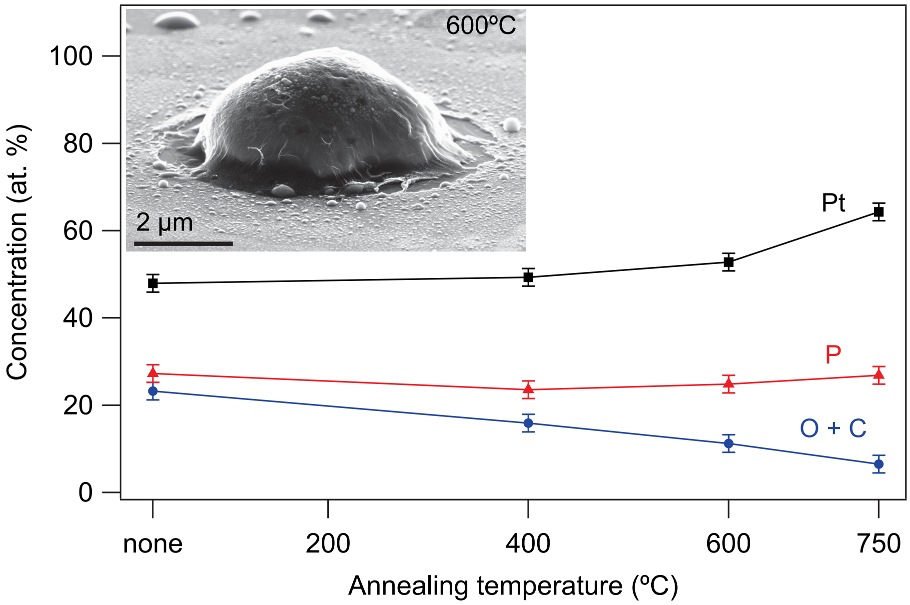

FIGURE 4.6: Deposit composition as a function of post-growth annealing temperature in vacuum (annealing time = 60 min). *Inset:* SEM image of a deposit acquired after a 600°C annealing treatment.

(where 2 at.% is the P detection limit). The Pt concentration of ~ 94 at.% is indistinguishable from that of a high purity, reference Pt film. The remaining ~ 5 at.% (4.7b) consists of oxygen and carbon, likely due to an oxide layer and oxygen-containing hydrocarbon contaminants that build up on the deposit surface [174] during WDS analysis.

Post-growth annealing at 400°C did not cause structural decomposition of the deposits (see, for example, the image in figure 4.5b which shows a deposit that had been annealed in H_2O for 60 min). However, some degree of shrinkage is expected as a result of purification [80, 81].

Annealing in H_2O at 250°C yields the same trend as at 400°C, but significantly longer times (approaching 24 hours) are needed to achieve equivalent Pt content (figure 4.7). At 600°C, annealing times of < 40 min are needed to produce deposits which are indistinguishable from reference Pt films. However, the high temperature annealing treatment causes thermal decomposition of the deposits (as in high vacuum, see figure 4.6), and etching of the substrates in the vicinity of annealed deposits (shown in figure 4.8). Etching at high temperatures is ascribed to phosphoric acid (H_3PO_4) formed in a reaction with residual H_2O molecules present in the vacuum chamber, and is consistent with the reported [175] dependency of the etch rates of silicon and silicon dioxide on temperature.

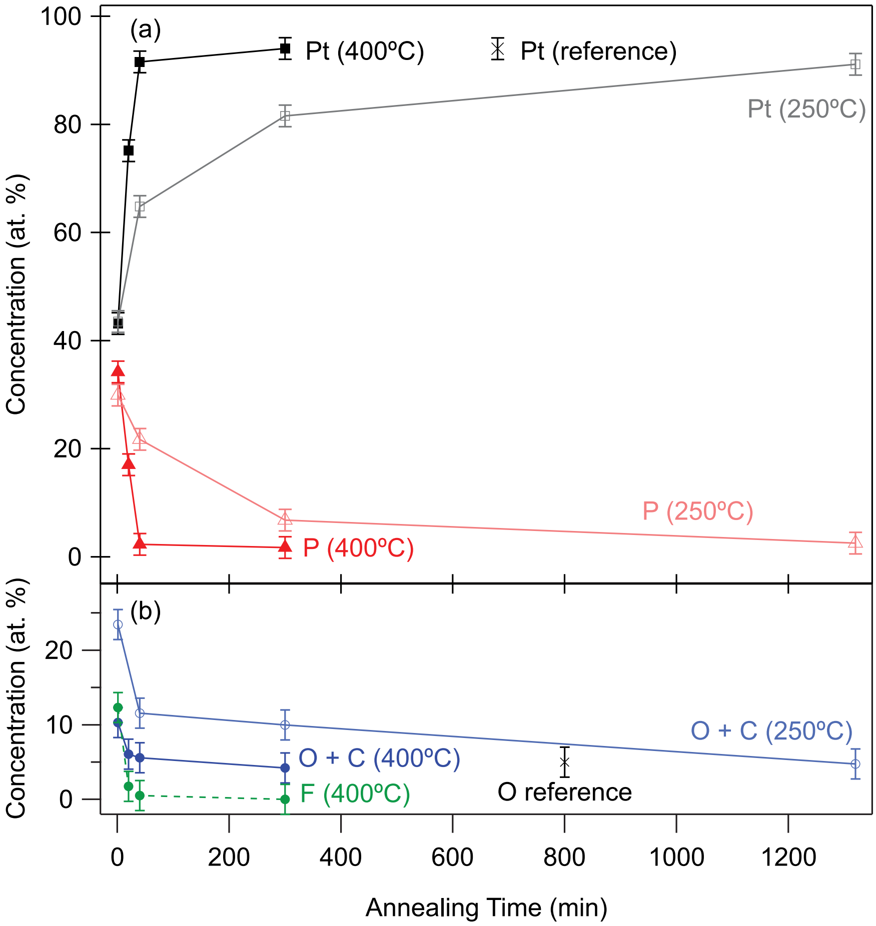

FIGURE 4.7: Composition of $Pt(PF_3)_4$-EBID deposits plotted as a function of annealing time in H_2O vapor at 250 and 400°C. Fluorine was detected only in the sample set annealed at 400°C, because it was stored in vacuum prior to WDS analysis. The concentration of Pt and P over time is shown in a) and O+C, F content over time is shown in b). The measured composition of a reference, high purity Pt film is also shown in the figure (×).

In the sample sets shown in figure 4.7, F was detected only in the one annealed at 400°C because it was stored in vacuum prior to WDS analysis (the F concentration decreased with time, as noted above). However, fluorine contamination is not of concern

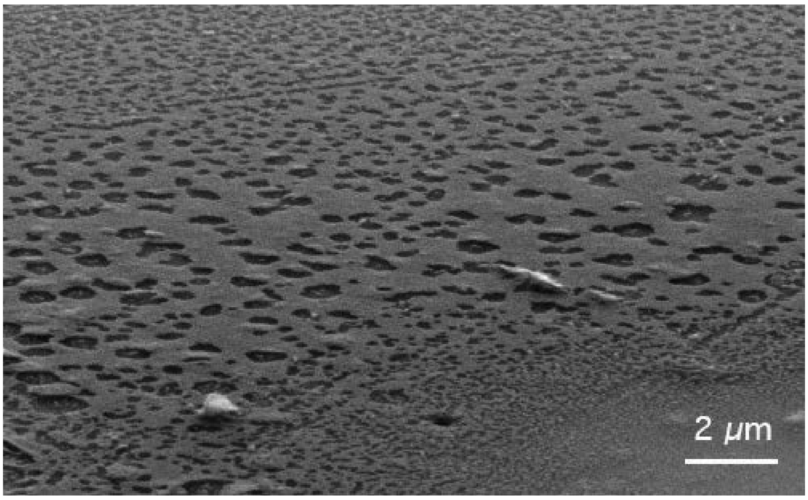

FIGURE 4.8: Etch pits in the substrate surface near deposits subjected to a 600°C anneal in H_2O.

because the H_2O annealing treatment is very efficient at removing F, as seen in figure 4.7b.

4.5.4 Purification mechanism and generality of the purification technique

The annealing results indicate that removal of phosphorous by the H_2O annealing treatment is likely caused by: (i) thermal decomposition of H_2O at the sample surface into reactive species such as O, H and OH radicals, and (ii) reaction of P with these radicals to form volatile species that desorb from the solid during annealing. The volatile reaction products likely include P_4O_6, PH_3 and other phosphorus hydrides and oxides, some of which may decompose further as a result of additional reactions with H_2O.

The rate limiting step of the purification process is ascribed to diffusion through the bulk of either the reactive species or the reaction products. WDS can not be used to differentiate between these two mechanisms. It can, however, be used to show that P is removed from the deposit bulk by performing WDS as a function of electron beam energy. Figure 4.9 shows such data obtained using energies of 10, 15 and 20 keV, from a deposit that was $\sim$ 600 nm tall. The spectra show that at 20 keV, the electron beam penetrates the deposit, generating Si X-rays from the substrate but not generating any P K_α signal above the WDS detection limit. The absence of P shows that the H_2O annealing treatment can be used to purify bulk deposits. The underlying mechanism implies that the purification time will scale with deposit size and geometry. Diffusion most likely occurs throughout the amorphous, phosphorous-containing matrix, and along Pt grain boundaries (the deposits are known to be comprised of pure Pt nanocrystallites embedded in an impure, amorphous matrix [69]).

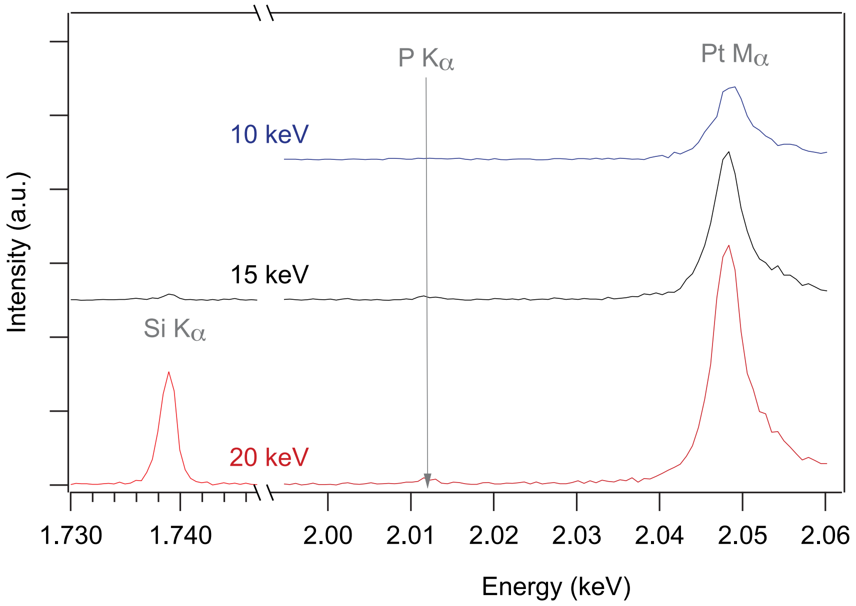

FIGURE 4.9: X-ray spectra obtained using electron beam energies of 10, 15 and 20 keV of a $Pt(PF_3)_4$-EBID deposit that had been purified using a 40 min, $400°C$ anneal in H_2O (deposit height ~600 nm).

The observed decay in F content with time at room temperature suggests that most of the fluorine is present in the form of residual fragments produced by partial decomposition of $Pt(PF_3)_4$. Fluorine also affects WDS analysis, and is responsible for variations in the measured O content of as-grown deposits such as that seen in figure 4.9b. Specifically, the greater the time between EBID growth and WDS analysis, the lower the measured F content and the greater the measured O and P content.

The WDS quantification method assumes a uniform distribution of the elemental constituents throughout the electron interaction volume. However, the detected F (as well as O and C impurities that build up during WDS) are most likely concentrated at the deposit surface, and the content of these impurities is therefore overestimated by WDS analysis. Despite these limitations, the H_2O annealing results show that the resulting Pt deposits are indistinguishable from reference Pt films, independent of the initial deposit composition. Specifically, variations in composition caused by deposition parameters such as the beam current density, the moisture content of the vacuum chamber used for EBID, and post-growth air exposure time do not affect the efficacy of the purification method. This is significant because, to date, the highest purity EBID-grown Pt deposits have been realised using $Pt(PF_3)_4$, which is water vapour sensitive and yields a deposit composition that varies with beam current density [67].

4.6 Conclusion

A method enabling localised, mask-free complex nanostructure deposition of pure platinum is demonstrated. The method employs a combination of room temperature, direct-write EBID using the inorganic precursor $Pt(PF_3)_4$, and low temperature ($\leq 400°\mathrm{C}$) post-growth annealing in H_2O. The annealing treatment removes phosphorous contaminants through a thermally-activated pathway involving fragmentation of H_2O adsorbates to produce O and H species that react with P to form volatile phosphorous hydrides and oxides.

4.7 Chapter contributions

Chris Elbadawi, Milos Toth and Charlene Lobo conceived the idea. Chris Elbadawi planned the experiments. Chris Elbadawi performed the EBID experiments, post growth annealing experiments and WDS analysis. Chris Elbadawi performed all programming. Chris Elbadawi wrote the chapter. Milos Toth and Charlene Lobo edited the chapter.

Chapter 5

Mechanisitic and stabilisation study of few-layer BP

5.1 Abstract

In order to take advantage of the unique properties of few-layer black phosphorus (FLBP), it must normally be protected from ambient environment by complex encapsulation and protection strategies. However, these strategies modify the surface chemistry of the material and make it unsuitable for many applications in gas sensing and catalysis. Here, we show that the degradation of pristine FLBP can be entirely prevented by introducing a single 150-200°C heat treatment. This simple method enables the stability of FLBP to be extended for up to 4 weeks per heat cycle in ambient environment. Electrical characterization of FLBP devices subjected to this heat treatment show no deterioration of electrical properties under extended electron beam irradiation in H_2O, in contrast to the immediate degradation of pristine FLBP held at room temperature. Surprisingly, FLBP can also be kept in pristine condition under electron irradiation in oxidizing environments (O_2 and NF_3).

5.2 Introduction

Few-layered black phosphorus (FLBP) is a two-dimensional (2D) material consisting of mono- and multi-layers of black phosphorus. This material comprises of puckered anisotropic layers consisting of sp3-hybridised bonds, and can be thinned down to a monolayer through mechanical and liquid exfoliation techniques [123, 176]. Optoelectronic properties that include high carrier mobility (up to $10^3 cm^2$/Vs for holes [5, 114]) and a tunable thickness-dependent direct band gap varying from 0.3 to 1.8eV [21] have made black phosphorus of all thicknesses a promising material for many applications including field effect and thin film transistors [18, 114], batteries [118], ultraprecise gas sensors [177–179], photonic [180], and biomedical devices [181, 182].

Unfortunately the deployment of few-layered black phosphorus (FLBP) in these applications is severely hampered by its high instability in ambient conditions, resulting in rapid degradation within a few days [118, 121, 183]. Several studies have examined the origins of this environmental degradation and have concluded that H_2O and O_2 exposure in combination with high energy electromagnetic (photon or electron) irradiation are required for the degradation reaction to occur [119, 184]. This reaction proceeds through the formation of a surface oxide layer (P_xO_y) [106, 119, 127], which is subsequently converted to phosphoric acid (H_xPO_y) species upon interaction with atmospheric water vapour or reactive oxygen species (ROS), thereby accelerating the degradation process [185]. Thus, in order to be employed in device applications, FLBP must be immediately encapsulated in materials that provide an effective barrier to the diffusion of water and ROS, such as ionic liquids, surface coordinating ligands, or amide solvents [122, 185–191]. The strategies that have so far resulted in long-term passivation (as indicated by preservation of electronic conductance up to 3 months in ambient) have been atomic layer deposition (ALD) of Al_2O_3 [115], encapsulation in hexagonal boron nitride (hBN) using dry transfer in inert environments [192], or protection with oxygen-sequestering ionic liquids [184]. However, these fabrication and protection strategies are both complicated and time-consuming, and because they modify the surface chemistry of FLBP, are not suitable for many applications in gas sensing and catalysis.

Following from the work performed on Phosphorus contaminants in Chapter 4, which indicate a decomposition and desorption pathway through the creation of phosphoric acid, attention was focused on the highly unstable FLBP. Here, the stability of FLBP is studied in a variety of well-controlled oxidizing (H_2O and O_2) and reducing (NF_3 and NH_3) environments, all in the dark but in the presence of energetic electron irradiation. Environmental scanning electron microscopy (ESEM) is used both to generate the reactive species and radicals that are responsible for FLBP degradation, and to conduct real-time imaging of the resulting reactions with black phosphorus. Few-layered black phosphorus is rapidly etched under an electron beam irradiation in a H_2O environment, but is surprisingly highly stable in both O_2 and NF_3. Under electron beam irradiation in NH_3, FLBP can be controllably etched with nanoscale resolution. it is shown that the degradation in H_2O can be entirely prevented by introducing a (150-200°C) heat treatment step, which enables the stability of pristine black phosphorus mono- and multi-layers to be extended for up to 4 weeks per heat cycle in an ambient environment. Electrical characterization of FLBP devices subjected to this temperature heat cycling process show no deterioration of electrical properties under extended electron beam irradiation in H2O, in contrast to the immediate degradation of pristine FLBP in an identical environment. This is the first demonstration of stable FLBP in the presence of H_2O and high energy irradiation without requiring a protective coating, and will open up new applications of FLBP in catalysis [193, 194], optoelectronic, and sensing devices [195, 196].

5.3 Methods and materials

Few-layered black phosphorus were micro mechanically exfoliated from commercial black phosphorus crystals (Smart Elements) onto a silicon substrate with a 100 nm thermal oxide layer. The average thickness of a FLBP were found to be approximately 50 nm as shown in figure 5.1. The exfoliated FLBP flakes were shielded from light and stored in a low vacuum desiccator to prevent reaction with air or moisture.

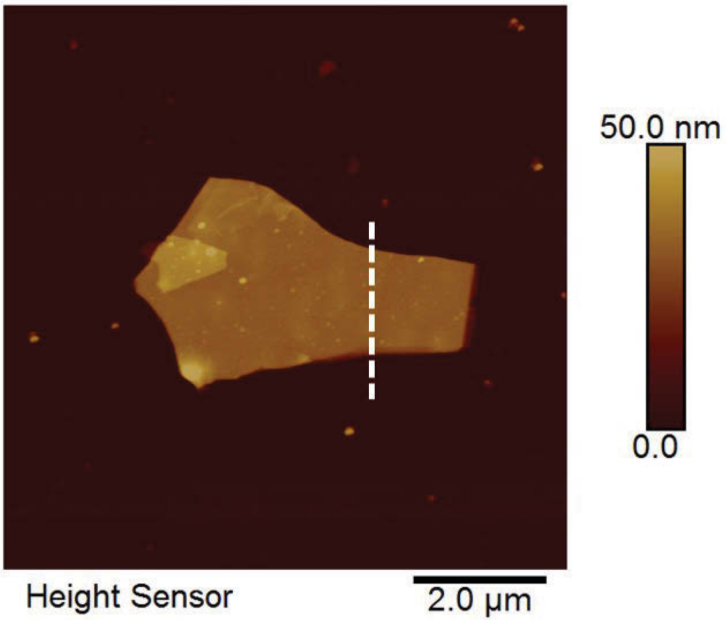

FIGURE 5.1: Typical Atomic Force Microscopy (AFM) image of a few-layered black phosphorus flake used for ESEM experiments.

In order to study the degradation process taken in low-pressure gaseous environments, FLBP flakes were imaged in real time using a magnetic-field-assisted helix gaseous secondary electron detector. The FLBP was loaded into the ESEM chamber, which was then pumped down to a base pressure of $3 \times 10_{-4}$ Pa (Fig. 5.2). *In-situ* electron beam irradiation in O_2, H_2O, and NH_3 environments was conducted in ESEM mode at 15 keV accelerating voltage and 5.6 nA beam current. Each FLBP sample was irradiated for 1 hour under a gas pressure of 8 Pa. For experiments using gases other than water, a cold trap was employed to minimise the effect of residual H_2O. The electron beam was rastered over a 24x18 μm rectangular region, using a scan rate of 1.68 ms per line and 952 lines per frame, equating to an electron beam flux of 2.3×10^{19} electrons cm^{-2}min^{-1}.

Temperature dependent experiments were performed using a custom hot stage built for the ESEM chamber. Each FLBP sample was irradiated at 15keV and 5.3nA at 5000x magnification (averaged current density of 4.42×10^{17} electrons cm^{-2}min^{-1}) in an atmosphere of 8 Pa pure gas (H_2O, O_2, NH_3).

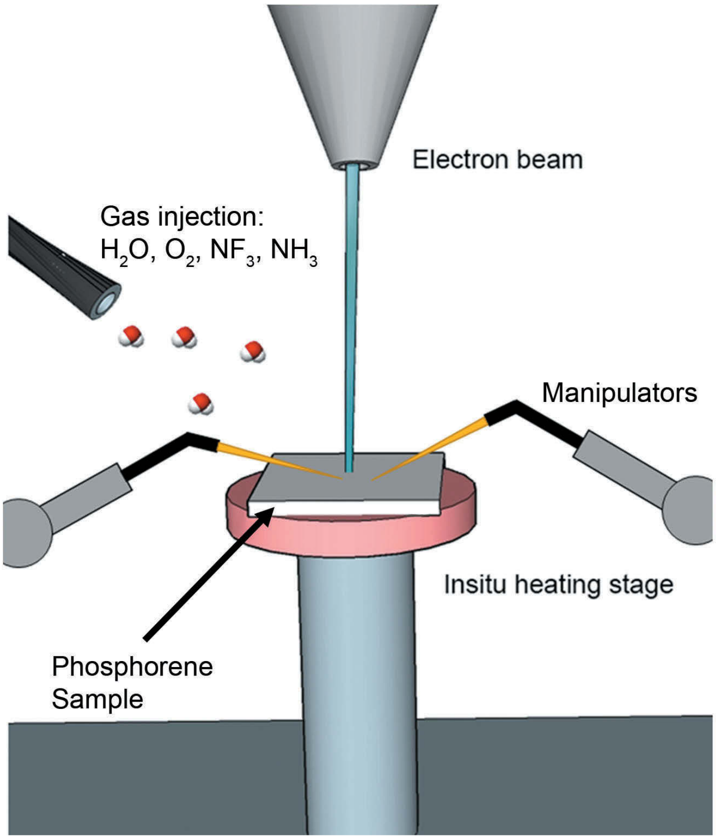

FIGURE 5.2: The setup used for ESEM experiments on FLBP, highlighting the in-situ heating, gas injection and electrical measurement capabilities.

Raman spectroscopy was performed using a Renishaw inVia Raman spectrometer system equipped with a Leica DMLB microscope and a 17 mW, 633 nm Renishaw helium neon laser source. Energy dispersive X-ray spectroscopy (EDS) analysis was performed using the Zeiss Evo LS15 with extended pressure, Bruker SDD EDS Quantax 400 system at 5 keV accelerating voltage.

Two-terminal electronic devices were fabricated on mechanically-exfoliated FLBP on 300 nm SiO_2/Si substrates. After the transfer, a photoresist layer was spin-coated at 4,000 rpm for 45 s followed by $100°C$ soft bake. The electrode patterns were UV-exposed using a mask aligner system (MA6, SUSS MicroTech) and subsequently developed. The metal electrodes Cr/Au (10/100 nm) were then deposited on the developed patterns using electron beam evaporation. Finally, the lift-off in acetone was carried out to reveal the required metallic contact pads for micro-probes and electrical measurement.

In-situ two-point electrical measurements were conducted using Kleindiek Nanotechnik nanomanipulators installed on the SEM stage (Fig 5.2). A Keithley 3612 B source measurement unit was used to measure the output current as a function of input drive voltage (-1 to +1 mV) in a two-point measurement between Cr/Au (10/100 nm) metal electrodes with a spacing of 5 μm.

5.3.1 In-situ VPSEM of few-layer BP degradation

To gain a greater understanding of the FLBP degradation mechanism, untreated FLBP flakes with an average thickness of 50 nm (Fig. 5.1) were subjected to electron beam irradiation in oxidizing (8 Pa H_2O or O_2) and reducing (8 Pa NH_3 or NF_3) environments in the dark. The experimental setup used to conduct *in-situ* ESEM experiments is illustrated in Figure 5.2. Irradiation in 8 Pa H_2O for 60 minutes resulted in the formation of P_xO_y bubbles (Fig 5.3a and 5.3b, followed by the reaction of these bubbles with water (Fig. 5.3c), leading to complete degradation of the FLBP after 18 minutes (Fig. 5.3d). Prior studies suggest that the bubbling is caused by dissociative chemisorption of oxygen onto the FLBP flakes [106, 118, 119]. When water diffuses onto the oxide bubbles, phosphoric acid (H_3PO_4) is produced in a highly exothermic reaction, resulting in a reaction-diffusion front [197] that rapidly leads to complete degradation of the FLBP. Compositional analysis of a partially degraded FLBP flake (Fig. 5.3e) by energy dispersive X-ray spectroscopy (EDS) shows a sharp decrease in phosphorus content (Fig. 5.3f) and increase in oxygen content (Fig. 5.3g) compared to pristine FLBP. Unfortunately phosphorus oxides were not detected due to the overlap with Raman peaks originating from the Si substrate (Fig. 5.4).

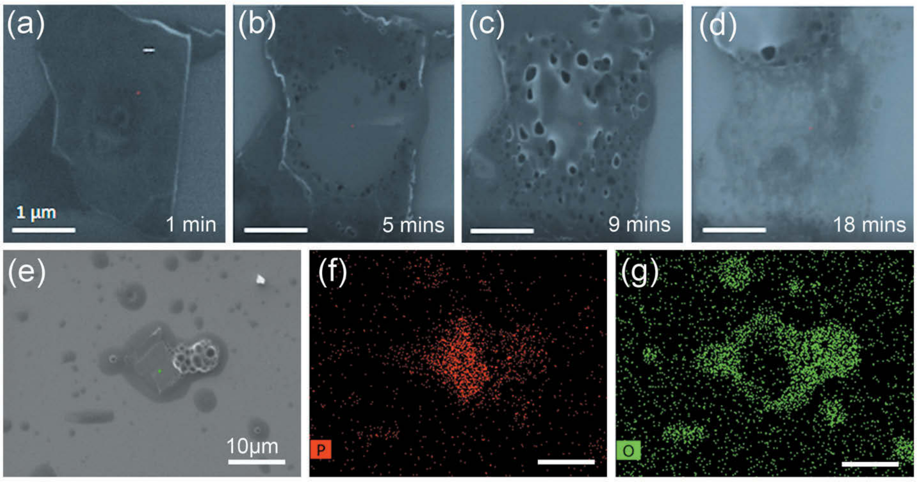

FIGURE 5.3: (a - d) A FLBP flake in a sequence of screen captures during a 1 hour irradiation in the presence of H_2O. An accelerating voltage of 15 kV and electron beam flux of 2.3×10^{19} electrons $cm^{-2}min^{-1}$ is used and the scale bar is 1 μm. (e) SEM image of a semi degraded FLBP flake with the compositions of P (f) and O (g) respectively illustrated highlighting the regions of degradation.

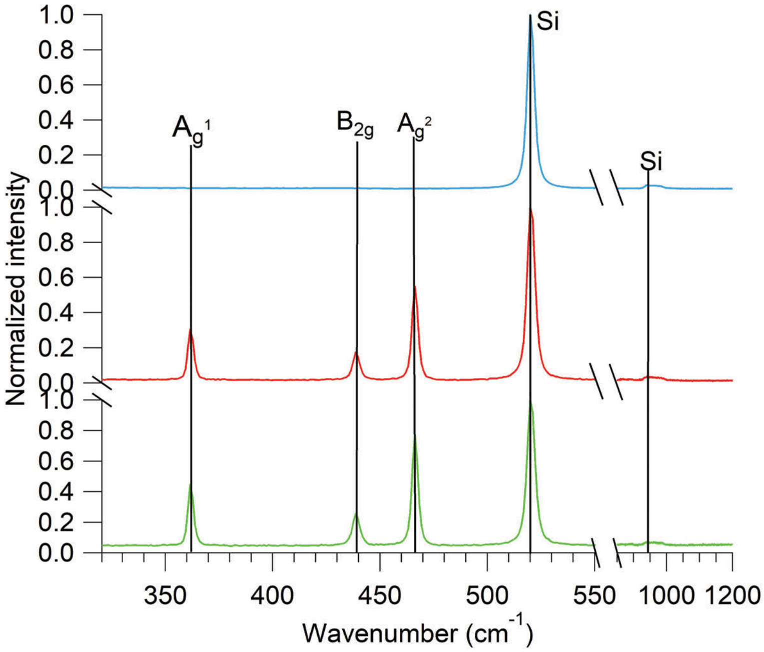

FIGURE 5.4: Typical Raman spectrum of three different FLBP flake after exposure to atmosphere. The silicon peaks are also shown, which overlap with phosphorus oxide peaks.

As discussed by Martel and co-workers [119], the number of FLBP layers can be characterized by the frequency shift of the A_g^1 Raman peak from its bulk position (466 cm^{-1}), and oxidation/degradation is characterised by a reduction in Raman intensity and concomitant decrease in the A_g^1/A_g^2 peak ratio (peak ratios less than 0.6 are indicative of basal plane oxidation). Following irradiation in 8 Pa H_2O for 60 minutes, the degraded FLBP flake (Fig. 5.5a, right) has a much lower Raman intensity than the pristine flake (Fig. 5.5e, top), along with a greatly reduced A_g^1/A_g^2 peak ratio (0.4 compared to 0.9 for the pristine flake). No degradation is observed in H_2O in the absence of electron beam irradiation which is consistent with recent observations that humidity on its own does not cause degradation [184].

Degradation induced bubbles do not appear on the surface of FLBP irradiated in 8 Pa O_2 (Fig 5.5b, right), although some surface roughening does occur at the edges of the rastered beam pattern, due to a possible diffusion of residual H_2O in the ESEM chamber towards the electron beam irradiated area. In the absence of residual H_2O, which was removed by flowing the O_2 through a cold trap, no degradation occurs. This observation is in agreement with a recent study, which found that in the absence of energetic irradiation, the oxidation reaction only occurs in the simultaneous presence of both H_2O and O_2 [198].

The lack of oxidation and degradation in an O_2 environment is confirmed by analysis of the Raman spectrum, which shows a much smaller reduction in both Raman intensity and A_g^1/A_g^2 peak ratio (from 0.9 to 0.7) than is observed under equivalent pressures of H_2O (where the A_g^1/A_g^2 peak ratio drops to 0.4). Rather than being a result of black phosphorus oxidation, which normally results in $A_g^1/A_g^2 < 0.6$, the slight reduction in peak ratio in an O_2 environment may be due to the reaction with residual H_2O at the edge of the electron-irradiated region.

A previous DFT study has predicted that unlike oxidized black phosphorus, fully

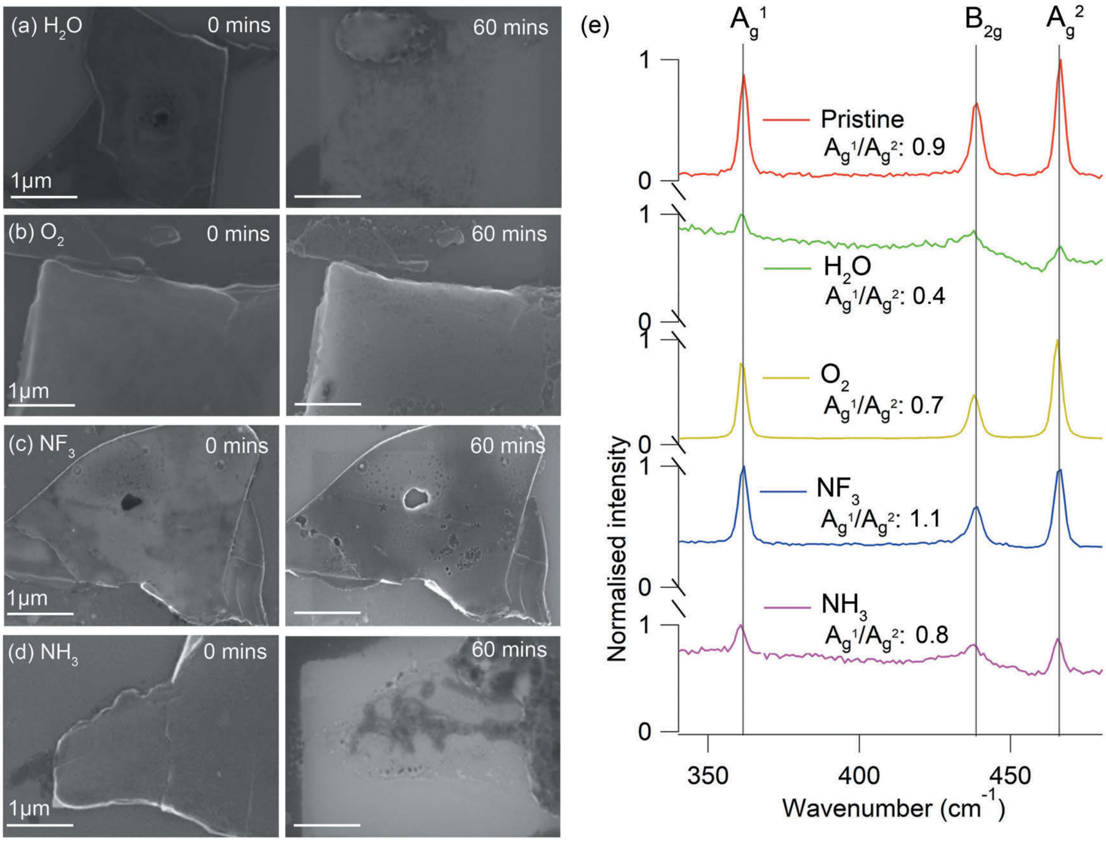

FIGURE 5.5: (a - d) SEM images of FLBP before (left) and after (right) 60 minute electron beam irradiation in O_2, NF_3, NH_3, H_2O environments at 8 Pa chamber pressure. Irradiation and imaging were conducted at an accelerating voltage of 15 kV and electron beam flux of 2.3×10^{19} electrons $cm^{-2}min^{-1}$. The scale bar is 1 μm. e) Normalised Raman spectra from pristine FLBP (top), and from each of the flakes shown in (a - d). Phosphorus oxides were not detected due to the overlap with Raman peaks originating from the Si substrate (Fig. 7.4).

fluorinated flakes should be dynamically stable, while hydrogenated black phosphorus should be unstable [199]. In order to test this prediction, pristine black phosphorus was irradiated in 8 Pa NF_3 and NH_3 under the identical conditions as irradiation in H_2O and O_2. It is found that the electron beam irradiation in NF_3 does not cause degradation of the FLBP (Fig. 5.5c). As is the case for electron irradiation in O_2, there is only some roughening at the edges of the electron beam irradiated area due to dissociation of residual H_2O molecules diffusing in from outside the irradiated area. The Raman signal has a slightly greater A_g^1/A_g^2 peak ratio than pristine FLBP (1.1 compared to 0.9), which may be suggestive of electron beam induced surface fluorination [43]. Evidence of residual H_2O is also shown in figure 5.6, where a FLBP flake is irradiated for over 3 hours in high vacuum conditions and slight roughening and degradation is seen over a much larger time-frame compared with H_2O irradiation.

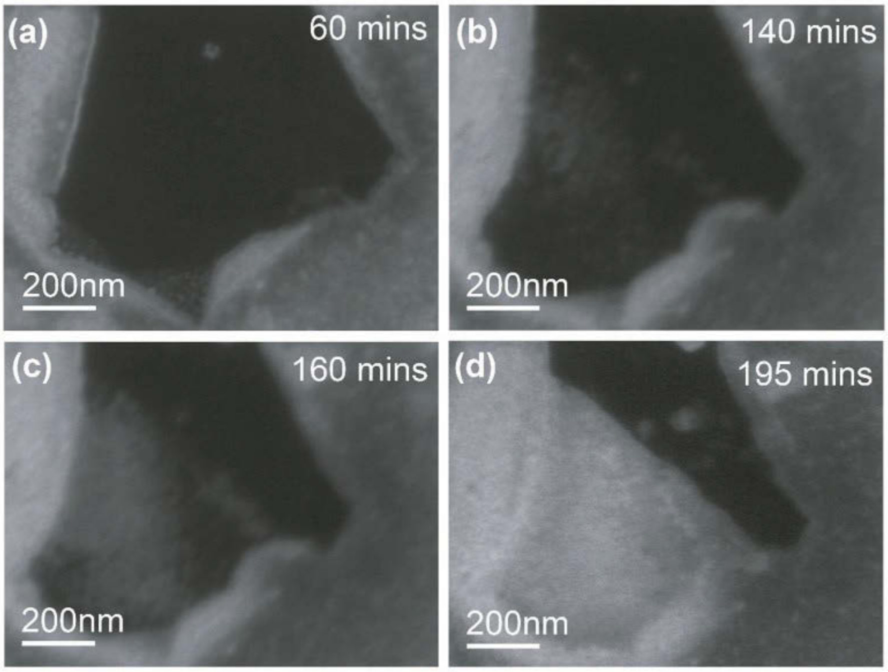

FIGURE 5.6: (a - d) SEM images of FLBP after a 195 minute electron beam irradiation in high vacuum conditions. Irradiation and imaging were conducted at an accelerating voltage of 15 kV and electron beam flux of 2.3×10^{19} electrons $cm^{-2}min^{-1}$.

Electron beam irradiation in an NH_3 environment results in complete etching and volatilization of the FLBP in a highly localized manner, see figure 5.7. Unlike the H_2O process, a reaction-diffusion front due to the production of phosphoric acid was not observed. The electron-induced reaction in NH_3 results in the production of hydrogen radicals, which likely react with FLBP to form phosphine (PH_3) gas. This NH_3 induced etching mechanism is expected to be much more localised than the H_2O mediated process, potentially enabling electron beam patterning of FLBP with nanoscale resolution, as was recently demonstrated for hBN [94] in 7. Roughening at the flake edge was observed, however this is likely due to backscattered electrons as is discussed in much more details in section 7.4. Strategies to eliminate or bypass the effect of the BSE yield are also given.

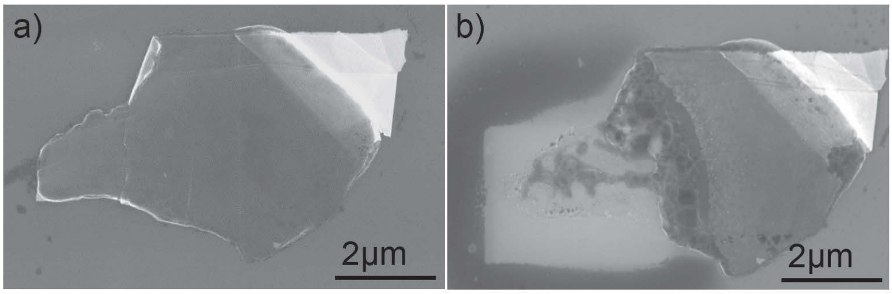

FIGURE 5.7: (a - b) SEM images of FLBP before (left) and after (right) 60 minute electron beam irradiation in a NH_3 environments at 8 Pa chamber pressure. Irradiation and imaging were conducted at an accelerating voltage of 15 kV and electron beam flux of 2.3×10^{19} electrons $cm^{-2}min^{-1}$.

5.3.2 Few-layer BP stabilization by high temperature cycling

Having shown that FLBP degradation only occurs under a simultaneous exposure to H_2O and electron irradiation, the utility of temperature cycling is explored to prevent or halt FLBP degradation. A series of electron irradiations in 8 Pa H_2O was performed at temperatures ranging from RT to 150°C (Fig. 5.8a-d). Due to the increasing reaction rate with increasing temperature, the onset time for degradation of the FLBP decreases from 12 minutes at RT (Fig. 5.8a) to just over 2 minutes at 100°C (Fig. 5.8e). However, at 150°C and above, (Fig. 5.8c) FLBP degradation completely stops, presumably because the very low residence time of surface adsorbed water at these temperatures

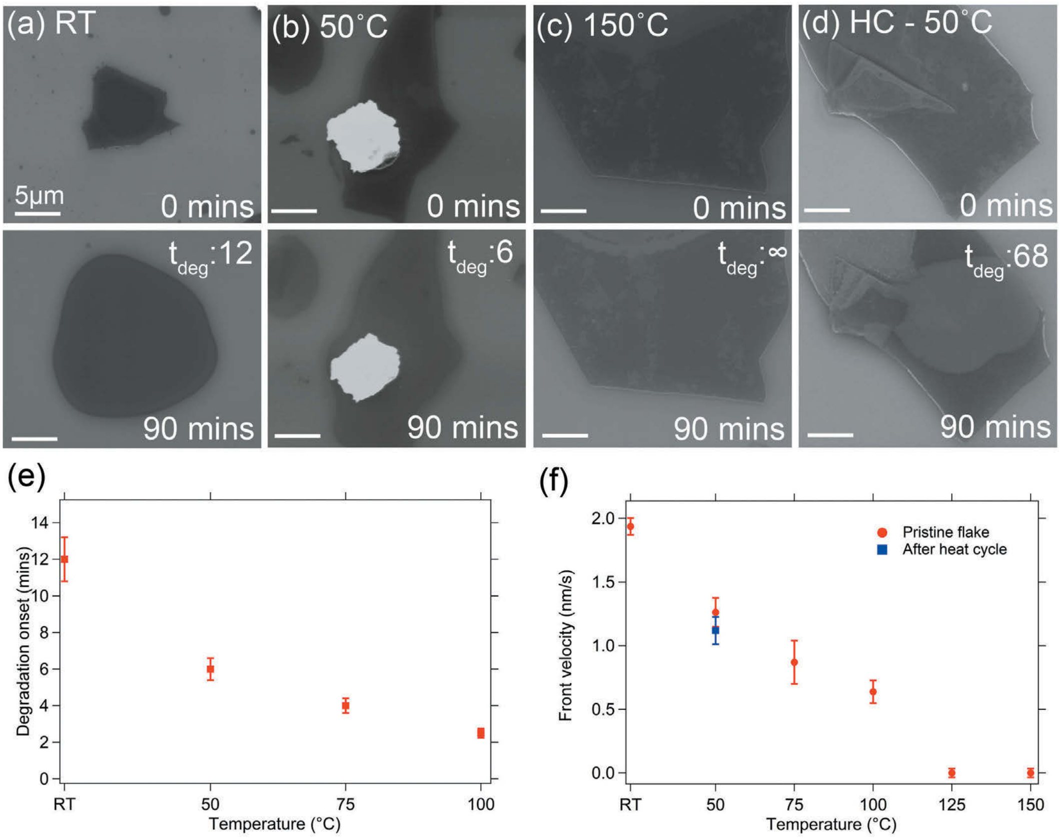

FIGURE 5.8: (a - d) Temperature dependence of the electron-beam induced FLBP reaction with H_2O. SEM images were taken before and after 60 min. electron irradiation (15 kV, 4.42×10^{17} electrons cm^{-2}min^{-1}) in 8 Pa H_2O at (a) RT (b) 50°C, (c) 150°C, and (d) 50°C following a single heat treatment cycle (HC) in which the temperature was held at 150°C for 90 minutes. The onset time at which degradation began is indicated as t_{deg}. e) Onset time for degradation (t_{deg}, min.) at each temperature. f) Front velocity of the reaction product formed by electron beam irradiation in H_2O at RT-150°C, measured on pristine FLBP flake (red), and on a heat-treated FLBP flake (150°C, 90 min.)

($< 10^{-7}$ s) prohibits the electron-induced generation of ROS. When the temperature was reduced below 50°C after being held at 150°C for 90 minutes, the FLBP began to degrade again (Fig. 5.8d). However, the degradation onset time (68 minutes) is greatly increased compared to that of a pristine FLBP flake irradiated at 50°C without heat cycling (6 mins) (Fig 5.8b). This is most likely due to the desorption of surface adsorbed and intercalated water when the temperature is raised above 100°C.

The velocity of the liquid product (H_xPO_y species) created by the electron beam induced reaction between H_2O and FLBP can be tracked by analysis of videos taken during *in-situ* electron irradiation. The front velocity at each temperature was calculated from analysis of video screen captures taken during the reaction at times 175, 240 and 300 s after the onset of degradation [197] (Fig. 5.9).

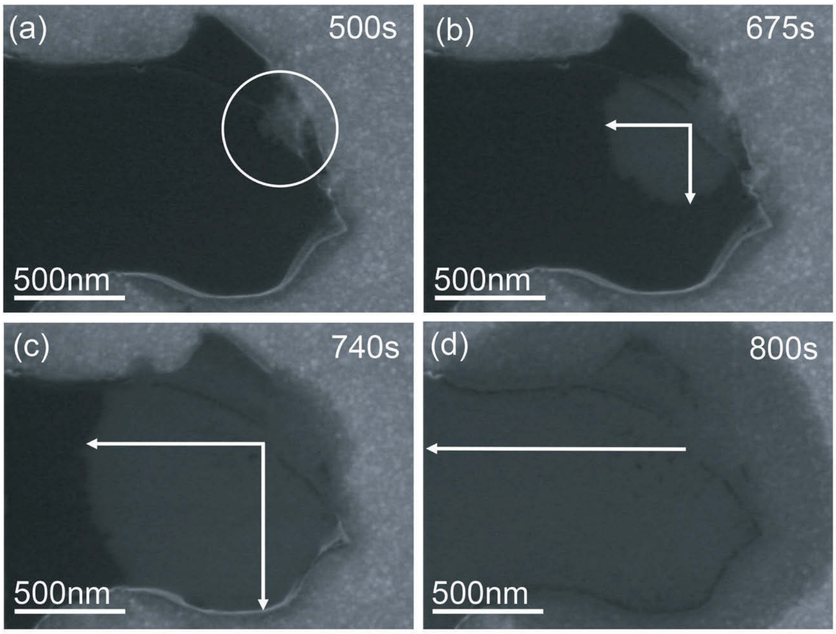

FIGURE 5.9: A series of SEM screen captures were taken over time, showing the starting location of formation of phosphoric acid highlighted by the white circle in a). (b - d) is showing the evolution and diffusion (indicated by the white arrows) of phosphoric acid over time. E-beam irradiation was performed at 15 keV.

ImageJ processing software was used to measure the distance of the reaction-diffusion front from the origin at five locations in each screen capture, enabling estimation of an average front velocity at each temperature. The front velocity decreases with increasing temperature between RT and 100°C, due to the reduced residence time of H_2O, which leads to a reduced rate of production of phosphoric acid species (Fig. 5.8f). As discussed earlier, above 100°C, the residence time of H_2O is too short for the electron beam induced reaction to take place.

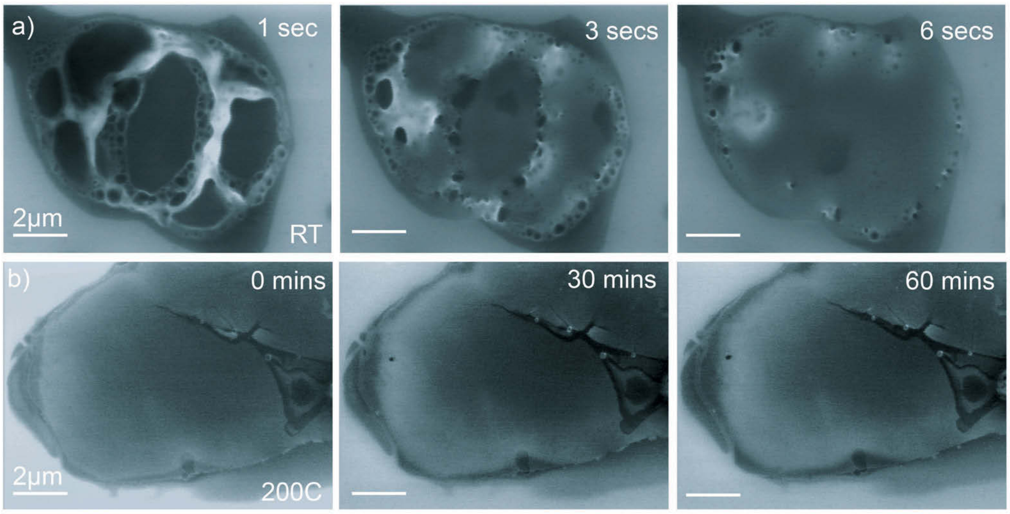

FIGURE 5.10: (a - b) Electron beam processing of untreated FLBP flakes that had been protected from light in ambient environment for 2 weeks. A time series of SEM images was captured in 8 Pa H_2O at (a) RT and (b) 200°C. Both irradiations were performed at 15 keV at a flux of 2.3×10^{19} electrons $cm^{-2}min^{-1}$.

Next, FLBP flakes were aged in dark ambient condition for two weeks to allow for a build up of H_2O. The FLBP was subsequently irradiated in a H_2O environment (Fig. 5.10). In total it took less than 10 seconds for complete degradation of the FLBP to occur (Fig. 5.10a). At the beginning of electron beam irradiation (1-3 s), the intercalated water bubbles to the surface and reacts violently with the FLBP. After 6 s, the electron beam induced reaction between the FLBP and H_2O is almost complete, and the liquid reaction product begins to diffuse. A similar flake aged under the same conditions was then held at 200°C for 1 hour to desorb surface adsorbed and intercalated H_2O, followed by further irradiation in a H_2O environment (Fig 5.10b). After 60 minutes, no sign of degradation is seen. Subsequent exposure to ambient conditions showed that the aged, irradiated and heat treated few-layered black phosphorus began to degrade after approximately 4 weeks, while a similar aged FLBP flake irradiated in O_2 began to degrade after 14 days (Fig. 5.11).

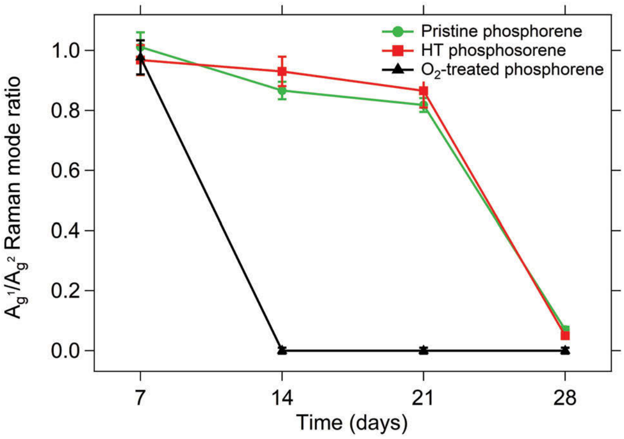

FIGURE 5.11: Degradation of FLBP Raman modes monitored over time in ambient conditions. Figure shows Raman modes of pristine, heat treated and O_2 irradiated FLBP flakes over 7, 14, 21 and 28 days.

Further stability studies were also undertaken on the O_2 and NF_3 irradiated FLBP flakes to test the viability of passivating the flakes with fluorine or oxygen surface terminations. EDS mapping of these flakes directly after irradiation are shown in figure 5.12. The EDS results indicate oxidation being present on the O_2 and NF_3 aged flakes compared with the heat treated aged flake which shows very little oxidation content in figure 5.12a.

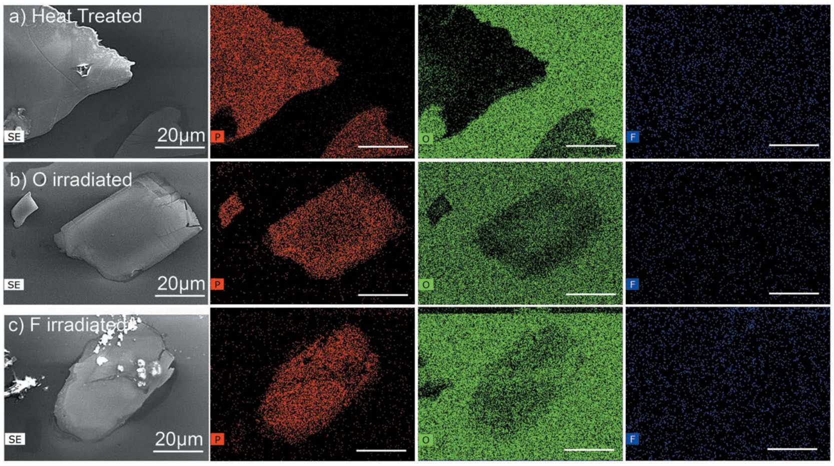

FIGURE 5.12: EDS study performed on heat treated and e-beam irradiated few-layer black phosphorus flakes. (a) shows heat treated flakes, (b) Oxygen e-beam irradiated, (c) e-beam irradiated in a fluorine environment and their corresponding EDS P, O and F content through X-ray mapping. All EDS mapping was performed at 5 kV in high vacuum.

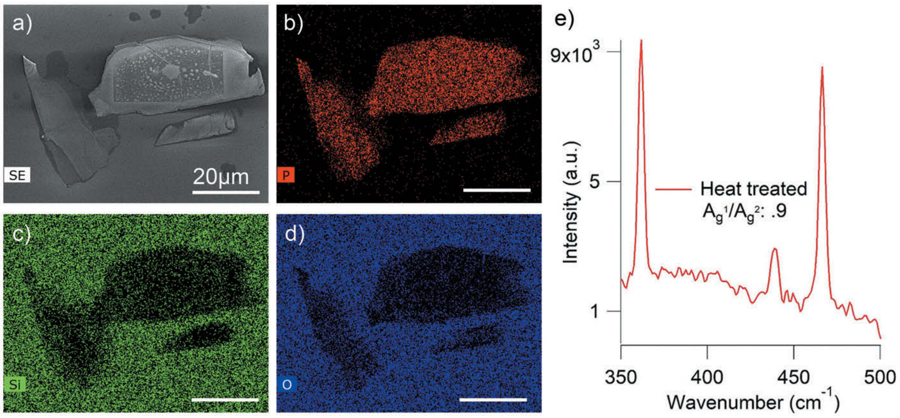

FIGURE 5.13: The FLBP flake shown in (a) was analysed by EDS for (b) P, (c) Si, and (d) O at 5 keV in HV. A Raman spectrum taken after the heat treatment, electron beam irradiation and EDS is shown in (e), confirming that the FLBP remains in pristine condition.

EDX mapping (Fig. 5.13a-d) of an aged FLBP flake treated with a single heat cycle at 200°C followed by electron beam irradiation in 8 Pa H_2O under identical conditions as those used for pristine FBLP (Fig. 5.13(a-d)) show that both pristine and aged, heat-treated flakes have the same average oxygen content. This is supported by the Raman data shown in Fig. 5.13e, which has a A_g^1/A_g^2 peak ratio of 0.9, identical to that of pristine FLBP (Fig. 5.5e). Thus, heat cycles at temperatures of 150-200°C can be used to restore aged FLBP, which contains a substantial amount of surface-adsorbed and intercalated water, to pristine condition.

5.3.3 Electrical characterisation

Finally, *in-situ* electrical measurements were performed on a FLBP flake in vacuum and H_2O under electron beam irradiation at both 150°C and RT using the nanomanipulator setup shown in Fig. 5.2.

An SEM image of this flake with electrical contacts is shown in Fig. 5.14a. The conductance was measured at 150°C in HV (3x10^{-4} Pa) under constant electron beam irradiation (15 keV, 4.42×10^{17} electrons $cm^{-2}min^{-1}$). At 150°C, the conductance is constant at 6x10^{-4} S under constant electron beam irradiation (Fig 5.2b, red line).

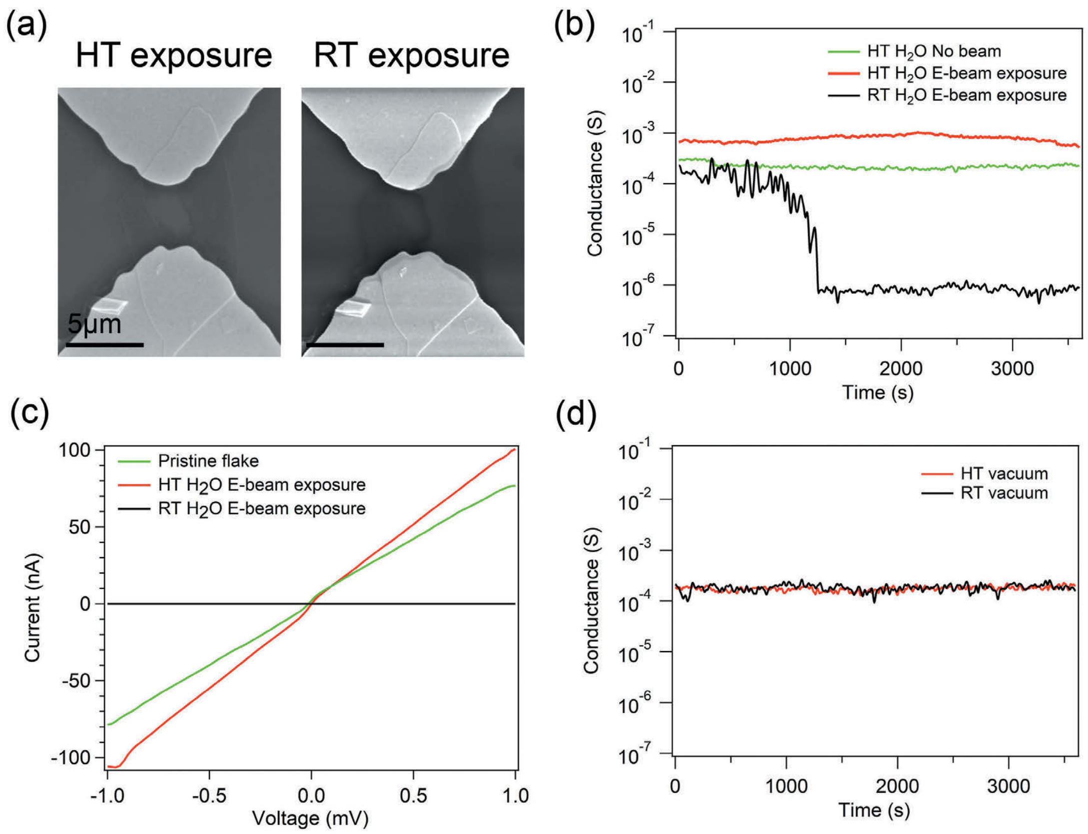

FIGURE 5.14: a) SEM screen captures taken during electron beam irradiation of FLBP flakes in a H_2O environment at 150°C and at RT. Electron irradiation was performed at 15 kV at a flux of 4.42×10^{17} electrons $cm^{-2}min^{-1}$. b) Conductance of the same FLBP flake as a function of irradiation time at 150°C and RT. (c) IV characteristics before and after the heat treatment. (d) Conductance of the same flake measured at 150°C and RT in HV (3×10^{-4} Pa).

However, under continuous electron irradiation in H_2O at RT, the conductance declines continuously, reaching a baseline of 10^{-6} S. After approximately 20 minutes of irradiation at RT, the device failed. IV curves were also acquired before and after electron beam irradiation at 150°C (Fig. 5.2c). The IV characteristics and conductance both improved after the heat cycle, showing that the heat treatment effectively restores the FLBP to pristine condition. A conductance measurement was also performed at 150°C and at RT and a similar value of $2x10^{-4}$ S is shown in fig. 5.2d. This illustrates the heat treatment performed has little effect on the conductance of FLBP and is able to restore the electronic characteristics of a partially degraded flake.

5.4 Conclusion

In conclusion, it is shown that FLBP can be kept in pristine state and degradation can be entirely prevented by heat treatment (150-200°C), enabling the stability of pristine mono- and multi-layer black phosphorus to be extended for up to 4 weeks per heat cycle in ambient environment. Electrical characterization of FLBP devices subjected to this moderate heat cycling process show no deterioration of electrical properties under extended electron beam irradiation in H_2O, in contrast to the immediate degradation of pristine FLBP. This is the first demonstration of stable FLBP in the presence of H_2O and high energy irradiation without requiring a protective coating, and will open up new applications of FLBP in catalysis, optoelectronic, and sensing devices.

5.5 Chapter contributions

Chris Elbadawi, Milos Toth, Igor Aharonovich and Charlene Lobo conceived the idea. Chris Elbadawi performed the electron beam induced irradiations in various environmental conditions, Raman analysis, EDS analysis and electrical characterisation experiments. Zaiquan Xu and Charlene Lobo assisted with electrical characterisation and James Bishop helped with electron irradiation. Roger Tormo Qerault assisted with electron beam irradiations, raman analysis and EDS analysis and helped design figure 2. Sumeet Walia provided AFM data and exfoliated the BP flakes. Chris Elbadawi designed all other figures. Chris Elbadawi and Charlene wrote and edited the chapter.

Chapter 6

Deterministic engineering and photo-physical characterization of single photon emitters in hBN

6.1 Abstract

Hexagonal boron nitride (hBN) is an emerging two dimensional material for quantum photonics owing to its large bandgap and hyperbolic properties. Here two approaches are reported for engineering quantum emitters in hBN multilayers using either electron beam irradiation or annealing, and characterize their photophysical properties. The defects exhibit a broad range of multicolor room temperature single photon emissions across the visible and the near infrared spectral ranges, narrow line widths of sub 10 nm at room temperature, and a short excited state lifetime, and high brightness. Remarkably, the emitters are extremely robust and withstand aggressive annealing treatments in oxidizing and reducing environments. These results constitute the first step towards deterministic engineering of single emitters in 2D materials and hold great promise for the use of defects in boron nitride as sources for quantum information processing and nanophotonics.

6.2 Introduction

Hexagonal boron nitride (hBN) is a van Der Waals material that has recently emerged as a fascinating platform for room temperature quantum photonics due to the discovery of stable room temperature quantum emitters [141], realization of sub diffraction focusing and guiding [138, 151], super-resolution imaging [11], and tunable phonon polariton propagation [140, 200] While the optical properties of bulk hBN have been studied thoroughly [17, 135, 201], detailed photo-physical properties of its two dimensional counterpart are scarce. In particular, the luminescent properties of hBN under sub-band-gap excitation remain largely unexplored.

In this work, it is shown that single emitters in hBN can be deterministically engineered using electron irradiation and can withstand various aggressive annealing treatments in reactive gaseous environments, which do not change their spectral properties. The photo-physical properties of the ultra bright room temperature single photon emitters found in hBN was then characterised, showing the photoluminescence spectra, polarization properties and autocorrelation relationship. These results pave the way to robust, room temperature quantum photonic devices that employ defect centers in hBN as key building blocks.

6.3 Methods and materials

6.3.1 Liquid exfoliated hBN flakes and annealing treatments under different gas environments

Grid-marked native oxide Si (100) substrates were cleaned by ultrasonication in acetone and ethanol combined with light mechanical abrasion. Samples were prepared by drop-casting 100 μL of ethanol/water solution containing 200 nm pristine h-BN flakes (Graphene Supermarket) onto marked substrates and allowed to dry.

Argon and O_2 annealing was carried out in a tube furnace (Lindberg Blue). The tube furnace was evacuated to low vacuum (10^{-3} keV) by means of a scroll pump then purged for 30 minutes under 10 sccm of Ar or O_2 flow with pressure regulated at 1 keV. The substrate was then heated under 10 sccm of argon flow or $500°C$ under 10 sccm of O_2 flow and held at a fixed temperature for 30 minutes, then allowed to cool to room temperature under continuous gas flow.

H_2 and NH_3 annealing was carried out in dedicated vacuum chamber. The chamber was evacuated to high vacuum (10^{-8} keV) by means of a turbo molecular pump then purged for 30 minutes under 10 sccm of H_2 and NH_3 flow respectively with pressure regulated at 40 keV. The substrate was then heated to $500°C$ under 10 sccm H_2 or NH_3 flow and held at this temperature for 30 minutes, then allowed to cool to room temperature under continuous gas flow.

6.3.2 Mechanically exfoliated large flake hBN and ion implantation procedures

Sample fabrication: hBN layers were exfoliated from a bulk hBN material using standard scotch tape techniques. Figure 6.1a shows an optical image of the exfoliated material. Flakes with diameters of up to tens of microns were obtained. A reference sample and six substrates with exfoliated flakes were prepared for processing by ion implantation and electron irradiation. Ion implantation was explored using boron (B), boron-nitrogen (BN) complexes, silicon and oxygen ions with the corresponding implantation details provided in figure 6.1b. B and BN were selected to test whether the formation probability of intrinsic defects would increase, generating mostly vacancies and interstitials, while silicon and oxygen atoms were chosen to determine whether the emitters are related to common impurities. Indeed, oxygen is known to be trapped within hBN lattice during growth and exfoliation [202].

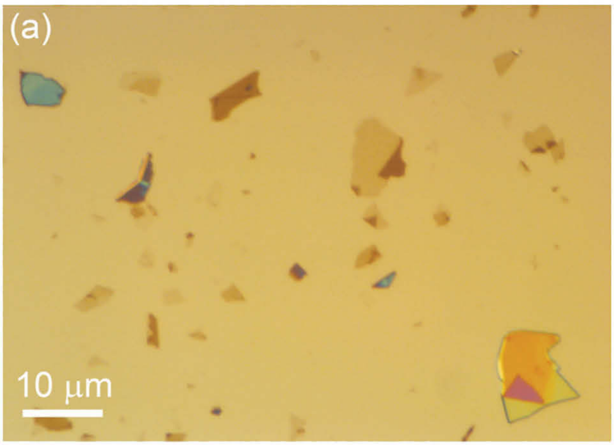

(b)

Sample	Irradiation	Annealing
B^- irradiated	energy: 50 keV, fluence: 10^{10} ion/cm^2, temp: RT	850°C 30 min 1 Torr Ar
BN^- irradiated	energy: 50 keV, fluence: 10^{10} ion/cm^2, temp: RT	
O^- irradiated	energy: 70 keV, fluence: 10^{10} ion/cm^2, temp: RT	
Si^- irradiated	energy: 50 keV, fluence: 10^{10} ion/cm^2, temp: RT	
Reference	—	
e-beam	energy: 15keV, e-fluence: 5 x 10^{18} (e/cm2) temp: RT	—

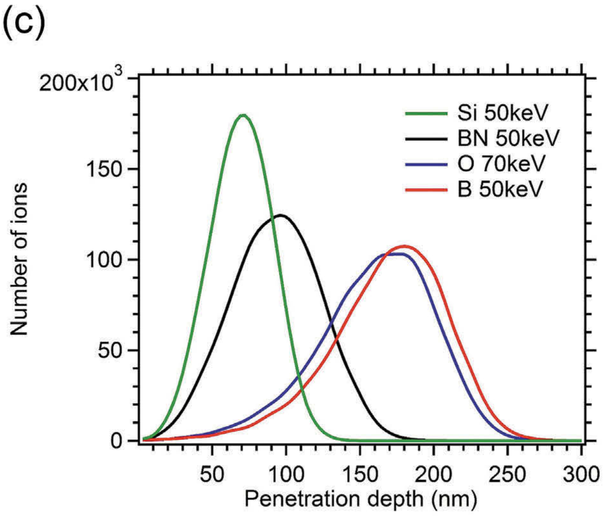

FIGURE 6.1: (a) Optical image of exfoliated hBN flakes. (b) Table of the investigated samples comprised of a reference sample, four samples that were implanted by ions, and one by electron beam irradiation. (c) shows Monte Carlo modelling of ion projections as a function of penetration depth.

Figure 6.1c utilizes Monte Carlo modelling using SRIM (stopping range of ions in matter) software of the various implanted species into the hBN lattice. The end of range for the ions is below 200 nm, which is the upper range of the studied hBN flakes.

6.3.3 Electron-beam irradiation

The substrates prepared for electron beam irradiation underwent photolithography procedures and subsequent metal deposition to create a hard mask grid. The substrates were then prepared as described above for liquid exfoliated and mechanically exfoliated hBN flakes. The grid allowed for easy identification of areas to characterize optically before and after electron beam irradiation.

Electron-beam irradiation experiments were performed in a variable pressure FEI field emission gun scanning electron microscope. A low vacuum environment of H_2O at a pressure of 8 Pa was used for all experiments. The hBN flakes were then located using a magnetic field assisted gas ionization cascade detector, and electron beam irradiation was performed using a focused Gaussian electron beam which was scanned in a raster fashion as a function of time up to one hour over an area of 600 μm^2. An accelerating voltage of 15 kV and beam current of 1.4 nA were used for all electron beam irradiation experiments.

An accelerating voltage of 15 kV was used and the electron beam fluence delivered to the exposed area was $5 \times 10^{18} e^-/cm^2$ (this is much lower than that needed to cause electron beam induced etching of hBN [94], see Chapter 7). The irradiation process is stopped by electron beam blanking.

6.3.4 Optical characterization

A continuous wave (CW) 532 nm laser (Gem 532^{TM}, Laser Quantum Ltd.) was used for excitation and scanning. The laser was directed through a Glan-Taylor polarizer

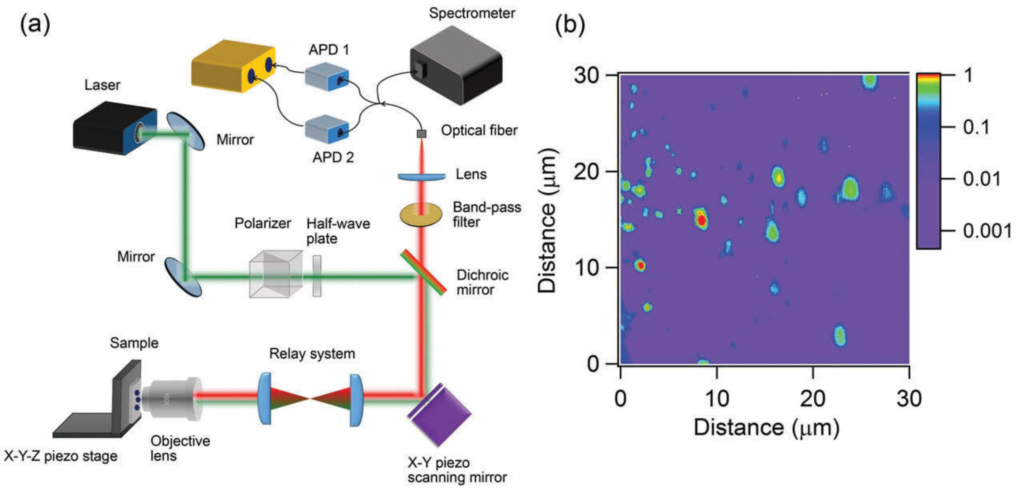

FIGURE 6.2: (a) Hanbury Brown and Twiss confocal setup used in this study. (b) Typical fluorescence confocal map taken from a hBN multilayer sample that was annealed in argon at $850°C$. Approximately half of the bright spots on the map are single photon emitters, with some very bright emitters exhibiting large lateral intensity profiles. The excitation source was a 532nm, 300mW CW laser. The confocal map is plotted with a log-scale color bar to better visualize dim spots.

(Thorlabs Inc.) and a half waveplate, and focused onto the sample using a high numerical aperture (NA = 0.9, Nikon) objective lens. Scanning was performed using an X-Y piezo scanning mirror (FSM-300). The collected light was filtered using a 532 nm dichroic mirror (532 nm laser BrightLine$^{\text{TM}}$, Semrock) and an additional long pass filter (Semrock). The signal was then coupled into a graded index fiber, where the fiber aperture serves as a confocal pinhole. A fiber splitter was used to direct the light to a spectrometer (Acton SpectraPro$^{\text{TM}}$, Princeton Instrument Inc.) or to two avalanche photodiodes (Excelitas Technologies$^{\text{TM}}$) used for single photon counting. A confocal setup is shown in figure 6.2.

Single photon sources are detected using correlation measurements in this work. The measurements were performed using a time-correlated single photon counting module (PicoHarp300$^{\text{TM}}$, PicoQuant$^{\text{TM}}$). The presented $g^{(2)}(\tau)$ curves were not corrected for background luminescence. The collected $g^{(2)}(\tau)$ curves were fit using a 3 level system equation:

$$g^{(2)}(\tau) = 1 - (1 + a)e^{(-\lambda_1 \tau)} + ae^{(-\lambda_2 \tau)} \tag{6.1}$$

where λ_1 and λ_2 are decay rates for radiative and the metastable states, respectively.

As the $g^{(2)}(\tau)$ statistically shows the probability of detecting the difference in arrival times for two photons, it is expected a $g^{(2)}(0) = 0$ for a single photon source. However, due to background luminescence and timing jitter in the system, obtaining a $g^{(2)}(0)$ of 0 or close to 0 is obscured. Therefore, a $g^{(2)}(0) < 0.5$ has been widely accepted to indicate a single photon source [144, 203].

Excitation polarization of the single photon emitters was controlled using a half wave plate, while the emission polarization was measured using a linear polarizer at maximum excitation polarization. The polarization behaviour is fit by:

$$I = I_0 cos^2 \theta_i \tag{6.2}$$

where I_0 is the initial intensity and θ_i is the angle between the initial polarization direction of light and the transmission axis of the polarizer.

6.4 Results and discussion

6.4.1 Emitter fabrication

Two different processes for engineering of the emitters were developed, based on annealing and electron beam irradiation, illustrated schematically in figure 6.3a. Either method can be used to create the studied defects in hBN. The annealing method was optimized by varying the annealing temperature of as-grown flakes in an inert environment. Each annealing treatment was performed for 30 minutes under 1 keV of argon. Figure 6.3b shows that the number of stable defect centers found by confocal

PL increases with annealing temperature, indicating that defect diffusion and lattice relaxation occur in the flakes. This behavior is similar to the well-studied nitrogen vacancy center in diamond [204, 205].

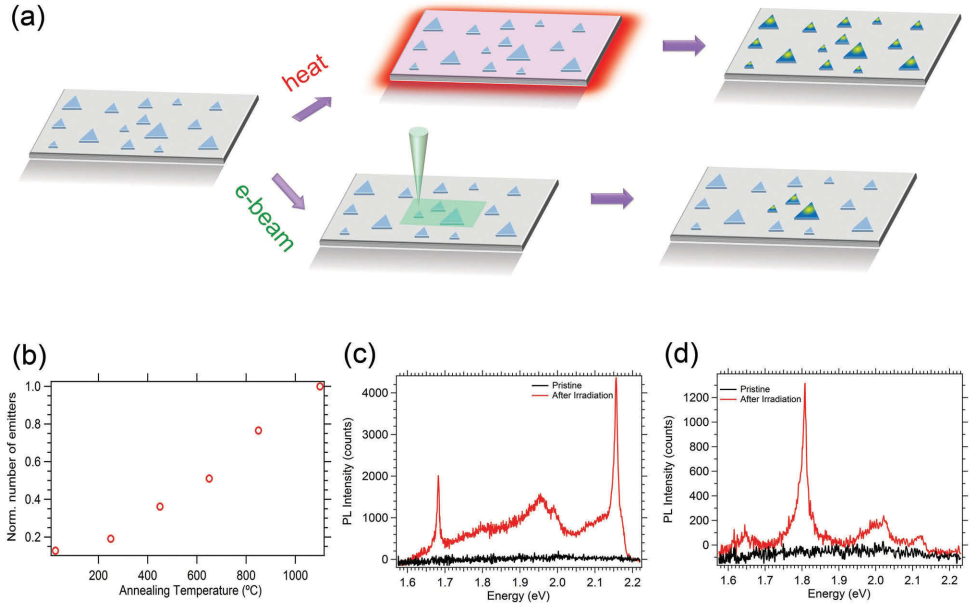

FIGURE 6.3: Generation of emitters in hBN. (a) Schematic illustration of two independent processes that yield emitters – annealing and electron beam irradiation. As-grown, dropcast hBN flakes are either annealed in an argon environment, or irradiated by an electron beam in a low vacuum H_2O (8 Pa) environment. (b) Normalized number of stable, bright single emitters as a function of annealing temperature found in hBN multilayers. Each data point was taken from a unique sample that was annealed at a singe temperature. (c, d) Examples of PL spectra from emitters fabricated by an electron beam. Each pair shows data recorded from a fixed sample region before (black curve) and after (red curve) electron irradiation.

The second process involves electron beam irradiation performed using a scanning electron microscope. The as-grown flakes were first deposited on a silicon substrate and pre-characterised by confocal PL mapping (see figure 6.2) and spectroscopy. Then, particular sample regions were irradiated by a 15 keV, 1.4 nA electron beam for one hour in a low vacuum, H_2O vapor environment [156] (the H_2O prevents electron beam deposition of carbon [206] that is luminescent and modifies PL spectra). A detailed description of the irradiation experiments is provided in the experimental methods section, 6.3. The pre-characterised sample regions were then re-measured using the confocal PL microscope. Figure 6.3(c,d) shows photoluminescence spectra recorded before (black curve) and after electron irradiation (red curve) from two sample regions. Luminescent defects were created by the electron beam in each case. Importantly, no annealing was performed before or after the electron beam irradiation treatments. These results therefore demonstrate two distinct robust methodologies for engineering of the emitters in hBN.

The influence of electron beam irradiation on pristine hBN flakes in a H_2O environment was studied further and compared with e-beam irradiation in high vacuum under the same irradiation parameters highlighted in the experimental section. Five separate exposures of 60×60 μm were conducted in each environment. Confocal mapping was compared before and after the e-beam irradiation on pristine hBN flakes. A greater percentage of emitter formation is found after a 1 hour scan in H_2O then high vacuum. In a typical confocal scan upward of 15 distinct emitters would be found after a 1 hour exposure in H_2O over an area of 60×60 μm. This is in contrast to 1 or 0 emitters being found after a 1 hour irradiation in high vacuum. A typical collection of PL spectrum from a 60×60 μm area is shown in figure 6.4a, highlighting the number of emitters found in a single confocal scan after H_2O (figure 6.4a) irradiation and compared to the typical emitter formation in a high vacuum environment (figure 6.4b).

An example SEM image and a confocal scan before and after a 1 hour e-beam irradiation in H_2O are shown in figure 6.5a-d. The irradiated region is highlighted with an orange box on the corresponding figures 6.5b,d. A reduction in particles can be seen inside this region when comparing SEM images in figures 6.5b,d, indicating a reduction in contaminants and possible etching of hBN. PL spectra are also compared of a single photon emitter found after the 1 hour irradiation and is indicated by the yellow box in figure 6.5. The comparision PL spectra is highlighted in figure 6.5e showing the spectra at that location before and after e-beam irradiation in H_2O. An order of magnitude difference in PL intensity is also shown in figure 6.5f when comparing the same spot before and after e-beam irradiation.

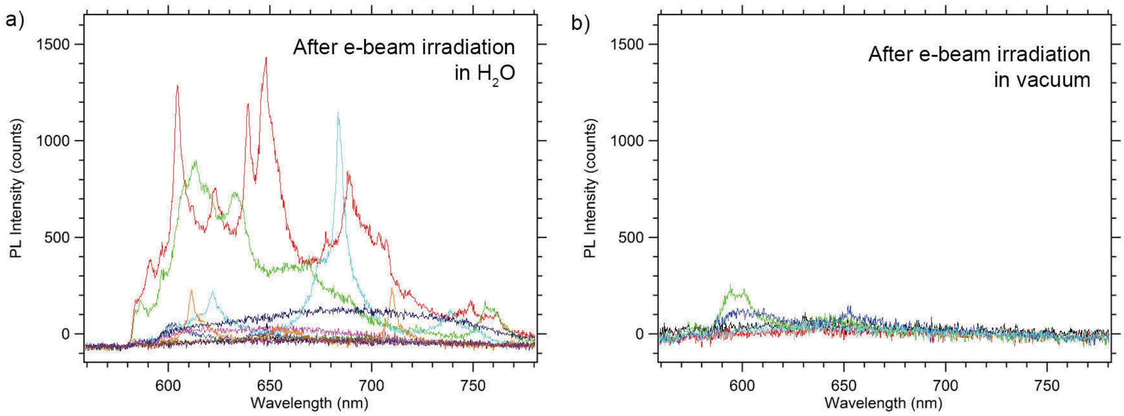

FIGURE 6.4: PL spectra highlights the (a) number of emitters found in a single 80×80 μm confocal scan after a 1 hour e-beam exposure in a H_2O environment (8 Pa) and in a high vacuum environment (3×10^{-4} Pa) (b). 15 keV accelerating voltage was used with $5 \times 10^{18}e^-/cm^2$ electron fluence.

As electron beam irradiation in a H_2O environment has shown to remove organic contamination, it could be plausible that contamination may be quenching emitters in hBN. A low power RF plasma in an O_2 environment was employed for 2 hours to remove organic contaminations from a hBN sample. Up to 100 PL spectra was then taken on the sample area and no emitters were found, a sample of these spectra are shown in figure 6.6. This seems to suggest that contamination cannot be solely responsible for quenching of emitters.

As will be covered in Chapter 7, electron beam induced etching of hBN occurs at high electron beam dosages. As the electron beam fluence used in this study, $5 \times 10^{18}e^-/cm^2$ is much lower than that needed to cause electron beam induced etching of hBN (above $1 \times 10^{20}e^-/cm^2$), it is possible the electron beam is creating a low amount of defect sites. This will likely result in emitters being located in the topmost monolayers of hBN. Therefore under continuous irradiation it is likely defects can be created and destroyed resulting in a low probability of emitter formation under electron beam irradiation in H_2O. An example of emitters being selectively removed from nanodiamonds through the use of EBIE is shown appendix B. To summarise that work briefly, EBIE was performed in a H_2O environment and used to selectively etch surface

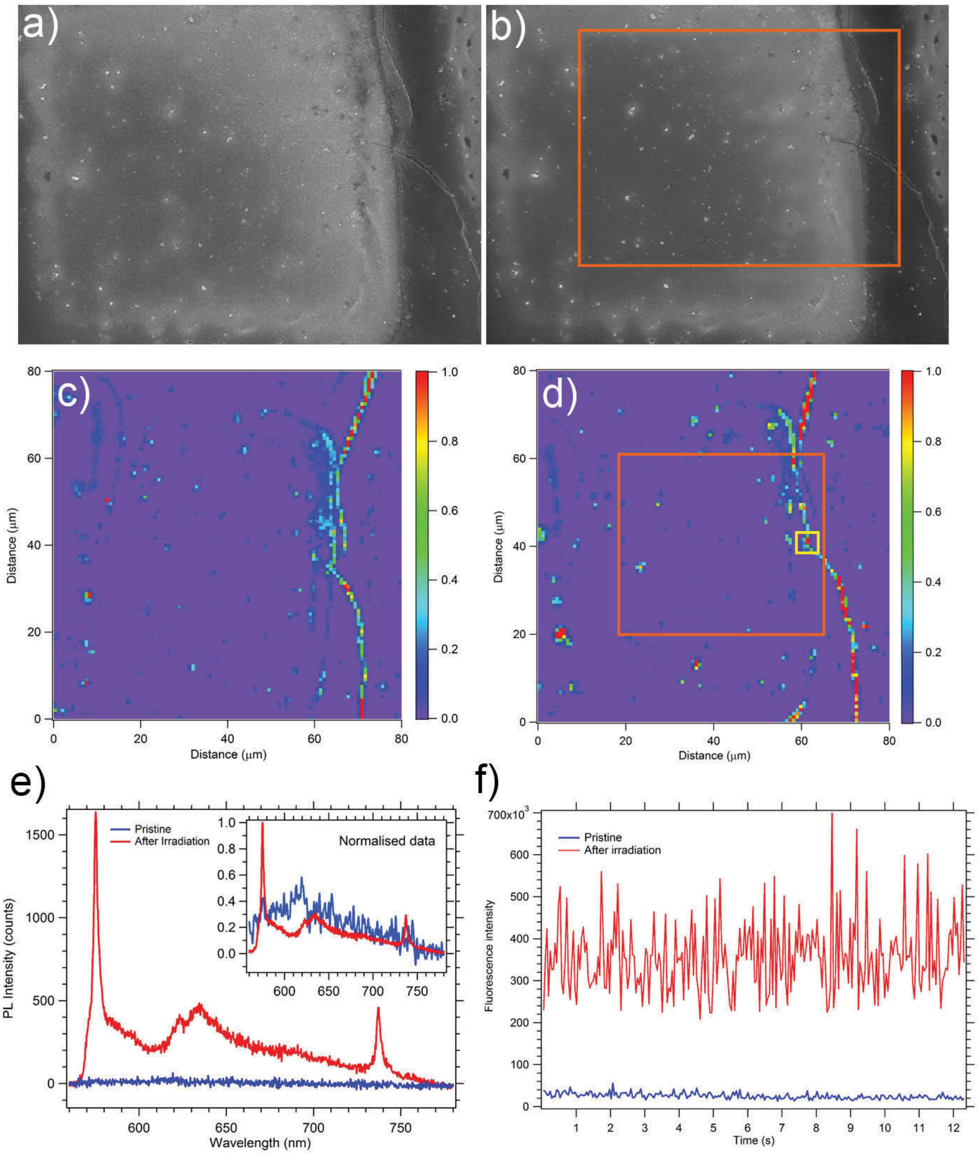

FIGURE 6.5: SEM images (a,b) and confocal scans (c,d) are shown before and after a 1 hour e-beam irradiation (15 keV, $5 \times 10^{18} e^{-}/cm^{2}$ electron fluence) of hBN flakes in a H_2O environment, region irradiated is highlighted with an orange box. The confocal scan area of 80×80 μm was used and the orange box indicates the e-beam irradiated area in (b,d). PL spectra (e) and PL intensity (f) is plotted of a hBN emitter which is highlighted by the yellow box in (d).

defects in nanodiamonds containing silicon vacancy rich defect emission. PL spectra was taken before and after EBIE of nanodiamonds and the study shows selective removal of narrowband SPE located at secondary nucleation sites and twin boundaries, these results are showcased in appendix B.

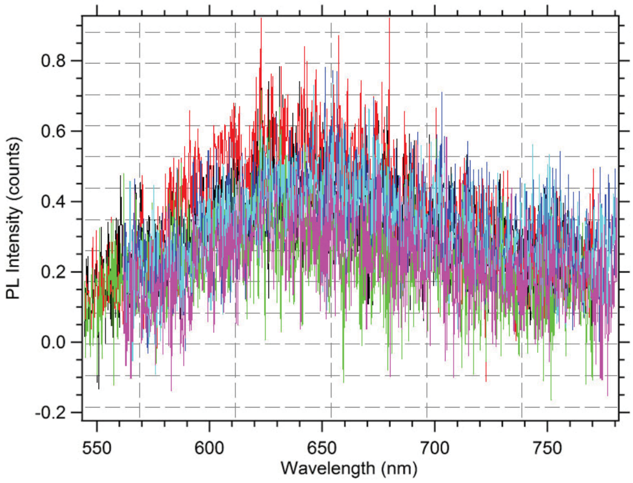

FIGURE 6.6: PL spectra is illustrated on a selection of hBN flakes which have been treated with a 5W delocalised RF plasma in a O_2 environment for 2 hours.

6.4.2 Emitter stability

Next, the stability of the emitters in various gaseous environments were studied. These properties are important both from a technological point of view, since the emitters can potentially be used as sensors or quantum light sources in harsh chemical environments, and for understanding their chemical origin, as annealing in different gases can modify defect emission properties [43, 207]. First, the defect fabrication study (figure 6.3(b)) was leveraged to create emitters by annealing a sample for half an hour in Ar at $850°C$. The sample was then characterized by confocal PL, annealed sequentially at $500°C$ for one hour each in hydrogen, oxygen and ammonia environments, and re-characterized by PL after each annealing step. Spectra from two stable emitters are shown in figure 6.7 (a) and (c), respectively. The fluorescence from the emitters remains unmodified even after annealing in both oxidizing and reducing environments. Figure 6.7(b, d) shows corresponding autocorrelation $g^{(2)}(\tau)$ curves for the two emitters recorded for each emitter after the initial argon annealing treatment (black curve) and after the final annealing step performed in an ammonia environment (red curve). All autocorrelation curves show that $g^{(2)}(\tau) < 0.5$, proving unambiguously that the emitters are point defects that act as single photon sources. The data convincingly prove the robustness of the emitters and the persistence of their quantum nature.

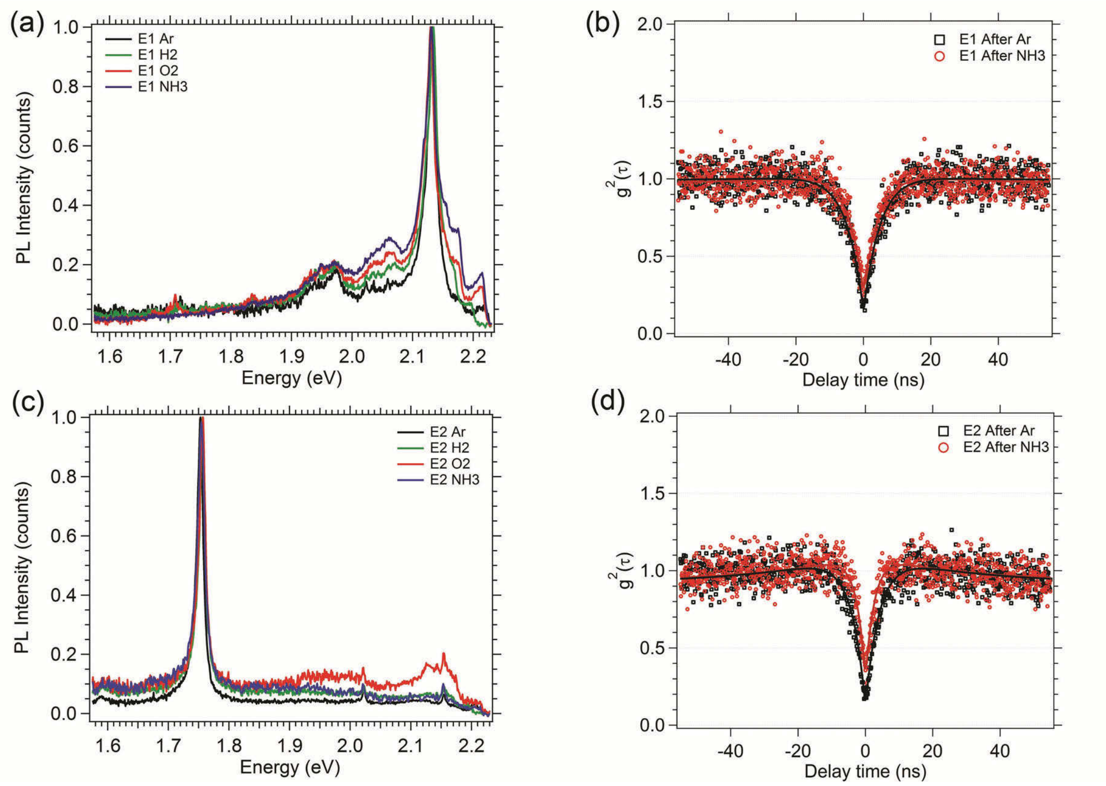

FIGURE 6.7: Stability of the emitters. (a,c) Normalized luminescence recorded at room temperature from two emitters (E1 and E2) after sequential annealing in argon, hydrogen, oxygen and ammonia. (b, d) Corresponding antibunching measurements proving that the quantum nature of the defects persists after the sequential set of 30 min anneals performed in H_2, O_2 and NH_3 environments.

The annealing results provide important insights into the nature of the emitters. First, the luminescent defect is likely to have a vacancy in its crystallographic structure. This is because of the clear increase in formation probability with annealing temperature, a behavior that is very typical of vacancy-related complexes in solids [205, 208]. Second, it is likely that the emitters are charge neutral. If the emitters were negatively charged, annealing in a hydrogen environment would have been expected to modify the charge state and modify or eliminate the emission. This behavior is exemplified by the NV center in diamond which switches from the negative to the neutral charge state upon annealing in hydrogen (and vice versa upon annealing in oxygen) [205, 208]. Similarly, many negatively charged emitters in GaN are switched off upon annealing in hydrogen [209]. Positively charged defects are not considered, as positively charged single photon emitters in solids have not been observed thus far. Finally, the emitters that are stable upon annealing cannot be surface states, as has been observed for some TMDs [210]. It is also most likely the case for a study that was performed on 2D MoO_3, where stability of emitters found was highly sensitive to the environment. Photo bleaching would occur within 20 seconds for all emitters in ambient environment, attempts were made to stabilise these emitters and the study can be found in appendix C. Surface states are often unstable, and are expected to be modified upon annealing in different reactive environments. However, that while many of the emitters were absolutely stable and resisted all the annealing treatments, each annealing step did create some new emitters, and quench some emitters. Both of these effects are demonstrated in figure 6.8.

In figure 6.8, the sample was first annealed in Ar at $850°C$ to generate emitters, and the black spectra in 6.8(a-c) were acquired from three different sample regions. (a) The green spectrum was acquired after annealing in H_2 from the same region as the black spectrum, and shows the disappearance of a number of emission lines (indicated by red arrows). (b) The red spectrum was acquired after the final annealing step in NH_3 from the same region as the black spectrum, and shows the appearance of a number of emission lines (indicated by green arrows). (c) The green and blue spectra were acquired after annealing in H_2 and O_2, respectively, and show the appearance and disappearance of a number of emission lines. No systematic trends were observed as a function of gas species. Instead, annealing in all three reactive environments caused the generation and quenching of some emission lines, and on average, more emitters were generated than destroyed after each annealing step. This behavior is expected based on the Ar annealing data shown in figure 6.3(b). The quenching of some of the

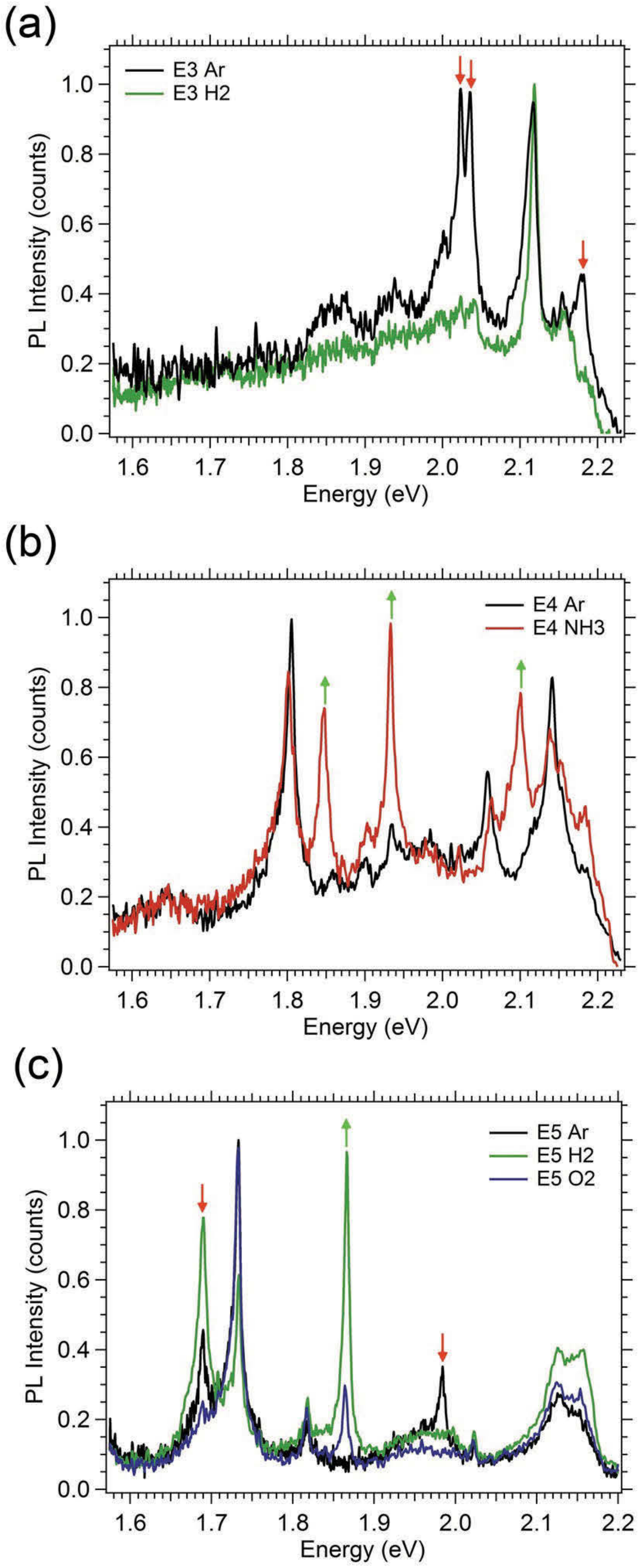

FIGURE 6.8: Emitter creation and destruction upon sequential annealing at 500°C for 30 min each in H_2, O_2 and NH_3 environments.

emitters is also not surprising. It merely indicates that some of the emitters are unstable, possibly because they are located in the topmost monolayers or edges of hBN flakes and hence sensitive to the annealing treatments.

6.4.3 Emitter photo-physical characterisation

Next, photo-physical characterisation of typical hBN emitters that have been engineered will be given. Figure 6.9a shows a simplified schematic of the confocal photoluminescence (PL) setup used to characterize hBN. The measurements were performed at room temperature using either a 532 nm continuous-wave (CW) laser, or a 510 nm pulsed laser as an excitation source for lifetime measurements. A photoluminescence survey was performed and collected spectra of various single defect centers in hBN. A representative range of room temperature PL spectra is shown in figure 6.9b,c. The emitters have narrow zero phonon lines (ZPLs) at energies in the range of 1.6 – 2.2 eV.

The emitters can be classified into two general groups based on their ZPL energy and phonon side band (PSB) spectral shapes. Group 1 (figure 6.9b) consists of emitters with ZPL energies of 576 nm (2.15 eV), 583 nm (2.13 eV), 602 nm (2.06 eV), 633 nm (1.96 eV), and 652 nm (1.90 eV). Emitters in this group exhibit relatively broad and asymmetric ZPL line shapes with pronounced low energy tails. The spectra also contain pronounced doublet PSBs, further characterisation on the PSB is performed on isotopic b10 hBN in section 6.4.4. Group 2 (figure 6.9c) is comprised of emitters at lower energies, with ZPLs centered on 681 nm (1.82 eV), 696 nm (1.78 eV), 714 nm (1.74 eV), and 762 nm (1.63 eV). Notably, these emitters have narrower, more symmetric ZPLs, with phonon sidebands that are weak compared to Group 1.

A Hanbury Brown and Twiss (HBT) setup was used to verify single photon emission from these defects. Figure 6.9e shows second-order autocorrelation functions $g^{(2)}(\tau)$ recorded from representative emitters selected from each group, with ZPLs centered on 633 nm (Group 1 emitter), and 714 nm (Group 2 emitter). Both curves

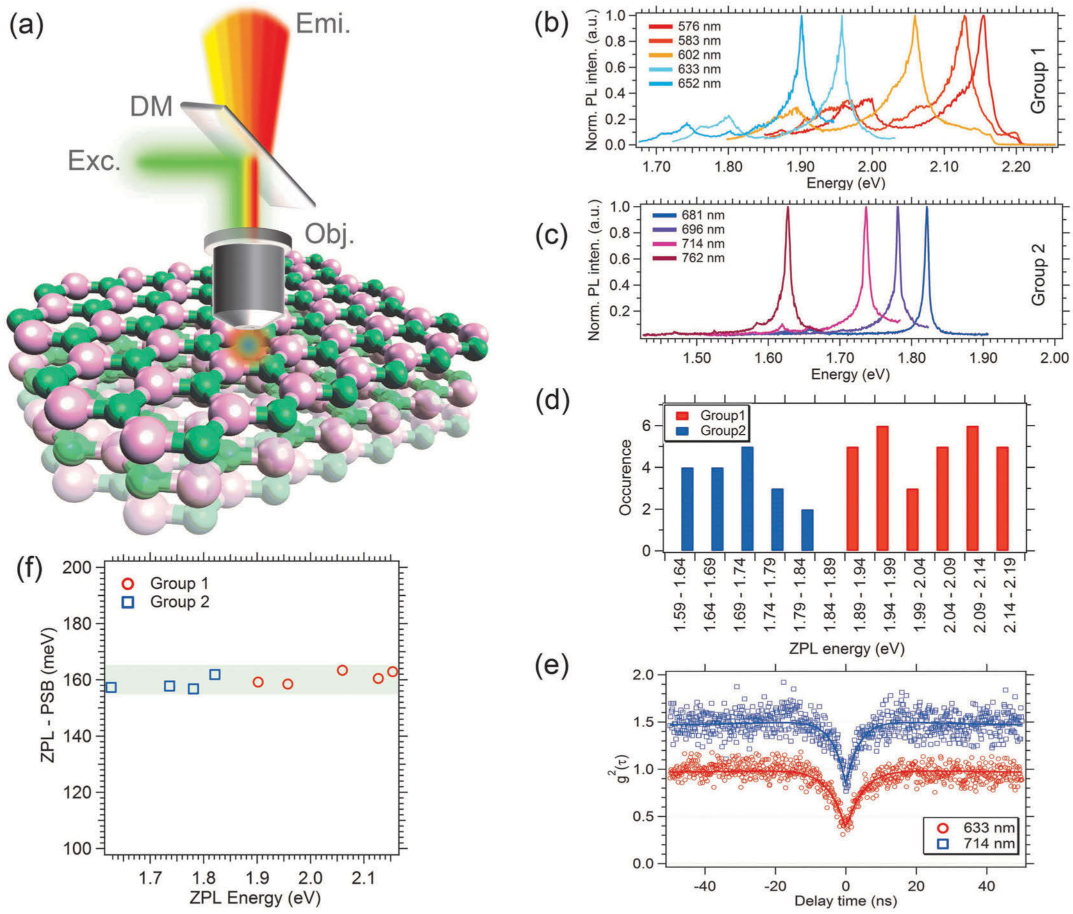

FIGURE 6.9: Multicolor photoluminescence from point defects in hBN. (a) Simplified schematic of the photoluminescence setup showing the excitation and emission of a defect center in a hBN lattice. The objective lens, dichroic mirror, excitation source and emission are denoted by Obj., DM, Exc., and Emi., respectively. (b) Five examples of emitters in Group 1 and (c) four examples of emitters in Group 2. (d) Histogram of ZPL energy for numerous emitters in group 1 (red) and group 2 (blue). Each spectrum was acquired from a separate sample region at room temperature using a 300 μW CW 532 nm laser. (e) Second order autocorrelation functions showing that $g^{(2)}(0)$ = 0.39 and 0.34, respectively. The $g^{(2)}(\tau)$ functions were acquired using an excitation power of 300 μW, an acquisition time of 20 sec, and were normalized without background correction. (f) Difference in the energy of the ZPL and PSB versus ZPL energy.

show that $g^{(2)}(0) < 0.5$, proving unambiguously that the defects are point defects that act as single photon emitters. The $g^{(2)}(\tau)$ were not background-corrected and fit using a three level model.

It is important to note that emitters in both groups exhibit a similar energy gap difference of 160 5 meV between the ZPL and the PSB (figure 6.9f). These values indicate that the associated coupled localized vibrations (phonon modes) are very similar, and the defects responsible for all spectra have similar crystallographic structure [211, 212]. Hence, the two groups likely correspond to two similar defects that reside in different local dielectric environments. The variation in ZPL position within each group may be contributed to by variations in local strain and dielectric environment.

Next, a detailed analysis is presented of the photophysical properties of the two emitters whose $g^{(2)}(\tau)$ curves are shown in figure 6.9e, which are representative of emitters in each of the two groups shown in figure 6.9b,c. To obtain the optical transition lifetimes of these emitters, a time-resolved fluorescence measurement was performed using a 510 nm pulsed laser with a 20 MHz repetition rate and 100 ps pulse width. As is seen in figure 6.10a, the lifetimes of the two emitters were extracted using single exponential fits, yielding values of 2.9 and 6.7 ns for the centers with ZPLs at 633 nm and 714 nm, respectively (the onsets of the decay curves should be ignored since they correspond to the response of our experimental setup).

Fluorescence saturation behavior was characterized by measuring PL intensity as a function of excitation power. The results are shown in figure 6.10b, and the data were fit using the expression:

$$I = I_\infty P/(P + P_0) \tag{6.3}$$

I_∞ and P$_{sat}$ are the emission rate and excitation power at saturation [213], respectively. The resulting emission rates at saturation for the 633 nm and 714 nm emitters

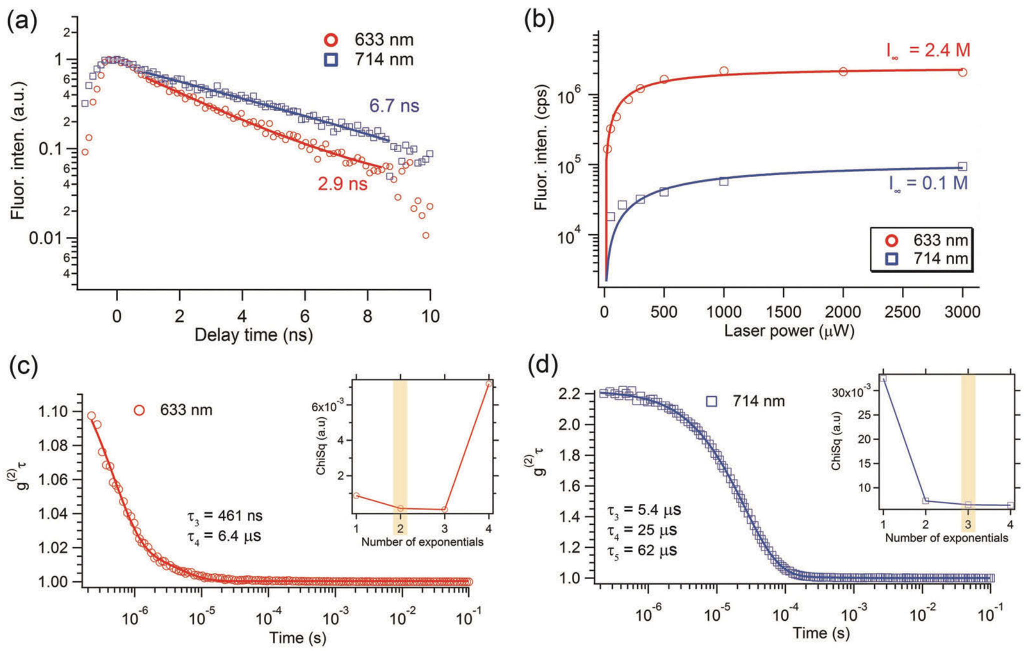

FIGURE 6.10: Photophysical properties of the defects. (a) Time-resolved fluorescence measurements showing radiative transition lifetimes of the emitters. A 80 μW, 510 nm pulsed laser with a repetition rate of 20 MHz and a pulse width of 100 ps was used as the excitation source. The solid lines are fits obtained using single exponential decay functions. (b) Fluorescence saturation curves and corresponding theoretical fits calculated using a three level model. (c, d) Second order autocorrelation function, $g^{(2)}(\tau)$, recorded over a longer time scale from the two color centers presented in Fig. 6.9 with ZPLs at 633 (c) nm and 714 nm (d). The corresponding solid traces are theoretical fits to the experimental data. Insets show the fitting residue χ^2 versus the number of exponentials used in the fitting functions. The yellow bands indicate optimal fits realized when the number of exponentials and the residues are simultaneously minimized.

are 2.4×10^6 and 0.1×10^6 counts/s, at P_{sat} = 310 μW and 770 μW, respectively.

To gain further insights into the observed variation in emitter brightness, autocorrelation functions were measured over longer time scales up to 0.1 seconds. These measurements provide information about the presence of other metastable states with longer decay times [214–216]. Figure 6.9c,d shows long timescale photon antibunching curves for the two color centers. By applying an increasing number of components in the multi-exponential fitting function, a fitting function with a least number of exponentials and lowest fitting residue (χ^2) was obtained for each center. Additional metastable states associated with the investigated emitters were found to be τ_3 = 0.46 μs and τ_4 = 6.4 μs for the emitter with ZPL at 633nm. For the emitter at 714nm they were; τ_3 = 0.46 μs, τ_4 = 6.4 μs and τ_5 = 6.4 μs.

These measurements account for the difference in the overall brightness of the two emitters. The brighter 633 nm defect has fewer metastable states with shorter lifetimes, while the 714 nm defect exhibits multiple additional metastable states with relatively long lifetimes. The differences in lifetimes of both radiative and non-radiative transitions between the two emitters are indicative of local environmental effects such as the presence of neighboring impurities or the proximity of a center to the surface or the edge of a multilayer hBN flake.

6.4.4 Emitters in isotopic B10-hBN and the PSB

In this section isotopically enriched B10-hBN flakes are used to confirm the correlation between the ZPL and PSB for single photon emitters found in hBN. This will be done by comparing to the standard naturally abundant hBN flakes by Taniguchi et al. [217] used throughout this chapter. These standard hBN flakes were grown by a high temperature, high pressure process [217]. The B10-hBN was supplied by Edgar et al. [218] which was produced at atmospheric pressures with temperatures of 1550°C [218, 219]. The boron source used in this growth process comprised of isotopically enriched boron-10. 95% B-10 isotope was incorporated into the resulting hBN crystals produced. The samples were prepared by mechanically exfoliating the B10-hBN crystal onto a Si substrate which were pretreated at 450°C in air to rid of any organic contaminants followed with an annealing step at 850°C in Ar for 30 min to activate emitters in the B10-hBN. Emitter formation, PL, polarisation, autocorrelation and saturation characterisation of SPEs in b10-hBN were also studied.

Starting with two B10-hBN flakes, figure 6.11a,b illustrates an abundance of emitters found when comparing to standard hBN large flakes [220]. The defect density

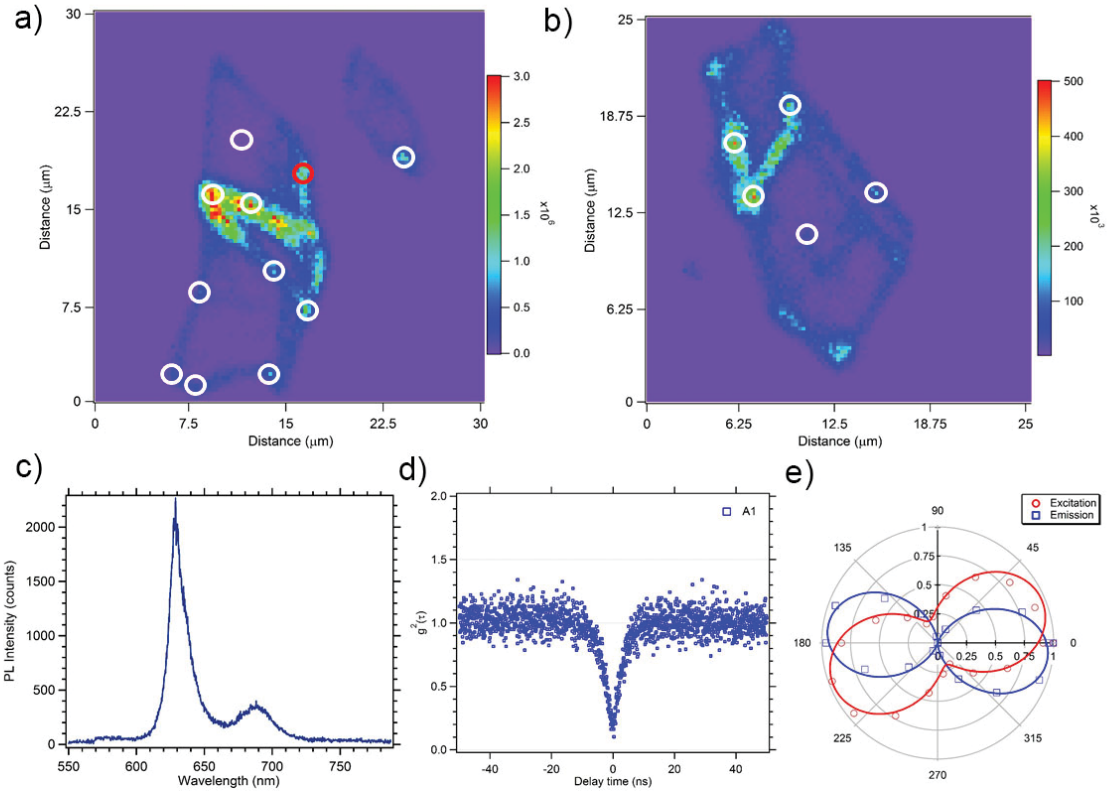

FIGURE 6.11: (a,b) Confocal scans on B10-hBN large flakes are illustrated with white circles indicating emitters found. PL spectrum (c), autocorrelation measurement (d) and polarisation results are shown for the emitter highlighted by the red circle in (a). 300 μW 532 nm laser used for excitation.

is most likely a result of the growth technique which was performed at much lower pressures with impurities such as carbon, nickel and chromium present during fabrication of the hBN. Therefore it is not unreasonable to imagine that a higher defect rate would be present in the B10-hBN at the surface and embedded in the crystal when comparing to the standard hBN. The emitters are also very stable, unlike the standard hBN flakes [220]. The emitters are capable of withstanding higher laser power excitation, on the order of 1-2 mW (see figure 6.12), which as a result allows for very bright emitters to be found. An example of a B10-hBN emitter fluorescence saturation behavior was characterized by measuring PL intensity as a function of excitation power in figure 6.12, and the data were fit using the expression shown in equation 6.3. This is one of the brightest SPEs recorded at room temperature, saturating above 3 million counts per second. Next, PL characterisation was performed on one of the SPEs found to probe the similarities between the emitters and those found in standard hBN flakes. This SPE is highlighted in figure 6.11a with a red circle. The PL spectra resembles an emitter found in group 1 SPEs of standard hBN with the ZPL located at 629 nm, as seen in figure 6.11c. In fact all emitters ZPLs in B10-hBN were found at different wavelength positions, spanning the range of group 1 and 2 emitters, most likely indicating the same or similar defects being formed as in standard hBN. Autocorrelation measurements prove this is a SPE with a $g^{(2)}(0)$ value < 0.5 and shows dipole like full polarisation as shown in figure 6.11d,e respectively.

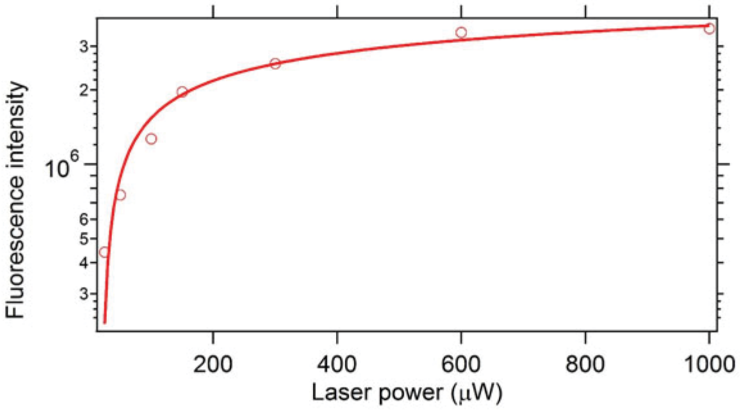

FIGURE 6.12: A saturation curve is shown of a very bright B10-hBN single photon emitter.

Now, raman data was collected using an excitation laser at 633 nm for the B10-hBN and for the standard hBN. A difference of 28 cm^{-1} was shown in figure 6.13, for the hBN in-plane vibrational mode (E_{2g}) [221]. This equates to a difference in energy of 3.5 meV and will be used to determine whether a shift of that magnitude occurs between the difference of ZPL and PSB of b10-hBN and standard hBN.

Emitters at similar peak positions for B10-hBN and standard hBN were then found and peak fitting analysis performed to find the energy values of their ZPL and corresponding PSB, these results are shown in figure 6.14a,b for a group 1 emitter and figure 6.14c,d for a group 2 emitter. The ZPL and PSB peak positions are highlighted in figure 6.14 and the calculated difference in energy for the group 1 and group 2 B10-hBN

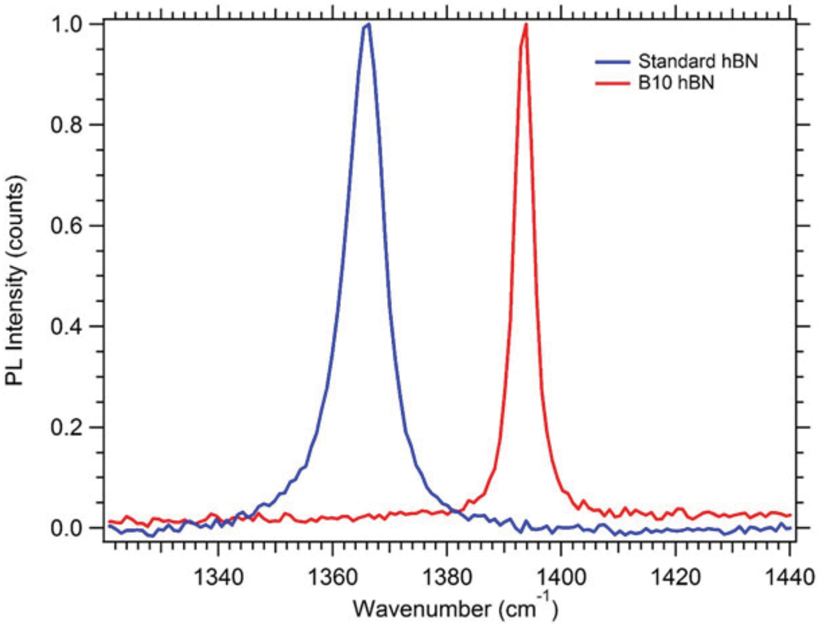

FIGURE 6.13: Raman (E_{2g}) mode is displayed for a standard hBN flake (blue line) and B10-hBN flake (red line).

and standard hBN was 9.2 meV and 14meV respectively. The energy shift between the ZPL and PSB are found to be in the right direction consistently and give evidence to prove that the peak following the ZPL is indicative of the PSB. However the magnitude of the shift shows uncertainty in the values when comparing to the 3 meV energy shift found in the (E_{2g}) in-plane stretching mode, this is most likely due to consistent deviations in the curve fitting analysis.

6.4.5 Toward deterministic fabrication of emitters

In this section, the formation and localization of narrowband quantum emitters in large standard flakes (up to tens of microns wide) of hBN was studied. A deterministic electron beam induced irradiation technique to fabricate the emitters in specific hBN flakes was used. Figure 6.15a, b shows a flake before and after electron beam irradiation by a 15 keV electron beam in a H_2O vapour environment (see methods). Figure 6.15c shows photoluminescence spectra recorded from the pristine flake (blue) and after the irradiation treatment (red). Note that the spectra were recorded from the

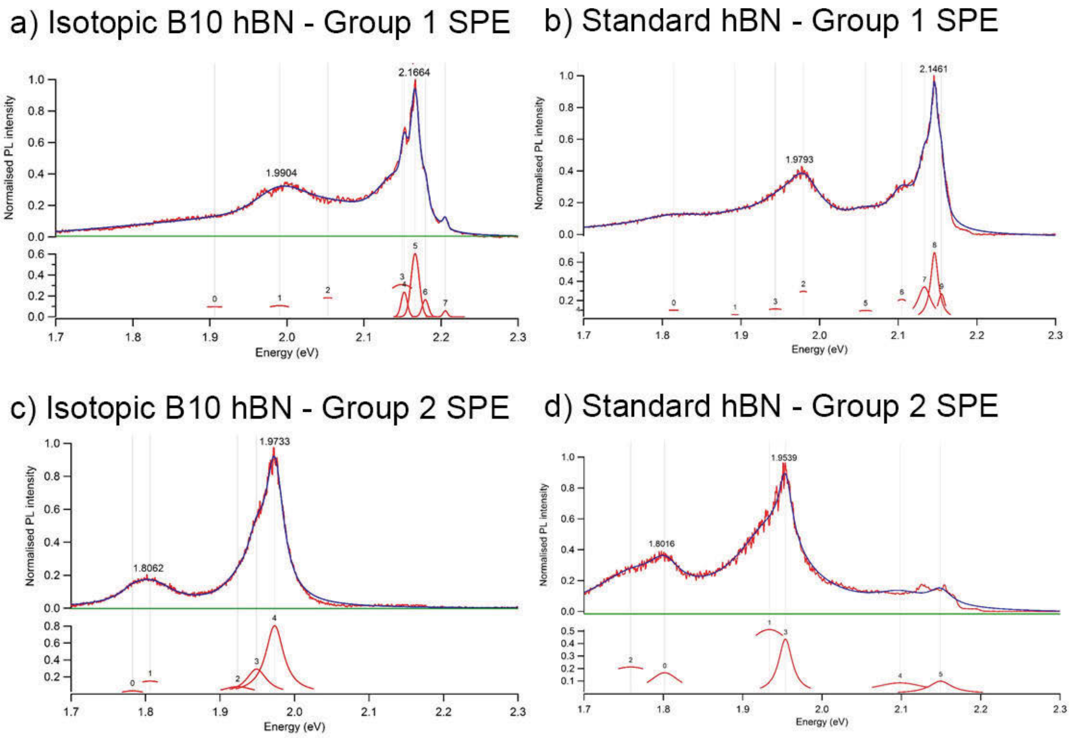

FIGURE 6.14: Peak fitting for a B10-hBN and standard hBN group 1 (a), (b) and group 2 (c), (d) emitter are shown. The ZPL and corresponding PSB positions are highlighted with their respective energy values.

same location, as indicated by the white circles in (a) and (b). The inset is a $g^{(2)}(\tau)$ function that proves the probed emitter is a single photon source. Figure 6.15d shows the corresponding polarization measurements from the same emitter. Most of the emitters created show full polarization in both excitation and emission as seen in 6.15d. The polarisation behaviour is therefore indicative of a dipole like emitter. The misalignment between the excitation and the emission polarizations is likely due to redistribution of the excited electronic states.

This sample containing the emitter in figure 6.15 was not annealed after electron beam irradiation because the annealing is not required for emitter activation, in contrast to emitters generated by the ion and laser irradiation treatments [220]. This can be explained by the fact that ion implantation and laser irradiation generates significant

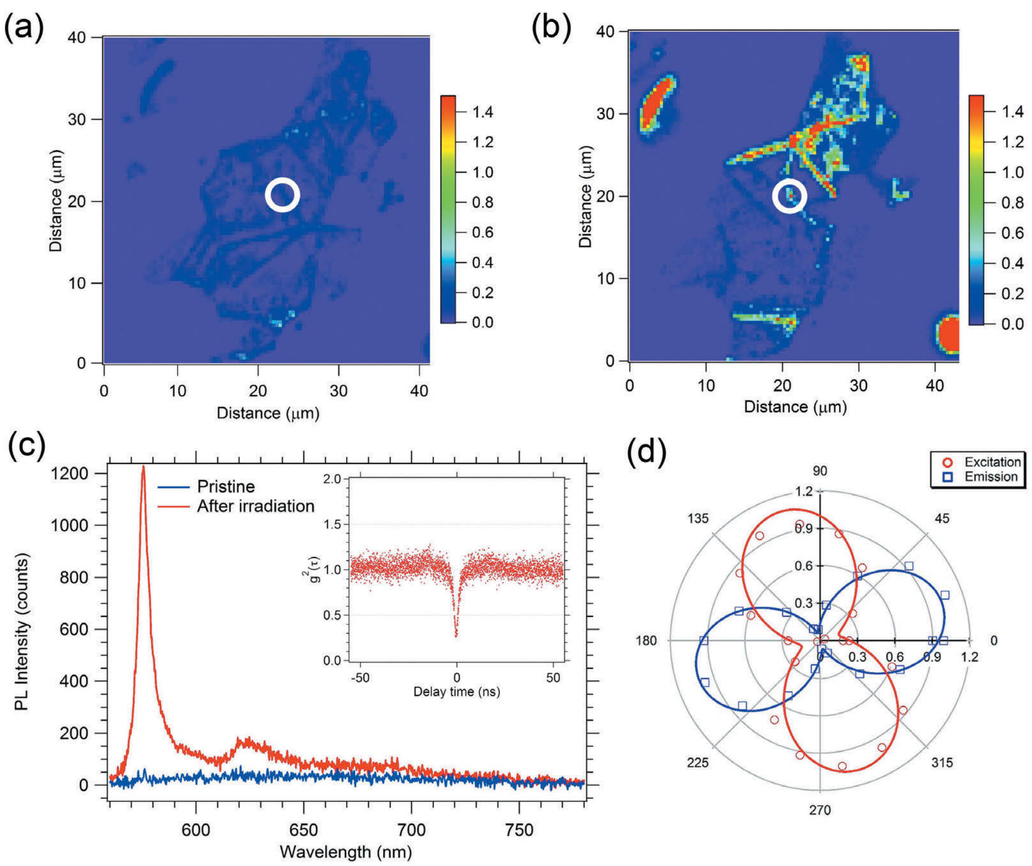

FIGURE 6.15: Fabrication of emitters by electron beam irradiation. Confocal map of the same flake before (a) and after (b) electron beam irradiation. The energy of the beam is 15 keV. (c) Spectra recorded from a particular location before (blue curve) and after (red curve) irradiation. Inset, a $g^{(2)}(\tau)$ curve confirming the formed defect is a single photon source. (d) excitation and emission polarization from the same defect. The sample was not annealed after electron irradiation.

damage in the hBN lattice that partly recovers during annealing. On the other hand, irradiation by 15 keV electrons in H_2O vapour is a more subtle process that chemically reforms the lattice, with minimal damage to the surrounding crystallographic environment [94]. The electron beam approach is therefore appealing as it allows emitter fabrication and localization in a single step, without the use of lithographic masks or post-processing treatments. The electron beam created emitters were located consistently at flake edges and grain boundaries. Further work is needed to determine whether the electron beam creates new defects or activates pre-existing defects that are present in as-grow hBN.

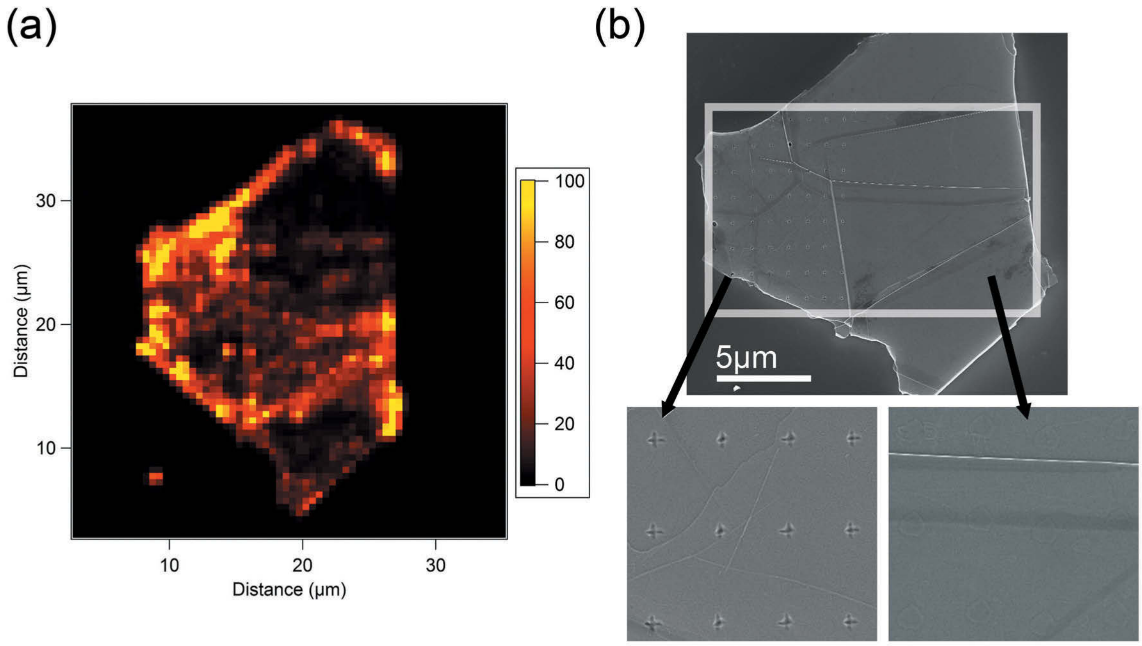

FIGURE 6.16: (a) and (b) confocal PL mapping on the hBN flake that was e-beam irradiated before and after Ar plasma etching. The right hand side shows an SEM image of electron beam patterned hBN flake and accompanying zoomed in electron beam patterns etched into the hBN (cross patterns on left and defocused spots on the right).

Next, electron beam irradiation was used in conjunction with an Argon plasma treatment, which has also been employed to increase the yield of engineered single emitters in hBN by a factor of seven [222]. A post annealing process in Ar was then required to stabilize the emitters further. To explore the possibility of greater deterministic placement of single photon emitters in hBN, electron beam induced etching was employed to created periodic features to fabricate new edges, such as nano-crosses, over the hBN flakes prior to plasma etching and annealing. Figure 6.16a show the confocal PL mapping on E-beam irradiated flakes before and after plasma etching. The white boxes in figure 6.16b illustrates the E-beam etched areas which show an enhanced brightness corresponding to the electron beam irradiated regions compared with the non-irradiated areas of the flake. Single photon emitters were found in the vicinity of the e-beam created features, which suggests the localized synthesis of emitters in hBN at edge sites created by the e-beam. Figure 6.16b shows a scanning electron microscopy (SEM) image of the resulted hBN flake using EBIE, the designed centre-to-centre distance of each etch region is $1\mu m$.

By combining the ability to direct-write edge sites and defects within the hBN lattice using EBIE and the plasma treatment preference to create single photon defects at crystal edges and grain boundaries (as shown in previous fabrication techniques [220, 222, 223]), it is possible to take an additional step towards deterministic fabrication of single emitters in hBN as a much larger quantity of emitter formation is seen with this combined technique (approximately 30:1 emitter creation ratio).

6.5 Conclusion

In conclusion, two robust methodologies were presented to engineer room temperature multicolor single photon emission, based on annealing and electron beam irradiation. Moreover, it was shown the emitters are stable even after annealing in harsh gaseous environments such as oxygen, hydrogen and ammonia. By analyzing spectral features of these emitters, the results infer that there are at least two groups of defects. Although the emitters in the two groups exhibit significant differences in their spectral characteristics, they share similar local phonon energies and therefore are likely to have a similar chemical structure. Finally, it is shown that electron beam induced etching and an argon plasma can be used to fabricate the emitters deterministically on a particular flake. Overall, the emitters are polarized and optically photostable and therefore are very promising for employing quantum emitters in 2D materials for emerging applications in nanophotonics and nanoscale sensing devices.

6.6 Chapter contributions

Chris Elbadawi, Sumin Choi, Trang Trong Toan, Milos Toth, Igor Aharonovich and Charlene Lobo conceived the idea and planned the experiments. Chris Elbadawi performed the electron beam irradiations and photophysical characterisation (confocal mapping, PL spectra, polarisation and autocorrelation measurements). Trang Trong Toan performed hBN annealing statistics and photophysical characterisation and design for figure 9 and 10. Daniel Totonjian performed annealing experiments. Zaiquan Xu performed the plasma etching experiments. Chris Elbadawi performed the Monte Carlo simulations. Sumin Choi designed fig 1 a,b. Chris Elbadawi designed all other figures. Chris Elbadawi, Sumin Choi, Trang Trong Toan, Charlene Lobo, Igor Aharonovich and Milos Toth wrote and edited the chapter.

Chapter 7

Electron beam directed etching of hBN

7.1 Abstract

Hexagonal boron nitride (hBN) is a wide bandgap Van Der Waals material with unique optical properties that make it attractive for two dimensional (2D) photonic and optoelectronic devices. However, broad deployment and exploitation of hBN is limited by a lack of suitable material and device processing and nano prototyping techniques. Here a high resolution, single step electron beam technique for chemical dry etching of hBN is presented. Etching is achieved using H_2O as a precursor gas, at both room temperature and elevated hBN temperatures. The technique enables damage-free, nano scale, iterative patterning of supported and suspended 2D hBN, thus opening the door to facile fabrication of hBN-based 2D heterostructures and devices.

7.2 Introduction

hBN is a layered material with a wide range of applications in electronics [136], photonics [137, 138] and catalysis [139]. In particular, the two-dimensional form of hexagonal boron nitride (hBN) has recently attracted considerable interest for quantum technologies [141], polaritonics, and as a unique natural hyperbolic metamaterial [138, 140]. However, the applicability and wide deployment of hBN in scalable devices is presently limited by a lack of suitable nanoscale processing techniques, particularly growth and etching.

Etching of hBN is typically realized by high temperature annealing in H_2/Ar [224, 225] or oxidizing environments [226], or by reactive ion etching (RIE) [227]. However, the annealing techniques do not allow deterministic fabrication of desired hBN patterns and geometries, and RIE requires cumbersome, multi-step alignment and masking procedures. Direct-write patterning has been demonstrated by high energy electron [228–230] and ion bombardment [227, 231] using transmission electron microscopy (TEM) and focused ion beam (FIB) techniques. These techniques have limited applicability because the TEM approach requires the use of electron-transparent substrates, and FIB damage compromises surrounding and underlying materials from severe ion beam damage and ion implantation.

Here a direct-write, high resolution process for deterministic chemical dry etching of hBN is presented. The etching is performed using a scanning electron microscope (SEM) simply by using H_2O vapor as an etch precursor gas (irradiation in other gaseous environments and conditions, such as NF_3 and NH_3 is discussed in appendix D). The single step process, illustrated schematically in Fig. 7.1a, is highly versatile, works at room and elevated temperatures, and enables iterative fabrication of arbitrary nano scale patterns defined simply by the scan pattern of the electron beam. As the electron beam fluence used in this study, $1 \times 10^{20} e^{-}/cm^{2}$ is much higher then the beam fluences used in Chapter 6 ($5 \times 10^{18} e^{-}/cm^{2}$) it is shown that the etching rate scales with electron beam dosages. The etching can be performed at room temperatures, and at elevated substrate temperatures, consistent with a revised model of gas-mediated electron beam induced etching (EBIE) that was proposed recently [232] in order to explain H_2O-mediated EBIE of single crystal diamond. These findings expand the toolkit for deterministic nanoscale processing of hBN, and provide independent evidence for a model of EBIE [232] in which the critical, rate-limiting role of electrons in EBIE is stimulated desorption of etch reaction products rather than the

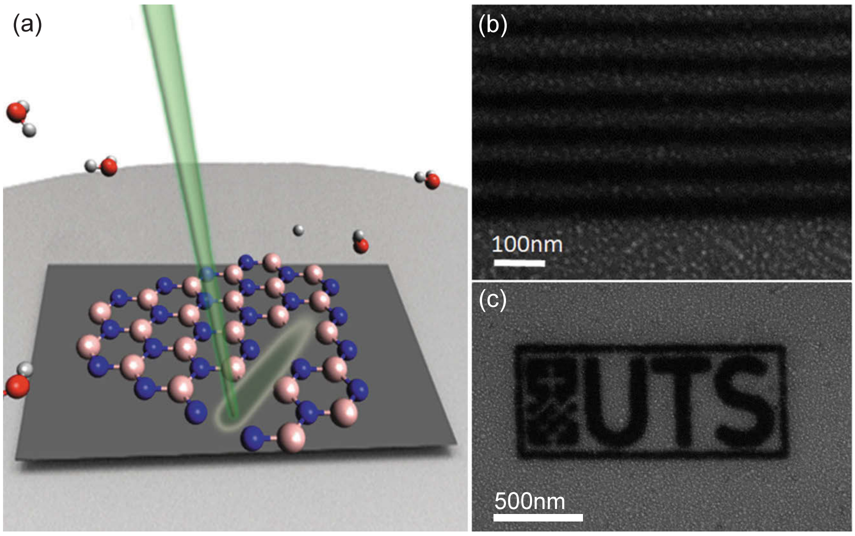

FIGURE 7.1: (a) Schematic illustration of electron beam induced etching of hBN performed using H_2O vapor as the etch precursor. (b, c) Patterns fabricated in hBN. Dark areas are regions from which hBN was removed by the electron beam. The surface roughness seen in the images is caused by backscattered electrons exiting the sample beyond the region irradiated by the beam.

dissociation of surface-adsorbed precursor molecules.

7.3 Methods and materials

Bulk hBN grown by a high temperature, high pressure process [217] was mechanically exfoliated onto a Si(111) substrate covered with a native oxide layer. The exfoliated hBN flakes on Si were rinsed with acetone and IPA and dried under flowing N_2. To perform EBIE [44, 45, 233–236], the hBN samples were mounted onto a heating stage in a customized FEI field emission SEM [237] and plasma treated overnight at room temperature with a mild 15W delocalised plasma in a low vacuum O_2 environment of 13 Pa to remove carbon contaminants resulting from the exfoliation process. The plasma treatment improves EBIE repeatability and enables quantitative measurements of etch rates [238], but does not result in etching or damage to the hBN. A comparison of a hBN flake before and after a plasma cleaning treatment is shown in figure 7.2, showing that no damage occurs to the hBN flake during the mild plasma treatment process. The plasma treatment is not necessary for the EBIE of hBN to occur but is used to minimise contaminantion and thus increase reproducibility of experiments.

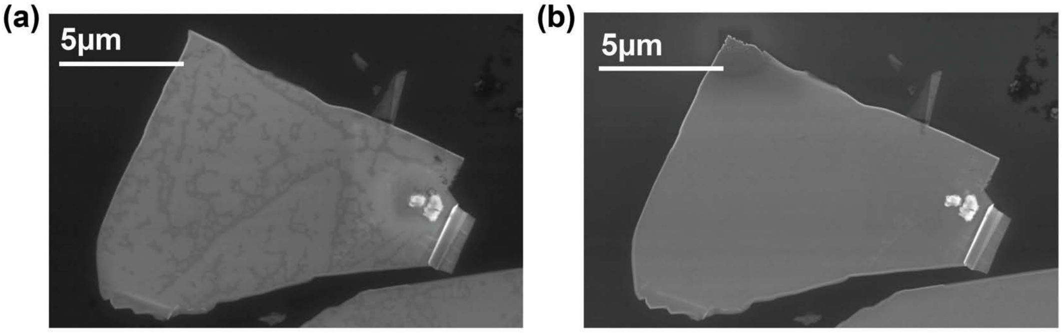

FIGURE 7.2: (a) SEM image of a typical hBN flake before plasma cleaning treatment. (b) Same hBN flake after a plasma cleaning treatment (note EBIE experimentation was undertaken in the top corner of the flake)

Following plasma cleaning, the system was pumped down to high vacuum and the chamber was filled with water vapor to a pressure of 8 Pa (electron irradiation of hBN in high vacuum gave rise to extremely slow etch rates attributed to the presence of residual H_2O in the SEM chamber [239]). The electron beam current was fixed at 1.35 nA for all EBIE experiments, and the beam energy was either 25 keV or 15 keV. Etching was done using a focused, Gaussian electron beam, except for etch pits made to characterize the etch rate as a function of time and temperature (Fig. 7.13), which were fabricated using a stationary top-hat beam with a diameter of 200 nm. Etch pit depths were measured by atomic force microscopy (AFM). Auger electron analysis was performed ex-situ using a nano-Auger Electron Spectrometer (AES, Omicron nanoSAM), in ultrahigh vacuum conditions.

7.4 Results and discussion

Electron beam irradiation in the presence of H_2O vapor gives rise to localized etching of hBN, and the beam can be scanned to create arbitrary, complex patterns deterministically. As examples, an array of waveguides is shown in Fig. 7.1b, and the logo of the University of Technology Sydney in Fig. 7.1c. The etch technique is very versatile, but gives rise to the surface roughness seen around the etched patterns. To understand and mitigate this roughening, the time evolution of the etched surface was characterised. Initially (i.e., at low electron fluences), the etch process causes roughening of the hBN surface, followed by complete removal of hBN under the electron beam. The time-evolution of the surface morphology is seen in Fig. 7.3a where regions 1 to 5 correspond to areas of a hBN flake that were irradiated with electron beam fluences of 1.7, 5.1, 11, 19 and 33×10^{20} cm^{-2}, respectively. Fig. 7.3b shows Auger electron spectra taken from each of the 5 regions shown in Fig. 7.3a. Regions 1-4 contain boron and nitrogen, and both elements are absent from region 5. The spectra also show that the intensity of the O^{KLL} oxygen peak increases monotonically with electron fluence, and it is most intense in region 5. Thus the increase in oxygen is attributed to the native silicon oxide layer of the substrate. The residual fragments seen in regions 1-4 (Fig. 7.3a) are comprised of boron and nitrogen, as is illustrated by the high resolution secondary electron image, and the boron, nitrogen and oxygen Auger maps shown in Fig. 7.3c. Raman spectroscopy was also undertaken before and after EBIE of hBN and shows no change to the hBN Raman line. Figure 7.4 displays Raman spectra taken before and after EBIE in the rastered region labeled 'Area 1' in the inset. The hBN Raman line shows no shift, suggesting that no damage occurs to the hBN during electron beam irradiation and etching of the material.

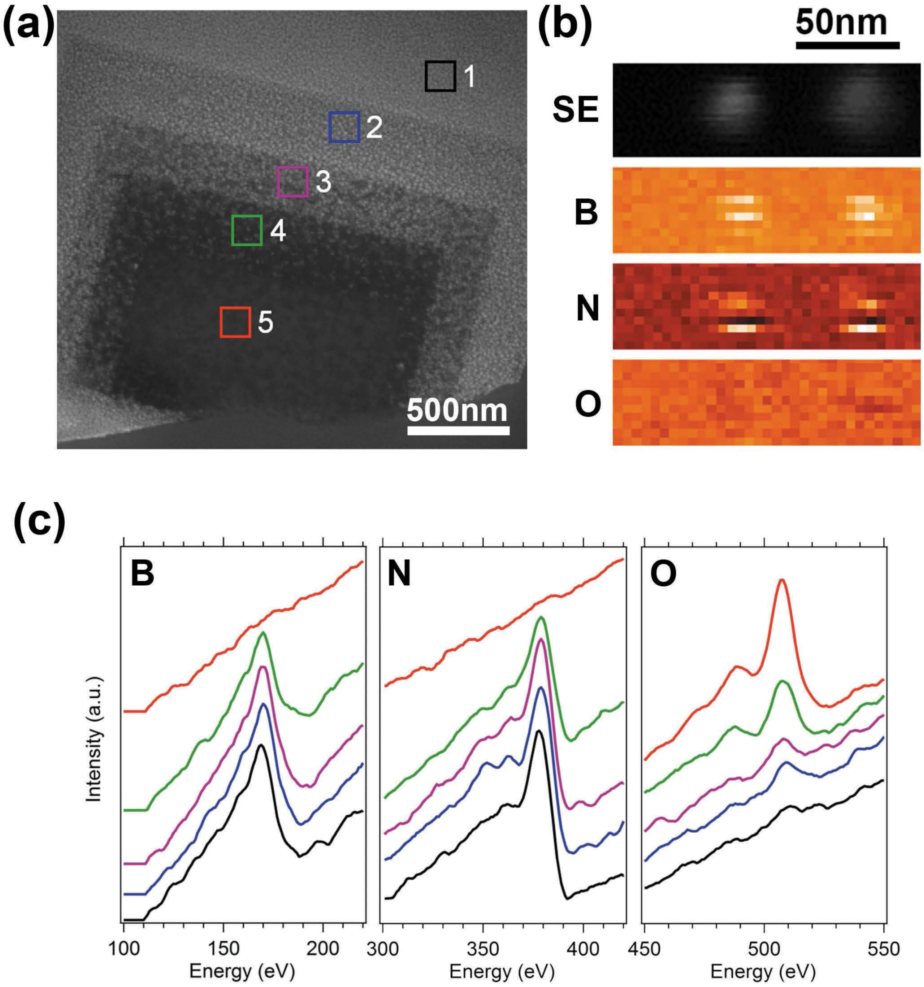

FIGURE 7.3: (a) Flake of hBN that was processed using 5 electron doses corresponding to electron beam fluences of 1.7, 5.1, 11, 19 and 33×10^{20} cm^{-2} (regions 1-5, respectively). (b) Secondary electron (SE) image and Auger maps of boron nitride fragments generated during etching, highlighting composition maps of B, N and O. (c) Auger electron spectra acquired from the 5 regions shown in (a). The peaks correspond to the 170 eV B^{KLL}, 379 eV N^{KLL} and 507 eV O^{KLL} Auger lines. The electron beam energy and current used for Auger analysis were 5 keV 1 nA, respectively.

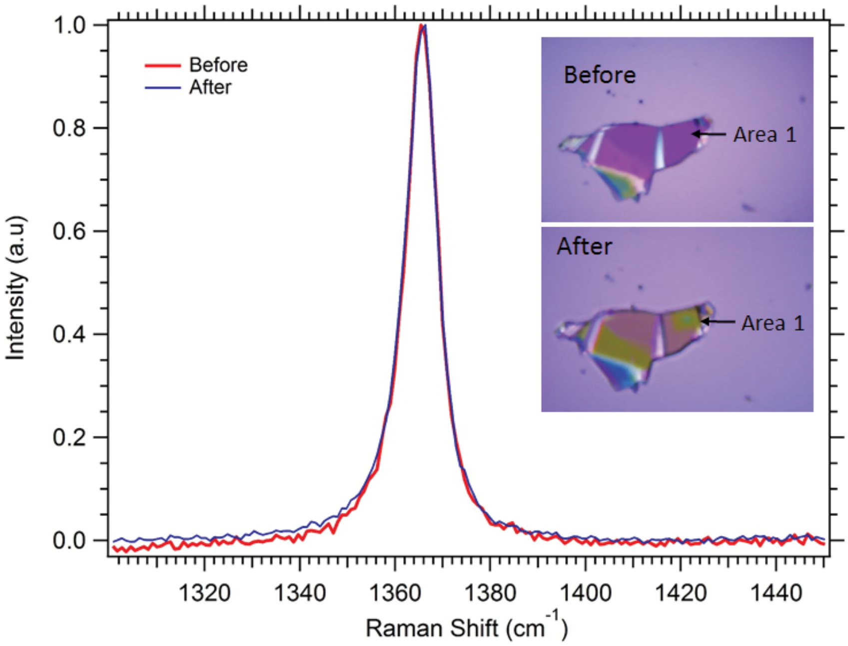

FIGURE 7.4: Raman spectra from hBN in Area 1 before and after EBIE processing. The Raman laser wavelength was 632 nm with a 2 micron diameter spot size.

The crystallographic structure of the fragments was confirmed by selected area electron diffraction (SAED). Fig 7.5a is a TEM image of a hBN flake that contains a hole (bottom right-hand corner) etched by EBIE. Fig. 7.5b is a SAED pattern taken from a pristine region of the flake that had not been etched by EBIE, while Fig 7.5c,d shows patterns from two regions indicated on the TEM image, at the periphery of the etch pit. The material in regions (c) and (d) is residue left behind by incomplete etching. All three diffraction patters were indexed as hBN, confirming that the corresponding contrast seen in SEM images (Fig. 7.1b,c and 7.3a) corresponds to hBN fragments. Hence, both the Auger and TEM data show that, during the initial phase of EBIE, low dose electron exposure gives rise to the formation of hBN fragments with a diameter of $\sim$ 30 nm, prior to complete volatilization and removal of the boron and nitrogen constituents.

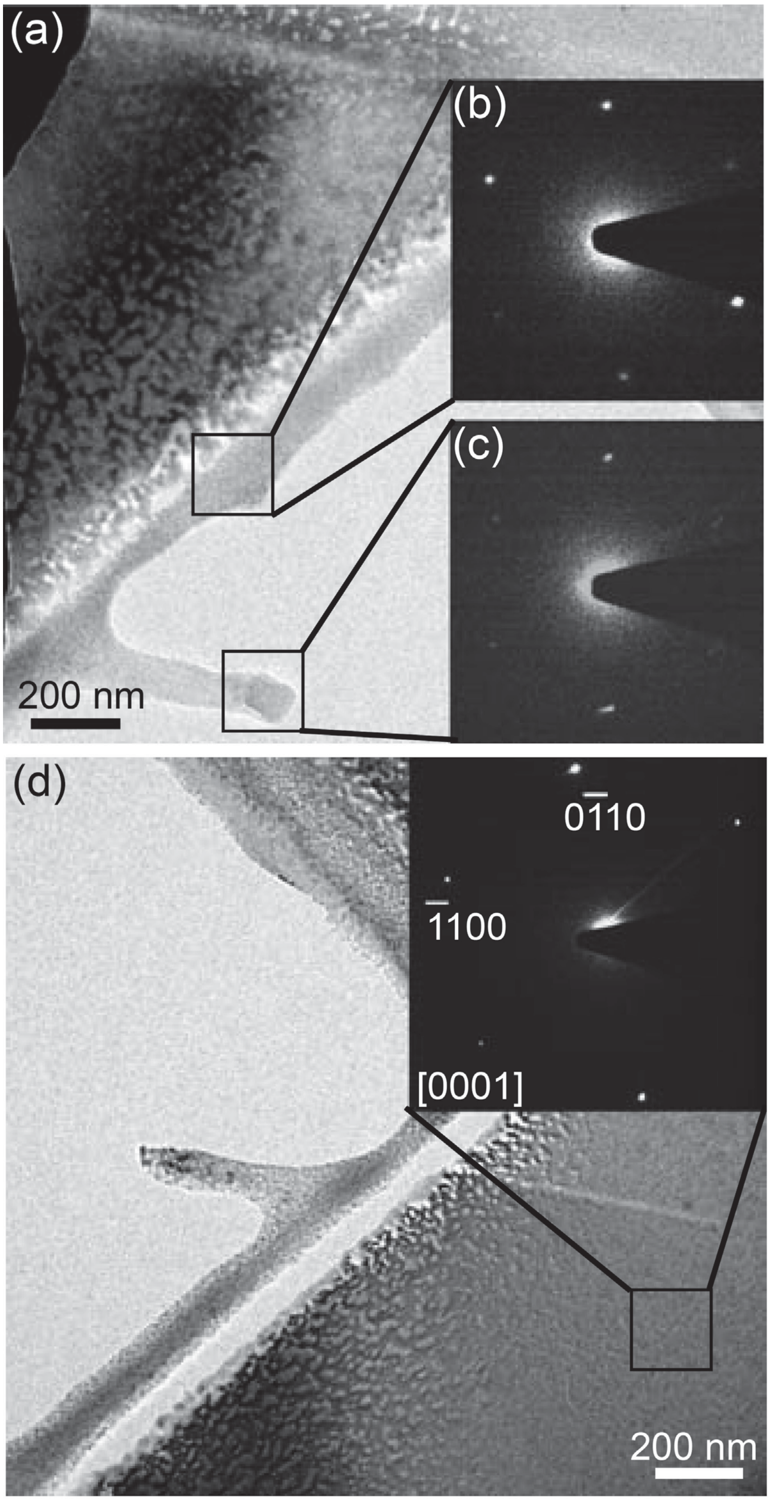

FIGURE 7.5: (a)TEM image of a hBN flake that contains an etch pit (bottom right-hand corner) fabricated by EBIE. The insets (b) and (c) show selected area electron diffraction patterns from the regions indicated on the image. The region indicated in (d) shows a pristine area of the hBN flake and the inset shows its corresponding selected area electron diffraction pattern. All patterns were indexed as hBN.

The hBN fragmentation process is problematic for practical applications of the etch technique because it occurs beyond the immediate area irradiated by the electron beam, and hence damages hBN around the patterned nanostructures (see Fig. 7.1b,c. There are some notable exceptions where small fragments of hBN can be advantageous. As an example, variable conductive properties or restructuring of hBN has been theorised when combined with fluorinated and hydrogenated edge sites, more information can be found in appendix D.

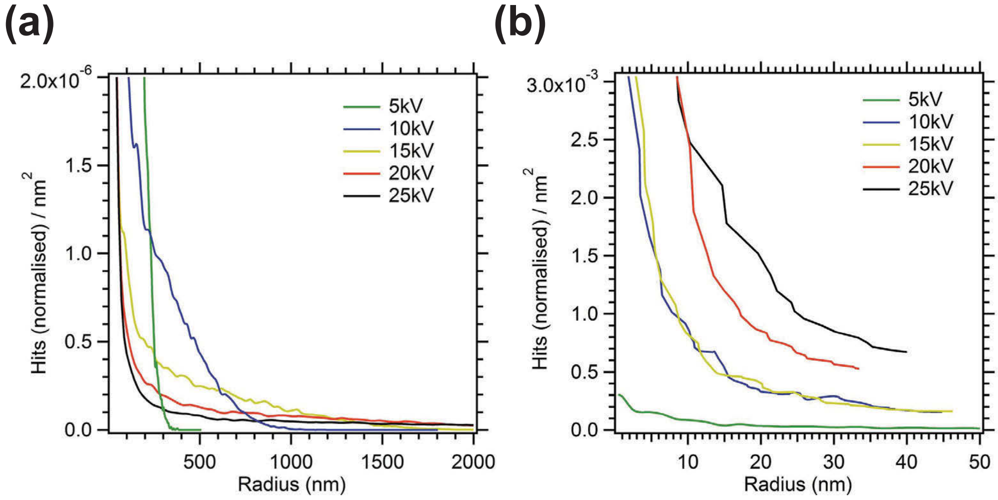

FIGURE 7.6: Monte Carlo simulations comparing the normalized hits (electrons per nm^2) on the (a) Si membrane-supported hBN and (b) unsupported hBN against the radial spread of BSEs for accelerating voltages between 5 and 25 kV. A large reduction in the BSE range can be seen when comparing the simulated hits on and off the Si membrane.

The delocalised damage in areas beyond the e-beam irradiated regions are attributed to incomplete etching caused by backscattered electrons (and so-called ‘type II’ secondary electrons [153]) that are emitted from the sample after a number of scattering events in the bulk substrate below the hBN. Monte Carlo simulations were carried out to show how both the BSE range and yield (electron hits per nm^{-2}) taper off dramatically away from the primary beam location when comparing hBN regions on the Si membrane (Figure 7.6a) and over a hole (Figure 7.6b). The substrate used in all ’on-membrane’ simulations consisted of a 90nm thick oxide layer on a 500 μm Si membrane, which can be considered an infinite substrate. For the hBN over a hole, no BSEs were detected beyond a radius of 50nm from the primary beam axis for all accelerating voltages studied, indicating that the majority of etching of the hBN is due to primary and SE electrons.

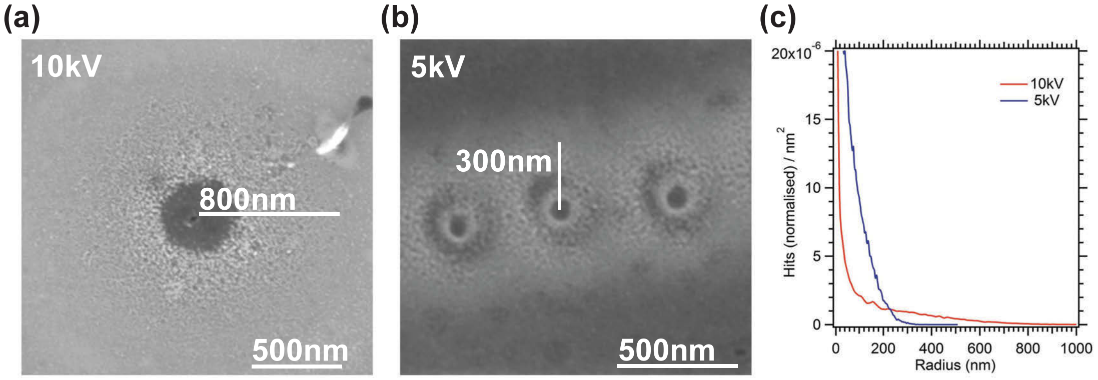

FIGURE 7.7: Correlation of radial extent of surface roughening as observed by SEM and expected BSE range at 10 and 5 kV primary beam energies. (a) SEM image of a single spot etched into a hBN flake at 10kV. The degree of roughening reduces with radial distance from the spot, extending to a distance of ≈ 800 nm. Similarly, (b) shows an SEM image of a series of holes etched into the same hBN flake at 5kV, showing that roughening is observed up to 300 nm from the primary beam location. (c) shows two Monte Carlo simulations comparing the normalized hits of electrons per nm^2 against the radial spread of BSEs at primary beam energies 5 and 10kV, showing good agreement with the observed range of surface roughening.

Figure 7.7 shows SEM images of holes etched into hBN using a 10 and 5 kV primary electron beam. The observed range of roughening of the hBN at 10kV (Fig. 7.7a) and 5kV (Fig. 7.7b) on a silicon substrate matches the simulated BSE ranges of 800 and 300 nm respectively (Fig. 7.7c), providing further confirmation of the role of BSEs in causing surface roughening of the hBN outside the primary electron beam radius. These results prove that the delocalised damage is indeed caused by backscattered electrons emitted from the sample.

The effect of the BSE can be suppressed simply by minimizing the size of the electron interaction volume in the sample. This can be achieved either by using a low energy electron beam (e.g. 1 keV whereby the width of the electron interaction volume in most materials is on the order of 10 nm [240]) or by eliminating the bulk Si substrate. The latter is demonstrated in Fig. 7.8a by a series of lines etched into a hBN flake suspended over a hole in a Si membrane with a 90nm thermal oxide layer. Fig. 7.8b is a close-up view of the lines, and clearly shows the presence of fragmented hBN around lines that were etched into hBN residing on the Si membrane (left), and absence of such fragments around regions suspended over a hole (right).

Further SEM images showing the differences in surface roughness of the suspended and non-suspended hBN are shown in Figure 7.9. Within the red box the contrast has been enhanced to accentuate the suspended hBN lines, while in the blue box, the contrast has been enhanced to highlight the hBN on the Si membrane. It should be noted that a small amount of roughening or etching would be expected on the suspended lines as they were located and imaged using the electron beam. Figure 7.9b shows that some roughening of the hBN occurs at the interface of the Si membrane and hole due to backscattered electrons escaping from the side wall of the Si membrane. This roughening disappears further towards the centre of the hole. The reduction in interaction volume is illustrated in Fig. 7.8c by electron trajectories simulated for a suspended 100 nm thick flake of hBN (left), and for the same flake residing on a bulk Si substrate (right). The simulations were performed for a 15 keV electron beam using the Monte Carlo package CASINO [172].

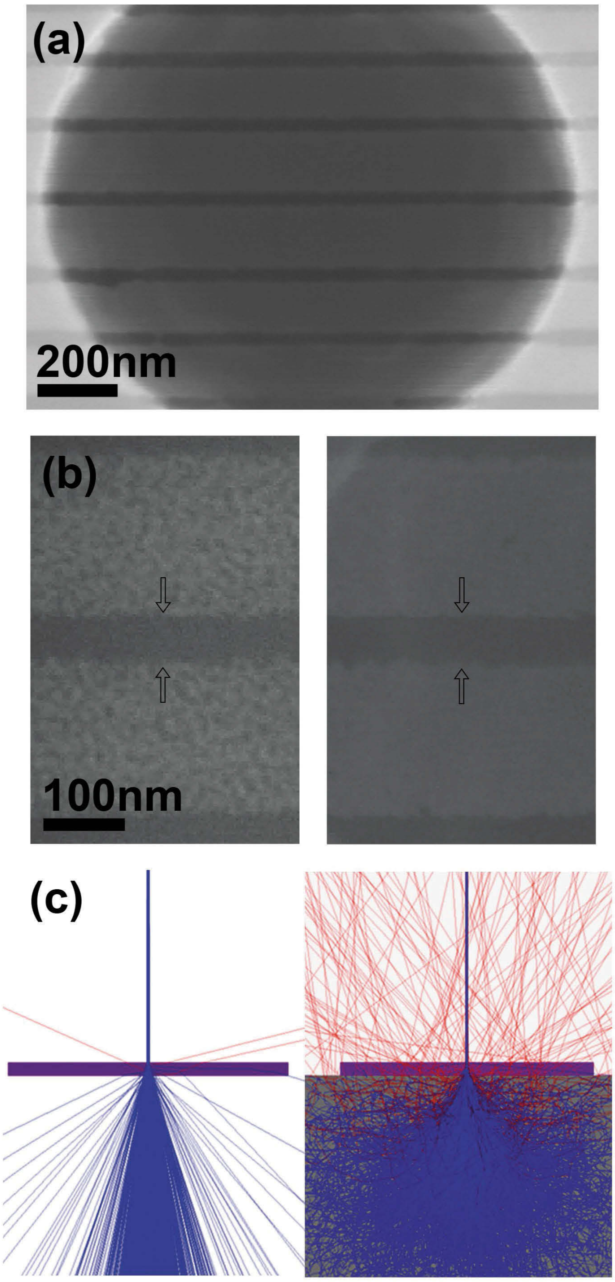

FIGURE 7.8: (a) A series of horizontal lines etched into a hBN flake suspended over a 1.3 micron hole in a Si membrane with a 90 nm thermal oxide layer. (b) Close-up image of similar lines (indicated by arrows) showing the presence (left) and absence (right) of surface roughness in hBN residing on top of a bulk substrate and over a hole, respectively. (c) Electron trajectories in a suspended 100 nm multilayer of hBN, and in the same hBN residing on top of a bulk Si substrate. Red lines represent electrons that backscatter out of hBN. The roughness seen in (b) is attributed to backscattered electrons.

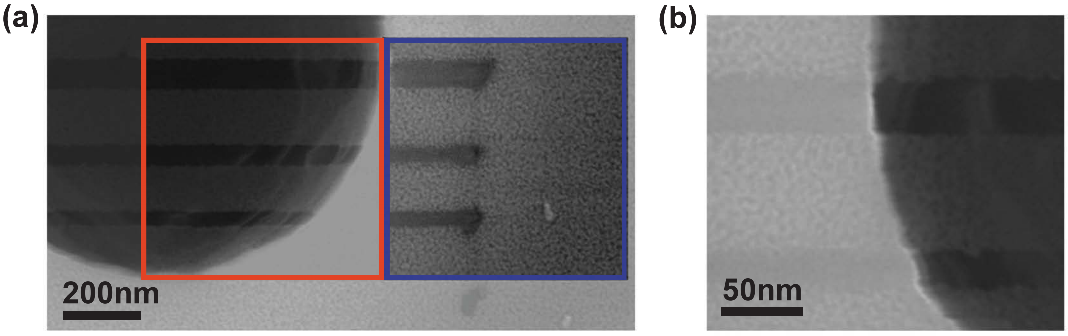

FIGURE 7.9: (a) SEM image of a series of horizontal lines etched into a hBN flake suspended over a 1.3 micron hole in a Si membrane. The hBN lines indicated within the blue box have been contrast enhanced to emphasize the increased surface roughening compared to the suspended lines within the red marked region. (b) Magnified SEM image at the interface of the Silicon and hole of the silicon membrane showing a gradient of reduced roughening as the hBN flake extends over the hole.

Two examples of how to effectively eliminate the interaction volume are shown in figure 7.10a,b. In both instances the bulk substrate is removed either through the use of a membrane or suspension. The use of a membrane as shown 7.10a allows for conventional etching to be performed as the hBN flake sits a top of a 50nm SiN membrane. At high accelerating voltages (20-30 keV), minimal electron backscatter occurs allowing for high resolution patterning, an example of a 500nm nanoribbon array is displayed in figure 7.10c. This is compared to suspended hBN on a holey Si substrate as highlighted in 7.10b. Using this method allows for a range of uses that are not suitable in the conventional form, a couple of examples include creation of photonic crystals to utlise the contrasting refractive index or creating of micro-mechanical resonators as shown in 7.10d.

While performing EBIE on a suspended hBN flake, an interesting response was exhibited in the form of twisting. The suspended hBN under electron beam irradiation and in a 8 Pa H_2O environment would experience folding in a direction opposite where it had been severed from the remaining flake, an example of this process is shown in figure 7.11. The hBN flake was shaped into a cross, then the left, top and bottom ends were severed from the remaining flake, with the right edge kept intact.

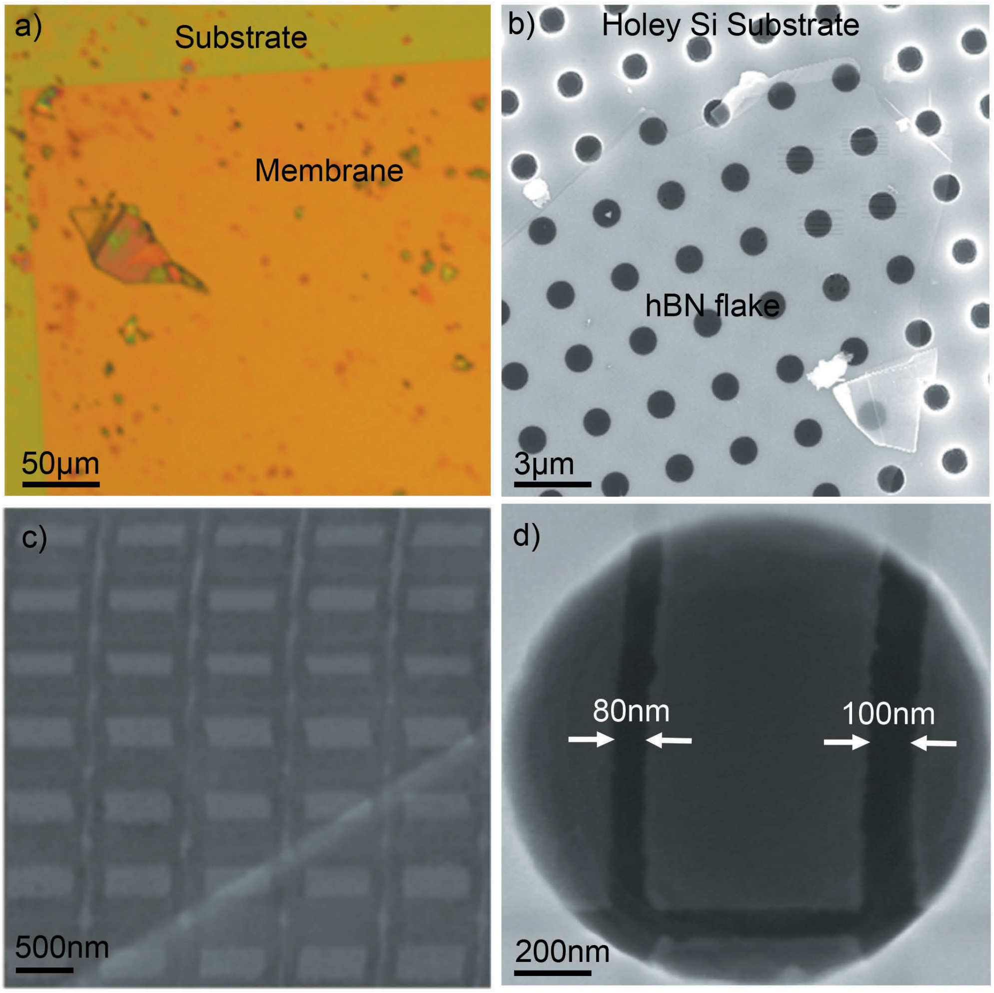

FIGURE 7.10: (a) Optical image of large hBN flakes mechanically exfoliated on a 50nm thick SiN membrane. (b) SEM of large hBN flake exfoliated on a 1μm holey Si substrate. (c) SEM image of an array of 500nm nanoribbons etched atop SiN membrane. (d) SEM image of a micro-mechanical resonator etched into a suspended hBN. A 25 keV beam and 0.5 nA, highly focused Gaussian beam was used during e-beam irradiations.

Then under continuous full frame e-beam irradiation the engineered cross would fold in on itself in the direction of the right edge. Interestingly under localised irradiation the folding of hBN was quite limited. Another engineered cross was created in H_2O and then the process was tested in a high vacuum environment. No notable changes would occur to the engineered cross under e-beam irradiation for 30 mins in high vacuum. This would indicate the folding occurring due to the chemical reaction taking place under e-beam irradiation in the presence of H_2O. The most likely explanation would be due to the rapid denitrogenation of the hBN material causing restructuring of the hBN lattice. The etch mechanism and chemical reaction pathways are further described in section 7.4.1 and 8.4.1 respectively.

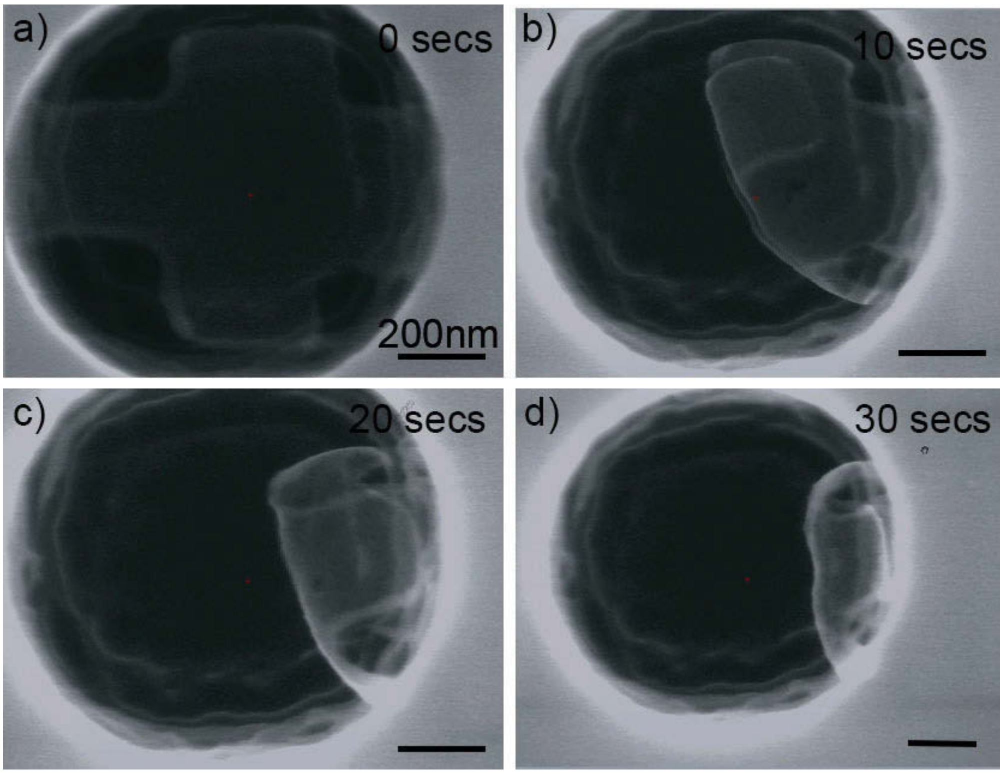

FIGURE 7.11: (a - d) Showcase a series of SEM screenshots of a suspended hBN flake taken at the onset of folding over time.

This result can be likened to an origami like procedure, where proper shaping using e-beam patterning initially can result in the creation of a variety of complex structures. An example of how this can be utilised is shown in figure 7.12. On the left a series of suspended nanoribbons are created with localised horizontal etches and no evidence of folding. This is compared to a single nanoribbon in figure 7.12b which underwent an additional full raster e-beam irradiation resulting in folding of the outer edges of the nanoribbon towards the centre, potentially creating a nanotube bridge structure. It is important to note that this procedure only works on suspended flakes as the adhesion energy for the hBN flake on Si is greater then the rotational force being applied during the chemical reaction process.

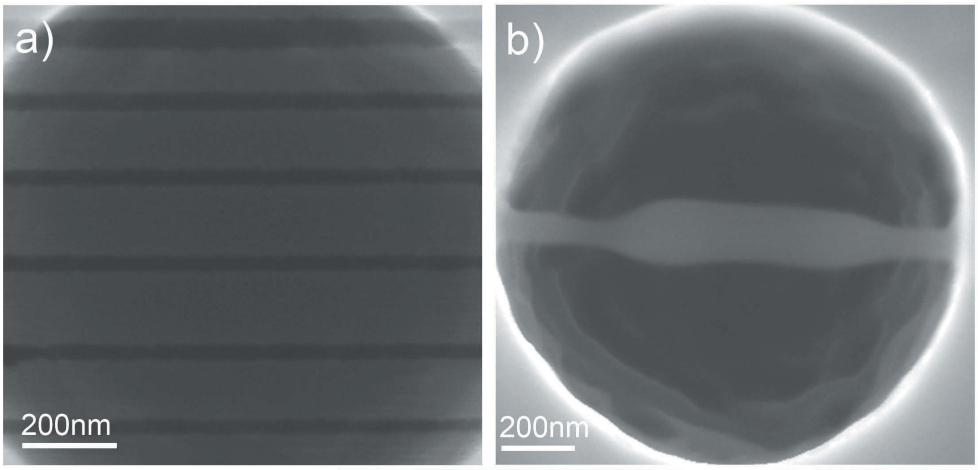

FIGURE 7.12: (a) Showcase a series of nanoribbons etched using e-beam horizontal line scans. A single nanotube bridge structure is highlighted in (b) which was created using e-beam horizontal line scans and additional full frame e-beam irradiation.

7.4.1 hBN etch process

Having demonstrated the ability to etch hBN, the etch process will now be characterised to gain an understanding of the mechanism. Etch rate dependencies on temperature [232] and time [238] have previously provided key insights into the underlying mechanisms. Hence, Fig. 7.13 shows plots of etch pit depth versus (a) time and (b) temperature (up to 325°C), revealing that the etch rate is independent of both parameters. The fact that the etch rate does not increase with time indicates that the electron beam does not create chemically active defects below the top monolayer [238] of hBN. The independence on temperature implies that the H_2O precursor molecules dissociate spontaneously, generating chemisorbed species (such as H, O and OH) that bond to the surface and can contribute to etching, irrespective of the substrate temperature [232] (up to a temperature of at least 325°C). The dissociation likely takes place at defects or edges of hBN sheets. Preferential chemisorption at defects may explain the fragmentation of hBN flakes (seen in Fig. 7.3a) that precedes the complete removal of hBN by EBIE.

Evidence for the molecular species of the nitrogen and boron-containing reaction products that desorb from the substrate during etching are discussed further in chapter 8. These molecules are extremely difficult to detect due to the low absolute reaction

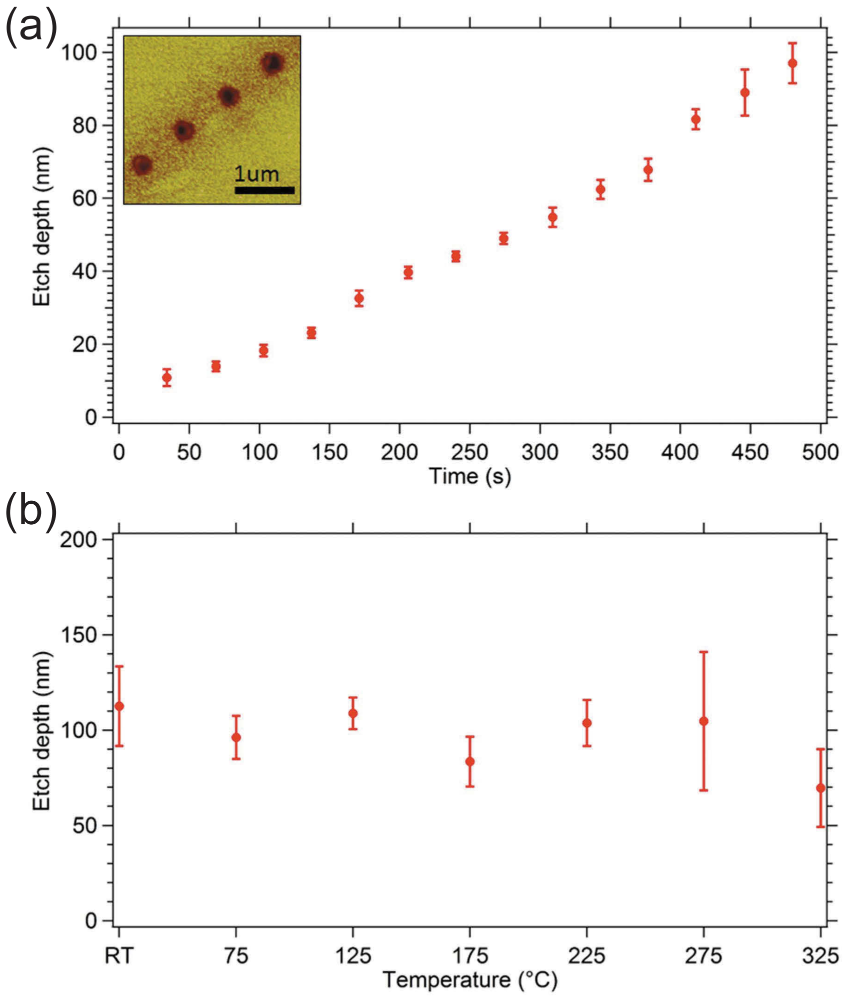

FIGURE 7.13: (a) Etch pit depth plotted as a function of etch time at room temperature. The inset is an AFM image of some of the etch pits used to make the plot. (b) Etch pit depth of hBN versus temperature. The electron beam dwell time was 10 minutes at each temperature.

product generation rates of EBIE. However, it is noted that the formation of volatile nitrogen-containing molecules is not surprising, as there exist numerous potential candidates such as N_2, N_2O and NO_2. Potential pathways for volatilization of boron are less obvious and may involve the production of borane (BH_3) or boric acid (H_3BO_3).

It is noted that the temperature-independence of the etch rate seen in Fig. 7.13b implies that the critical role of electrons in the etch process is not to dissociate physisorbed precursor molecules (i.e. H_2O), as this would result in a rapid, exponential decrease in etch rate with increasing temperature. Instead, a likely key role of the electrons is stimulated desorption of the final reaction products, as has been argued recently for the case of H_2O EBIE of single crystal diamond [232].

7.5 Conclusion

In conclusion, a novel H_2O-mediated electron beam induced etching process is demonstrated which enables high resolution patterning of hBN with nanoscale resolution. The etch process likely proceeds through spontaneous dissociative chemisorption of H_2O at defects and at the edges of hBN sheets, fragmentation of hBN into nanoscale hBN fragments, and volatilization of the nitrogen and boron constituents. The etch rate is found to be temperature independent, indicating the role of the electrons is to remove the final reaction products rather than dissociate the H_2O precursor molecules. These results will advance the understanding of hBN chemical stability and accelerate its use in practical optoelectronic and photonic devices.

7.6 Chapter contributions

Chris Elbadawi, Charlene Lobo and Milos Toth planned the experiments. Chris Elbadawi performed the AFM, EBIE and Raman experiments. John Scott performed TEM experiment and figure and Miroslav Kolibal performed Auger electron spectroscopy. Chris Elbadawi performed the Monte carlo simulations. Chris Elbadawi designed all figures (excluding figure 7.5). Chris Elbadawi wrote the chapter. Charlene Lobo and Milos Toth edited the chapter.

Chapter 8

Substrate assisted bottom-up etching using EBIE

8.1 Abstract

Electron beam induced etching is a promising nanofabrication procedure capable of high resolution etching of materials using economically viable and abundant precursors. The mechanisms involved using this technique are quite intricate and understanding of these mechanisms are desired. EBIE typically involves etching a mono-elemental material, however in this work, EBIE of a two element crystalline system, hexagonal Boron Nitride is performed and the electron-substrate interaction mechanism are studied. The volatile product formed which is thought to be nitric acid is a result of the e-beam induced reaction of the etch precursor, H_2O and the substrate hBN. The localised formation of nitric acid is then utilized to etch other materials simultaneously. This is the first reported instance of a multiple step EBIE process and includes the novelty of directional etching.

8.2 Introduction

Nanofabrication is an integral part of material processing for device manufacturing. However, these techniques which include top down etching/deposition or bottom up deposition have limitations in their approach. They require strict multiple alignment steps and masking which cannot influence obscured layers. This has driven demand for new forms of nanofabrication such as focused electron beam induced processing. This technique has allowed for manipulation of materials with fantastic precision and fidelity at very high resolutions and has drawn considerable appeal in terms of the novel capabilities offered, these include; 3D nanoprinting [28, 29], pattern formation [40], surface functionalization [43] and the ability to deposit and etch a wide variety of materials in a one-step maskless process [35, 82, 94].

Here a new and unique way of chemically dry etching multiple materials simultaneously is introduced. This process is deterministic and is achieved through a multiple step reaction process by simply using electron beam induced processing and a single precursor, H_2O as the initial etchant gas. This is made possible by etching the substrate and using the subsequent volatile by-product which are produced locally to act as a reactive etchant for a material atop of the substrate. This unique approach to etching is the first reported instance and is shown as a schematic in figure 8.1. The particular system used in this work involves the use of electron beam induced etching (EBIE) of hBN which has been outlined in Chapter 7 and a previous study [94]. As a consequence of EBIE of hBN, the volatile by-products formed during EBIE then allows the simultaneous etching of silver nanowires (Ag NWs) which have been dropcast directly on the hBN.

Etching of hBN and Ag are typically done via chemical wet etching [241–244], or by reactive ion etching (RIE) [227, 245–248]. The chemicals involved are typically harsh with the addition of lengthy masking procedures. Focused ion beam milling has also been used for patterning of hBN, [227, 231, 249], which results in ion implantation and inherent damage to the crystalline material. The EBIE process is damage free [94] and uses only the precursor H_2O, which is abundant, economical and environmentally friendly. This system has then been extensively studied in order to explain and gain a greater understanding into the chemical reaction pathways which in turn presents a wide range of possibilities to manipulate the etching of multiple materials simultaneously and selectively as well as allowing for unique nanofabrication features, such

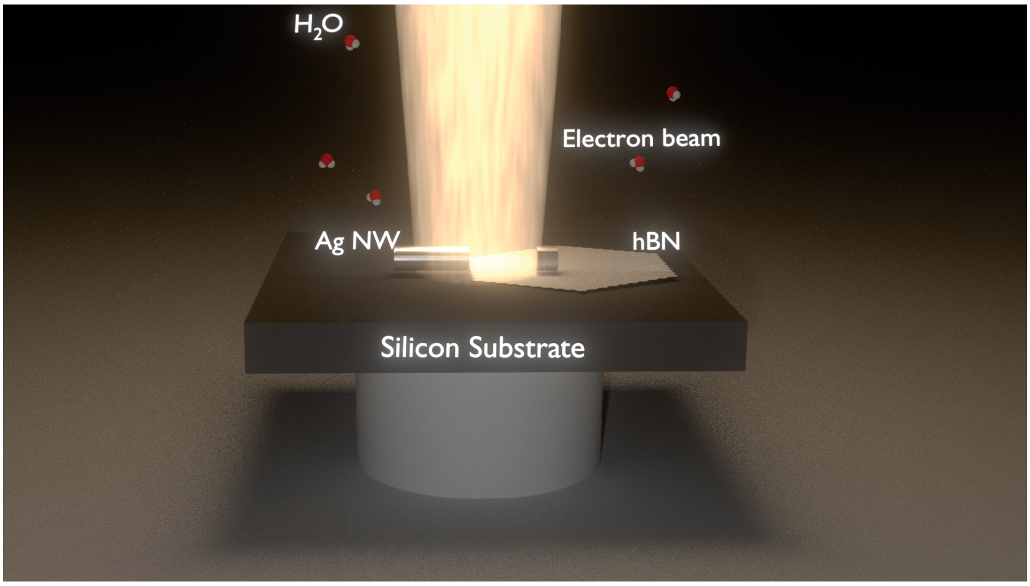

FIGURE 8.1: The electron beam induced etching system for hBN is illustrated in this figure and also highlights the localised etching of Ag directly under the etched hBN.

as undercutting of materials which give advantageous applications for use in lasing [152, 250, 251], photonic crystals [252, 253] and plasmonics [211].

8.3 Methods and materials

The substrates used in this study include hBN, Aluminum Nitride (AlN) and Gallium Nitride (GaN). Bulk hBN was obtained by Taniguchi et al. which were grown by a high temperature, high pressure process [217] and then mechanically exfoliated onto a Si(111) sample, while a 0.5mm thick AlN substrate was purchased from MTI corporation and used. The GaN substrates were grown by Berhane et al. using Metal-Organic Chemical Vapour Deposition (MOCVD) technique [254]. The substrates were ultrasonicated with acetone and IPA, ethanol and dried under flowing N_2.

As-synthesized Single crystal Ag nanowires [255] were prepared with ascorbic acid (AA) and deionized water. The Ag nanowire solution was then diluted to a ratio of 50:1, using 99.99 % IPA drop cast onto a Si(111) substrate covered with a native oxide layer for all experiments involving Ag nanowires. The samples were then loaded in a variable pressure FEI Nova NanoSEM field emission gun scanning electron microscope. The system was pumped down to a base pressure of 3×10^{-4} Pa. This solution was then dropcast onto the prepared substrates of hBN, AlN and GaN. The substrates were then loaded into a FEI Nova NanoSEM field emission gun scanning electron microscope and pumped to high vacuum ($3{\times}10^{-4}$ Pa). The chamber was then filled with water vapor to a pressure of 8Pa and the Ag nanowires on hBN/AlN/GaN were located using a gas cascade magnetic field assisted helix detector. Electron beam irradiation was performed using a focused Gaussian electron beam profile using a raster pattern and the irradiation process was recorded in real time. All EBIE was performed using a 15 keV beam and 4 nA beam current and electron flux of $1.34 \times 10^{20} e^{-} cm^{-2} s^{-1}$, unless otherwise stated.

8.4 Results and discussion

Complex high resolution patterning has been realized using EBIE of hBN in the presence of H_2O as previously reported [94]. Expanding on the previous work, it is shown that as a result of the dry chemical etching of hBN, the etching of Ag NWs is enabled locally under electron beam irradiation as shown in figure 8.2a. To understand the process of etching the nanowires the role of the substrate, H_2O and electron beam in this system must be investigated further. The etching of the Ag nanowires only occurs when the nanowires are lying over hBN flakes in the presence of H_2O and under electron beam induced etching of hBN. If these parameters are not met the precise etching of the Ag nanowires will not take place as shown in figure 8.2b,c, where the hBN and H_2O were removed from the system respectively. Do note, roughening of the Ag nanowires can still be seen in vacuum, this is due to the presence of residual H_2O in the SEM chamber which gives rise to a very slow etch rates of the hBN and the Ag nanowires [239]. This result indicates during the EBIE of hBN, a reactive etchant

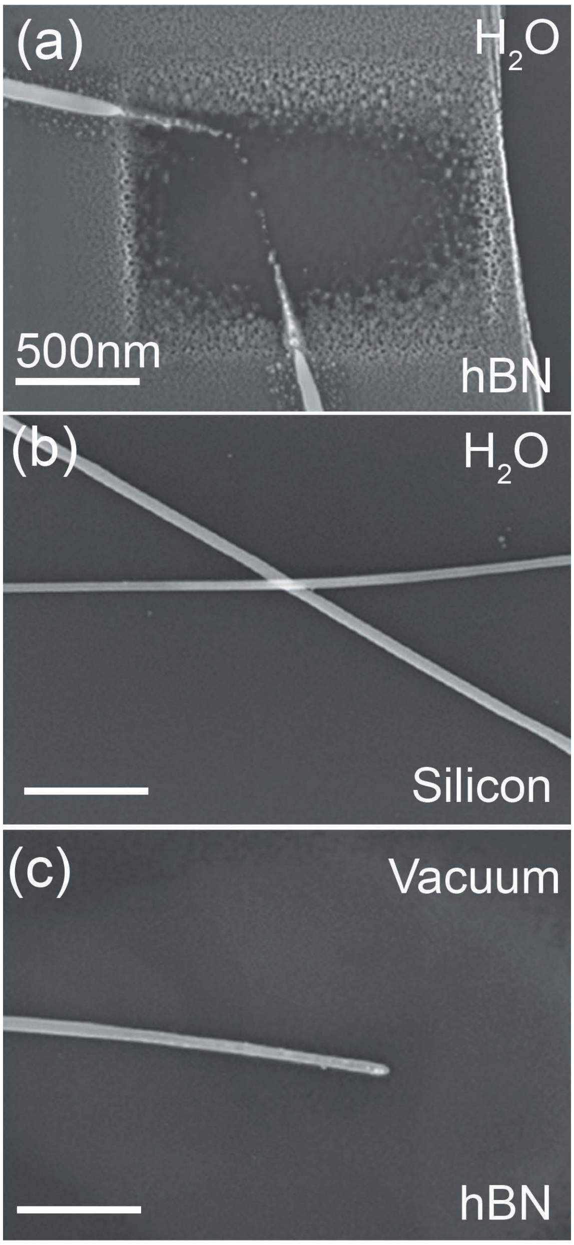

FIGURE 8.2: SEM images of Ag nanowires in various environmental conditions. a) Ag NW on hBN in the presence of H_2O. b) Ag NWs on Si in the presence of H_2O. c) Ag NWs on hBN in high vacuum. All irradiations were performed for 1 hour using 15keV and an electron flux of 1.34×10^{20}.

of silver is formed which then chemically dry etches the Ag NWs locally.

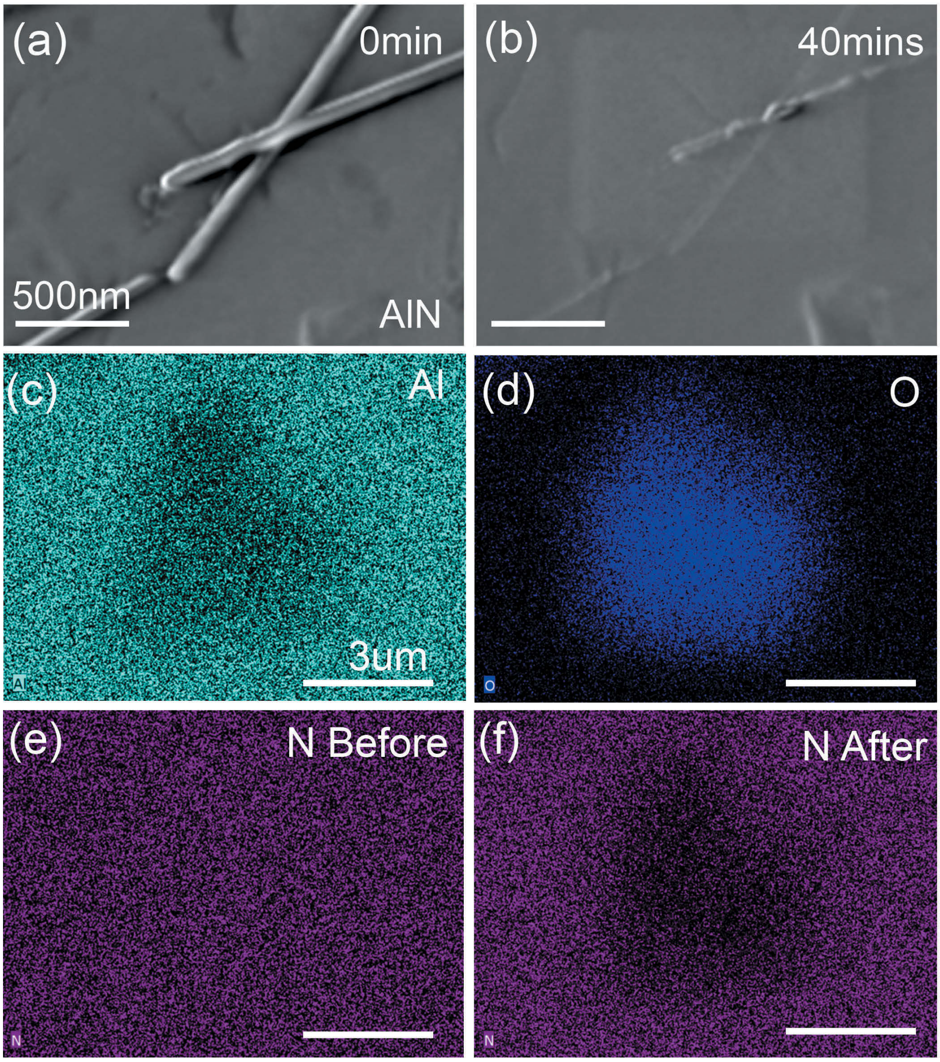

FIGURE 8.3: SEM images (a) before and (b) after an electron beam exposure of Ag nanowires on AlN in a H_2O environment. Electron irradiation was performed for 40 mins at 15 keV and 4 nA. A 2 hour e-beam exposure was then performed on a seperate region on the AlN substrate in a 16 Pa H_2O environment at 15 kV and 6 nA. EDS mapping on the AlN irradiated region was performed in high vacuum in (c - d) highlighting the change in Al and O content. EDS mapping of N was also performed highlighting the change in N concentration before and after the 2 hour e-beam exposure (e - f). EDS mapping was performed at 3.5 keV and 1 nA.

Next, electron beam irradiation was performed on AlN and GaN substrates in a H_2O environment. This was to confirm the necessity of nitrogen in the two step etching process described and introduce the ability to use other substrates containing nitrogen to etch Ag. Figure 8.3a and b show before and after a 40 minute e-beam irradiation of Ag nanowires on a AlN substrate. Very similar results to hBN are seen in terms of etching of Ag nanowires under electron beam irradiation. However, unlike hBN, the AlN substrate is not etched effectively in this process as shown in 8.3c and d. EDS analysis showed reduction of N content in the electron beam irradiated region and an increase in O content, indicating denitrogenation and oxidation of the AlN substrate as shown in fig 8.3e and f. The removal of nitrogen is then likely to follow similar reaction pathways as seen with hBN (see figure 8.2a), resulting in the etch of Ag nanowires. These results show an innovative and robust way to use multiple substrates to act as an etchant through creation of reactive species locally under e-beam irradiation.

However, not all nitrogen containing substrates will result in this two step etching process as denitrogenation is needed, an example of this is shown in figure 8.4. Before and after electron irradiation of a GaN substrate in a H_2O environment is highlighted in 8.4a and b, negligible etching of the Ag nanowires is seen. EDS mapping analysis performed (Shown in fig 8.4c-e) does not show any variance of the nitrogen and gallium content in the e-beam irradiated region on the GaN substrate. This is most likely due to the rapid creation of a passivating oxide layer on GaN. This can be seen with a higher oxygen content present in the e-beam irradiated region in fig 8.4f. As gallium oxide typically shows high stability [256], the oxide passivation layer most likely acts to prohibits denitrogenation of the GaN material under e-beam irradiation in a H_2O environment. A table of Ag NW etching compatibility from experiments performed thus far is shown in table 8.1.

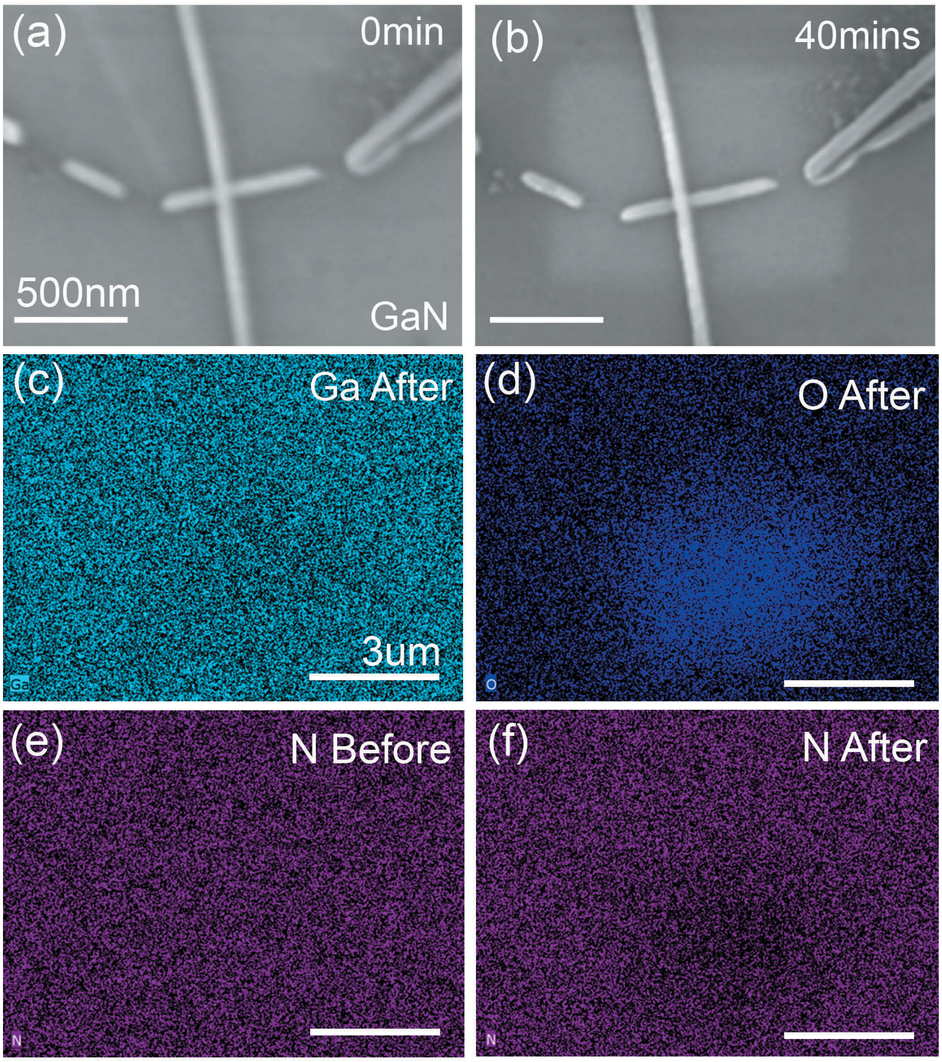

FIGURE 8.4: SEM images (a) before and (b) after an electron beam exposure of Ag nanowires on GaN in a H_2O environment. Electron irradiation was performed for 40 mins at 15 keV and 4 nA. Similarly, EDS mapping was then performed in high vacuum on a separately irradiated region in (c - d) showing the changes of Ga and O concentration respectively. The e-beam exposed region was irradiated for 2 hour e-beam in a 16 Pa H_2O environment at 15 kV and 6 nA. EDS mapping was also performed before and after e-beam exposure highlighting changes in N concentration in (e - f). EDS mapping was performed at 3.5 keV and 1 nA.

8.4.1 Chemical reaction pathway

In the previous study, EBIE of hBN found in Chapter 7 [94] it is shown that the precursor H_2O decomposes spontaneously on highly active edge and defect sites in the hBN caused by e-beam irradiation to form radicals such as OH, O and H. Then, under

TABLE 8.1: Ag nanowire etching compatibility

Substrate	Environment	Ag NW etching	N radicals present
hBN	H_2O	Yes	Yes
hBN	Vacuum	No	No
AlN	H_2O	Yes	Yes
Si	H_2O	No	No
GaN	H_2O	No	No
Si (See appendix E)	N_2 + H_2O plasma	Yes	Yes
hBN	O_2	No	No

continual e-beam irradiation the complete volatilisation of the hBN occurs. Focusing on the potential products that could be formed with hBN and H_2O and also etch silver can then be narrowed down to the volatilization of nitrogen and nitrogen containing species such as NO or NO_2 which readily react with H_2O to form nitric acid (HNO_3) [243]. Nitric acid is known to etch Ag and also readily reacts with boron to form boric acid which can be used to explain the complete volatilisation locally of hBN and Ag nanowires [243].

As illustrated in figure 8.5, the reaction mechanism likely involves the following reaction pathways. In previous studies [257, 258] electrons have been accelerated in humid air mixtures. H_2O upon impact with the electron beam give neutral OH radical production pathways mainly through electron attachment or electron impact, as shown respectively below:

$$e^- + H_2O \longrightarrow H^- + OH$$

$$e^- + H_2O \longrightarrow e^- + H + OH$$

Given the low vacuum water vapour conditions performed in these experiments, e-beam localised creation of OH will most likely occur as adsorbates on edge and defect sites of hBN [94, 259]. Under continuous electron beam irradiation of a N containing substrate it is shown that denitrogenation occurs (see figure 8.3). This nitrogen can then react with neutral OH to form nitric oxide (NO) as shown in previous low vacuum studies [260] and is outline below:

$$OH + N^{+} \longrightarrow NO + H^{+}$$

As an abundance of H^{+} from the previously discussed reactions would be present in the vapour phase [261], hydroperoxyl (HO_2) and OH radicals may form through the transfer of a hydrogen atom to H_2O vapour as occurs in the upper atmosphere [261, 262] and is shown below:

$$OH + OH \longrightarrow HO_2 + H$$

Again similar to processes in the upper stratosphere [263–265], nitric oxide can react with hydroperoxyl radicals and form nitric acid, as outline below:

$$NO + HO_2 \longrightarrow NO_2 + OH$$
$$NO_2 + OH \longrightarrow HNO_3$$

These reactions would likely occur as adsorbates where a higher local partial pressure of these radicals would be present under the electron beam. Now, with the localised creation of nitric acid it is believed nitric acid reacts with the Ag NWs and also boron to allow the etching of Ag NWs and boron to occur in the form of $AgNO_3$ and H_3BO_3 as shown in figure 8.5. Further evidence of this volitilsation under e-beam irradiation will be shown in the next section.

8.4.2 Etching via electron stimulated volatile solute $AgNO_3$

As it is suggested that nitric acid etches the Ag NWs in the form of $AgNO_3$, we now study the e-beam irradiation of $AgNO_3$ in a H_2O environment using the same experimental conditions as described in section 8.3. $AgNO_3$ was dropcast and crystallized on a Si(111) substrate and exposed to electron beam irradiation in a H_2O environment (8 Pa) and vacuum. After a 20 minute irradiation, $AgNO_3$ material is removed in the presence of H_2O only, as shown in figure 8.6. It is proposed that an electron stimulated volatile solute of $AgNO_3$ is formed in a H_2O environment. The exact nature of volatilising $AgNO_3$ in these conditions is unknown, one possibility may be $AgNO_3$ becomes soluble to adsorbed H_2O and due to the positively charged nature of the substrate that is experienced in ESEM conditions, a Ag^+ would be repelled from the positively charged substrate. However, this is a highly speculative mechanism and will be difficult to confirm due to the low product generation rates found during EBIE processes. EDS mapping analysis was performed on this exposed region as shown in figure 8.6 b-e, confirming the removal of Ag, N and O species. However, etching of $AgNO_3$ in the rastered regions is sometimes incomplete. EDS analysis shows a N to O ratio of 1:2 suggesting a silver nitrite ($AgNO_2$) may also be formed which is much less water soluble, or simply a greater oxygen level seen is due to a competing process of oxide formation on Ag.

The etching of Ag and boron is then thought to take place under e-beam exposed regions through the following reaction pathway as illustrated in figure 8.5. The reaction and complete volatilization of the Ag nanowires and hBN under an electron beam is therefore proposed to take place through the creation of electron stimulated volatile solutes in the form of $AgNO_3$ and H_3BO_3 due to localised $4\,HNO_3$ formation under the e-beam in a H_2O environment. Further experimentation and evidence was performed to confirm the necessity of these radicals. This was done by introducing

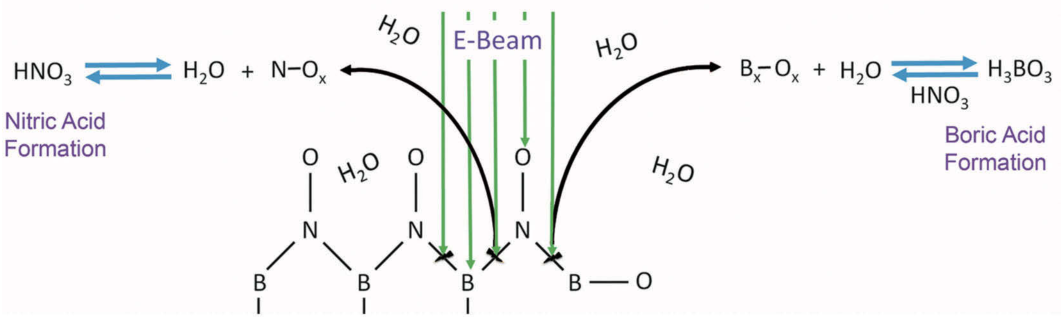

FIGURE 8.5: The proposed chemical reaction pathway and complete volatilisation of hBN is shown via a schematic during electron beam induced etching in a H_2O environment.

a N_2 and H_2O delocalised plasma during electron beam exposures. The results also show localised etching of Ag NWs and is shown in appendix E.

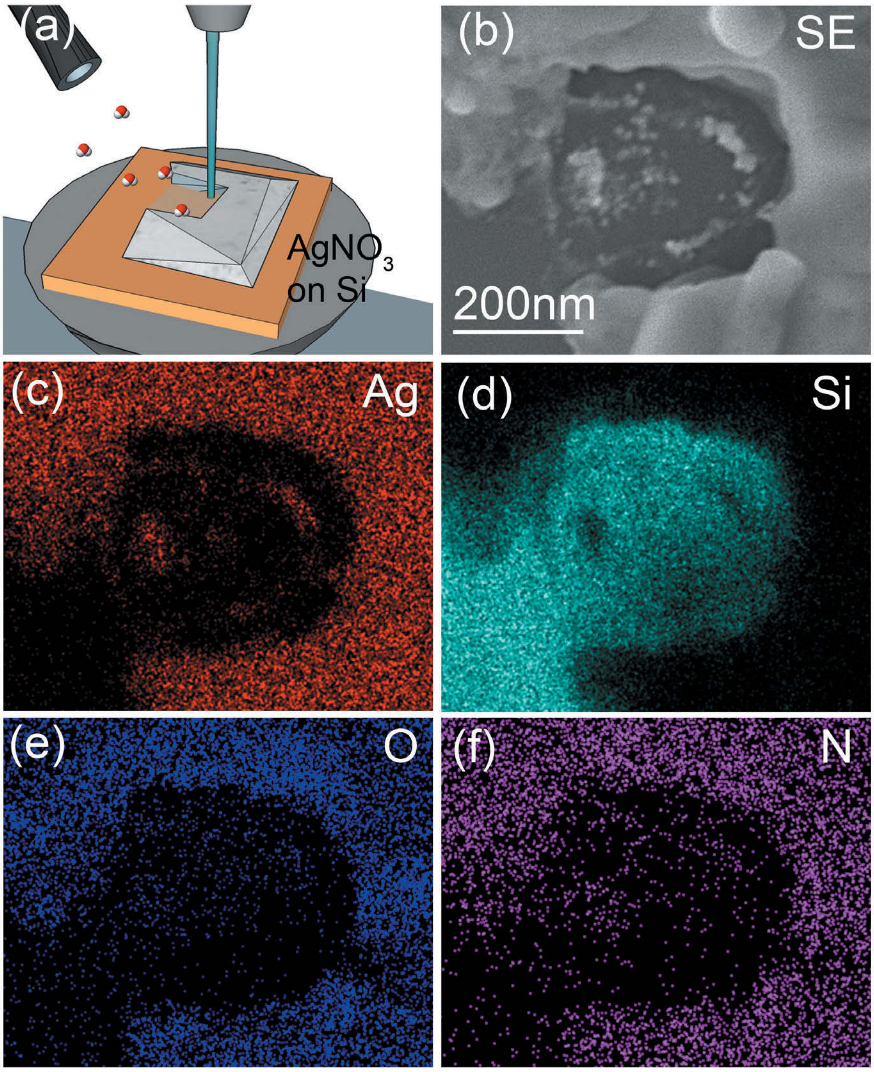

FIGURE 8.6: A graphic is used in (a) to portray the electron beam induced etching of $AgNO_3$ dropcast and crystallise on a Si substrate in a H_2O environment (8 Pa). An SEM image (b) of the etched region after a 60 min exposure, and (c - f) show the compositional mapping of the etched region for Ag, Si, O and N respectively. Electron beam irradiation was performed at 15 keV and 0.47 nA and EDS mapping performed at 5 keV.

8.4.3 Directional etching

As this process has shown to be localised, the creation of the etchant product must take place in the area under electron irradiation. This localisation is shown in figure 8.2a. As the SEM chamber is held under low vacuum conditions and the etchant product is formed from reactants supplied by the substrate, there will be a decrease in partial pressure of reactive products as the distance from the substrate surface increases. This has shown to cause directional etching of Ag nanoparticles atop of the hBN substrate as shown schematically in figure 8.7a and on a Ag nanowire in figure 8.7e. The degree of under-etching is dictated by the dwell time of the electron beam in H_2O and the thickness of the hBN. This is shown in Figure 8.7c, where a nanoparticle which has been irradiated for 30 minutes has a lower degree of under-etching compared with figure 8.7d which was irradiated for 60 minutes using an electron flux of $1.34 \times 10^{20} e^{-} cm^{-2} s^{-1}$ for both irradiations respectively. This can be compared with a typical pristine nanoparticle which has not undergone electron beam irradiation and shows no signs of under-etching (figure 8.7b). This is a distinct novelty of this etching technique and given the right combination of precursor and substrate to be etched, enables the ability to under-etch any material in a controllable fashion for potential use for plasmonics, lasing and photonic crystal cavities.

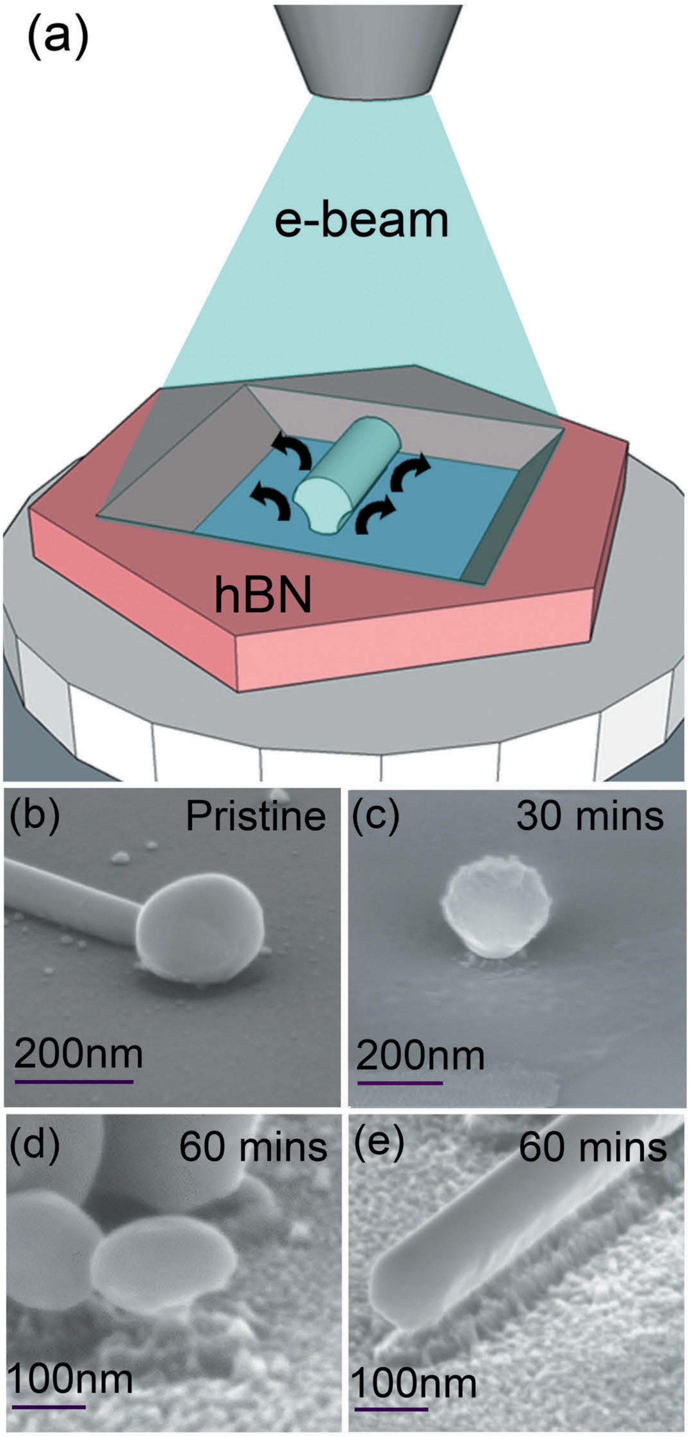

FIGURE 8.7: A schematic is shown in (a) of the directionality of the etchant products created via the electron beam induced etching of hBN which results in undercutting of Ag nanowires and particles. A SEM image of a typical pristine Ag nanoparticle (b) and varying degrees of undercutting after 30mins (b) and 60mins (c) of electron irradiation in H_2O environment. Undercutting is also shown for a Ag nanowire after 60 mins of electron irradiation in a H_2O environment. Irradiations were performed at 15 kV and $1.34 \times 10^{20} e^{-} cm^{-2} s^{-1}$ electron flux

8.5 Conclusion

In this work, a novel and unique two step etching technique was highlighted, unlocking fascinating chemistry on the nanoscale and enabling opportunities of etching a new range of resilient materials simultaneously such as hBN and silver, which were not possible before. This is achieved via the use of an abundant and economical precursor, H_2O, in an environmental scanning electron microscope. It was also shown that this technique has the added advantage of etching directionality allowing for very difficult etches such as undercutting of materials to be performed.

8.6 Chapter contributions

Chris Elbadawi conceived the idea and planned the experiments. Chris Elbadawi performed the Electron beam irradiations and EDS analysis. Johannes Fröch assisted with EDS on GaN and AlN and Kerem Bray designed the figure 8.1 schematic. Chris Elbadawi designed all other figures. Chris Elbadawi and Charlene Lobo wrote and edited the chapter.

Chapter 9

Conclusions

9.1 Summary

The work undertaken in this project has focused on achieving a deep understanding of the intricate mechanisms and relationships involved in FEBIP.

Controlling the electron beam dwell time, size and spacing allowed for the construction of complex freestanding structures and patterns. To gain these results, precise and consistent electron beam placement was achieved through the creation of a scanning program, which acts to control the scanning coils of the SEM. This then enabled accurate and reproducible data acquisition. The nanostructures in this work were fabricated by EBID and the chemical composition, specifically for the inorganic $Pt(PF_3)_4$ precursor, was analysed. The changes in growth and composition were systematically distinguished by varying parameters during EBID experimentation and significant inroads into understanding the electron beam and precursor interplay allowed for highly detailed fully 3D freestanding structures to be constructed reproducibly.

Extensive post processing on the EBID deposits created resulted in the formulation of a post processing technique that is capable of the complete removal of unwanted by-products and contaminants from EBID deposits created using the $Pt(PF_3)_4$ precursor leaving behind pure platinum deposits. The purification is attributed to an efficient H_2O decomposition pathway coupled with annealing at elevated temperatures that leads to volatilization of phosphorous contaminants into a meta-phosphoric acid state, leaving behind pure platinum deposits. This purification process has been refined to allow for minimal deformation or structural changes to the deposit which will be important for nanostructures created using EBID in terms of their capabilities and functionality given the right post processing conditions in terms of temperature, pressure and anneal time.

Next, focusing on gas-mediated EBIE, it was found possible to explain through experimentation, the fundamental processes that are involved in electron beam irradiation of the 2D materials; few-layer BP and hBN. This was performed by systematically varying parameters, such as accelerating voltage, electron current, temperature and gaseous environments. This allowed for further unraveling of the electron-precursor-solid relationship.

The work performed on few-layer BP resulted in a deep understanding of the degradation mechanism and provide insight into the nature of the chemical reaction pathways itself via exposure of FLBP flakes under electron beam irradiation in various controlled gaseous environments. Real time imaging showed accelerated degradation of few-layer BP under H_2O whilst being stable under the gases O_2 and NF_3. This narrowed down the degradation mechanism and allowed for introduction of preventative measures to stop this degradation. Temperature-dependent experiments was performed, and found to remove intercalated H_2O built up in the flakes. By removing the H_2O source, formation of phosphoric acid was prevented in ambient conditions and fully stabilised the few-layer BP. This technique can be used in cycles to repeatedly remove H_2O and pave the way for integration of few-layer BP into high-performance optoelectronic devices and gas sensors in ambient conditions.

The next results will be focusing on the 2D material hBN. First, defect generation in hBN was demonstrated by using low electron fluences in a H_2O environment. Through defect generation, engineering of room temperature multicolor single photon emitters was shown. These emitters were shown to be stable even after annealing in harsh gaseous environments such as oxygen, hydrogen and ammonia. Finally, it is shown that electron beam induced etching and an argon plasma can be used to fabricate the emitters deterministically on a particular flake. The photophysical properties of the emitters were studied and overall, the emitters are bright, fully polarizable and optically photostable. These results will advance the understanding of hBN chemical stability and accelerate its use in practical optoelectronic and photonic devices.

Following from the defect generation results the focus was shifted to form a novel method to etch hBN deterministically using H_2O-mediated electron beam induced etching was demonstrated. The etch process was shown to proceed through spontaneous dissociative chemisorption of H_2O at defects and at the edges of hBN sheets, fragmentation of hBN into nanoscale hBN fragments, and volatilization of the nitrogen and boron constituents. The etch rate is found to be temperature independent, indicating the role of the electrons is to remove the final reaction products rather than dissociate the H_2O precursor molecules. This is one of the first steps to selectively etch a range of two-dimensional materials and first reported instance of etching a multi-elemental material using EBIE.

As the EBIE of hBN involves a two element crystalline system (Boron and Nitrogen), understanding of the mechanism is taken a step further, as the roles of the electron beam, precursor and substrate are not as straightforward as most EBIE systems which typically involve etching a mono-elemental material. A novel and unique two step etching technique was highlighted, unlocking fascinating chemistry on the nanoscale. The mechanism is based on the formation of reactive products during EBIE of hBN which extends to etch other materials locally, and shown experimentally with Boron and Silver. This is the first reported instance of using a solid substrate as an etchant and as a result a multiple step EBIE process is realised, with the novelty of directional etching.

The intricate reaction mechanisms realised also paved the way for a new hybrid EBIE process know as plasma enhanced EBIE. This work has showcased an innovative way to drive new chemical reactions locally using electron beam induced etching and introduction of a delocalised plasma. Possible insights are made into the precursor-electron beam relationship with the combination of insitu radical generation of precursor molecules, and deterministic creation of highly active surface sites, expands the range of etchable materials using EBIE which were not possible before.

These results broaden the scope of material selection available in FEBIP and increase the applicability through exploitation of the novel aspects to enhanced the versatility of FEBIP as a prominent tool for nanofabrication of 2D materials.

9.2 Future Work

There is appeal for further broadening of the techniques successfully employed in this work for future research. Specific goals include:

9.2.1 Plasma and EBIE

The plasma enhanced EBIE technique is the first instance of using an in-situ plasma and e-beam irradiation concurrently, this is discussed in more detail in appendix E. This process has opened up a new range of chemical reactions that occurs at the electron beam/target material interface. A comprehensive set of experimentation will be done to find the best compromise between plasma power, pressure and beam current density. The next step would be to showcase a wider range of etch-able materials using this technique which fit the parameters of the system described. This technique can then be tailored to target new materials by mimicking established wet or dry etch techniques. Overall this will potentially improve the range of etch-able materials for EBIE.

Considering preliminary results gained from this work there are several possible experiments being contemplated to further enhance the investigations undertaken. As a byproduct of the in-situ delocalised plasma, a large amplification and enhancement in the imaging is seen under specific parameters. The mechanism of this amplification is yet to be uncovered and further experimentation will be needed to provide a clearer picture of the enhancement pathway.

9.2.2 Undercutting

Undercutting is used to create resonating disks to showcase plasmonic and photonic enhancement. Utilisiation of the undercutting ability via directional etching can provide a means to deterministically undercut materials such as silver for plasmonic coupling and enhancement and ZnO for photonic enhancement.

9.2.3 hBN and few-layer BP

Material restructuring/functionalization

Further controlled experimentation and analysis should be performed on the functionalization of hBN and BP. It is predicted that the bandgap and optical properties can be tuned with size and termination of hBN and few-layer BP. Preliminary results indicated material response and restructuring occurring under electron beam irradiation in NH_3 and NF_3 environments for hBN (see appendix D) and controllable EBIE of few-layered BP in a NH_3 environments.

Few-layer BP applications

Preliminary variable sensing capabilities was seen during in-situ electrical measurements on few-layer BP. The electrical response of few-layer BP at high temperatures in various gases was shown to vary with high sensitivity. Subtle shifts in conductance was also seen corresponding to slight changes in temperature.

hBN applications

hBN emitters formed in the infrared (IR) region can also propagate along hBN through phonon polaritons. As no emitters have been detected in the IR region thus far, further emitter creation and photoluminescence studies will need to take place in the IR. This IR emitter can then be coupled with the hBN directly which can be patterned deterministically using EBIE of hBN. Extending this idea further, integration of plasmonic EBID deposits directly on emitters created via defect creation can also allow for plasmonic enhancement or propagation along the plasmonic deposit formed.

Appendix A

Scanning program code

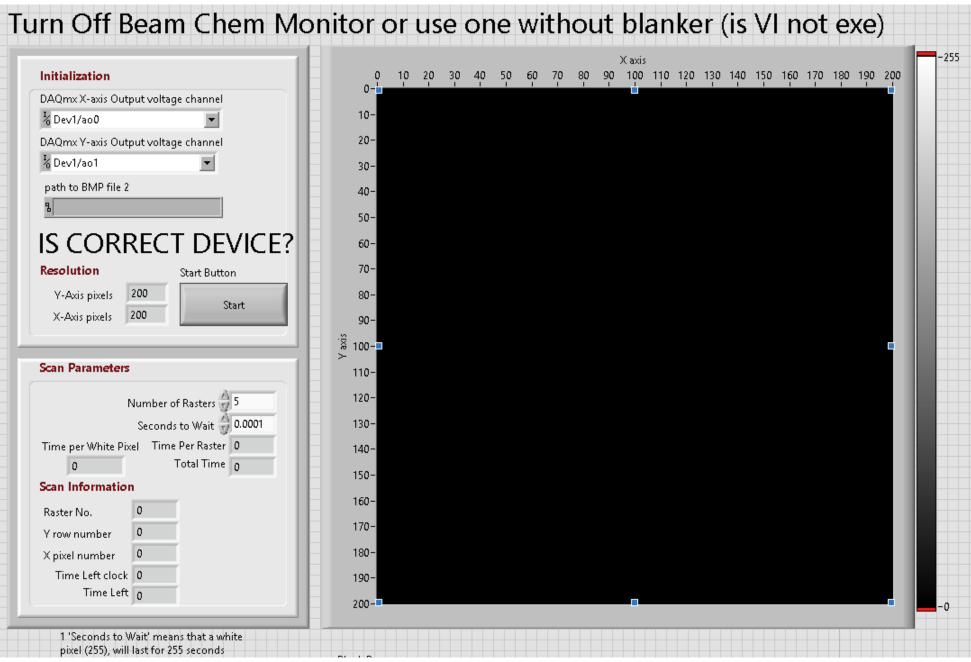

Turn Off Beam Chem Monitor or use one without blanker (is VI not exe)

Initialization

DAQmx X-axis Output voltage channel: Dev1/ao0

DAQmx Y-axis Output voltage channel: Dev1/ao1

path to BMP file 2

IS CORRECT DEVICE?

Resolution

Y-Axis pixels: 200

X-Axis pixels: 200

Scan Parameters

Number of Rasters: 5

Seconds to Wait: 0.0001

Time per White Pixel: 0

Time Per Raster: 0

Total Time: 0

Scan Information

Raster No.: 0

Y row number: 0

X pixel number: 0

Time Left clock: 0

Time Left: 0

1 'Seconds to Wait' means that a white pixel (255), will last for 255 seconds

FIGURE A.1: The front panel interface created in LabVIEW is illustrated for the scanning program created. Inputs files and variable parameters are controlled on the left hand side. Beam location and output pattern is displayed on the right hand side.

The front panel interface for scanning program is illustrated in figure A.1. On starting the program a prompt message will appear to select the image file of interest. The initialisation is found on the top left of the front panel and involves selection of the output analogue voltage channels for the x and y scan coils. Resolution will automatically be updated according to the image file chosen and scaled to maximise the scan coil range.

The image file output will be displayed on the right hand side graph, as well as the location of the electron beam. The scan parameters allow for variable adjustment of the dwell time of the electron beam and number of rasters for the pattern. Time per raster and total time will be displayed. The start button starts the scan and the scan information will be continuously updated, providing X, Y pixel numbers, raster number and time remaining.

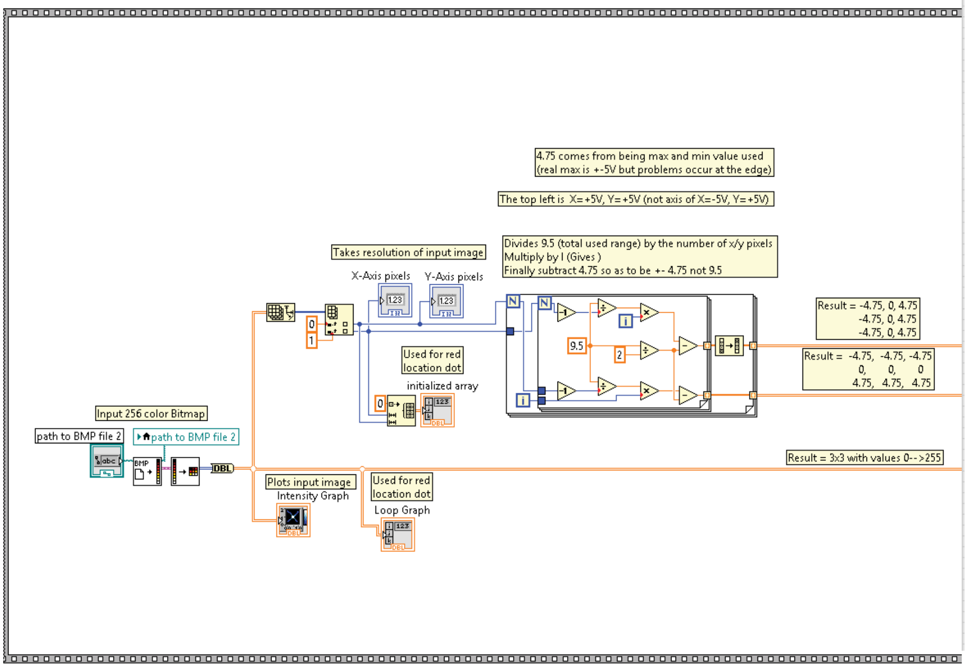

Input 256 color Bitmap

Takes resolution of input image

Used for red location dot

Plots input image

Used for red location dot

4.75 comes from being max and min value used
(real max is +-5V but problems occur at the edge)

The top left is X=+5V, Y=+5V (not axis of X=-5V, Y=+5V)

Divides 9.5 (total used range) by the number of x/y pixels
Multiply by I (Gives)
Finally subtract 4.75 so as to be +- 4.75 not 9.5

Result = -4.75, 0, 4.75
-4.75, 0, 4.75
-4.75, 0, 4.75

Result = -4.75, -4.75, -4.75
0, 0, 0
4.75, 4.75, 4.75

Result = 3x3 with values 0-->255

FIGURE A.2: Initialization and inputs back panel screenshot for the scanning program. From the left to right, the first step is to input the image file which flattened into a 2D array of values. The values are rescaled for the beam scanning coils in this back panel.

The back-panel for the initialisation and inputs for the scanning program is shown in figure A.2. From the left hand side, select the input image file which is flattened into a 2D array of values. The values are then plotted on an intensity graph to mimic the image. The values are then rescaled to conform to the scanning coil voltage range.

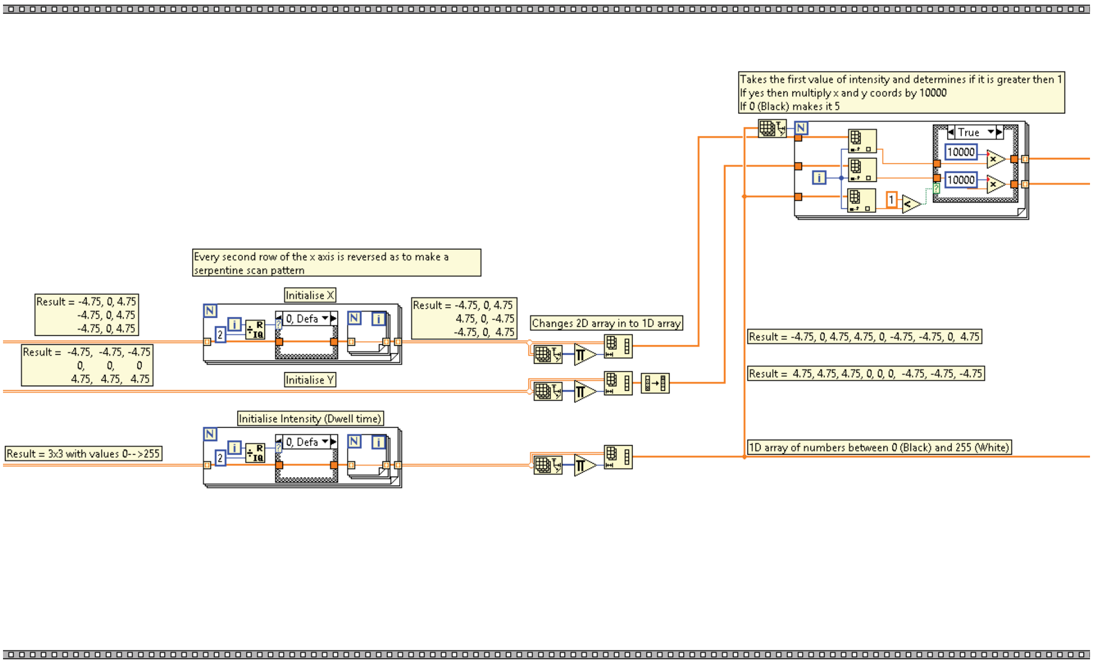

Takes the first value of intensity and determines if it is greater then 1
If yes then multiply x and y coords by 10000
If 0 (Black) makes it 5

Every second row of the x axis is reversed as to make a serpentine scan pattern

```
Result = -4.75, 0, 4.75
         -4.75, 0, 4.75
         -4.75, 0, 4.75

Result =  -4.75,  -4.75, -4.75
           0,      0,     0
           4.75,   4.75,  4.75

Result = -4.75, 0, 4.75
          4.75, 0, -4.75
         -4.75, 0,  4.75

Result = 3x3 with values 0-->255
```

Changes 2D array in to 1D array

```
Result = -4.75, 0, 4.75, 4.75, 0, -4.75, -4.75, 0,  4.75
Result =  4.75, 4.75, 4.75, 0, 0, 0,  -4.75, -4.75, -4.75
```

1D array of numbers between 0 (Black) and 255 (White)

FIGURE A.3: Data rearrangement of the array screenshot for scanning order. Each row of data is reversed for serpentine scanning and a 2D array is converted to a 1D array of data.

The next step involves reversing every 2nd row of the 2D array so the scanning coils pattern in an efficient manner following a serpentine path as shown in the back-panel screenshot, figure A.3. The 2D array is the converted into a one-dimensional (1D) array so single voltage values can be fed into the data acquisition device for the x and y axis individually.

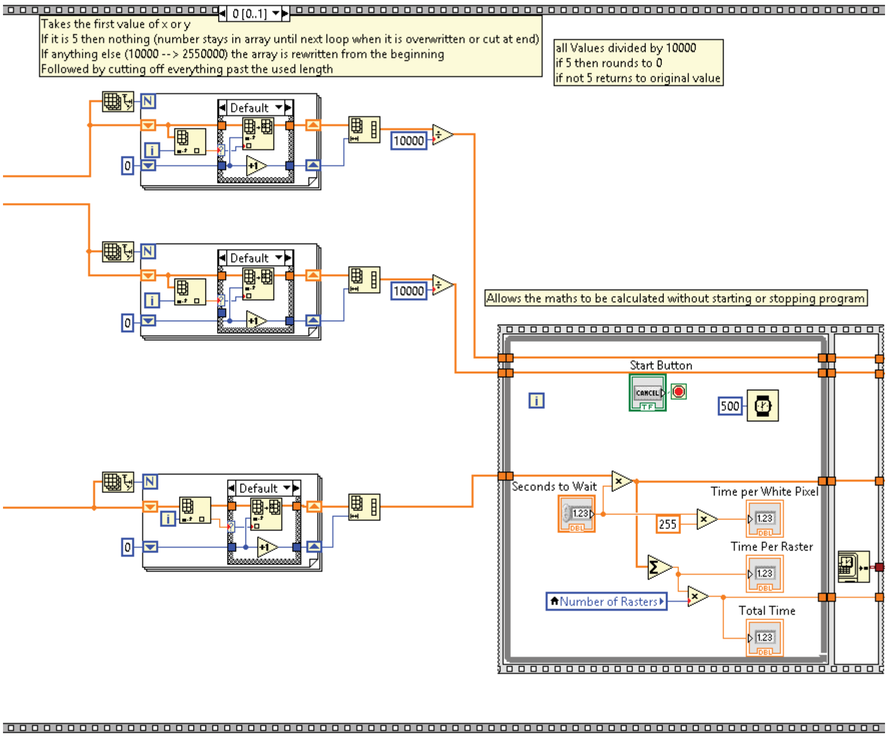
Takes the first value of x or y
If it is 5 then nothing (number stays in array until next loop when it is overwritten or cut at end)
If anything else (10000 --> 2550000) the array is rewritten from the beginning
Followed by cutting off everything past the used length

all Values divided by 10000
if 5 then rounds to 0
if not 5 returns to original value

Allows the maths to be calculated without starting or stopping program

FIGURE A.4: Back panel data removal and multiplication of screenshot. Each pixel value is multiplied through a loop of its value to vary the dwell time per pixel. Zero pixel values are removed through a shift register.

The 1D array is then reshaped to customise the dwell time of each individual pixel, as highlighted in figure A.4. Each pixel value is multiplied through a loop of its value and pixels with a 0 value are removed via a shift register to make sure the scanning coils do not dwell in this location.

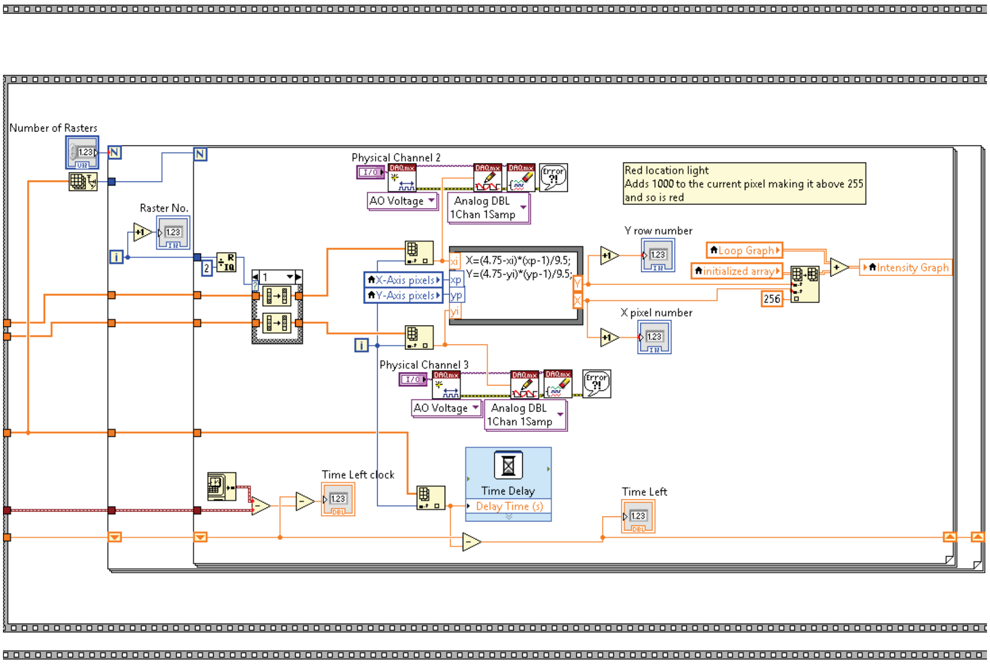

```
X=(4.75-xi)*(xp-1)/9.5;
Y=(4.75-yi)*(yp-1)/9.5;
```

Red location light
Adds 1000 to the current pixel making it above 255
and so is red

FIGURE A.5: The backpanel of the output is is shown in this screenshot. The 1D array is output to a physical x and y analog voltage channel. The number of rasters chosen determines how many loops of the pattern are performed.

The array is then output to a physical x and y analog voltage channel with their respective value fed into the NIDAQ board at the prescribed dwell time chosen during initialisation, this is shown in figure A.5. The number of rasters also chosen during initialisation determines the number of loops for this pattern to be output. The x and y location value is then also plot on the right hand side of the front panel to give a continuous feedback of the electron beam location. Time per pattern and time remaining are also calculated here and displayed on the front panel as well as the digital x and y co-ordinates.

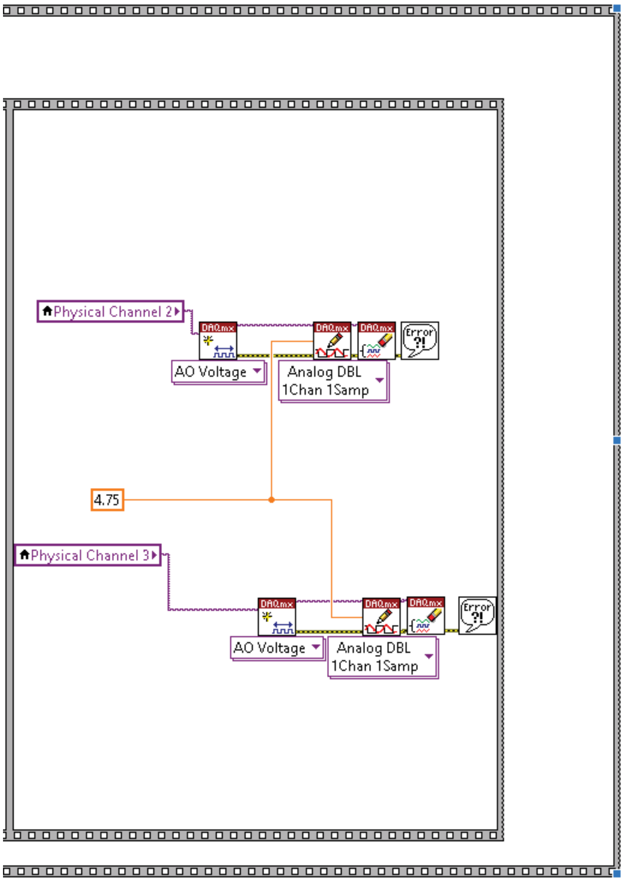

FIGURE A.6: Beam blanking backpanel screenshot for the scanning program is shown. The beam is placed to the topmost left when the program is idle.

When the pattern is complete or yet to initialise, the beam is put in the beam blanking position, and the back panel for this is illustrated in figure A.6. The blanked position is located on the topmost right of the scanning coils voltage to not effect the patterned work. A manual beam blanking override is also placed on the front panel to remove the beam from the pattern at any time during the scanning.

Appendix B

EBIE of narrowband Single Photon emitters in Nanodiamonds

B.1 Introduction

Fluorescent nanoparticles with bright, narrowband emissions are highly sought after for applications in biolabeling [266], quantum communications [267], and sensing [268]. Diamond nanocrystals are attracting major attention in this regard due to their ability to host room temperature, photostable single photon emitters [269]. Several known optically active defects such as the nitrogen vacancy (NV) [270] and silicon vacancy (SiV) [271] have been studied extensively, and their photo-physical properties are well understood. Yet, diamonds can host many other color centers that have not been explored to date [272, 273] and their origin remains unknown. During CVD, a growing diamond crystal often incorporates silicon and other impurities [274]. This has been utilized extensively to engineer SiV and other single photon emitters [275, 276]. In this study EBIE of nanodiamonds is used to show that narrowband, single photon emitters in CVD-grown nanodiamonds (full width at half-maximum (fwhm) < 5 nm) are localized predominantly at extended morphological defects such as twin boundaries and secondary nucleation sites.

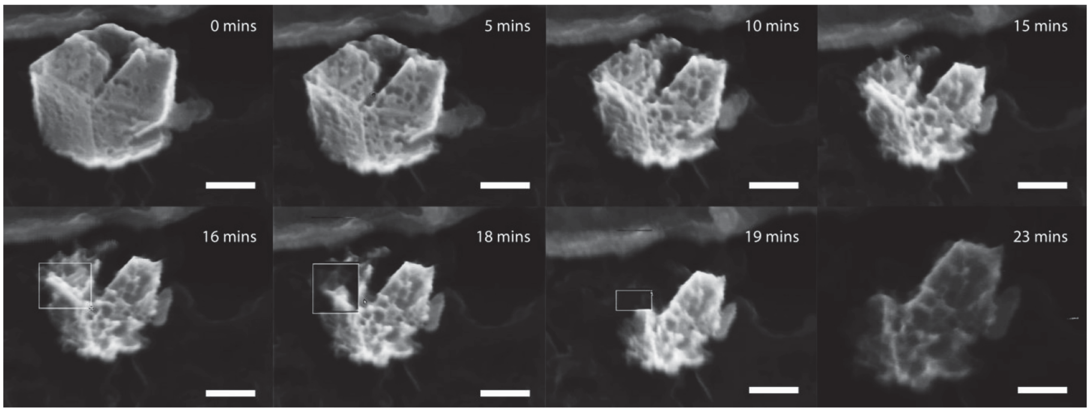

FIGURE B.1: SEM image sequence showing deterministic EBIE of a CVD grown nanodiamond on a silicon substrate. The scale bar is 500 nm. The bottom row shows reduced-area-EBIE demonstrating selective removal of a specific nanodiamond region.

B.2 Methods

The growth of nanodiamonds was performed using a microwave plasma CVD reactor with a hydrogen/methane ratio of 100:1 at 60 torr, a microwave power of 900 W from 46 nm detonation nanodiamond seeds. To achieve reproducible identification of individual nanodiamonds by photoluminescence and scanning electron microscopy, a grid pattern was deposited after the growth using standard photolithography procedure (AZ1505 photoresist).Electron beam induced etching was performed using a customised FEI Field Emission SEM (accelerating voltage = 15 kV, beam current = 1.35 nA, water vapour pressure = 8 Pa). The nanodiamonds were located using the SEM. Specific areas of the nanodiamonds were then selectively etched by raster scanning, which also enabled real time imaging of the etched nanodiamonds (figure B.1). The etching process is then stopped by blanking the electron beam.

B.3 Results and discussion

Figure B.2a,b show PL spectra recorded from individual defective and pristine nanodiamonds, respectively, grown on a silicon substrate. The insets show the corresponding SEM images of the nanodiamonds and schematic illustrations of their geometries for clarity. The nanodiamond in figure B.2a exhibits morphological defects, while figure B.2b shows a nearly perfect nanocrystal with a cuboctahedral symmetry [277]. The PL spectrum from the nearly perfect nanodiamond shown in figure B.2b is dominated by the SiV emission at 738 nm. A peak at 630 nm (1.967 eV) was observed in all the studied nanodiamonds. This centre is normally observed in CVD diamond films and is especially pronounced in nitrogen-doped films [272]. In the current work, the origin of this particular defect is not discussed. The results illustrate that morphological defects correlate with the narrowband emission lines (indicated by an arrow in figure B.2a). The morphological defects include major twinning that often occurs between the <111> planes of icosahedral nanodiamonds [278] (seen as dimples between adjacent triangular facets of the nanodiamonds) and secondary nucleation sites, a common morphological defect that forms when a nanodiamond nucleates on a pre-existing crystal, which forms a grain boundary along the nucleation site. Figure B.2c shows an additional spectrum recorded from a defective nanodiamond that exhibits a narrow, intense emission line at 700 nm, and figure B.2, panel d shows a second order correlation function, $g^{(2)}(\tau)$, which confirms that the line is a single photon emitter (as evidenced by the dip below 0.5 at $g^{(2)}(0)$). The autocorrelation measurement (figure B.2d) was performed using a band-pass filter illustrated using gray dotted lines in figure B.2c. The data were corrected for background using the equation $g_m^{(2)}(\tau) = [(g^{(2)} - (1 - p^2)]/p^2$ where p is the ratio between the emitter signal and the total count rate. In this particular case, 20% of the total signal was background related. The data were fit using a three-level model. Most of the narrowband lines that were observed in our experiments are in fact from single photon emitters indicating that they are point defects that are localized at the extended morphological defects visible in SEM images.

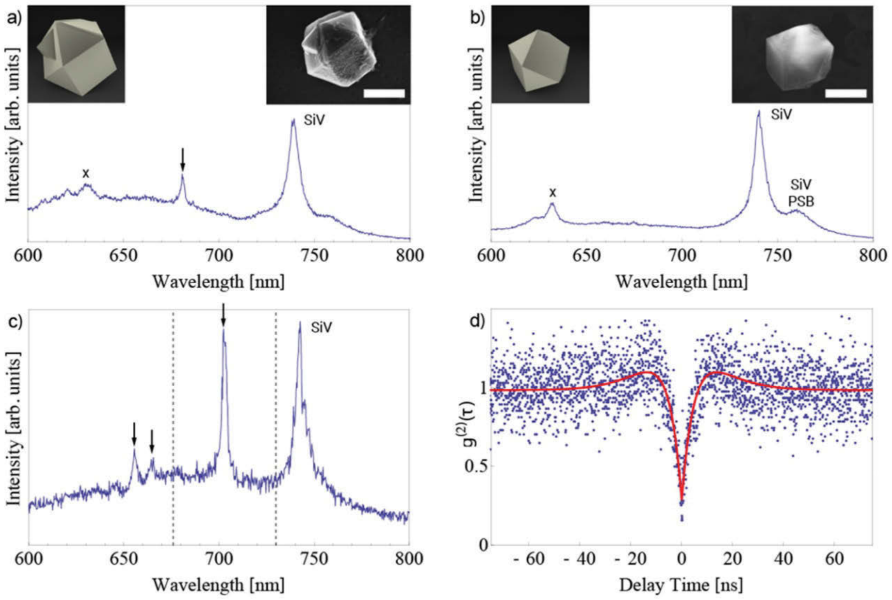

FIGURE B.2: (a) PL spectrum from a single nanodiamond containing morphological defects. (b) PL spectrum from a nearly perfect nanodiamond crystal. Insets in panels a and b are SEM images of the nanodiamonds and schematic illustrations of their geometries. Scale bars in both images are 500 nm. (c) PL spectrum from a different nanodiamond with morphological defects showing a narrow line at 700 nm. (d) Second-order autocorrelation function $g^{(2)}(\tau)$, recorded from the spectral region indicated by dashed lines in panel c. The dip at zero delay time indicates a single photon emitter. The solid red line is a fit to the data. The samples were grown on a silicon substrate, and the strong emission at 738 nm corresponds to the SiV center. Peak assignments: SiV = silicon vacancy, SiV PSB = silicon vacancy phonon sideband, X = CVD related peak at 630 nm, and the arrows indicate narrow-band emitters studied in this work.

To prove that the narrowband emitters are indeed localized at morphological defects, several nanodiamonds were selected and using electron beam induced etching (EBIE) in a H_2O environment the morphological defects were removed deterministically (figure B.3a). A time-lapse SEM image sequence showing EBIE of a single nanodiamond is shown in figure B.1. SEM images of the same nanodiamond taken before and after etching are shown in figure B.3b and c, respectively. The residual nanodiamond in figure B.3c is circled for clarity and is approximately 200 nm in size. The narrowband emission lines seen in figure B.3d (blue spectrum, taken prior to EBIE) were removed by the EBIE process (red spectrum). Yet, the remaining nanocrystal still exhibits a strong SiV emission (738 nm), which shows that the nanodiamonds are sufficiently large to host optically active color centers. These results solidify the hypothesis that the narrowband emissions in fluorescent nanodiamonds are point defects that decorate extended morphological defects such as twin boundaries and secondary nucleation sites.

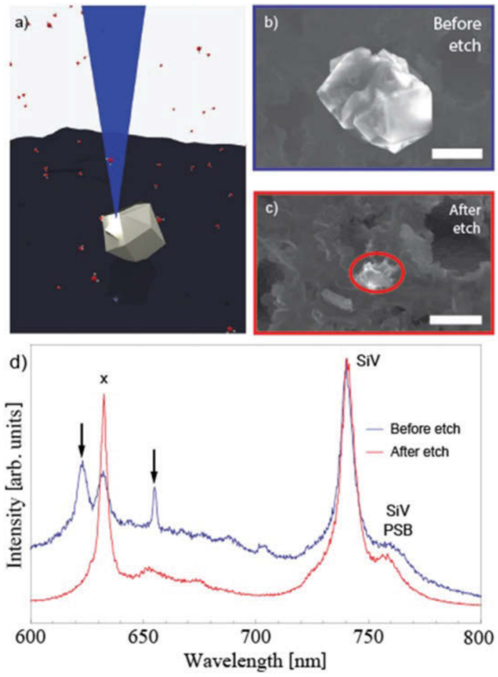

FIGURE B.3: (a) Schematic showing selective etching of an individual nanodiamond. (b, c) SEM images of the diamond crystal before and after electron beam induced etching. The red circle denotes the etched diamond. Scale bars in both images are 500 nm. (d) PL spectra collected before (blue curve) and after (red curve) the etch process. Spectra normalized to SiV peak. Peak assignments: SiV = silicon vacancy, PSB = silicon vacancy phonon sideband, X = CVD related peak at 630 nm, and the arrows indicate narrowband emitters.

B.4 Conclusion

Evidence is shown for a direct correlation between morphological defects, such as secondary nucleation sites and twin boundaries, and narrowband single photon emitters in nanodiamonds using EBIE of nanodiamonds. Removal of grain boundaries from nanodiamonds was also performed using EBIE which resulted in the elimination the narrowband emission lines.

B.5 Appendix contributions

Kerem Bray, Chris Elbadawi, Milos Toth, Igor Aharonovich and Charlene Lobo conceived the idea and planned the experiments. Chris Elbadawi performed the electron beam induced etching and imaging. Kerem Bray performed PL experiments and designed figures. Kerem Bray, Russell Sandstrom, Chris Elbadawi, Milos Toth, Igor Aharonovich and Charlene Lobo wrote and edited the appendix section.

Appendix C

Instability of Molybdenum trioxide monolayer emitters

C.1 Introduction

The thermally stable α-MoO$_3$ is another example of a 2D material with various promising applications in the field of optoelectronic [279] and sensing applications [280]. α-MoO$_3$ has shown excellent carrier mobilities and variable controlled band structure [281]. The polymorph structures of MoO$_3$ including α-MoO$_3$ are known to be sensitive to oxygen based defects [282]. Small changes in the concentration of oxygen vacancy defects can vary the properties of the material dramatically and understanding of this oxygen vacancy defect has enabled applications such as enhanced charge storage solutions [283]. In this work a photoluminescence study is conducted to probe the defects in the α-MoO$_3$ polymorph.

C.2 Methods

α-MoO$_3$ was exfoliated in solution using an ultrasonic probe [278], and dropcast onto a Si substrate. Confocal microscopy was then performed using a continuous wave (CW) 532 nm laser and a 0.7 NA objective. Excitation and scanning was performed in standard atmospheric conditions and in high vacuum using 300μW and 500μW of power respectively. More information on the confocal setup can be found in section

6.3.4.

C.3 Results and discussion

Performing PL on the prepared samples in high vacuum resulted in the discovery of defect emitters in α-MoO_3 as evidenced by the PL spectra captured in figure C.1b,d. Autocorrelation measurements were also performed and the $g^{(2)}(0)$ of the emitters was found to be 0.46 and 0.31 as is shown in figure C.1a,c proving to be SPE as both values recorded were under 0.5. After around 30 minutes both emitters failed, showing instability under continuous laser irradiation, indicating laser induced damage or restructuring of the defect.

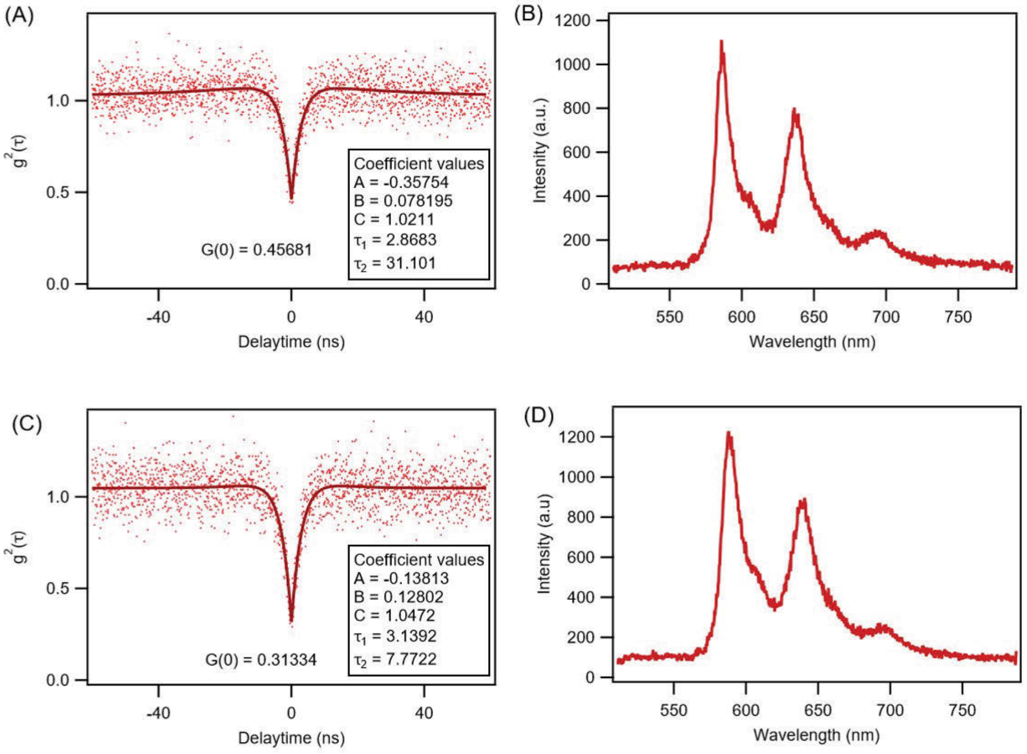

FIGURE C.1: Single photon emitters in MoO_3 monolayers. (a),(c) autocorrelation measurements of emitters found in (b), (d) respectively. Measurements were performed in high vacuum using a 500 μW laser power and 0.7 NA objective.

α-MoO$_3$ SPE stability measurements were then recorded for 20 minutes in high vacuum as shown in figure C.2a,c. Photoluminescent bleaching occurred after around 7 minutes of exposure to the emitter found in figure C.2c. The emitter found in figure C.2a however did not photobleach after 20 mins and a PL spectra was taken before and after the laser irradiation as shown in figure C.2b. Do note that this emitter eventually failed approximately 30 minutes after laser irradiation. The PL spectra for all emitters found in high vacuum show spectral stability and no signs of modification until the point of failure in the form of photobleaching.

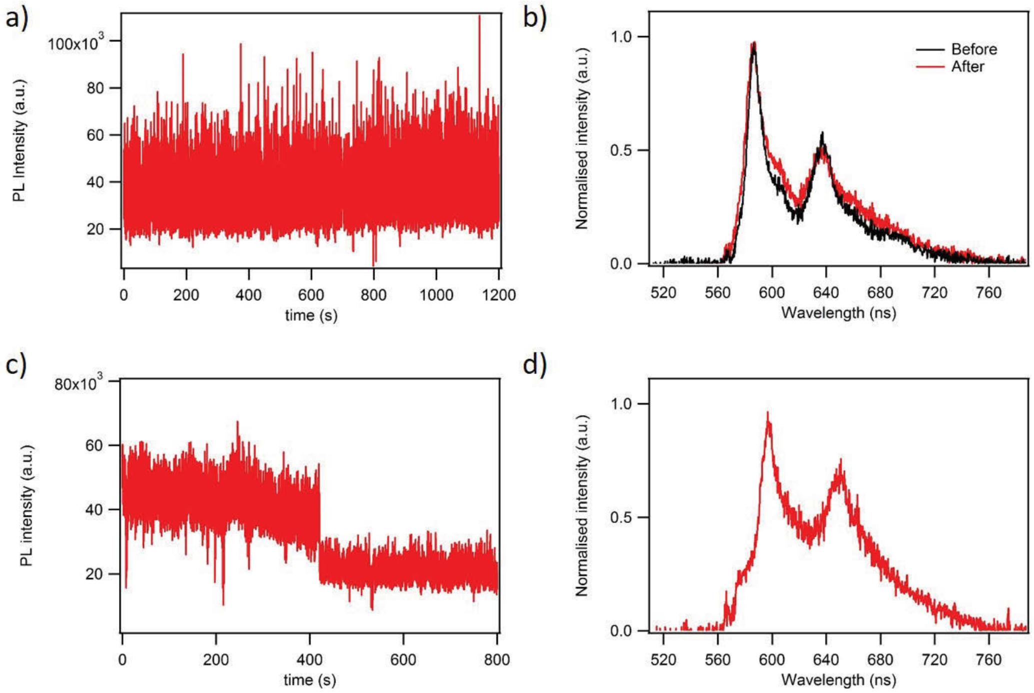

FIGURE C.2: (a), (b) PL stability over a 20 minute period and corresponding PL spectra in (b), (d). (b) shows spectra before and after stability measurements and (d) shows before only as photoluminescent bleaching occurred. after around 7 minutes of exposure. Measurements were done in vacuum at 500 μW power and 0.7 NA aperture.

Next the α-MoO$_3$ SPE stability measurements were recorded in standard atmospheric conditions using the same laser parameters as described above. A dramatic increase in the instability was found for all emitters probed, a sample of stability measurements are shown in figure C.3a,b. All emitters probed in atmosphere failed within 20 seconds and the blinking nature of these emitters are highlighted in figure C.3b. This result indicates that the defects are located in the topmost layers of α-MoO$_3$ as the emitters experience extreme sensitivity to the local environment in standard atmospheric conditions and under laser irradiation.

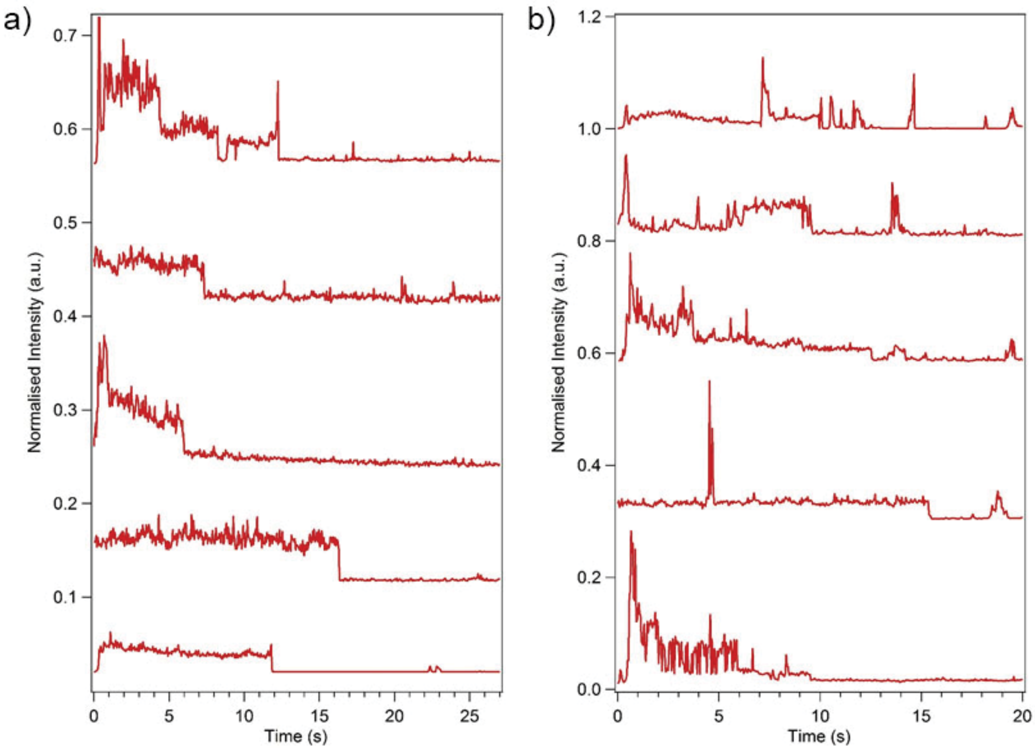

FIGURE C.3: (a) PL intensity of a number of different α-MoO$_3$ emitters in standard atmospheric conditions. (b) PL intensity highlighting the blinking nature of these emitters under laser irradiation. All measurements were done in atmosphere at 300 μW using a 532 nm laser and 0.7 NA aperture.

Next, a comparison of the PL spectrum of the α-MoO$_3$ SPE found in high vacuum and standard atmospheric conditions is shown in figure C.4. In all PL spectra acquired under high vacuum, the ZPL (590 nm) and PSB (645 nm) showed excellent spectral stability for a number of emitters as shown in figure C.4b. However PL spectral acquisitions performed in standard atmospheric conditions showed variable changes to the ZPL and PSB positions. Following a single emitter found, several PL acquisitions were taken over time as shown in figure C.4b, where a spectral shift of the ZPL is seen starting from 595 nm to 620 nm, a similar shift is also seen for the corresponding PSB. The SPE soon failed after these acquisitions. It is believed chemical reactions are taking place with the local environment under laser induced irradiation causing chemical damage and restructuring of the α-MoO$_3$. A few methods to isolate and stabilise the emitters was attempted. Various capping layers such as 20 nm layers of carbon and silica were applied over the α-MoO$_3$ to protect from the local environment. Unfortunately no SPE were found in vacuum or standard atmospheric conditions after the application of these layers, again indicating sensitivity to the local environment. Heating was also performed up to 300 °C, however this caused a change in the crystal structure of the material and PL emissions similar to the α-MoO$_3$ SPE were no longer found.

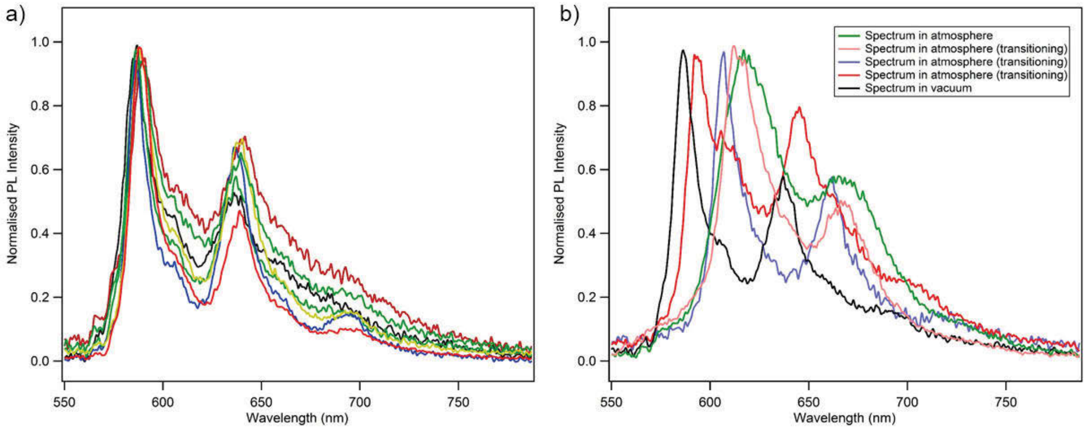

FIGURE C.4: A number of Pl spectra for various emitters found in high vacuum conditions are plotted in (a). (b) PL spectra from a single emitter in standard atmospheric conditions over time and a PL spectra from an emitter in high vacuum as a reference (black line). All measurements were done in atmosphere or high vacuum at 300 μW using a 532 nm laser and 0.7 NA aperture.

C.4 Conclusion

A discovery of extremely unstable single photon emitters was made in the 2D material α-MoO_3. Studying the PL characteristics, the emitters were found to be highly sensitive to standard atmospheric conditions under laser irradiation which caused chemical damage and restructuring of the α-MoO_3 defects. Steps were taken to improve the stability of the emitter with an extension of up to 30 minutes found using a high vacuum environment, but ultimately no long term stabilisation technique was found.

C.5 Appendix contributions

Chris Elbadawi, Igor Aharonovich and Charlene Lobo conceived the idea and planned the experiments. Chris Elbadawi performed all experiments and designed all figures. Chris Elbadawi wrote and edited the appendix section.

Appendix D

NF_3 irradiation of hBN

A recent first-principle investigation on the effects of edge terminated OH and H groups on hBN showed potential variable conducting properties. It was found that the energy gap between the highest occupied molecular state and lowest unoccupied state would vary based on edge termination [284]. Fluorine terminated hBN has also been reported to show a reduction in the band gap of hBN to approximately 3 eV [285]. As only the edge terminated regions were affected it was necessary to increase the edge to in-plane area ratio of the hBN sheets [286].

In this work the aim was to irradiate a hBN flake in a H_2O environment to create small hBN fragmentations (more details on this process can be found in section 7.4). The next step involved fluorination or hydrogenation of the hBN fragments using NF_3 and NH_3 irradiation which has previously been employed using electron beam irradiation [278]. The changes in conductivity were then monitored during irradiation using the *in-situ* nanomanipulator setup as shown in chapter 5. Unfortunately, no changes to the conductivity was detected under prolonged irradiation of 90 mins in H_2O, NF_3 and NH_3 with an electron fluence of 1.63×10^{20} electrons cm^{-2}. However during the intial stages of irradiation changes to the SE contrast on the e-beam exposed hBN flake occured and varied depending on the type of precursor gas introduced.

Localised darkening of the hBN flake is seen to occur with irradiation of NF_3 and H_2O. The contrast returns to its original contrast level after further H_2O irradiation,

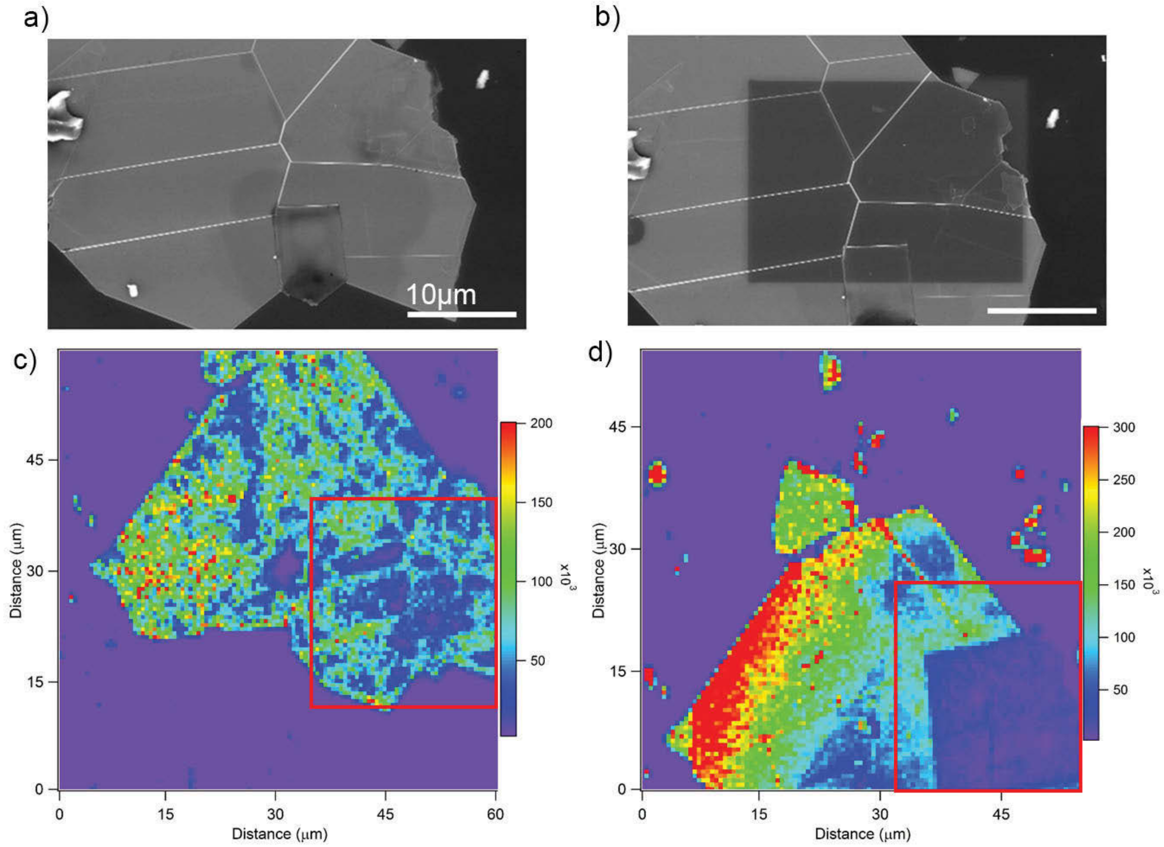

FIGURE D.1: SEM images of a large hBN flake before (a) and after (b) e-beam irradiation in a NF$_3$ environment. Confocal scans of the NF$_3$ irradiated region are also taken before and after. E-beam parameters of 15keV and an electron fluence of 1.63×10^{20} was used. PL was performed using a 532 nm laser at 300 μW.

whereas the contrast remains in a darkened state after further NF$_3$ irradiation, a comparision is shown in figure D.1a,b. As the SE contrast is linked to the electron affinity, this result indicates a change in surface termination and that fluorination of hBN possibly increases the energy barrier for electron ejection. The opposite effect is seen with hydrogen termination which causes a brightening effect when NH$_3$ e-beam irradiation is performed. Carbon contamination may also be a cause of the contrast change in NF$_3$, however this is unlikely as carbon contamination results in a general reduction in contrast of all features, however what is seen in figure D.1b, the contrast changes are localised on the hBN flake with no reduction in features. Confocal microscopy was then performed using a 532nm laser to see any changes to the photoluminescence response of the possible fluorine terminated hBN material and to rule out carbon contamination which typically results in bright and broadband emission over the visible region. From the result shown in figure D.1c,d irradiation of hBN in NF$_3$ shows a very localised and prominent quenching effect of the PL signal highlighted by the red box in figure D.1c,d. As a 532nm laser was used, the quenching effect likely indicates a change to a sub bandgap transition state rather then a variation of the hBN bandgap. Next, annealing is performed on the flake in an Ar environment for 30 mins (figure D.2a) and then extended to 60 mins (figure D.2b), followed with confocal microscopy after every anneal step. The result shows that the quenching effect diminishes after a 30 minute Ar anneal and is effectively reversed after a 60 mins Ar anneal, signifying a reverse of the surface termination of hBN and ruling out carbon contamination.

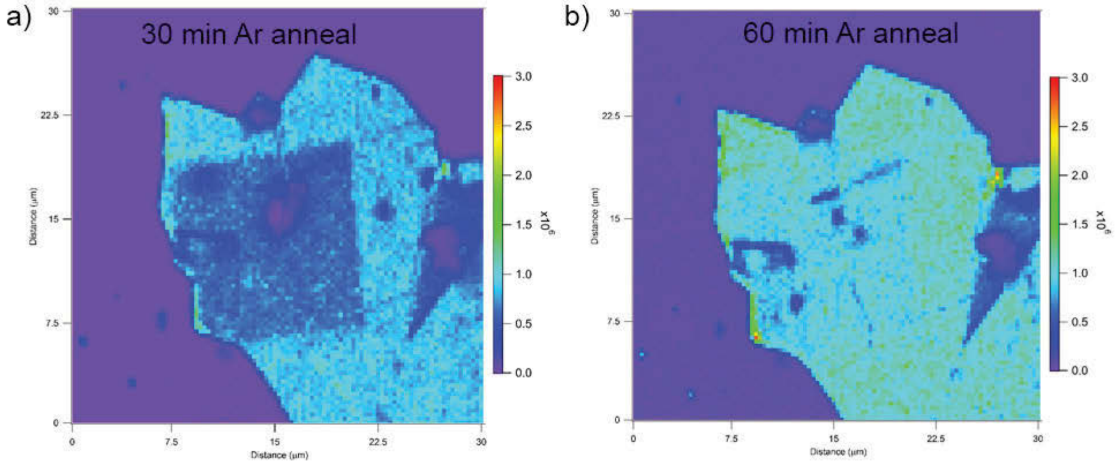

FIGURE D.2: Confocal scans on a NF$_3$ e-beam irradiated large hBN flake after Ar anneals performed for 30 minutes (a) and 60 minutes (b).

A gradient exposure in NF$_3$ was then performed to study a range of electron fluences of 1.81×10^{19} to 6.67×10^{20} electrons cm^{-2} as shown in figure D.3. Again we see darkening of the irradiated region as shown in figure D.3. Confocal scans were then performed on this gradient exposure, in the region of 1.81×10^{19} to 3.78×10^{20} electrons cm^{-2} quenching of the hBN flake is seen (excluding edges of hBN). At the higher electron dosages indicated by the region A1 in figure D.3b and an electron fluence of 3.78×10^{20} to 6.67×10^{20} electrons cm^{-2} a distinct PL signal appears as shown

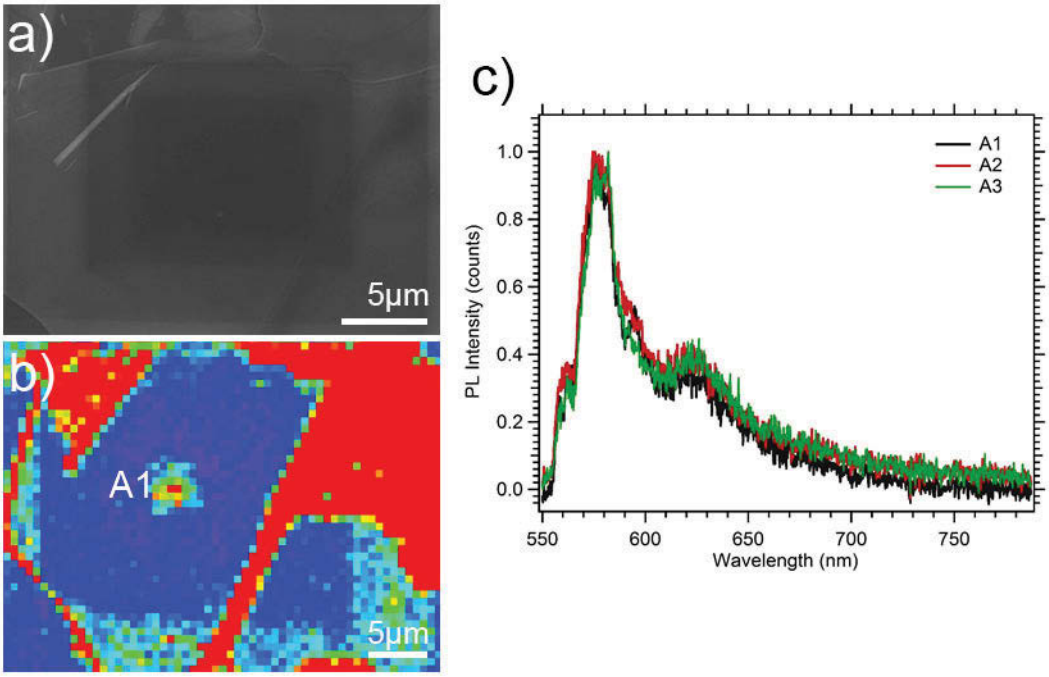

FIGURE D.3: SEM image (a) and confocal scan (b) of a large hBN flake e-beam irradiated in a NF_3 environment as a function of increasing electron beam fluence with the range of 1.81×10^{19} to 6.67×10^{20} electrons cm^{-2}. (c) shows PL spectra taken from three regions highlighted as A1 in (b).

in figure D.3c. This emission behaviour is unlike other emitters found in hBN as a consistently sharp PL profile at the same wavelength position is seen at all locations. Autocorrelation measurements were also taken and no dip was seen and therefore no single photon emitters detected. This could be due a number of reasons, for example as this peak shows up consistently in the region of A1, clusters of emitter formation may of occurred effectively reducing the chances of single photon emission. As the emission peak is consistent this fluorination could give an indication of a specific type of defect being formed in hBN. Another explanation could be a change in the structure of the hBN top layers due to semi fluorination, which is predicted to result in semi-metal or metal like behaviour [287]. An *in-situ* environmental photoyield spectroscopy setup is currently being installed which will enable the continued characterisation of these results.

D.1 Appendix contributions

Chris Elbadawi, Milos Toth, Igor Aharonovich and Charlene Lobo conceived the idea and planned the experiments. Chris Elbadawi performed all experiments and designed all figures. Chris Elbadawi wrote and edited the appendix section.

Appendix E

Plasma enhanced EBIE

E.1 Introduction

Electron beam induced etching (EBIE) has previously been deployed to etch a limited range of materials [35, 94, 288]. The limiting factor is due to limited choice of available etch precursors. In contrast, the scope of plasma etch processes extends much further in terms of etch-able materials via robust radical generation [289, 290]. In this work, a new hybrid-EBIE plasma process is explored as it extends nicely with AgNW etching work completed in Chapter 8 and has been subsequently deployed in a recently accepted publication [291]. It is the 1st proof-of-concept demonstration of an *in-situ* plasma and e-beam combination. Localised etching of Ag NWs using this procedure is thought to occur following a similar reaction process outlined in section 8.4.1. This is suggested through the combination of in-situ radical generation of precursor molecules via the delocalised plasma, and deterministic creation of highly active surface sites via the electron beam. The precursors used in this process include the use of N_2 and H_2O which are abundant, economical and environmentally friendly. Having the ability of etching silver and possibly other noble and transition metals directly at the nanoscale with clean and economically viable precursors has huge advantages, as these metals play a significant role in many phenomena and accompanying applications. These include photonic, optoelectronic and electroluminescent devices [292, 293], catalysis [294–297], plasmonics [298, 299] and roles in photo-catalysis [300], nanolasing [301], surface enhanced Raman spectroscopy [302] and bio-systems [303].

E.2 Methods and materials

E.2.1 Single crystal Ag nanowires preparation

The single crystal Ag NWs were grown using a rapid synthesis procedure [255, 304] (further details can be found in Chapter 8) and diluted to a ratio of 50:1, using 99.99% IPA.

E.2.2 Delocalised plasma parameters

The Evactron model c remote plasma unit was used for all EBIE experiments comprising of a plasma. A RF power of 5.5 Watts and frequency of 13.5 MHz was used for all plasma enhanced EBIE experiments. The plasma was sparked on an external port of the Nova NanoSEM chamber which results in a delocalised plasma within the chamber. Nitrogen was introduced into the chamber at a pressure of 7.5 Pa and H_2O introduced at 2.5 Pa for all plasma enhanced EBIE experiments, unless otherwise stated.

E.2.3 Electron beam parameters

All EBIE and plasma enhanced experiments were performed using 15 keV accelerating voltage, with 0.47 nA over a 1.1 μm^2 raster scan area using a focused Gaussian electron beam profile and the irradiation process was recorded in real time using a Helix detector immersion lens, which allows for ultra-high resolution imaging in a low vacuum environment. The raster consisted of 968 lines and a line dwell time of .8ms and all irradiations were performed for 20 minutes unless otherwise stated.

E.3 Results and discussion

Figure E.1a,b highlights the differing results achieved with and without a delocalised plasma in the system, respectively. Without a delocalised plasma present, no changes occurs to the Ag nanowires (Ag NWs) in a number of different environments including N_2, H_2O and N_2+H_2O over a 20 minute irradiation period, as shown in figure E.1a. Using the same environmental parameters with the addition of a delocalised plasma, in the presence of $N_2 + H_2O$ results in localized etching of Ag NWs under the electron beam, as illustrated in figure E.1b. This result suggests that the electron beam does not efficiently generate N radicals necessary for etching of Ag to occur (the reaction pathways for this etching process is illustrated in section 8.4.1). However, introducing a delocalised plasma into the system enables the generation of these radicals. The role of the electron beam then, is to create highly active surface sites on the Ag via bond breakage [39, 94] allowing for these radicals to further react deterministically on the Ag NWs.

The order of introduction of $N_2 + H_2O$ is likely an essential component for this technique to work. Introducing a delocalised plasma with H_2O only results in the complete non-volatile delocalised oxidation and degradation of the single crystal Ag NWs, this result is also shown in 8.1b. However, sparking a plasma with N_2 in the system, suggests no changes to the Ag NWs but indicates a passivating nature on the delocalised Ag NWs. By introducing H_2O into a N_2 plasma, does not result in the oxidation and degradation of the delocalised Ag NWs, but localised etching of Ag directly under the electron beam as shown in figure 8.1b H_2O + N_2.

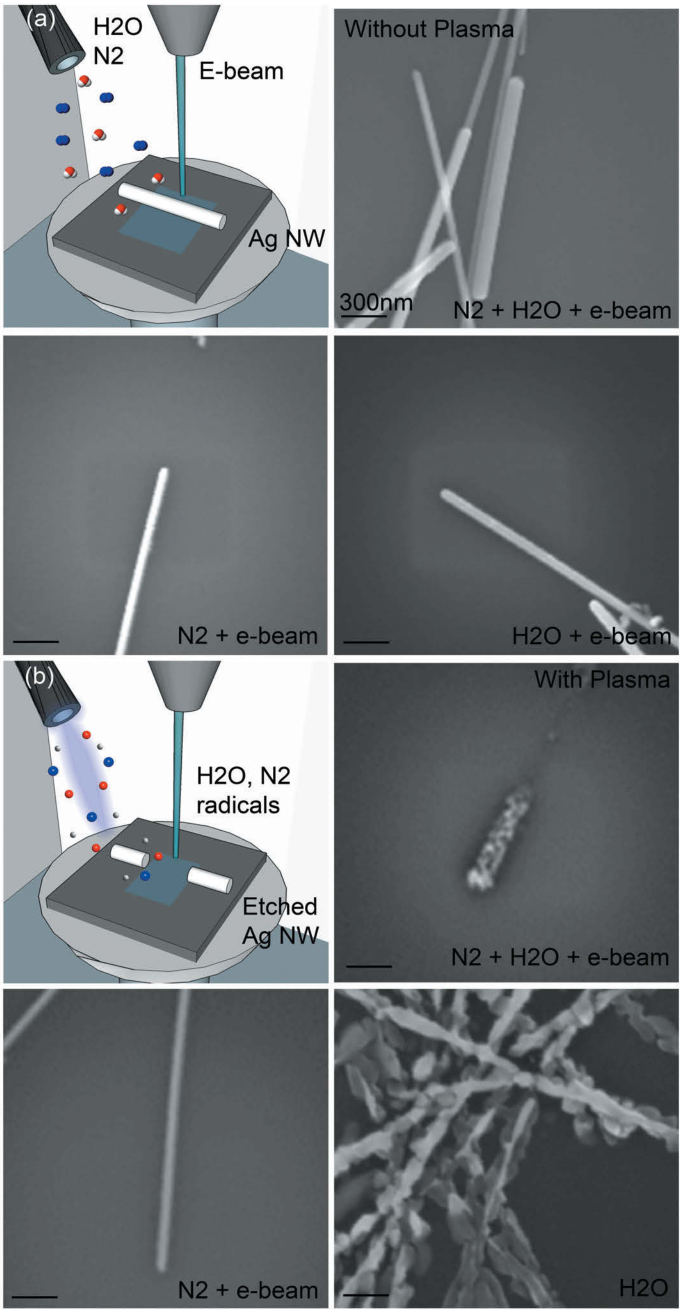

FIGURE E.1: A workflow summary of the plasma enhanced electron beam induced etching process is be shown. (a) illustrates a schematic of the electron beam irradiation process, followed by SEM images taken after 20 min electron beam irradiations of Ag nanowires on a SiO substrate in a N_2(7.5 Pa), H_2O(2.5Pa) and N_2 + H_2O (10 Pa) environment respectively. (b) illustrates a similar schematic, but with the addition of a delocalized plasma during gas flow. The corresponding SEM images were taken after a 20min e-beam exposure in N_2(7.5 Pa), H_2O(2.5 Pa) and N_2+H_2O(10 Pa) plasma environments. Electron beam irradiations were performed at 15 kV and beam current of 5.7 nA over a 1.1 μm^2 area.

The possible roles of N_2 and H_2O were then further broken down by isolating N and H radicals via a NH_3 plasma and irradiating for 20 minutes, this is shown in figure E.2. No observable changes are seen to occur to the Ag NWs in the presence of N and H radicals generated in a NH_3 plasma as can be seen in figure E.2c and d. Conversely, if N and O radicals are isolated, by introducing a N_2 + O_2 plasma, slight silver oxide formation is seen with no localised etching under electron beam exposure. Neither of these options were successful in etching Ag NWs and likely indicates that all three constituents (N, O and H) are necessary in a delocalised plasma for the etching of the Ag NWs under the electron beam, as discussed in section 8.4.1 where the N source is supplied via the substrate. This possibly indicates the importance of nitrogen as it is needed to passivate the nanowires from delocalised oxidation and degradation and to supply a source of nitrogen necessary for the reaction of Ag and nitric acid (again the chemical reaction pathways for etching of Ag are described in section 8.4.1). Due to the abundance of N radicals in the system as a higher proportion of N_2:H_2O precursor was used, there is a higher probability to terminate all Ag NWs on the substrate, while etching is restricted to generation of oxygen containing radicals under the e-beam to form the required nitrate species.

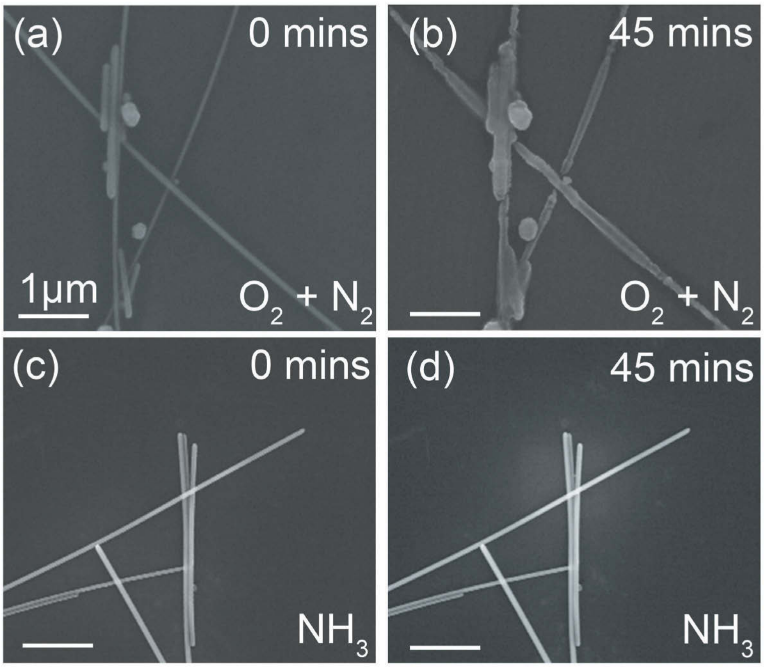

FIGURE E.2: SEM images were taken before (a) and after (b) a 45 min electron beam irradiation on Ag NWs on a SiO_2 substrate in a O_2(1.25Pa) + N_2(7.5Pa) delocalised plasma environment. c) and (d) before and after a 45 min exposure in a NH_3 (4 Pa) environment. Irradiation was performed at 15 kV, and 0.45 nA current over a $1.1 \mu m^2$ area.

E.3.1 Current dependent etching

Variable current experiments were undertaken next with a constant accelerating voltage, irradiation time and precursor pressure. The etching of the Ag NWs show a current dependence as illustrated in figure E.3. What may be occurring involves a competing process of oxidation and $AgNO_3$ volatilization. The role of the e-beam in this instance plays a detrimental role with increasing current density as there is a greater probability to breaks bonds and dissociate the $AgNO_3$ species leaving behind a stable silver oxide material as shown in figure E.3 b-d. This is then compared to figure E.3a which shows complete etching of the Ag NWs deterministically under e-beam irradiation and at a much lower current density.

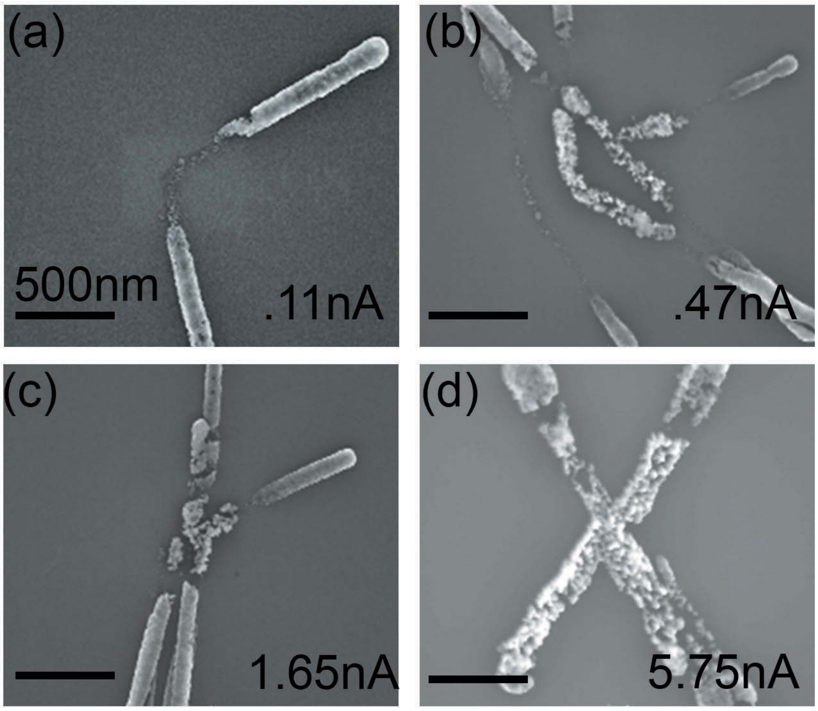

FIGURE E.3: A series of SEM images (a-d) of Ag NWs on a Si substrate after 20 mins of electron beam irradiations in a N_2(7.5 Pa) + H_2O(2.5 Pa) delocalised plasma environment as a function of increasing beam current, beam currents used denoted in the top right corner in a) – d). Electron beam accelerating voltage of 15 keV and 1.1 μm^2 area was used for all irradiations.

E.4 Conclusion

This work has showcased an innovative way to drive new chemical reactions locally using electron beam induced etching and introduction of a delocalised plasma. It is thought that the primary role of the electron beam in this instance is to locally create highly active surface sites. The role of the delocalised plasma was to generate the correct combination of radicals to attack and chemically dry etch the active surface sites on Ag made available under the electron beam. Further experimentations is currently being carried out to explain the results achieved and to extend the range of etch-able materials using this technique.

E.5 Appendix contributions

Chris Elbadawi and Milos Toth conceived the idea. Chris Elbadawi planned the experiments. Chris Elbadawi performed the delocalised plasma and electron beam irradiations and EDX analysis. Chris Elbadawi designed all figures. Chris Elbadawi wrote the appendix.

Bibliography

[1] Fengnian Xia et al. "Two-dimensional material nanophotonics". In: *Nature Photonics* 8.12 (2014), pp. 899–907.

[2] Paul Mulvaney. "Surface plasmon spectroscopy of nanosized metal particles". In: *Langmuir* 12.3 (1996), pp. 788–800.

[3] Ronald P Andres et al. "Self-assembly of a two-dimensional superlattice of molecularly linked metal clusters". In: *Science* 273.5282 (1996), p. 1690.

[4] Andres Castellanos-Gomez. "Why all the fuss about 2D semiconductors?" In: *arXiv preprint arXiv:1604.06425* (2016).

[5] Ganesh R Bhimanapati et al. "Recent advances in two-dimensional materials beyond graphene". In: (2015).

[6] Li Song et al. "Large scale growth and characterization of atomic hexagonal boron nitride layers". In: *Nano letters* 10.8 (2010), pp. 3209–3215.

[7] Joshua D Caldwell et al. "Sub-diffractional, volume-confined polaritons in a natural hyperbolic material: hexagonal boron nitride". In: *arXiv preprint arXiv:1404.0494* (2014).

[8] Han Liu et al. "Phosphorene: an unexplored 2D semiconductor with a high hole mobility". In: (2014).

[9] Anshuman Kumar et al. "Tunable light–matter interaction and the role of hyperbolicity in graphene–hBN system". In: *Nano letters* 15.5 (2015), pp. 3172–3180.

[10] Ruixiang Fei and Li Yang. “Strain-engineering the anisotropic electrical conductance of few-layer black phosphorus”. In: *Nano letters* 14.5 (2014), pp. 2884–2889.

[11] Peining Li et al. “Hyperbolic phonon-polaritons in boron nitride for near-field optical imaging and focusing”. In: *Nature communications* 6 (2015).

[12] S Dai et al. “Tunable phonon polaritons in atomically thin van der Waals crystals of boron nitride”. In: *Science* 343.6175 (2014), pp. 1125–1129.

[13] Frank HL Koppens, Darrick E Chang, and F Javier García de Abajo. “Graphene plasmonics: a platform for strong light–matter interactions”. In: *Nano letters* 11.8 (2011), pp. 3370–3377.

[14] E Del Corro et al. “Atypical Exciton–Phonon Interactions in WS2 and WSe2 Monolayers Revealed by Resonance Raman Spectroscopy”. In: *Nano letters* 16.4 (2016), pp. 2363–2368.

[15] Meysam Akhtar et al. “Recent advances in synthesis, properties, and applications of phosphorene”. In: *npj 2D Materials and Applications* 1.1 (2017), p. 5.

[16] Inanc Meric et al. “Current saturation in zero-bandgap, top-gated graphene field-effect transistors”. In: *Nature nanotechnology* 3.11 (2008), pp. 654–659.

[17] Toan T Tran et al. “Quantum emission from hexagonal boron nitride”. In: vol. 11. 1. Nature Publishing Group, 2016, pp. 37–41.

[18] Weinan Zhu et al. “Flexible black phosphorus ambipolar transistors, circuits and AM demodulator”. In: *Nano letters* 15.3 (2015), pp. 1883–1890.

[19] Fengnian Xia, Han Wang, and Yichen Jia. “Rediscovering black phosphorus as an anisotropic layered material for optoelectronics and electronics”. In: *Nature communications* 5 (2014), p. 4458.

[20] Jingsi Qiao et al. “High-mobility transport anisotropy and linear dichroism in few-layer black phosphorus”. In: *Nature communications* 5 (2014).

[21] Vy Tran et al. “Layer-controlled band gap and anisotropic excitons in few-layer black phosphorus”. In: *Physical Review B* 89.23 (2014), p. 235319.

[22] Zhe Luo et al. “Anisotropic in-plane thermal conductivity observed in few-layer black phosphorus”. In: *Nature communications* 6 (2015), p. 8572.

[23] Johannes V Barth, Giovanni Costantini, and Klaus Kern. “Engineering atomic and molecular nanostructures at surfaces”. In: *Nature* 437.7059 (2005), pp. 671–679.

[24] Ivo Utke, Stanislav Moshkalev, and Phillip Russell. *Nanofabrication using focused ion and electron beams: principles and applications*. Oxford University Press, Chapter 7, p. 286-321, 2012. Chap. 7, pp. 286–321.

[25] HWP Koops et al. “Conductive dots, wires, and supertips for field electron emitters produced by electron-beam induced deposition on samples having increased temperature”. In: *Journal of Vacuum Science & Technology B: Microelectronics and Nanometer Structures Processing, Measurement, and Phenomena* 14.6 (1996), pp. 4105–4109.

[26] Hans WP Koops et al. “Constructive three-dimensional lithography with electron-beam induced deposition for quantum effect devices”. In: *Journal of Vacuum Science & Technology B: Microelectronics and Nanometer Structures Processing, Measurement, and Phenomena* 11.6 (1993), pp. 2386–2389.

[27] Konrad Rykaczewski et al. “Maskless and resist-free rapid prototyping of three-dimensional structures through electron beam induced deposition (EBID) of carbon in combination with metal-assisted chemical etching (MaCE) of silicon”. In: *ACS applied materials & interfaces* 2.4 (2010), pp. 969–973.

[28] Jason D Fowlkes et al. “Simulation-Guided 3D nanomanufacturing via focused electron beam induced deposition”. In: *ACS nano* 10.6 (2016), pp. 6163–6172.

[29] Marco Esposito et al. “Nanoscale 3D chiral plasmonic helices with circular dichroism at visible frequencies”. In: *ACS Photonics* 2.1 (2014), pp. 105–114.

[30] Jason Brown et al. “Electrically conducting, ultra-sharp, high aspect-ratio probes for AFM fabricated by electron-beam-induced deposition of platinum”. In: *Ultramicroscopy* 133 (2013), pp. 62–66.

[31] M Rührig, S Porthun, and JC Lodder. “Magnetic force microscopy using electron-beam fabricated tips”. In: *Review of scientific instruments* 65.10 (1994), pp. 3224–3228.

[32] Katsuhisa Murakami and Mikio Takai. “Characteristics of nano electron source fabricated using beam assisted process”. In: *Journal of Vacuum Science & Technology B: Microelectronics and Nanometer Structures Processing, Measurement, and Phenomena* 22.3 (2004), pp. 1266–1268.

[33] Qing Tang et al. “Tuning band gaps of BN nanosheets and nanoribbons via interfacial dihalogen bonding and external electric field”. In: *Nanoscale* 6.15 (2014), pp. 8624–8634.

[34] Qunhong Weng et al. “Functionalized hexagonal boron nitride nanomaterials: emerging properties and applications”. In: *Chemical Society Reviews* 45.14 (2016), pp. 3989–4012.

[35] Aiden A Martin, Geoffrey McCredie, and Milos Toth. “Electron beam induced etching of carbon”. In: *Applied Physics Letters* 107.4 (2015), p. 041603.

[36] Sarah Goler et al. “Self-assembly and electron-beam-induced direct etching of suspended graphene nanostructures”. In: *Journal of Applied Physics* 110.6 (2011), p. 064308.

[37] Cornelius Thiele et al. “Controlled fabrication of single-walled carbon nanotube electrodes by electron-beam-induced oxidation”. In: *Applied Physics Letters* 99.17 (2011), p. 173105.

[38] Aiden A Martin, Milos Toth, and Igor Aharonovich. “Subtractive 3D printing of optically active diamond structures”. In: *Scientific reports* 4 (2014).

[39] Aiden A Martin et al. “Dynamic Pattern Formation in Electron-Beam-Induced Etching”. In: *Physical review letters* 115.25 (2015), p. 255501.

[40] Aiden A Martin, Matthew R Phillips, and Milos Toth. “Dynamic surface site activation: a rate limiting process in electron beam induced etching”. In: *ACS applied materials & interfaces* 5.16 (2013), pp. 8002–8007.

[41] Mingsheng Xu et al. "Graphene-like two-dimensional materials". In: *Chemical reviews* 113.5 (2013), pp. 3766–3798.

[42] Joshua O Island et al. "Environmental instability of few-layer black phosphorus". In: *2D Materials* 2.1 (2015), p. 011002.

[43] Toby W Shanley et al. "Localized chemical switching of the charge state of nitrogen-vacancy luminescence centers in diamond". In: *Applied Physics Letters* 105.6 (2014), p. 063103.

[44] Milos Toth. "Advances in gas-mediated electron beam-induced etching and related material processing techniques". In: *Applied Physics A* 117.4 (2014), pp. 1623–1629.

[45] Ivo Utke, Stanislav Moshkalev, and Phillip Russell. *Nanofabrication Using Focused Ion and Electron Beams*. Principles and Applications. Oxford University Press, USA, 2012.

[46] Willem F Van Dorp et al. "Approaching the resolution limit of nanometer-scale electron beam-induced deposition". In: *Nano letters* 5.7 (2005), pp. 1303–1307.

[47] W. F. Van Dorp et al. "Approaching the resolution limit of nanometer-scale electron beam-induced deposition". In: *Nano Lett.* 5.7 (Jan. 2005), pp. 1303–1307.

[48] Milos Toth et al. "Nanostructure fabrication by ultra-high-resolution environmental scanning electron microscopy." In: *Nano Lett.* 7.2 (Feb. 2007), pp. 525–530. ISSN: 1530-6984.

[49] Konrad Rykaczewski et al. "Maskless and resist-free rapid prototyping of three-dimensional structures through electron beam induced deposition (EBID) of carbon in combination with metal-assisted chemical etching (MaCE) of silicon." In: *ACS Appl. Mater. Interfaces* 2.4 (Apr. 2010), pp. 969–973. ISSN: 1944-8244.

[50] Amalio Fernández-Pacheco et al. "Three dimensional magnetic nanowires grown by focused electron-beam induced deposition". In: *Sci. Rep.* 3 (Mar. 2013), p. 1492. ISSN: 2045-2322.

[51] I. Utke et al. “High-resolution magnetic Co supertips grown by a focused electron beam”. In: *Appl. Phys. Lett.* 80.25 (Jan. 2002), pp. 4792–4794.

[52] V. Gopal et al. “Rapid prototyping of site-specific nanocontacts by electron and ion beam assisted direct-write nanolithography”. In: *Nano Lett.* 4.11 (Jan. 2004), pp. 2059–2063.

[53] Katja Hoeflich et al. “The Direct Writing of Plasmonic Gold Nanostructures by Electron-Beam-Induced Deposition”. In: *Adv. Mater.* 23.22-23 (June 2011), pp. 2657–2661.

[54] Martin Günter Jenke et al. “Toward Local Growth of Individual Nanowires on Three-Dimensional Microstructures by Using a Minimally Invasive Catalyst Templating Method”. English. In: *Nano Lett.* 11.10 (Oct. 2011), pp. 4213–4217.

[55] A Botman, J J L Mulders, and C W Hagen. “Creating pure nanostructures from electron-beam-induced deposition using purification techniques: a technology perspective.” In: *Nanotechnology* 20.37 (Sept. 2009), p. 372001. ISSN: 1361-6528.

[56] L. Rotkina, J.-F. Lin, and J. P. Bird. “Nonlinear current-voltage characteristics of Pt nanowires and nanowire transistors fabricated by electron-beam deposition”. In: *Appl. Phys. Lett.* 83.21 (2003), pp. 4426–4428. ISSN: 00036951.

[57] L. Rotkina et al. “Logarithmic behavior of the conductivity of electron-beam deposited granular Pt/C nanowires”. In: *Phys. Rev. B* 72.23 (Jan. 2005), p. 233407.

[58] F. Porrati et al. “Tuning the electrical conductivity of Pt-containing granular metals by postgrowth electron irradiation”. In: *J. Appl. Phys.* 109.6 (2011), p. 063715. URL: `http://www.scopus.com/inward/record.url?eid=2-s2.0-79953661192&partnerID=40&md5=2167e2a5190af8046c1deafeba87edbe`.

[59] F. Porrati et al. “Fabrication and electrical transport properties of binary Co-Si nanostructures prepared by focused electron beam-induced deposition”. English. In: *J. Appl. Phys.* 113.5 (2013), p. 053707.

[60] I. Utke et al. “Cross section investigations of compositions and sub-structures of tips obtained by focused electron beam induced deposition”. In: *Adv. Eng. Mater.* 7.5 (Jan. 2005), pp. 323–331.

[61] L Bernau et al. “Tunable Nanosynthesis of Composite Materials by Electron-Impact Reaction”. In: *Angew. Chem., Int. Ed.* 49.47 (2010), pp. 8880–8884.

[62] J. Li et al. “Evolution of the nanostructure of deposits grown by electron beam induced deposition”. In: *Appl. Phys. Lett.* 93.2 (2008), p. 023130.

[63] J. T. Li et al. “Interfacial mixing and internal structure of Pt-containing nanocomposites grown by room temperature electron beam induced deposition”. In: *J. Appl. Phys.* 107.10 (2010), p. 103540.

[64] R. Sachser et al. “Universal Conductance Correction in a Tunable Strongly Coupled Nanogranular Metal”. In: *Phys. Rev. Lett.* 107 (2011), 206803:1–5. URL: `http://link.aps.org/doi/10.1103/PhysRevLett.107.206803`.

[65] I. Utke et al. “Focused electron beam induced deposition of gold”. In: *J. Vac. Sci. Technol., B: Microelectron. Nanometer Struct.* 18.6 (2000), pp. 3168–3171.

[66] S. Wang et al. “Electron-beam induced initial growth of platinum films using Pt(PF[sub 3])[sub 4]”. In: *J. Vac. Sci. Technol., B: Microelectron. Nanometer Struct.* 22.4 (2004), pp. 1803–1806. ISSN: 0734211X.

[67] John D. Barry et al. “Electron beam induced deposition of low resistivity platinum from Pt(PF[sub 3])[sub 4]”. In: *J. Vac. Sci. Technol., B: Microelectron. Nanometer Struct.* 24.6 (2006), pp. 3165–3168. ISSN: 10711023.

[68] A. Botman, M. Hesselberth, and J. J. L. Mulders. “Investigation of morphological changes in platinum-containing nanostructures created by electron-beam-induced deposition”. In: *J. Vac. Sci. Technol., B: Microelectron. Nanometer Struct.* 26.6 (Jan. 2008), pp. 2464–2467.

[69] A. Botman et al. “Electron postgrowth irradiation of platinum-containing nanostructures grown by electron-beam-induced deposition from Pt(PF[sub 3])[sub

4]". In: *J. Vac. Sci. Technol., B: Microelectron. Nanometer Struct.* 27.6 (2009), pp. 2759–2763. ISSN: 10711023.

[70] Kees Landheer et al. "Low-Energy Electron-Induced Decomposition and Reactions of Adsorbed Tetrakis(trifluorophosphine)platinum [Pt(PF3)(4)]". In: *J. Phys. Chem. C* 115.35 (Sept. 2011), pp. 17452–17463.

[71] Samantha G. Rosenberg et al. "Substrate temperature and electron fluence effects on metallic films created by electron beam induced deposition". In: *J. Vac. Sci. Technol., B: Microelectron. Nanometer Struct.* 30.5 (2012), p. 051805. ISSN: 21662746.

[72] R Córdoba et al. "Microelectronic Engineering High-purity cobalt nanostructures grown by focused-electron-beam-induced deposition at low current". In: *Microelectron. Eng.* 87.5-8 (2010), pp. 1550–1553. ISSN: 0167-9317.

[73] J. J. L. Mulders, L M Belova, and A Riazanova. "Electron beam induced deposition at elevated temperatures: compositional changes and purity improvement". In: *Nanotechnology* 22.5 (Dec. 2011), p. 055302.

[74] James Bishop et al. "Role of Activated Chemisorption in Gas-Mediated Electron Beam Induced Deposition". In: *Phys. Rev. Lett.* 109.14 (Oct. 2012), p. 146103. ISSN: 0031-9007.

[75] K. Molhave et al. "Solid gold nanostructures fabricated by electron beam deposition". In: *Nano Lett.* 3.11 (Jan. 2003), pp. 1499–1503.

[76] A. Folch et al. "Electron-Beam Deposition Of Gold Nanostructures In A Reactive Environment". In: *Appl. Phys. Lett.* 66.16 (1995), pp. 2080–2082.

[77] A. Perentes and P. Hoffmann. "Focused electron beam induced deposition of Si-based materials from SiOxCy to stoichiometric SiO2: Chemical compositions, chemical-etch rates, and deep ultraviolet optical transmissions". In: *Chem. Vap. Deposition* 13.4 (Jan. 2007), pp. 176–184.

[78] T. Lukasczyk et al. “Electron-beam-induced deposition in ultrahigh vacuum: Lithographic fabrication of clean iron nanostructures”. In: *Small* 4.6 (Jan. 2008), pp. 841–846.

[79] T. Lukasczyk et al. “Generation of Clean Iron Structures by Electron-Beam-Induced Deposition and Selective Catalytic Decomposition of Iron Pentacarbonyl on Rh(110)”. In: *Langmuir* 25.19 (Jan. 2009), pp. 11930–11939.

[80] Matthew H. Ervin et al. “Annealing of electron beam induced deposits of platinum from Pt(PF[sub 3])[sub 4]”. In: *J. Vac. Sci. Technol., B: Microelectron. Nanometer Struct.* 25.6 (2007), pp. 2250–2254. ISSN: 10711023.

[81] Anastasia V Riazanova et al. “Pattern Shape Control for Heat Treatment Purification of Electron-Beam-Induced Deposition of Gold from the Me2Au(acac) Precursor”. In: *Langmuir* 28.14 (Apr. 2012), pp. 6185–6191.

[82] A Botman, JJL Mulders, and CW Hagen. “Creating pure nanostructures from electron-beam-induced deposition using purification techniques: a technology perspective”. In: *Nanotechnology* 20.37 (2009), p. 372001.

[83] Joachim Mayer et al. “TEM sample preparation and FIB-induced damage”. In: *MRS bulletin* 32.5 (2007), pp. 400–407.

[84] HF Wong et al. “Investigation of reactive ion etching induced damage in GaAs–AlGaAs quantum well structures”. In: *Journal of Vacuum Science & Technology B: Microelectronics Processing and Phenomena* 6.6 (1988), pp. 1906–1910.

[85] Michael J Burek et al. “Free-standing mechanical and photonic nanostructures in single-crystal diamond”. In: *Nano letters* 12.12 (2012), pp. 6084–6089.

[86] KS Novoselov et al. “2D materials and van der Waals heterostructures”. In: *Science* 353.6298 (2016), aac9439.

[87] R Lariviere Stewart. “Insulating films formed under electron and ion bombardment”. In: *Physical review* 45.7 (1934), p. 488.

[88] James Hillier. “On the investigation of specimen contamination in the electron microscope”. In: *Journal of Applied Physics* 19.3 (1948), pp. 226–230.

[89] AV Krasheninnikov and F Banhart. “Engineering of nanostructured carbon materials with electron or ion beams”. In: *Nature materials* 6.10 (2007), p. 723.

[90] Milos Toth et al. “Nanostructure fabrication by ultra-high-resolution environmental scanning electron microscopy”. In: *Nano letters* 7.2 (2007), pp. 525–530.

[91] I Utke et al. “Focused electron beam induced deposition of gold”. In: *Journal of Vacuum Science & Technology B: Microelectronics and Nanometer Structures Processing, Measurement, and Phenomena* 18.6 (2000), pp. 3168–3171.

[92] AE Ennos. “The origin of specimen contamination in the electron microscope”. In: *British Journal of Applied Physics* 4.4 (1953), p. 101.

[93] Shinji Matsui, Toshinari Ichihashi, and Masanobu Mito. “Electron beam induced selective etching and deposition technology”. In: *Journal of Vacuum Science & Technology B: Microelectronics Processing and Phenomena* 7.5 (1989), pp. 1182–1190.

[94] Christopher Elbadawi, Lu HuaáLi, et al. “Electron beam directed etching of hexagonal boron nitride”. In: *Nanoscale* 8.36 (2016), pp. 16182–16186.

[95] James Bishop et al. “Role of activated chemisorption in gas-mediated electron beam induced deposition”. In: *Physical review letters* 109.14 (2012), p. 146103.

[96] Michael Huth et al. “Focused electron beam induced deposition: A perspective”. In: *Beilstein journal of nanotechnology* 3 (2012), p. 597.

[97] I Utke et al. “Thermal effects during focused electron beam induced deposition of nanocomposite magnetic-cobalt-containing tips”. In: *Microelectronic engineering* 73 (2004), pp. 553–558.

[98] Ara Chutjian, Alan Garscadden, and Jogindra M Wadehra. “Electron attachment to molecules at low electron energies”. In: *Physics reports* 264.6 (1996), pp. 393–470.

[99] PC Post et al. “Parallel electron-beam-induced deposition using a multi-beam scanning electron microscope”. In: *Journal of Vacuum Science & Technology B,*

Nanotechnology and Microelectronics: Materials, Processing, Measurement, and Phenomena 29.6 (2011), 06F310.

[100] K_ Kanaya and S Okayama. “Penetration and energy-loss theory of electrons in solid targets”. In: *Journal of Physics D: Applied Physics* 5.1 (1972), p. 43.

[101] N Silvis-Cividjian et al. “The role of secondary electrons in electron-beam-induced-deposition spatial resolution”. In: *Microelectronic engineering* 61 (2002), pp. 693–699.

[102] Pierre Hovington, Dominique Drouin, and Raynald Gauvin. “CASINO: A new Monte Carlo code in C language for electron beam interaction—Part I: Description of the program”. In: *Scanning* 19.1 (1997), pp. 1–14.

[103] Kostya S Novoselov et al. “Electric field effect in atomically thin carbon films”. In: *science* 306.5696 (2004), pp. 666–669.

[104] Ruben Mas-Balleste et al. “2D materials: to graphene and beyond”. In: *Nanoscale* 3.1 (2011), pp. 20–30.

[105] Xi Ling et al. “The renaissance of black phosphorus”. In: *Proceedings of the National Academy of Sciences* 112.15 (2015), pp. 4523–4530.

[106] Damien Hanlon et al. “Liquid exfoliation of solvent-stabilized few-layer black phosphorus for applications beyond electronics”. In: *Nature communications* 6 (2015).

[107] Baisheng Sa et al. “Strain engineering for phosphorene: the potential application as a photocatalyst”. In: *The Journal of Physical Chemistry C* 118.46 (2014), pp. 26560–26568.

[108] Ankit Jain and Alan JH McGaughey. “Strongly anisotropic in-plane thermal transport in single-layer black phosphorene”. In: *Scientific reports* 5 (2015).

[109] Qun Wei and Xihong Peng. “Superior mechanical flexibility of phosphorene and few-layer black phosphorus”. In: *Applied Physics Letters* 104.25 (2014), p. 251915.

[110] AS Rodin, A Carvalho, and AH Castro Neto. “Strain-induced gap modification in black phosphorus”. In: *Physical review letters* 112.17 (2014), p. 176801.

[111] Ruixiang Fei et al. “Enhanced thermoelectric efficiency via orthogonal electrical and thermal conductances in phosphorene”. In: *Nano letters* 14.11 (2014), pp. 6393–6399.

[112] Tu Hong et al. “Polarized photocurrent response in black phosphorus field-effect transistors”. In: *Nanoscale* 6.15 (2014), pp. 8978–8983.

[113] Yan Li, Shengxue Yang, and Jingbo Li. “Modulation of the electronic properties of ultrathin black phosphorus by strain and electrical field”. In: *The Journal of Physical Chemistry C* 118.41 (2014), pp. 23970–23976.

[114] Likai Li et al. “Black phosphorus field-effect transistors”. In: *Nature nanotechnology* 9.5 (2014), pp. 372–377.

[115] Joshua D Wood et al. “Effective passivation of exfoliated black phosphorus transistors against ambient degradation”. In: *Nano letters* 14.12 (2014), pp. 6964–6970.

[116] Han Wang et al. “Black phosphorus radio-frequency transistors”. In: *Nano letters* 14.11 (2014), pp. 6424–6429.

[117] Michele Buscema et al. “Fast and broadband photoresponse of few-layer black phosphorus field-effect transistors”. In: *Nano letters* 14.6 (2014), pp. 3347–3352.

[118] Gaoxue Wang et al. “Degradation of phosphorene in air: understanding at atomic level”. In: *2D Materials* 3.2 (2016), p. 025011.

[119] Alexandre Favron et al. “Photooxidation and quantum confinement effects in exfoliated black phosphorus”. In: *Nature materials* 14.8 (2015), p. 826.

[120] Steven P Koenig et al. “Electric field effect in ultrathin black phosphorus”. In: *Applied Physics Letters* 104.10 (2014), p. 103106.

[121] Andres Castellanos-Gomez et al. “Isolation and characterization of few-layer black phosphorus”. In: *2D Materials* 1.2 (2014), p. 025001.

[122] Jiajie Pei et al. “Producing air-stable monolayers of phosphorene and their defect engineering”. In: *Nature communications* 7 (2016), p. 10450.

[123] Joohoon Kang et al. “Solvent exfoliation of electronic-grade, two-dimensional black phosphorus”. In: *ACS nano* 9.4 (2015), pp. 3596–3604.

[124] Angelo Ziletti et al. “Oxygen defects in phosphorene”. In: *Physical review letters* 114.4 (2015), p. 046801.

[125] Zhen Zhu and David Tománek. “Semiconducting layered blue phosphorus: a computational study”. In: *Physical review letters* 112.17 (2014), p. 176802.

[126] Gaoxue Wang, Ravindra Pandey, and Shashi P Karna. “Effects of extrinsic point defects in phosphorene: B, C, N, O, and F adatoms”. In: *Applied Physics Letters* 106.17 (2015), p. 173104.

[127] MT Edmonds et al. “Creating a stable oxide at the surface of black phosphorus”. In: *ACS applied materials & interfaces* 7.27 (2015), pp. 14557–14562.

[128] A Yoshihara et al. “Surface Brillouin scattering in black phosphorus”. In: *Physical Review B* 34.10 (1986), p. 7467.

[129] Kainen L Utt et al. “Intrinsic defects, fluctuations of the local shape, and the photo-oxidation of black phosphorus”. In: (2015).

[130] Kenji Watanabe and Takashi Taniguchi. “Hexagonal boron nitride as a new ultraviolet luminescent material and its application”. In: *International Journal of Applied Ceramic Technology* 8.5 (2011), pp. 977–989.

[131] KS Novoselov et al. “Two-dimensional atomic crystals”. In: *Proceedings of the National Academy of Sciences of the United States of America* 102.30 (2005), pp. 10451–10453.

[132] Lu Hua Li et al. “Large-scale mechanical peeling of boron nitride nanosheets by low-energy ball milling”. In: *Journal of materials chemistry* 21.32 (2011), pp. 11862–11866.

[133] Valeria Nicolosi et al. “Liquid exfoliation of layered materials”. In: *Science* 340.6139 (2013), p. 1226419.

[134] Cem Sevik et al. “Characterization of thermal transport in low-dimensional boron nitride nanostructures”. In: *Physical Review B* 84.8 (2011), p. 085409.

[135] Kenji Watanabe, Takashi Taniguchi, and Hisao Kanda. “Direct-bandgap properties and evidence for ultraviolet lasing of hexagonal boron nitride single crystal”. In: *Nature materials* 3.6 (2004), p. 404.

[136] Yi Lin and John W Connell. “Advances in 2D boron nitride nanostructures: nanosheets, nanoribbons, nanomeshes, and hybrids with graphene”. In: *Nanoscale* 4.22 (2012), pp. 6908–6939.

[137] Kenji Watanabe, Takashi Taniguchi, and Hisao Kanda. “Direct-bandgap properties and evidence for ultraviolet lasing of hexagonal boron nitride single crystal”. In: *Nature Materials* 3.6 (2004), pp. 404–409. ISSN: 1476-4660.

[138] Joshua D. Caldwell et al. “Sub-diffractional volume-confined polaritons in the natural hyperbolic material hexagonal boron nitride”. In: *Nature Communications* 5 (2014), p. 5221. ISSN: 2041-1723.

[139] Kohei Uosaki et al. “Boron Nitride Nanosheet on Gold as an Electrocatalyst for Oxygen Reduction Reaction: Theoretical Suggestion and Experimental Proof”. In: *Journal of the American Chemical Society* 136.18 (2014), pp. 6542–6545.

[140] S Dai et al. “Tunable phonon polaritons in atomically thin van der Waals crystals of boron nitride”. In: *Science* 343.6175 (2014), pp. 1125–1129.

[141] Toan Trong Tran et al. “Quantum emission from hexagonal boron nitride monolayers”. In: *Nature Nanotechnology* 11.1 (2015), pp. 37–41. ISSN: 1748-3395.

[142] Daniel Kleppner. “Inhibited spontaneous emission”. In: *Physical Review Letters* 47.4 (1981), p. 233.

[143] Susumu Noda, Masayuki Fujita, and Takashi Asano. “Spontaneous-emission control by photonic crystals and nanocavities”. In: *Nature photonics* 1.8 (2007), pp. 449–458.

[144] Mark Fox. *Quantum optics: an introduction*. Vol. 15. OUP Oxford, 2006.

[145] Simon Bone and Matias Castro. “A brief history of quantum computing”. In: *Imperial College in London, http://www. doc. ic. ac. uk/˜ nd/surprise_97/journa l/vol4/spb3* (1997).

[146] Glosser.ca. *Bloch Sphere.svg*. URL: `https://en.wikipedia.org/wiki/Bloch_sphere#/media/File:Bloch_Sphere.svg`.

[147] Igor Aharonovich, Dirk Englund, and Milos Toth. "Solid-state single-photon emitters". In: *Nature Photonics* 10.10 (2016), pp. 631–641.

[148] Andre K Geim and Irina V Grigorieva. "Van der Waals heterostructures". In: *arXiv preprint arXiv:1307.6718* (2013).

[149] Joshua D Caldwell et al. "Low-loss, infrared and terahertz nanophotonics using surface phonon polaritons". In: *Nanophotonics* 4.1 (2015), pp. 44–68.

[150] Joshua D Caldwell et al. "Atomic-scale photonic hybrids for mid-infrared and terahertz nanophotonics". In: *Nature nanotechnology* 11.1 (2016), pp. 9–15.

[151] S Dai et al. "Subdiffractional focusing and guiding of polaritonic rays in a natural hyperbolic material". In: *Nature communications* 6 (2015).

[152] Sanfeng Wu et al. "Monolayer semiconductor nanocavity lasers with ultralow thresholds". In: *nature* 520.7545 (2015), p. 69.

[153] Joseph Goldstein et al. *Scanning electron microscopy and X-ray microanalysis: a text for biologists, materials scientists, and geologists*. Springer Science & Business Media, 2012.

[154] Bradley L Thiel and Milos Toth. "Secondary electron contrast in low-vacuum/environmental scanning electron microscopy of dielectrics". In: *Journal of applied physics* 97.5 (2005), p. 4.

[155] Toby W Shanley et al. "Role of gas molecule complexity in environmental electron microscopy and photoelectron yield spectroscopy". In: *ACS applied materials & interfaces* 8.40 (2016), pp. 27305–27310.

[156] BL Thiel et al. "Two-stage gas amplifier for ultrahigh resolution low vacuum scanning electron microscopy". In: *Review of scientific instruments* 77.3 (2006), p. 033705.

[157] Charlene J Lobo et al. "Electron beam induced chemical dry etching and imaging in gaseous NH3 environments". In: *Nanotechnology* 23.37 (2012), p. 375302.

[158] Hendrix Demers et al. “Three-dimensional electron microscopy simulation with the CASINO Monte Carlo software”. In: *Scanning* 33.3 (2011), pp. 135–146.

[159] VD Scott and G Love. “Formulation of a universal electron probe microanalysis correction method”. In: *X-Ray Spectrometry* 21.1 (1992), pp. 27–35.

[160] Nicholas WM Ritchie et al. “Is Scanning Electron Microscopy/Energy Dispersive X-ray Spectrometry (SEM/EDS) Quantitative?” In: *Scanning* 35.3 (2013), pp. 141–168.

[161] Cepheiden. *EDX-Atommodell.gif*. URL: `https://commons.wikimedia.org/wiki/File:Atom_model_for_EDX_DE.svg`.

[162] Feng Liu, M Hohage, and MG Lagally. *Encyclopedia of Applied Physics*. 1999.

[163] Eric Lifshin. “Electron microprobe analysis”. In: *Materials Science and Technology* (1994).

[164] Chuan C Chang. “Auger electron spectroscopy”. In: *Surface Science* 25.1 (1971), pp. 53–79.

[165] David B Williams and C Barry Carter. “The transmission electron microscope”. In: *Transmission electron microscopy*. Springer, 1996, pp. 3–17.

[166] Gerd Binnig, Calvin F Quate, and Ch Gerber. “Atomic force microscope”. In: *Physical review letters* 56.9 (1986), p. 930.

[167] John Wiley & Sons Inc. *Characterization of Materials*. John Wiley & Sons, Incorporated, 2002. ISBN: 9780471266969.

[168] Shu-Lin Zhang. *Raman spectroscopy and its application in nanostructures*. John Wiley & Sons, 2012.

[169] A. J. M. Mackus et al. “Local deposition of high-purity Pt nanostructures by combining electron beam induced deposition and atomic layer deposition”. In: *J. Appl. Phys.* 107.11 (June 2010), p. 116102.

[170] S. Randolph, A. Botman, and M. Toth. In: *Particle* 30 (2013), pp. 672–677.

[171] Charlene J Lobo et al. “Electron beam induced chemical dry etching and imaging in gaseous NH3 environments.” In: *Nanotechnology* 23.37 (Oct. 2012), p. 375302.

[172] P. Hovington, D. Drouin, and R. Gauvin. “CASINO: A new Monte Carlo code in C language for electron beam interaction .1. Description of the program”. In: *Scanning* 19.1 (Jan. 1997), pp. 1–14.

[173] J. F. Friedman et al. “Electron attachment to $Ni(PF_3)_4$ and $Pt(PF_3)_4$.” In: *J. Chem. Phys* 128 (Mar. 2008), p. 104303.

[174] J Hern, G I Goldstein, and D. C. Joy. *Introduction to Analytical Electron Microscopy*. Plenum Press, 1st edition, 1979.

[175] W. Van Gelder and V. E. Hauser. “The Etching of Silicon Nitride in Phosphoric Acid with Silicon Dioxide as a Mask”. In: *J. Electrochem. Soc.* 114.8 (1967), pp. 869–872. ISSN: 00134651.

[176] Jack R Brent et al. “Production of few-layer phosphorene by liquid exfoliation of black phosphorus”. In: *Chemical Communications* 50.87 (2014), pp. 13338–13341.

[177] Manisha B Erande, Mahendra S Pawar, and Dattatray J Late. “Humidity sensing and photodetection behavior of electrochemically exfoliated atomically thin-layered black phosphorus nanosheets”. In: *ACS applied materials & interfaces* 8.18 (2016), pp. 11548–11556.

[178] Carmen C Mayorga-Martinez, Zdeněk Sofer, and Martin Pumera. “Layered black phosphorus as a selective vapor sensor”. In: *Angewandte Chemie* 127.48 (2015), pp. 14525–14528.

[179] Soo-Yeon Cho et al. “Superior Chemical Sensing Performance of Black Phosphorus: Comparison with MoS2 and Graphene”. In: *Advanced Materials* 28.32 (2016), pp. 7020–7028.

[180] Yijun Xu et al. “Selenium-Doped Black Phosphorus for High-Responsivity 2D Photodetectors”. In: *Small* 12.36 (2016), pp. 5000–5007.

[181] Jundong Shao et al. “Biodegradable black phosphorus-based nanospheres for in vivo photothermal cancer therapy”. In: *Nature communications* 7 (2016).

[182] Hyun Uk Lee et al. “Black phosphorus (BP) nanodots for potential biomedical applications”. In: *Small* 12.2 (2016), pp. 214–219.

[183] Sumeet Walia et al. “Defining the role of humidity in the ambient degradation of few-layer black phosphorus”. In: *2D Materials* 4.1 (2016), p. 015025.

[184] Sumeet Walia et al. “Ambient Protection of Few-Layer Black Phosphorus via Sequestration of Reactive Oxygen Species”. In: *Advanced Materials* (2017).

[185] Qionghua Zhou et al. “Light-Induced Ambient Degradation of Few-Layer Black Phosphorus: Mechanism and Protection”. In: *Angewandte Chemie* 128.38 (2016), pp. 11609–11613.

[186] Joon-Seok Kim et al. “Toward air-stable multilayer phosphorene thin-films and transistors”. In: *Scientific reports* 5 (2015).

[187] Saptarshi Das, Marcel Demarteau, and Andreas Roelofs. “Ambipolar phosphorene field effect transistor”. In: *ACS nano* 8.11 (2014), pp. 11730–11738.

[188] Junhong Na et al. “Few-layer black phosphorus field-effect transistors with reduced current fluctuation”. In: *ACS nano* 8.11 (2014), pp. 11753–11762.

[189] Xiaolong Chen et al. “High-quality sandwiched black phosphorus heterostructure and its quantum oscillations”. In: *Nature communications* 6 (2015), p. 7315.

[190] Y Cao et al. “Quality heterostructures from two-dimensional crystals unstable in air by their assembly in inert atmosphere”. In: *Nano letters* 15.8 (2015), pp. 4914–4921.

[191] Yuetao Zhao et al. “Surface coordination of black phosphorus for robust air and water stability”. In: *Angewandte Chemie* 128.16 (2016), pp. 5087–5091.

[192] Ahmet Avsar et al. “Air-stable transport in graphene-contacted, fully encapsulated ultrathin black phosphorus-based field-effect transistors”. In: *ACS nano* 9.4 (2015), pp. 4138–4145.

[193] Lu Li et al. “Phosphorene as a Polysulfide Immobilizer and Catalyst in High-Performance Lithium–Sulfur Batteries”. In: *Advanced Materials* 29.2 (2017).

[194] Mohammad Ziaur Rahman et al. “2D phosphorene as a water splitting photocatalyst: fundamentals to applications”. In: *Energy & Environmental Science* 9.3 (2016), pp. 709–728.

[195] Liangzhi Kou, Thomas Frauenheim, and Changfeng Chen. “Phosphorene as a superior gas sensor: selective adsorption and distinct I–V response”. In: *The journal of physical chemistry letters* 5.15 (2014), pp. 2675–2681.

[196] Shumao Cui et al. “Ultrahigh sensitivity and layer-dependent sensing performance of phosphorene-based gas sensors”. In: *Nature communications* 6 (2015), p. 8632.

[197] Harm Hinrich Rotermund. “Imaging surface reactions with a photoemission electron microscope”. In: *Journal of electron spectroscopy and related phenomena* 98 (1999), pp. 41–54.

[198] Zehua Hu et al. “Water-Catalyzed Oxidation of Few-Layer Black Phosphorous in Dark Environment”. In: *Angewandte Chemie International Edition* (2017).

[199] DW Boukhvalov et al. “Chemical modifications and stability of phosphorene with impurities: a first principles study”. In: *Physical Chemistry Chemical Physics* 17.23 (2015), pp. 15209–15217.

[200] S Dai et al. “Graphene on hexagonal boron nitride as a tunable hyperbolic metamaterial”. In: *Nature nanotechnology* 10.8 (2015), pp. 682–686.

[201] Guillaume Cassabois, Pierre Valvin, and Bernard Gil. “Hexagonal boron nitride is an indirect bandgap semiconductor”. In: *arXiv preprint arXiv:1512.02962* (2015).

[202] Mladen Petravic et al. “Decoration of nitrogen vacancies by oxygen atoms in boron nitride nanotubes”. In: *Physical Chemistry Chemical Physics* 12.47 (2010), pp. 15349–15353.

[203] I Aharonovich et al. “Diamond-based single-photon emitters”. In: *Reports on progress in Physics* 74.7 (2011), p. 076501.

[204] J Botsoa et al. “Optimal conditions for N V- center formation in type-1b diamond studied using photoluminescence and positron annihilation spectroscopies”. In: *Physical Review B* 84.12 (2011), p. 125209.

[205] JO Orwa et al. “Engineering of nitrogen-vacancy color centers in high purity diamond by ion implantation and annealing”. In: *Journal of applied physics* 109.8 (2011), p. 083530.

[206] Milos Toth et al. “Contamination-free imaging by electron induced carbon volatilization in environmental scanning electron microscopy”. In: *Journal of Applied Physics* 106.3 (2009), p. 034306.

[207] K-MC Fu et al. “Conversion of neutral nitrogen-vacancy centers to negatively charged nitrogen-vacancy centers through selective oxidation”. In: *Applied Physics Letters* 96.12 (2010), p. 121907.

[208] Sébastien Pezzagna et al. “Creation and nature of optical centres in diamond for single-photon emission—overview and critical remarks”. In: *New Journal of Physics* 13.3 (2011), p. 035024.

[209] Shuji Nakamura et al. “Hole compensation mechanism of p-type GaN films”. In: *Japanese Journal of Applied Physics* 31.5R (1992), p. 1258.

[210] Humberto R Gutiérrez et al. “Extraordinary room-temperature photoluminescence in triangular WS2 monolayers”. In: *Nano letters* 13.8 (2012), pp. 3447–3454.

[211] Kevin CY Huang et al. “Electrically driven subwavelength optical nanocircuits”. In: *Nature Photonics* 8.3 (2014), pp. 244–249.

[212] VM Huxter et al. “Vibrational and electronic dynamics of nitrogen-vacancy centres in diamond revealed by two-dimensional ultrafast spectroscopy”. In: *Nature Physics* 9.11 (2013), pp. 744–749.

[213] Christian Kurtsiefer et al. “Stable solid-state source of single photons”. In: *Physical review letters* 85.2 (2000), p. 290.

[214] Oliver Neitzke et al. “Investigation of line width narrowing and spectral jumps of single stable defect centers in ZnO at cryogenic temperature”. In: *Nano letters* 15.5 (2015), pp. 3024–3029.

[215] J Bernard et al. “Photon bunching in the fluorescence from single molecules: A probe for intersystem crossing”. In: *The Journal of chemical physics* 98.2 (1993), pp. 850–859.

[216] L Fleury et al. “Nonclassical photon statistics in single-molecule fluorescence at room temperature”. In: *Physical review letters* 84.6 (2000), p. 1148.

[217] T. Taniguchi and K. Watanabe. “Synthesis of high-purity boron nitride single crystals under high pressure by using Ba-BN solvent”. In: *Journal of Crystal Growth* 303.2 (2007), pp. 525–529.

[218] Yoichi Kubota et al. “Hexagonal Boron Nitride Single Crystal Growth at Atmospheric Pressure Using Ni- Cr Solvent”. In: *Chemistry of Materials* 20.5 (2008), pp. 1661–1663.

[219] Timothy B Hoffman et al. “Optimization of Ni–Cr flux growth for hexagonal boron nitride single crystals”. In: *Journal of Crystal Growth* 393 (2014), pp. 114–118.

[220] Sumin Choi et al. “Engineering and localization of quantum emitters in large hexagonal boron nitride layers”. In: *ACS applied materials & interfaces* 8.43 (2016), pp. 29642–29648.

[221] Yumeng Shi et al. “Synthesis of few-layer hexagonal boron nitride thin film by chemical vapor deposition”. In: *Nano letters* 10.10 (2010), pp. 4134–4139.

[222] Zai-Quan Xu et al. “Atomic Engineering of Single Photon Sources in 2D Boron Nitride Zai-Quan”. In: *arXiv preprint arXiv:1704.05154* (2017).

[223] Toan Trong Tran et al. “Robust multicolor single photon emission from point defects in hexagonal boron nitride”. In: *ACS nano* 10.8 (2016), pp. 7331–7338.

[224] Lifeng Wang et al. "Growth and Etching Kinetics: Growth and Etching of Monolayer Hexagonal Boron Nitride (Adv. Mater. 33/2015)." In: *Advanced materials* 27.33 (2015), pp. 4948–4948.

[225] Subash Sharma et al. "Opening of triangular hole in triangular-shaped chemical vapor deposited hexagonal boron nitride crystal". In: *Scientific Reports* 5 (2015), pp. 10426–10426.

[226] Yunlong Liao et al. "Oxidative Etching of Hexagonal Boron Nitride Toward Nanosheets with Defined Edges and Holes". In: *Scientific Reports* 5 (2015), p. 14510. ISSN: 2045-2322.

[227] Zheng Liu et al. "In-plane heterostructures of graphene and hexagonal boron nitride with controlled domain sizes". In: *Nature Nanotechnology* 8.2 (2013), pp. 119–124.

[228] Jannik C. Meyer et al. "Selective Sputtering and Atomic Resolution Imaging of Atomically Thin Boron Nitride Membranes". In: *Nano Letters* 9.7 (2009), pp. 2683–2689. ISSN: 1530-6992.

[229] Litao Sun, Florian Banhart, and Jamie Warner. "Two-dimensional materials under electron irradiation". In: *MRS Bulletin* 40.1 (2015), pp. 29–37.

[230] Gyeong Hee Ryu et al. "Atomic-scale dynamics of triangular hole growth in monolayer hexagonal boron nitride under electron irradiation". In: *Nanoscale* 7.24 (2015), pp. 10600–10605.

[231] S. Linas et al. "Nanochannel arrays etched into hexagonal boron nitride mesomembranes by a focused ion beam". In: *Rsc Advances* 5.61 (2015), pp. 49231–49234.

[232] Aiden A. Martin et al. "Dynamic Pattern Formation in Electron-Beam-Induced Etching". In: *Physical Review Letters* 115.25 (2015), pp. 255501–255501.

[233] Christopher R Arumainayagam et al. "Low-energy electron-induced reactions in condensed matter". In: *Surf. Sci. Rep.* 65.1 (Jan. 2010), pp. 1–44.

[234] I. Utke, P. Hoffmann, and J. Melngailis. “Gas-assisted focused electron beam and ion beam processing and fabrication”. In: *J. Vac. Sci. Technol. B* 26.4 (2008), pp. 1197–1276.

[235] S. J. Randolph, J. D. Fowlkes, and P. D. Rack. “Focused, nanoscale electron-bearn-induced deposition and etching”. In: *Critical Reviews In Solid State And Materials Sciences* 31.3 (2006), pp. 55–89.

[236] Ivo Utke and Armin Goelzhaeuser. “Small, Minimally Invasive, Direct: Electrons Induce Local Reactions of Adsorbed Functional Molecules on the Nanoscale”. In: *Angew Chem Int Edit* 49.49 (2010), pp. 9328–9330.

[237] M. Toth et al. “Nanostructure fabrication by ultra-high-resolution environmental scanning electron microscopy”. In: *Nano Letters* 7.2 (2007), pp. 525–530.

[238] Aiden A Martin, Matthew R Phillips, and M Toth. “Dynamic Surface Site Activation: A Rate Limiting Process in Electron Beam Induced Etching”. In: *ACS Applied Materials & Interfaces* 5.16 (Aug. 2013), pp. 8002–8007.

[239] Aiden A Martin, Geoffrey McCredie, and Milos Toth. “Electron beam induced etching of carbon”. In: *Applied Physics Letters* 107.4 (2015), p. 041603.

[240] DC Joy and S Luo. “An empirical stopping power relationship for low-energy electrons”. In: *Scanning* 11.4 (1989), pp. 176–180.

[241] Wing C Hui. “Secret of formulating a selective etching or cleaning solution for boron nitride (BN) thin film”. In: *Microelectronics, MEMS, and Nanotechnology*. International Society for Optics and Photonics. 2004, pp. 143–153.

[242] Son V Nguyen and David M Dobuzinsky. *Method for etching boron nitride*. US Patent 5,536,360. 1996.

[243] Yunlong Liao et al. “Oxidative etching of hexagonal boron nitride toward nanosheets with defined edges and holes”. In: *Scientific reports* 5 (2015).

[244] Younan Xia, Enoch Kim, and George M Whitesides. “Microcontact printing of alkanethiols on silver and its application in microfabrication”. In: *Journal of The Electrochemical Society* 143.3 (1996), pp. 1070–1079.

[245] Zheng Liu et al. “In-plane heterostructures of graphene and hexagonal boron nitride with controlled domain sizes”. In: *Nature nanotechnology* 8.2 (2013), pp. 119–124.

[246] Nasim Alem et al. “Atomically thin hexagonal boron nitride probed by ultrahigh-resolution transmission electron microscopy”. In: *Physical Review B* 80.15 (2009), p. 155425.

[247] SD Park et al. “Effects of Additive Gases on Ag Etching using Inductively Coupled Cl˜ 2-Based Plasmas”. In: *JOURNAL-KOREAN PHYSICAL SOCIETY* 42 (2003), S804–S808.

[248] Phucanh Nguyen, Yuxiao Zeng, and TL Alford. “Reactive ion etch of patterned and blanket silver thin films in Cl 2/O 2 and O 2 glow discharges”. In: *Journal of Vacuum Science & Technology B: Microelectronics and Nanometer Structures Processing, Measurement, and Phenomena* 17.5 (1999), pp. 2204–2209.

[249] Emily Aradi et al. “Ion beam modification of the structure and properties of hexagonal boron nitride: An infrared and X-ray diffraction study”. In: *Nuclear Instruments and Methods in Physics Research Section B: Beam Interactions with Materials and Atoms* 331 (2014), pp. 140–143.

[250] Adele C Tamboli et al. “Room-temperature continuous-wave lasing in GaN/InGaN microdisks”. In: *Nature photonics* 1.1 (2007), pp. 61–64.

[251] Daniela Stange et al. “Optically pumped GeSn microdisk lasers on Si”. In: *ACS Photonics* 3.7 (2016), pp. 1279–1285.

[252] David O Bracher and Evelyn L Hu. “Fabrication of high-Q nanobeam photonic crystals in epitaxially grown 4H-SiC”. In: *Nano letters* 15.9 (2015), pp. 6202–6207.

[253] Parag B Deotare et al. “High quality factor photonic crystal nanobeam cavities”. In: *Applied Physics Letters* 94.12 (2009), p. 121106.

[254] Amanuel M Berhane et al. “Bright Room-Temperature Single-Photon Emission from Defects in Gallium Nitride”. In: *Advanced Materials* 29.12 (2017).

[255] Toan Trong Tran et al. “Facile Self-Assembly of Quantum Plasmonic Circuit Components”. In: *Advanced Materials* 27.27 (2015), pp. 4048–4053.

[256] John Åhman, Göran Svensson, and Jörgen Albertsson. “A reinvestigation of β-gallium oxide”. In: *Acta Crystallographica Section C: Crystal Structure Communications* 52.6 (1996), pp. 1336–1338.

[257] Bernie M Penetrante, J Norman Bardsley, and Mark C Hsiao. “Kinetic analysis of non-thermal plasmas used for pollution control”. In: *Japanese journal of applied physics* 36.7S (1997), p. 5007.

[258] JD McKinley Jr, David Garvin, and MJ Boudart. “Production of Excited Hydroxyl Radicals in the Hydrogen Atom-Ozone Reaction”. In: *The Journal of Chemical Physics* 23.5 (1955), pp. 784–786.

[259] Amir Pakdel, Yoshio Bando, and Dmitri Golberg. “Plasma-assisted interface engineering of boron nitride nanostructure films”. In: *Acs Nano* 8.10 (2014), pp. 10631–10639.

[260] J Harju, A Winnberg, and JGA Wouterloot. “The distribution of OH in Taurus Molecular Cloud-1”. In: *Astronomy and Astrophysics* 353 (2000), pp. 1065–1073.

[261] David R Bates and Marcel Nicolet. “The photochemistry of atmospheric water vapor”. In: *Journal of Geophysical Research* 55.3 (1950), pp. 301–327.

[262] Simone Aloisio and Joseph S Francisco. “Radical- Water Complexes in Earth’s Atmosphere”. In: *Accounts of chemical research* 33.12 (2000), pp. 825–830.

[263] David Hanson and Konrad Mauersberger. “Laboratory studies of the nitric acid trihydrate: Implications for the south polar stratosphere”. In: *Geophysical Research Letters* 15.8 (1988), pp. 855–858.

[264] Paul J Crutzen and Frank Arnold. “Nitric acid cloud formation in the cold Antarctic stratosphere: a major cause for the springtime ‘ozone hole’”. In: *Nature* 324.6098 (1986), pp. 651–655.

[265] Ryo Ono and Tetsuji Oda. “Measurement of hydroxyl radicals in an atmospheric pressure discharge plasma by using laser-induced fluorescence”. In: *Industry Applications Conference, 1998. Thirty-Third IAS Annual Meeting. The 1998 IEEE*. Vol. 3. IEEE. 1998, pp. 1777–1783.

[266] V Vaijayanthimala et al. “The long-term stability and biocompatibility of fluorescent nanodiamond as an in vivo contrast agent”. In: *Biomaterials* 33.31 (2012), pp. 7794–7802.

[267] Helena S Knowles, Dhiren M Kara, and Mete Atatüre. “Observing bulk diamond spin coherence in high-purity nanodiamonds”. In: *Nature materials* 13.1 (2014), pp. 21–25.

[268] Philipp Neumann et al. “High-precision nanoscale temperature sensing using single defects in diamond”. In: *Nano letters* 13.6 (2013), pp. 2738–2742.

[269] Igor Aharonovich and Elke Neu. “Diamond nanophotonics”. In: *Advanced Optical Materials* 2.10 (2014), pp. 911–928.

[270] Marcus W Doherty et al. “The negatively charged nitrogen-vacancy centre in diamond: the electronic solution”. In: *New Journal of Physics* 13.2 (2011), p. 025019.

[271] Elke Neu et al. “Single photon emission from silicon-vacancy colour centres in chemical vapour deposition nano-diamonds on iridium”. In: *New Journal of Physics* 13.2 (2011), p. 025012.

[272] Alexander M Zaitsev. *Optical properties of diamond: a data handbook*. Springer Science & Business Media, 2013.

[273] D Gatto Monticone et al. “Native NIR-emitting single colour centres in CVD diamond”. In: *New Journal of Physics* 16.5 (2014), p. 053005.

[274] J Achard et al. “Coupled effect of nitrogen addition and surface temperature on the morphology and the kinetics of thick CVD diamond single crystals”. In: *Diamond and related materials* 16.4 (2007), pp. 685–689.

[275] Stefania Castelletto et al. “Production of multiple diamond-based single-photon sources”. In: *Ieee Journal of Selected Topics in Quantum Electronics* 18.6 (2012), pp. 1792–1798.

[276] Takayuki Iwasaki et al. “Germanium-vacancy single color centers in diamond”. In: *Scientific reports* 5 (2015).

[277] Amanda S Barnard. “Shape-dependent confinement of the nanodiamond band gap”. In: *Crystal Growth & Design* 9.11 (2009), pp. 4860–4863.

[278] Jason Valentine et al. “Three-dimensional optical metamaterial with a negative refractive index”. In: *nature* 455.7211 (2008), p. 376.

[279] Junpeng Lu et al. “Ultrasensitive phototransistor based on K-enriched MoO3 single nanowires”. In: *The Journal of Physical Chemistry C* 116.41 (2012), pp. 22015–22020.

[280] K Galatsis et al. “Sol–gel prepared MoO 3–WO 3 thin-films for O 2 gas sensing”. In: *Sensors and Actuators B: Chemical* 77.1 (2001), pp. 478–483.

[281] Sivacarendran Balendhran et al. “Enhanced charge carrier mobility in two-dimensional high dielectric molybdenum oxide”. In: *Advanced Materials* 25.1 (2013), pp. 109–114.

[282] Katherine Inzani et al. “A van der Waals Density Functional Study of MoO3 and Its Oxygen Vacancies”. In: *The Journal of Physical Chemistry C* 120.16 (2016), pp. 8959–8968.

[283] Hyung-Seok Kim et al. “Oxygen vacancies enhance pseudocapacitive charge storage properties of MoO3-x”. In: *Nature materials* 16.4 (2017), pp. 454–460.

[284] Dana Krepel and Oded Hod. “Effects of Edge Oxidation on the Structural, Electronic, and Magnetic Properties of Zigzag Boron Nitride Nanoribbons”. In: *Journal of chemical theory and computation* 10.1 (2013), pp. 373–380.

[285] A Bhattacharya, S Bhattacharya, and GP Das. “Band gap engineering by functionalization of BN sheet”. In: *Physical Review B* 85.3 (2012), p. 035415.

[286] Zhuhua Zhang and Wanlin Guo. “Energy-gap modulation of BN ribbons by transverse electric fields: first-principles calculations”. In: *Physical Review B* 77.7 (2008), p. 075403.

[287] Yanli Wang and Yi Ding. “Structural, electronic, and magnetic properties of the semifluorinated boron nitride bilayer: a first-principles study”. In: *The Journal of Physical Chemistry C* 117.6 (2013), pp. 3114–3121.

[288] Aiden A Martin and Milos Toth. “Cryogenic electron beam induced chemical etching”. In: *ACS applied materials & interfaces* 6.21 (2014), pp. 18457–18460.

[289] Daniel L Flamm and Dennis M Manos. *Plasma Etching: An Introduction*. Academic Press, 1989.

[290] Orlando Auciello and Daniel L Flamm. *Plasma Diagnostics: Discharge parameters and chemistry*. Vol. 1. Academic Press, 2013.

[291] J Bishop et al. “Deterministic Nanopatterning of Diamond Using Electron Beams”. In: *ACS Nano* (2017).

[292] K Kalyanasundaram and M Grätzel. “Applications of functionalized transition metal complexes in photonic and optoelectronic devices”. In: *Coordination chemistry reviews* 177.1 (1998), pp. 347–414.

[293] Elisabeth Holder, Bea MW Langeveld, and Ulrich S Schubert. “New trends in the use of transition metal–ligand complexes for applications in electroluminescent devices”. In: *Advanced Materials* 17.9 (2005), pp. 1109–1121.

[294] Barry M Trost and Matthew L Crawley. “Asymmetric transition-metal-catalyzed allylic alkylations: applications in total synthesis”. In: *Chemical reviews* 103.8 (2003), pp. 2921–2944.

[295] Christopher K Prier, Danica A Rankic, and David WC MacMillan. “Visible light photoredox catalysis with transition metal complexes: applications in organic synthesis”. In: *Chemical reviews* 113.7 (2013), pp. 5322–5363.

[296] John D Aiken and Richard G Finke. “A review of modern transition-metal nanoclusters: their synthesis, characterization, and applications in catalysis”. In: *Journal of Molecular Catalysis A: Chemical* 145.1 (1999), pp. 1–44.

[297] William L Barnes, Alain Dereux, and Thomas W Ebbesen. “Surface plasmon subwavelength optics”. In: *nature* 424.6950 (2003), p. 824.

[298] Matthew Rycenga et al. “Controlling the synthesis and assembly of silver nanostructures for plasmonic applications”. In: *Chemical reviews* 111.6 (2011), pp. 3669–3712.

[299] Andrea Tao, Prasert Sinsermsuksakul, and Peidong Yang. “Tunable plasmonic lattices of silver nanocrystals”. In: *Nature nanotechnology* 2.7 (2007), pp. 435–440.

[300] Koichi Awazu et al. “A plasmonic photocatalyst consisting of silver nanoparticles embedded in titanium dioxide”. In: *Journal of the American Chemical Society* 130.5 (2008), pp. 1676–1680.

[301] Yu-Jung Lu et al. “Plasmonic nanolaser using epitaxially grown silver film”. In: *science* 337.6093 (2012), pp. 450–453.

[302] Shuming Nie and Steven R Emory. “Probing single molecules and single nanoparticles by surface-enhanced Raman scattering”. In: *science* 275.5303 (1997), pp. 1102–1106.

[303] Prashant K Jain et al. “Review of some interesting surface plasmon resonance-enhanced properties of noble metal nanoparticles and their applications to biosystems”. In: *Plasmonics* 2.3 (2007), pp. 107–118.

[304] Kylee E Korte, Sara E Skrabalak, and Younan Xia. “Rapid synthesis of silver nanowires through a CuCl-or CuCl 2-mediated polyol process”. In: *Journal of Materials Chemistry* 18.4 (2008), pp. 437–441.